# Quantum gas engineering for atomic clocks

by

**Lindsay I. Sonderhouse**

B.A., Reed College, 2013

M.S., University of Colorado Boulder, 2020

A thesis submitted to the

Faculty of the Graduate School of the

University of Colorado in partial fulfillment

of the requirements for the degree of

Doctor of Philosophy

Department of Physics

2021

Committee Members:

Jun Ye, Chair

Ana Maria Rey

James K Thompson

Scott A Diddams

Vanja Dukic

Sonderhouse, Lindsay I. (Ph.D., Physics)

Quantum gas engineering for atomic clocks

Thesis directed by Prof. Jun Ye

Optical atomic clocks with high precision allow minute frequency shifts to be measured in short timescales. Low instability requires an atomic frequency reference with a high quality factor that is prepared in the minimal amount of time. The advent of the Fermi-degenerate three-dimensional (3D) optical lattice clock demonstrated that significant advances in precision metrology can be made by incorporating ultracold quantum gases. This thesis focuses on improving the precision of Fermi-degenerate clocks beyond their initial record demonstration by optimizing the preparation, characterization, and scattering properties of degenerate Fermi gases (DFGs). We first demonstrate that the SU(N)-symmetric nuclear spin degree of freedom in $^{87}$Sr can be used as a tool to enhance cooling to quantum degeneracy. This allows us to rapidly prepare a DFG, evaporating to temperatures of 0.2 times the Fermi temperature in only 600 ms. With this and a new spin-polarizing method, we can prepare a spin-polarized degenerate gas in under 3 s. We also systematically study the thermodynamics of the gas, measuring up to a 20% reduction of the compressibility due to repulsive SU(N) interactions. We next explore how the natural lifetime of an atomic state can be increased by embedding excitations within a degenerate Fermi gas. With a light scattering experiment, we angularly resolve the suppression of the photon scattering rate and measure up to a factor of two reduction near the absorption direction, where the momentum transfer from the light is reduced. Our results agree with semiclassical calculations across a range of temperatures and Fermi energies. Finally, we discuss an experiment that attempts to directly measure an increase in the natural lifetime of a narrow-linewidth transition. This Pauli blocking mechanism provides a means to quantum engineer devices with decoherence rates below what nature would provide alone.

# Dedication

To all my mentors that have shown me how to think like a successful physicist and that have demonstrated unbounded patience and kindness.

# Acknowledgements

I cannot begin to thank people enough for making me the scientist I am today. Graduate school can be a rough time as you learn to be a competent scientist, and tough experiments require a great team to not only look at problems from many angles, but to provide support and encouragement along the way. I am beyond lucky to get the opportunity to work with such an excellent team, one that works hard, thinks critically, and takes considerable time out of their day to help and provide feedback to others. There is a certain special bond you make with people that you struggle very hard with on an important and fun problem. While you experience great frustration together, you also experience childlike wonder, a truly special feeling that tends to put all other things in life into perspective. For the science family I have developed here I am eternally grateful.

I first want to thank my advisor, Jun Ye. Jun is a one-of-a-kind scientist, perhaps the most optimistic and passionate scientist I have ever met. Jun has taught me to always be engaged with what other scientists are telling you, and to ask questions about the details as they are what really matter. He has also taught me how special it is to create a sense of urgency in others through enthusiasm. Getting others excited about what you are doing is certainly the best way to encourage hard work. He has spent so much time with each of his students, which is truly outstanding given how busy he is. I am incredibly grateful for how much feedback he has given me over the years, and how much he advocates for his students.

I was lucky enough to work closely with Christian Sanner for the majority of the work reported in this thesis. Christian is incredibly patient, kind, and knowledgeable about technical things such as optics, electronics, and imaging, but also about a range of fundamental physics topics. I have learned so much from him throughout my time here. I greatly admire his methodical attitude to solving problems, his communication skills, and his creativity. I will never forget the roller coaster of discoveries we experienced while working on the Pauli blocking project, and how we supported one another when the other was feeling pessimistic on progress (and, of course, when we were both down we could always count on Jun to lift up our spirits). I always looked forward to our daily ‘brainstorming’ sessions before going down to lab, something I hope to replicate in my future projects as it was always a beneficial alignment for the day and a chance to think critically and broadly about our project.

I worked with such a great number of other people. Ross Hutson always seems to know every answer, and has spent a lot of time helping others with FPGA programming among other things. He will succeed at whatever he decides to devote his time to. Aki Goban really helped me begin to step into the arena. Will Milner is an incredibly hard worker and is constantly looking for new things to do and problems to solve. With his dedication, he will continue to grow as a scientist throughout the rest of his life. Lingfeng Yan has remarkable fortitude. Ed Marti spent many helpful hours with me as a new student and always had a lot of insight into whatever problem I was facing. I am very grateful for the time I spent with Eric Oelker, a kind, thoughtful scientist who knows infinite things about feedback loops and electronics. I admire Sara Campbell’s attitude of self-determinism, and her immense technical skills. Colin Kennedy is a quick thinker and physics problem solver, as well as having his eye more broadly on interesting scientific problems. Toby Bothwell is a very practical physicist who likes to work on problems that will immediately improve the devices we work with. Alex Aeppli got up to speed very quickly on the Sr1 project and will be a great person to take over Sr1 in the future. Sarah Bromley’s outcome-oriented attitude is an inspiration. Shimon Kolkowitz gave me some of the best advice on giving talks I have ever received when I was a new PhD student. John Robinson is admirably technically competent. Maya Miklos is a fast learner, asks on-point questions, and knows an incredible amount about AMO. Ming Tso is a kind and a careful thinker. I’m positive Maya and him will do more than just squeeze their way towards success. Dhruv Kedar has incredible perseverance in addition to a wealth of knowledge on technical details and AMO physics. Alex Staron is incredibly positive and kind, and is a do'er. Craig Benko selflessly helped me at a hard stage of my graduate career. Wei Zhang is a very hard worker and is willing to spend a lot of his free time helping others. Thank you to Jan who always inspired an ego free curiosity in all aspects of science.

I am also grateful for Ana Maria Rey, who has always been very supportive of me and my development, and has provided a very fruitful experiment-theory collaboration. Thomas Bilitewski has been a great theory partner and has put up with my many questions, as has Asier Orioli. The machine and electronics shop members have been outstanding; I particularly admire Hans Green's optimism and happiness. Making others around you happy is one of the most significant ways you can positively affect this planet, and Hans always made my day a little brighter after I ran into him in the hallway. Thank you to all those in the computing department and the HR department. Thank you to the ultrastable laser folks at PTB who we have a great collaboration with and who always welcomed us warmly, including Thomas Legero, Dan Matei, Uwe Sterr, and Fritz Riehle. Thank you to Michele Giunta for being a great collaborator. Thank you to all the other defense committee members. Thank you to the DoD and the NDSEG fellowship program for providing my funding for my first few years. I have benefited from interaction with so many other people, including Luigi DeMarco, Lee Liu, Kyle Matsuda, Will Tobias, Giacomo Valtolina, Junru Li, Bryce Bjork, Tanya Roussy, Julia Cline, and many others. Thank you to my undergraduate physics professors who really fostered my growth and interest in physics.

The lessons I learned in my climate activism work bled over into my PhD work, and I would be remiss not to mention those people here. My climate work really taught me how to work with people, particularly those you disagree with. It taught me how to feel incredible fear (I'm leading how many meetings with Members of Congress today??) without letting it affect my actions. Kelsey Grant and Dan Palken made two phenomenal climate buddies. Ian Harrison is an incredible mentor. He tells you your strengths and your weaknesses in a frank and yet incredibly supportive way, and encourages you to stand up for yourself at all costs. Many other people contributed to my growth, including David Kline, Grant Couch, Susan Secord, and many others.

Kelsey Grant is one of my most cherished friends, and her passion, standards, work ethic, and values-oriented behavior inspire me daily. I can't wait until she is President as the world will be a better place. Steffi Couey is well-spoken, smart, thoughtful and uniquely empathetic. She inspires me daily to be a better, more understanding person. These two ladies really hold me up at every point in my life, and I hope to keep their friendships for the rest of my life. Numerous other friends have made my time here special - Christina Porter, Shaun Burd, Daniel Palken, Graham Greve, Adrian Merritt, Cole Perkinson, Zach Ulibari, Max Urmey, Val Phillips, James Greenberg, Peter Johnsen, Rachel Steinberg, Haley Piske, Liz Strong.

My family has been very supportive of my dedication to physics, and for that I am incredibly appreciative. Thank you to my dad, my mom, Dianne (my second mom), Amy, Aidan, and Ian. Finally, thank you to Jeffrey Moore, who has supported me immensely throughout my PhD. Thank you for respecting me as an independent individual, and for listening to my opinions and thoughts and taking them seriously, even if we disagree. Your introspection, lifelong learner attitude and desire to constantly improve inspire me daily.

# Contents

**Chapter**

# Tables

**Table**

# Figures

**Figure**

# Chapter 1

# Introduction to atomic clocks

Time is a physical quantity that has had practical relevance for the majority of human history. In our modern capitalist society, we often view time in terms of its monetary value, realizing that time, like energy, is a vital yet finite currency that is necessary to get anything done. Early agrarian cultures associated time with sustenance — Egyptians observed the annual flooding of the Nile River, and the Mayans were cognizant of the reproducibility of the optimal harvest time.

Time is unidirectional, irreversibly succeeding from past through present to the future. An interval separating two points on this timeline can be measured by a device that is cyclical in nature. Time is measured by counting the number of cycles that have passed during an interval. Numerous phenomena are cyclical and could serve as a standard for time. One example is Earth's revolution around the sun, which defines a year. The sun is a remarkably good timekeeping device due to its accessibility and reasonable stability (if the sun is high in the sky, it's around noon), but it has limitations. First, its definition of time is not stable as its location in the sky changes with the seasons, and Earth's rotation is gradually decreasing over time. Additionally, it is challenging to accurately measure time intervals below tens of minutes. Another example is a grandfather clock. Each half cycle of a grandfather clock takes a second, which allows time to be defined well over the course of seconds but poorly for much less than a second. Over many days, the error per cycle accumulates, meaning it does not work well over long timescales. Additionally, since the oscillation frequency depends on the length of the pendulum, it is difficult to create two grandfather clocks with the same definition of time.

To create an optimal definition of time, we need a system that works over many timescales and is accurate, stable, and consistent. High accuracy implies the time can be told with few systematic errors, while low instability means the answer doesn't change significantly with each measurement. A consistent definition implies that we can create two clocks at two different places, such as a clock in Paris and a clock in Boulder, and be able to arrive at exactly the same definition of time. Furthermore, how can we maximize the societal use of measuring this quantity?

To satisfy all these requirements, a clock consists of multiple components. A local oscillator (LO) keeps track of time over short timescales, and a frequency reference creates an absolute definition of time while also providing a stable standard over long timescales. Finally, clocks require a device that counts the number of oscillations of the clock. For example, since a grandfather clock works well over the course of seconds, it makes a decent LO. However, because of its accumulated error per cycle and the variance in the oscillation frequency with each clock, it makes a lousy frequency reference. The sun, on the other hand, is a better frequency standard, since it works well over the course of days and two people in the same neighborhood observe the same sky so that a common definition of time can be implemented. The sun and the grandfather clock can work in tandem, with the sun periodically updating the local oscillator to create a time standard that works over many timescales. This system works well enough for those trying to be home by dinnertime, but needs improvements for people who want modern GPS accuracy or precise navigation in deep space [1] .

The SI unit of time, the second, is currently defined as 9 192 631 770 periods between two hyperfine transitions in the unperturbed ground state of a $^{133}$Cs atom [2]. The hyperfine transition is probed with a microwave oscillator, which acts as the LO. Microwave electromagnetic radiation can be thought of as a grandfather clock except with a $10^{10}$ times higher oscillation frequency. This allows the Cs clock to achieve a much higher quality factor $Q = \nu/\Delta\nu$ than a grandfather clock. Energy transitions in atoms provide a stable frequency reference and a universal definition of time,

---

[1] See for example NASA's deep space atomic clock.

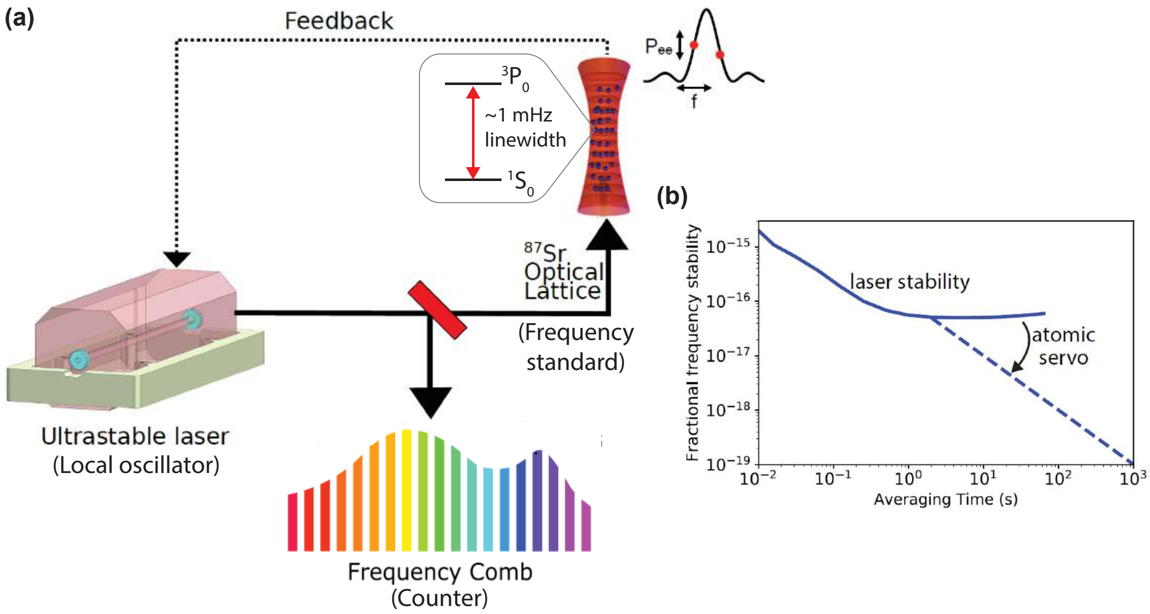

Figure 1.1: (a) Schematic of a modern atomic clock. A local oscillator that has good short term stability is referenced at long times to a narrow linewidth energy transition in an atom. Here, the frequency reference is represented by neutral atoms trapped in a 1D optical lattice clock, and the laser probes the 1 mHz linewidth $^1\mathrm{S}_0 - {}^3\mathrm{P}_0$ clock transition in $^{87}$Sr. The number of optical cycles is then counted with traditional counters by converting the optical signal to a microwave one using a frequency comb. (b) Example of the fractional frequency stability of an atomic clock. The stability at short times is determined by the local oscillator. At long times, the laser stability degrades and is corrected by the atomic reference, which acts as a frequency discriminator that provides feedback to the local oscillator.

since a transition frequency in a given element is identical for all atoms of the same isotope, as long as they are in the same environment.

Optical clocks capitalize on this idea and probe electronic transitions that operate at optical frequencies 4 orders of magnitude higher than a hyperfine transition. Fig. 1.1 outlines a modern atomic clock. The LO is a laser, where an oscillation cycle is defined by the laser wavelength and the speed of light. With the advent of ultrastable laser technology, the oscillation frequency can be defined with sub-Hz resolution, making modern ultrastable lasers incredibly pristine oscillators. At long times, the laser frequency drifts owing to environmental perturbations so that a long-term frequency standard is required. The LO excites a narrow linewidth transition in an atom, which when probing the slope of the atomic lineshape (red dots in Fig. 1.1) acts as a frequency discriminator that corrects the laser frequency and keeps the laser on resonance with the atomic transition. Finally, to count the rapid optical cycles of the clock, a frequency comb is utilized. A frequency comb allows a low noise conversion of optical frequencies into microwave, where traditional electronic counters can count the number of cycles.

As mentioned previously, accuracy and stability are two important variables for atomic clocks. Accuracy is how far away the measured clock transition frequency is from the true unperturbed value. A low uncertainty implies that the offset is very well known. In contrast, precision and stability define the noise of the measurement. A worse stability means that the standard deviation of frequency measurements is larger. It takes less time to average away the noise if the clock has a higher stability, allowing sub-Hz frequency shifts to be measured faster.

Both ion clocks and neutral atom optical clocks have surpassed Cs. Compared to ion clocks that generally trap single ions, neutral atom optical clocks interrogate thousands of atoms simultaneously. This grants a lower instability, and neutral atom optical clocks have demonstrated low $10^{-17}$ instability after averaging for 1 s [3, 4]. It currently takes Cs standards $10^{6}$ s to achieve a $10^{-17}$ level of instability [5]. Optical clocks have demonstrated systematic uncertainty over two orders of magnitude lower than a Cs clock, with accuracies in the low $10^{-18}$ [6, 7, 8, 9]. To achieve a low uncertainty, potential systematics that can shift the clock transition frequency have to be controlled and understood. Nuclear clocks are an exciting new research direction since the nucleus is expected to be less sensitive to external perturbations such as electromagnetic fields [10]. A prominent example is the $^{229}$Th clock, which features a long-lived few eV nuclear transition. Given the ability to connect ultrastable lasers at telecom wavelengths to the $\sim$150 nm nuclear transition frequency using an XUV frequency comb [11], this avenue of research is bound to have many exciting discoveries over the upcoming decades.

The exceptional accuracy and stability of optical atomic clocks drives the consideration of a redefinition of the SI second [12]. Moreover, besides timekeeping there are many exciting applications of atomic clocks. Because clocks are relatively insensitive to their external environments, they can be also used to detect small frequency shifts of the clock transition that are normally invisible to other experiments. As a result, precision metrology affects a range of applications in quantum sensing and fundamental science. Atomic clocks can enable relativistic geodesy [13, 14], which motivates physicists to develop transportable clocks that can be used outside the laboratory [15]. In addition, clocks can be used to detect possible drifts in fundamental constants [16, 17, 18], to test fundamental symmetries [19, 20], to look for the existence of ultralight dark matter candidates [21, 22, 23], and potentially to measure gravitational waves [24]. Optical clocks are also ideal many-body platforms to study light-matter and matter-matter interactions and to further our understanding of quantum science [25, 26, 27, 28]. Such fundamental physics applications are connected to the rapidly advancing frontier of quantum technology, and they also provide a necessary means to further improve atomic clocks. Physics that is uncovered at a given level of performance must be accounted for or circumvented for further improvement. This relation between time and physics can never fully be disentangled and is one of the drivers of our discoveries and passions.

In Section 1.1 we detail the various noise sources in atomic clocks that can lead to an increase in instability. In Section 1.2 we then outline next generation atomic clocks that attempt to solve the instability problems that have plagued past systems.

## 1.1 Noise sources in atomic clocks

Precision is essential to measuring small frequency shifts in short timescales. Our state-of-the-art clock uses an ultrastable laser referenced to a mHz-wide optical transition in trapped $^{87}$Sr atoms. Sources of instability are thus rooted in both the local oscillator and the matter-based frequency reference. Here we discuss limitations to the intrinsic stability of the frequency reference, quantum projection noise, and noise due to the local oscillator, called the Dick Effect.

### 1.1.1 Quantum projection noise

The intrinsic instability of an atomic clock is determined by quantum projection noise (QPN). When an atom is in a superposition of ground and excited states $|\psi\rangle = a\,|g\rangle + b\,|e\rangle$, measuring an atom in the ground or excited state is not deterministic but instead follows a binomial distribution, where the probability finding the atom in $|g\rangle$ ($|e\rangle$) is given by $p_a = |a|^2$ ($p_b = |b|^2$), assuming $|a|^2 + |b|^2 = 1$. This noise that is inherent to quantum mechanics is called quantum projection noise, since atoms are projected into a given state upon measurement [29]. If the atoms are uncorrelated, they can be regarded as independent so that the excited state variance is

$$\sigma_e^2 = Np_b(1-p_b)\,, \tag{1.1}$$

where $N$ is the total number of atoms. Converting this to an excitation fraction $P_{ee} = N_e/N$, where $N_e$ is the number of excited state atoms, gives us $\sigma^2_{P_{ee}} = p_b(1-p_b)/N$. Generally atomic clocks operate with $p_b = 0.5$, where the slope between the frequency and the excitation fraction is maximized. The excitation fraction noise can then be converted to fractional frequency noise $\delta\nu/\nu$ from the analytic shapes of the Rabi and Ramsey spectroscopy lineshapes. This gives

$$\sigma_y^{Rabi} = \frac{0.264}{T_p\nu}\sqrt{\frac{T_d+T_p}{N\tau}} \tag{1.2}$$

$$\sigma_y^{Ramsey} = \frac{1}{2\pi T_{dark}\nu}\sqrt{\frac{T_d+T_p}{N\tau}}\,, \tag{1.3}$$

where $T_p$ is the pulse time, $T_{dark}$ is the Ramsey dark time, $\tau$ is the averaging time, and $T_d$ is the dead time, or preparation time, of the atomic state. The dead time is typically not zero, since atomic clocks so far operate in a destructive fashion - the atomic sample is destroyed upon measurement so that the atoms have to be continually re-prepared, which takes time $T_d$. More details on this in the upcoming subsection.

In order to achieve a better intrinsic stability, it thus helps to 1.) operate a clock with more atoms $N$, 2.) maximize the coherence time $T_p$ (or $T_{dark}$), and 3.) reduce the preparation time $T_d$. With 1000 atoms, $T_p = 5$ s and $T_d = 1$ s, our QPN-limited stability for Rabi spectroscopy is $10^{-17}/\sqrt{\tau}$, and sub-$10^{-18}$ frequency shifts can be resolved in 100 s.

### 1.1.2 Dick effect

Comparisons between independent clocks generally have an instability above the QPN limit due to noise from the local oscillator called the Dick Effect [30]. The clock transition typically cannot be measured continuously, since most techniques that probe the excited state fraction are destructive and heat atoms out of the trap. As a result, an atomic clock operates in cycles of preparing the atomic sample, probing the clock transition, and reading out the quantum state. During state preparation and detection, also called the dead time, the laser frequency is not measured and thus acts like a flywheel. This periodic sample of the laser phase leads to aliasing of high frequency laser noise down to lower frequencies, and causes a random false frequency correction of the laser phase that can degrade the performance of a clock. The Dick effect stability is given by [30]

$$\sigma_y^2(\tau) = \frac{1}{\tau} \sum_{m=1}^{\infty} \frac{|G(n/T_c)|^2}{|G(0)|^2} S_y(n/T_c)\,, \tag{1.4}$$

where $T_c$ is the cycle time, $S_y(f)$ is the power spectral density of fractional frequency fluctuations of the laser at frequency $f$, and $G(f)$ is the Fourier transform of the response function, $g(t)$, defined by

$$\delta P_{ee} = \frac{1}{2} \int_0^{T_p} g(t) \delta\omega(t) dt\,. \tag{1.5}$$

That is, the sensitivity function defines how changes in the laser frequency $\delta\omega(t)$ over the coherent interrogation pulse changes the excitation fraction $P_{ee}$. To reduce the aliased signal, it is advantageous to have a high duty cycle, where the majority of time is spent coherently probing the atomic sample. Lower laser noise will also reduce the Dick effect.

Typically, independent clock stability of neutral atom clocks is limited by the Dick effect [6, 9, 31, 4]. However with the advent of ultrastable lasers based on crystalline materials, which are discussed in the next section, the Dick effect can be on par with state-of-the-art QPN stability [3]. In addition, interleaved interrogation of two atomic clocks in a zero-dead-time configuration can drastically reduce the Dick effect [4]. Synchronous measurements, performed between two atomic regions of a single clock [32] or between two separate systems [3, 33], can cancel the Dick effect and are useful if one is not using a clock as a time standard but instead to measure frequency shifts brought on by physical phenomena, such as the gravitational redshift.

## 1.2 Next-generation systems

Here we discuss next-generation systems whose goal is to increase the precision of atomic clocks. In subsection 1.2.1 we introduce a local oscillator that is composed of a laser locked to a Si reference cavity. The high quality factor and low temperatures afforded by this system permit a low thermal noise, and allow demonstration of record-breaking laser stability [34]. Next in subsection 1.2.2 we give an overview of a 3D optical lattice clock. Confinement of atoms on individual 3D lattice sites guards against interactions, and allows large numbers of atoms to be probed coherently for over 10 s, reducing QPN.

### 1.2.1 Ultrastable lasers with Si reference cavities

A state-of-the-art optical oscillator is composed of a laser that is locked to a stable passive resonator. Fundamentally, the frequency stability of the oscillator is limited by the length stability of the resonator. Barring technical noise, the length stability is given by the composite thermal noise of the substrates, spacer, and coatings that make up the resonator. For the majority of state-of-the-art cavities, the noise of the substrates and coatings are much larger than that of the spacer, so that we can write that the fractional frequency stability as $\sigma_{TN}^2 \propto \frac{T}{QEL^2}$, where $T$ is the temperature, $Q$ is the mechanical quality factor, $E$ is the Young's modulus, and $L$ is the cavity length. While the total thermal noise of the spacer depends on the length of the resonator, the thermal noise of the substrates and coatings do not. This is why the fractional length stability of the substrates and coatings is $\propto L^{-2}$, and the fractional length noise can thus be reduced by increasing the length of the resonator. However, the resulting increase in the vibration noise on the cavity and the temperature non-uniformity of the spacer create technical noise that is challenging to mitigate. These technical noise sources were overcome in a cavity that was 40 cm long in our group in 2013 [35, 36]. Thermal-noise-limited instability has been demonstrated in cavities as long as 48 cm [37]. However, increasing $L$ significantly beyond this length remains difficult. A different strategy is thus warranted for significant advances in ultrastable laser technology. Up

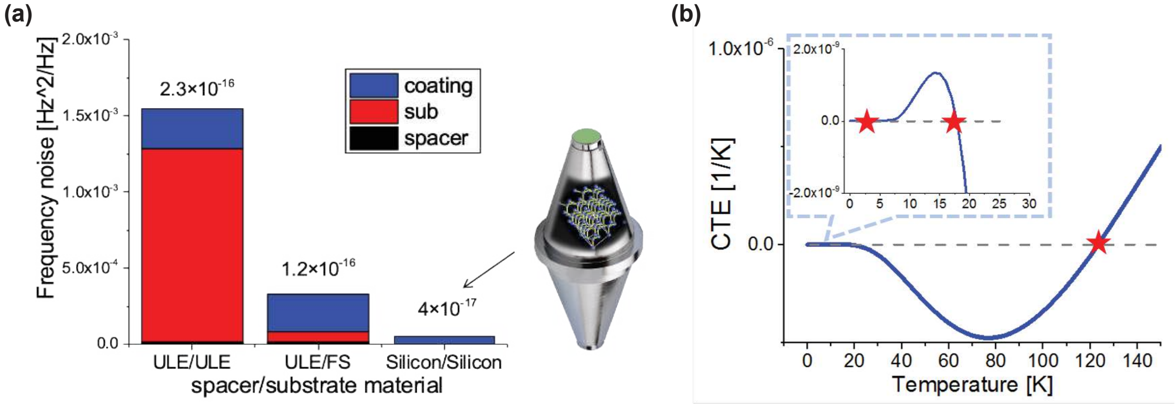

Figure 1.2: (a) Contributions of the substrate, spacer, and dielectric $SiO_2/Ta_2O_5$ coatings to the thermal noise for different spacer and substrate materials. The thermal noise is minimized when all-crystalline components are used. Here the frequency noise of the Si/Si cavity is calculated at 124 K. (b) Coefficient of thermal expansion (CTE) for Si. The CTE crosses zero at 124 K and 17 K, and trends towards zero as $T \to 0$.

until 2012, ultra-low expansion (ULE) glass was predominantly used as a spacer material in state-of-the-art cavities due to its low coefficient of thermal expansion (CTE) at room temperature. A significant advance was made when crystalline materials with more optimal material properties were considered. Crystalline materials such as Si have many orders of magnitude higher Q compared with conventional glass materials, and a large Young's modulus [38]. A crystalline cavity can thus demonstrate significantly lower thermal noise than one composed of amorphous materials, as shown in Fig. 1.2 (a). The stiffness of Si provides the additional benefit that the cavity is more robust against vibrations [38].

Thermal noise is also reduced when the cavity is operated at a lower temperature. However, technical limitations prevent ULE and other materials from working at cryogenic temperatures. Critical to demonstrating a thermal-noise limited cavity is the reduction of technical noise sources that can change the cavity length. Temperature fluctuations and vibrations constitute two major technical contributions that must be mitigated. ULE and other materials have an appreciable coefficient of thermal expansion (CTE) at cryogenic temperatures (the CTE instead passes zero

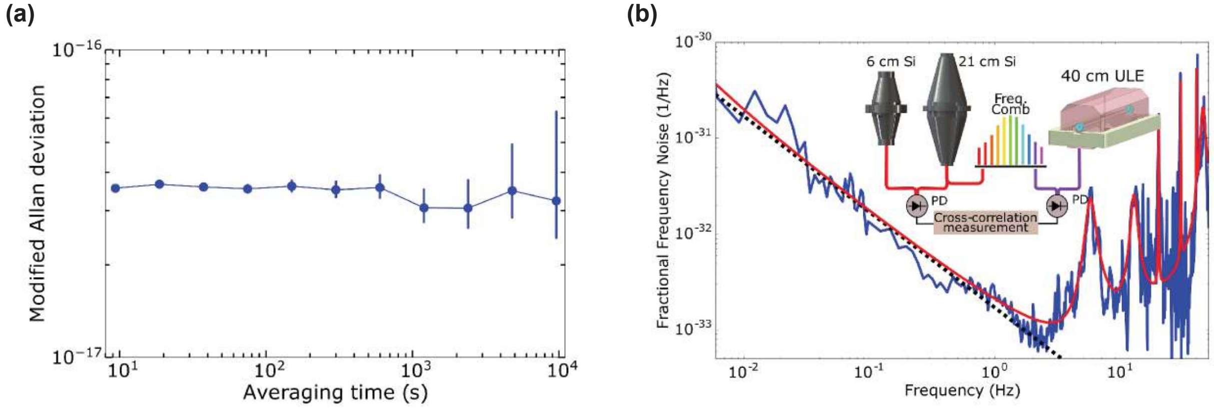

Figure 1.3: (a) Fractional frequency stability of the JILA ultrastable laser locked to a 124 K Si resonator (b) Frequency noise of the JILA 124 K ultrastable laser.

around room temperature). As such, operating these cavities at low $T$ can enhance the coupling between thermal fluctuations and the cavity length. In contrast, as shown in Fig. 1.2 (b), Si has a CTE zero crossing at 124 K and 17 K. In addition, as is true of all materials, the CTE trends towards zero as T approaches zero. Si cavities can thus operate at a lower T with a reduced coupling of thermal fluctuations to the cavity length.

Thus far, lasers locked to Si resonators at 124 K and 4 K have been developed at JILA and Physikalisch-Technische Bundesanstalt (PTB). Fig. 1.3 (a) shows the fractional frequency stability of a laser locked to a 124 K Si cavity, extracted using a three-cornered hat comparison [39] with a 4 K Si cavity and our second clock laser based on a 40 cm ULE cavity. The laser with a 124 K Si reference cavity demonstrated a thermal noise limited instability of $4 \times 10^{-17}$, corresponding to a coherence time up to 55 s at 1550 nm [34]. This was roughly a factor of two improvement in the thermal noise over our previous clock laser [35].

The JILA setup has an improved long-term stability thanks to a few upgrades. First, the intensity of the laser light is stabilized in the transmission port of the cavity, minimizing the cavity's thermal fluctuations due to changes in the intracavity power. Second, superpolished optics and better thermal control of the environment were added, both which reduce slowly drifting parasitic

| Index | $f_i$ (Hz) | $a_i$ (1/Hz$^3$) | $\Gamma_i$ (Hz) |
|---|---|---|---|
| 1 | 5.7 | 7.0e-34 | 1.0 |
| 2 | 12.7 | 1.5e-34 | 1.5 |
| 3 | 20.0 | 4.0e-34 | 0.1 |
| 4 | 30.0 | 5.0e-34 | 0.1 |
| 5 | 40.0 | 5.0e-34 | 0.1 |
| 6 | 50.0 | 1.0e-34 | 4 |
| 7 | 55.0 | 4.0e-34 | 1.2 |

Table 1.1: 124 K Si cavity resonance frequencies, amplitudes, and linewidths

etalons. These improvements lead to a thermal-noise-limited stability from $0.2 - 10^4$ s and a drift rate of the Si cavity below 60 $\mu$Hz/s [40], a more than two orders of magnitude improvement in the drift rate over our previous clock laser. An interesting question is if the drift rate of this cavity decreases over time. We are continuining to monitor the drift rate of this cavity, and as of the writing of this thesis, the lowest drift rate we have seen over the course of days is 30 $\mu$Hz/s. This ultralow drift makes Si cavities useful as stand-alone oscillators [40].

Fig. 1.3 (b) shows the frequency noise of the 124 K Si cavity, extracted using a cross-correlation measurement [41] between a 124 K Si cavity, a 4 K Si cavity, and our old 40 cm ULE clock laser [3]. From this measurement, we can extract a frequency noise model of the Si laser, given by

$$S_{laser}(f) = \frac{h_{-1}}{f} + h_0 + h_2 f^2 + \sum_{i=1}^{N} \frac{a_i f^2}{1 + (\frac{f - f_i}{\Gamma_i/2})^2} \,. \tag{1.6}$$

This model includes a white frequency noise term ($h_0 = 4 \times 10^{-34}$ Hz$^{-1}$), a flicker frequency noise term ($h_{-1} = 1.5 \times 10^{-33}$), a white phase noise term ($h_2 = 3 \times 10^{-36}$ Hz$^{-3}$), and a series of resonances that arise from for e.g. vibrations that are listed in Table 1.1.

Using the Si noise model quoted above, we can predict what the Dick effect-limited instability of the clock will be for different dead times and pulse times as shown in Fig. 1.4. The Dick effect stability quoted in this model was confirmed by transferring the stability of the 124 K Si cavity to the 698 nm clock transition using a frequency comb (see Chapter 3), and subsequently performing

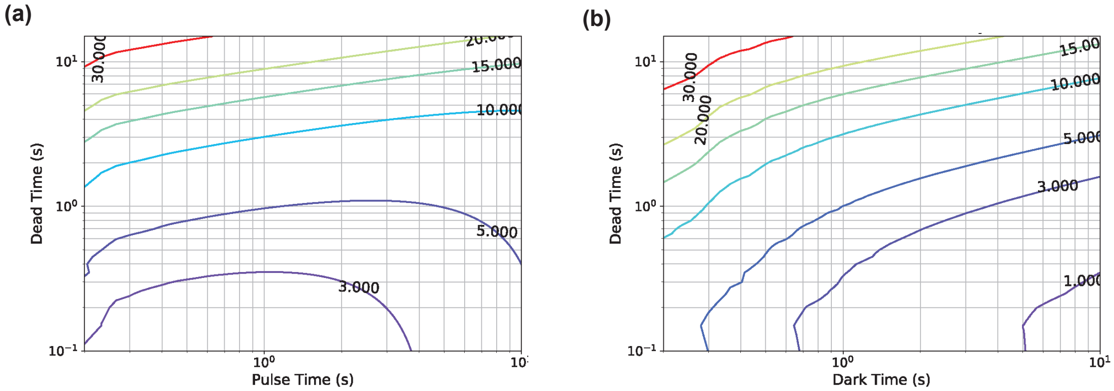

Figure 1.4: (a) Dick effect ($\times 10^{-17}$) at 1 s averaging time for different pulse times $T_p$ and dead times $T_d$, using Rabi spectroscopy. (b) Dick effect ($\times 10^{-17}$) at 1 s averaging time for different dark times $T_{dark}$ and dead times $T_d$, using Ramsey spectroscopy.

intercomparisons between two Sr atomic clocks [3] [2] . Prior to 2019, the Dick effect limited clock stability was around $10^{-16}/\sqrt{\tau}$ [31, 4, 42, 9]. With the implementation of the 124 K Si cavity, an independent clock stability of $4.8 \times 10^{-17}/\sqrt{\tau}$ was reached with a 570 ms pulse time and a 600 ms dead time [3]. Further improving the stability is possible with improvements in the coherence time and additional reduction of the dead time.

At 4 K, vibrations from the closed-cycle cryostat limited previous results [43]. With the addition of a custom-designed cryostat with many layers of thermal isolation and minimal coupling to the cooling mechanism [44], vibrations and thermal fluctuations were suppressed below the thermal noise floor to demonstrate a 4 K cavity with thermal-noise-limited instability of $6.5 \times 10^{-17}$ and a drift rate as low as 30 $\mu$Hz/s, the latter of which depends on the intracavity power [45].

Decreasing the Dick noise contribution will of course benefit from an improvement in the laser noise. As shown in Fig. 1.2 (a), the predominant noise contribution in a Si cavity is the mirror coating noise. Crystalline semiconductor coatings made from AlGaAs/GaAs epitaxial layers have demonstrated an order of magnitude reduction in Brownian noise at room temperature compared to commonly used dielectric mirror coatings [46]. These coatings also have high optical quality in

---

[2] More details on these measurements will be contained in upcoming theses.

the telecom band, producing a finesse up to 300,000 at 1550 nm with scattering and absorption losses of a few ppm [47]. Implementation of these coatings in a 4 K Si cavity could result in a thermal-noise floor in the lower half of the $10^{-18}$ range, roughly an order of magnitude better than the current state-of-the-art [34].

### 1.2.2 Three-dimensional optical lattice clocks

Neutral atom clocks probe thousands of atoms simultaneously, resulting in a favorable QPN. Typically optical lattice clocks consist of thousands of neutral atoms that are trapped, cooled to $\mu$K temperatures, and loaded into a 1D optical lattice so that atoms are confined to individual pancakes. The optical lattice reduces the effect of atomic motion on the transition probability of the atom. In particular, if the probe laser is along the direction of the optical lattice in the Lamb-Dicke regime, the recoil caused by the probe light is absorbed by the lattice so that the atom's motional state is unaffected [48]. Furthermore, the wavelength of the lattice laser can be set such that the polarizability of the ground state equals the polarizability of the excited clock state, creating equivalent trapping conditions for the two states. 1D optical lattice clocks (OLCs) have reached record accuracies of low $10^{-18}$ [6, 9], but since they only have strong confinement along one direction, they suffer from collisions between atoms that dephase and shift the clock frequency. These atomic interactions place a limit on the number of atoms per lattice pancake and maximum coherence time, and thus limit the achievable QPN.

One possible solution to this problem is to create a 1D optical lattice with a large beam waist [4], which increases the distance between atoms and thus reduces the interaction strength throughout the interrogation pulse. This solution is accompanied by various technical challenges that scale with the size of the atomic sample. For example, correctly modeling the temperature environment over the extended sample will be critical to correctly account for blackbody radiation, a leading systematic for many optical lattice clocks [6, 9] and ion clocks [8, 7].

An alternative scalable solution is to create a 3D optical lattice clock [49, 50], which is the

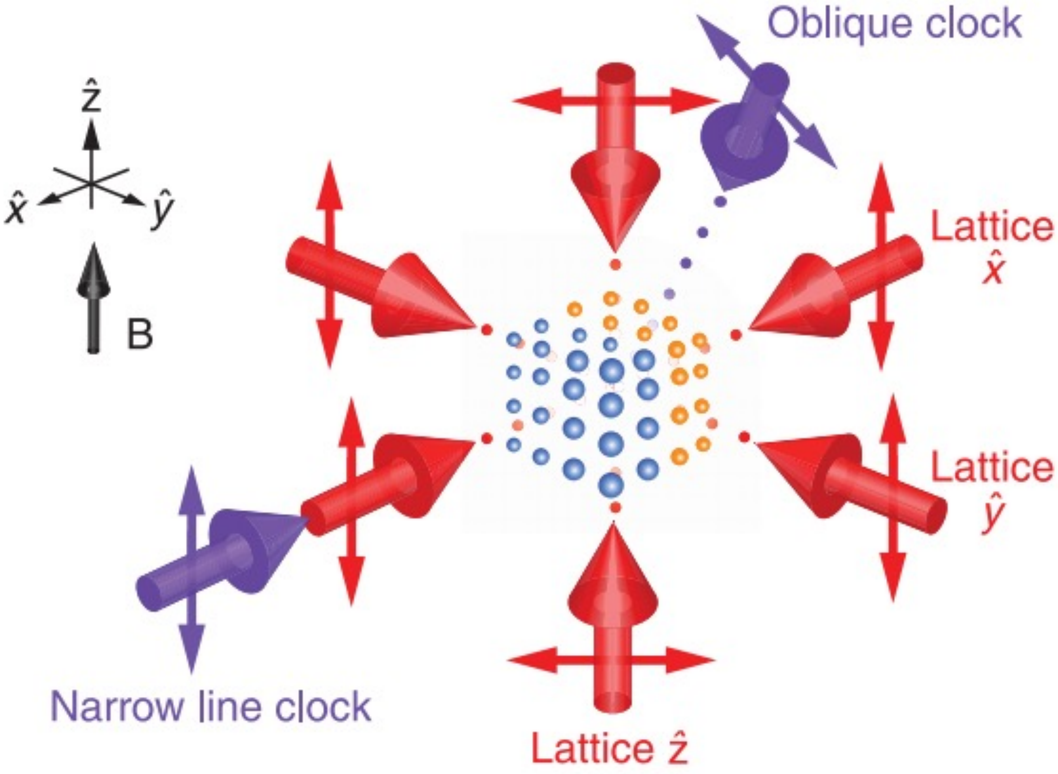

Figure 1.5: Schematic of a 3D optical lattice clock. Using retro-reflected laser beams along all three directions, single atoms are trapped on individual lattice sites, guarding the system against particle interactions. The large arrows represent the propagation direction, while the double arrows denote the polarization. The narrow line clock laser is phase stabilized to the $\hat{x}$ lattice beam. The oblique clock laser is used to measure sideband frequencies in along all three directions.

subject of this thesis. A spin-polarized, unity filled 3D lattice clock contains one atom per lattice site, as shown in Fig. 1.5, which removes contact interactions and thus reduces density shifts. 3D optical lattice clocks can thus support more atoms per unit volume than a traditional 1D optical lattice clock. Additionally, residual atoms in other spin states that create doubly occupied lattice sites have an interaction energy that is much larger than in a 1D lattice clock due to the significant spatial overlap between the wavefunction of the two atoms. These kHz interaction shifts are spectroscopically resolvable from singly-occupied sites given our sub-Hz resolution of the clock transition. The clock laser can consequently singularly address solely-occupied sites, guarding against contact interactions that affect the clock transition frequency. Interactions present in a 1D lattice clock can also dephase the atoms during the clock interrogation, reducing the atom-atom coherence time and thus the maximum allowable probe duration during spectroscopy. As discussed earlier, increasing the probe duration reduces not just QPN but also the Dick Effect, and is thus beneficial to obtain better clock stability.

To create a near-unity filled 3D optical lattice, it is necessary to load a Fermi-degenerate gas. Fermi-degenerate gases have entropy on the order of a few $k_B$ per particle, where $k_B$ is the Boltzmann constant. Adiabatically loading this low-entropy gas into the optical lattice allows only the lowest energy states to be occupied so that atoms are loaded into the ground band of the optical lattice with a minimal number of holes. 3D optical lattice clocks consequently require extra stages of cooling to prepare a near-$T = 0$ gas, as is discussed more in Chapter 3. We have demonstrated temperatures as low as 0.07 times the Fermi temperature [51], corresponding to only a few tens of parts per billion above absolute zero.

In the first implementation of this new technology, we demonstrated a record QPN of $1.5 \times 10^{-17}/\sqrt{\tau}$ [32, 49]. This was achieved using 6000 atoms with a coherent interrogation time of 4 s and a dead time around 16 s. We also observed atom-light coherence times up to 6 s, limited by the coherence time of the clock laser [35]. A long-standing question was whether a 3D optical lattice could support the small AC Stark shifts required for highly accurate optical clocks. To avoid interference effects, each lattice beam needs either orthogonal polarization or a different lattice frequency. Despite these challenges, we demonstrated state-independent trapping based on a proposal in Ref. [52] and measured the magic frequencies of each lattice beam to around 10 ppb [49]. Higher order Stark shifts such as hyperpolarizability, magnetic dipole, and electric quadrupole interactions [53], will be a fruitful subject for future study.

To extract the QPN and cancel the Dick effect, we take advantage of a high-resolution imaging system with an NA = 0.23 to spatially map the frequency shifts of our atomic sample [32]. The clock transition frequency can be compared in different parts of the atomic sample to

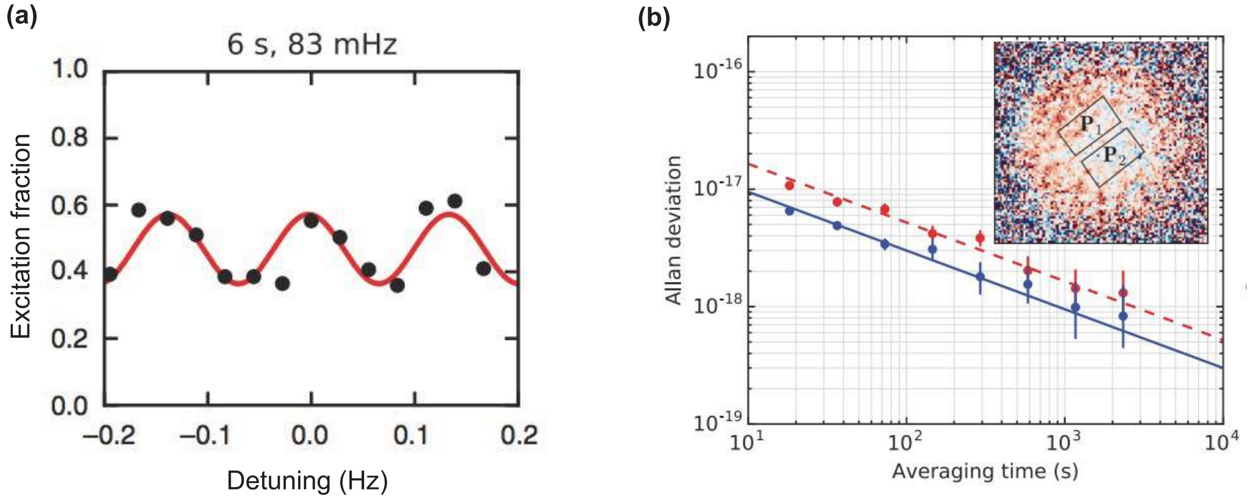

Figure 1.6: (a) Ramsey spectroscopy data, demonstrating a 6 s atom-light coherence time. (b) Fractional frequency stability of the frequency difference between two regions of the 3D optical lattice, $P_1$ and $P_2$. The blue solid line shows an instability of $3 \times 10^{-17}/\sqrt{\tau}$, which when extracting the QPN of the total ensemble with twice as many atoms gives an instability of $1.5 \times 10^{-17}/\sqrt{\tau}$. When the number of atoms is reduced by a factor of three in each region, the instability increases by $\sqrt{3}$, confirming the stability is governed by QPN. (inset) Spatially resolved image of the excitation fraction. The frequency difference is extracted between two regions with excitation probability $P_1$ and $P_2$.

perform a spatially resolved synchronous comparison. This technique rejects the Dick effect since all atoms in the sample see the same laser noise. The stability of this frequency comparison is thus limited by QPN. Spatially resolving frequency shifts can identify important clock systematics such as AC Stark shifts [32], dipolar interactions, and few-to-many-body physics [54]. In addition, since synchronous comparisons improve a measurement's precision, they open up the possibility of measuring gravitational redshifts at $10^{-19}$ stability within a single experiment.

Further improvements in the stability of 3D optical lattice clocks requires increasing the atom number and the coherence time, and decreasing the dead time. To further scale the atom number beyond what was demonstrated in Ref. [49], larger lattice waists can be used. A bigger challenge for 3D optical lattice clocks is the extended preparation time associated with preparing a Fermi degenerate gas. The workhorse technique for preparing a Fermi degenerate gas is evaporative cooling, which typically takes 10s of seconds. This prolonged dead time is significantly longer than the hundreds of ms dead time demonstrated in 1D optical lattice clocks. Decreasing the dead time to prepare a Fermi degenerate gas requires novel cooling techniques and is the subject of Chapter 4.

Coherence time limitations in 3D optical lattice clocks are an active field of study [55, 56, 57]. In particular, we found that our atom-atom coherence time was limited to 12 s [55], despite the 118 s lifetime [58] of the $^3P_0$ clock transition. This coherence time was found to be limited by Raman scattering of lattice photons from the deep 3D optical lattice. Raman scattering is reduced when the optical lattice is operated at lower lattice depths. However, an additional dephasing mechanism due to site-to-site tunneling is then introduced. The interplay between tunneling and Raman scattering leads to a maximum coherence time in our system of 12 s. Further improving the coherence time may be achieved by operating in the band-insulating regime, where tunneling is suppressed, or by operating with a larger lattice spacing. The latter requires different lattice geometries to maintain the magic wavelength for each optical beam.

Eventually, the coherence time of atomic clocks will be limited by the lifetime of the excited state. Such a limitation would be an exciting development. However, it is prudent to think of techniques that can engineer the coherence time beyond this seemingly fundamental limit. One mechanism to achieve this is by altering the density of available final atomic motional states. Measurements to observe this intriguing idea, predicted back in the 1980's, will be discussed in Chapters 5 and 6.

## 1.3 Outline of this thesis

The work reported in this thesis aims to increase the stability of quantum degenerate clocks by decreasing the preparation time of the system and increasing the coherent interrogation time. This thesis in particular highlights the essential interplay between improvements in quantum metrology, and understanding and exploiting advances in quantum physics. The outline of this thesis is as follows. First we will discuss the theory behind Fermi degenerate gases in Chapter 2. The consequences of Fermi statistics and the Pauli exclusion principle are profound and lead to striking physics, which will be detailed. The theory introduced in this chapter is the basis of many measurements we make throughout the rest of this thesis. Then, in Chapter 3 we discuss the experimental setup of the 3D optical lattice clock, with a particular focus on the spin polarizing sequence, imaging techniques, and stability transfer of the ultrastable laser referenced to a 124 K Si cavity, which operates at 1542 nm, to the narrow linewidth atomic transition at 698 nm.

In Chapter 4 we discuss new cooling techniques to rapidly create Fermi degenerate systems. By taking advantage of the many collisional partners a multi-spin component gas contains and the lack of inelastic loss for atoms with SU($N$) symmetry, we demonstrate a sub-3 s preparation time to reach deep degeneracy that includes only 600 ms of evaporation. This is roughly a factor of 5 decrease in the preparation time over our prior work. We also perform a detailed study of the enhanced SU($N$) interactions in the Fermi gas.

Chapters 5 and 6 outline efforts to quantum engineer the natural lifetime of the atomic state using Pauli blocking, which exploits the Pauli exclusion principle to prohibit decay of an excited atom to states already occupied by an identical fermion. In Chapter 5 we discuss experiments that successfully observe Pauli blocking on the $^1\mathrm{P}_1$ transition in a light scattering experiment that angularly resolves the suppression of the spontaneous emission rate. Chapter 6 details measurements made on the $^3\mathrm{P}_1$ transition that attempt to directly measure the lifetime of the atomic state as opposed to an angularly-resolved scattering rate. Finally, we conclude and provide an outlook for future research in Chapter 7.

# Chapter 2

# Degenerate Fermi gases

Studying and controlling the quantum many-body system that comprises neutral atom atomic clocks is essential for accurate and precise quantum metrology, and in tandem creates unique opportunities to advance our understanding of quantum science. Since atomic clocks use cold matter, the quantum statistics of the constituent atoms governs their behavior. The statistical properties of bosons and fermions dictates how particles interact. For example, the required asymmetric wavefunction of fermions implies that spin-polarized ground state fermions cannot interact at low temperatures. Since particle interactions cause frequency shifts and dephasing, this was an essential original argument for using fermions in neutral atom clocks.

The rich physics of Fermi-degenerate systems near $T = 0$ creates intriguing reasons to use such low temperatures in atomic clocks. Three-dimensional optical lattice clocks rely on loading a gas into the ground band of a 3D optical lattice. In order to load the lattice at high filling, it is necessary to load a Fermi-degenerate gas. Near $T = 0$ and without particle interactions, the textbook example of an ideal Fermi gas can be realized. Even though the system is theoretically simple, it provides many opportunities to build our physical understanding and to use new discoveries to advance quantum science. We will see an example of this when we discuss changing the decoherence rate of an atom by exploiting the well-known phenomena that is Pauli exclusion. Adding particle interactions creates a complex system that can describe for example the liquid state of electrons in a solid. These normal Fermi liquids are an active field of study, and we will see later on in this thesis that such interactions can be utilized for example for novel cooling mechanisms. The intriguing capabilities that are granted by the use of Fermi-degenerate systems requires a deep understanding of the quantum physics underlying them. In this chapter, we thus review the physics of Fermi gases. First we theoretically outline particle interactions and how they are simplified at low temperatures. We next detail the statistics and thermodynamics of noninteracting Fermi gases. We focus on observables such as the shape of the gas after releasing it from its confining potential, as well as the structure factor and corresponding density correlations of the gas. The quantum statistics produce striking results in both cases. The former gives rise to Pauli blocking of collisions and spontaneous decay, while the latter changes the compressibility and thus particle number fluctuations of the sample. Subsequently, we review the corresponding thermodynamics of interacting Fermi gases. We describe the expansion dynamics of an interacting sample and how interactions modify the system's compressibility.

## 2.1 Colliding fermions

In this section, we discuss scattering between fermions at low temperatures. The theory explains when interactions need to be considered to properly describe the system. Further details on non-interacting and interacting Fermi gases are the subject of the rest of the chapter.

In dilute atomic gases, interactions between particles are predominantly governed by pairwise collisions. Here, we will discuss elastic collisions[1] . Scattering theory is discussed in detail in many textbooks [59, 60]. For a spherically symmetric scattering potential $V(r)$, where $r$ is the distance between the particles, the wavefunction after scattering can be represented for $r \to \infty$ by

$$\psi(\mathbf{r}) = A\left[e^{i\mathbf{k_i}\cdot\mathbf{r}} + f(\mathbf{k}_i, \mathbf{k}_f)\frac{e^{ik_f r}}{r}\right]|s\rangle \ , \tag{2.1}$$

where $\mathbf{k}_i$ and $\mathbf{k}_f$ are the incoming and outgoing wave vectors, $A$ is a normalization constant, and $|s\rangle$ is the two-particle spin wavefunction. This equation consists of an incoming plane wave and an outgoing spherical wave with scattering amplitude $f(\mathbf{k}_i, \mathbf{k}_f)$, which can be expanded using spherical

---

[1] We neglect inelastic collisions, which matter at high densities.

harmonics into

$$f(\mathbf{k}_i, \mathbf{k}_f) = \frac{1}{k}\sum_{l=0}^{\infty}(2l+1)e^{i\delta_l}\sin\delta_l P_l(\cos\theta)\,, \tag{2.2}$$

where $\theta$ is the angle between $\mathbf{k}_i$ and $\mathbf{k}_f$, $l$ is the angular momentum of the partial wave, $\delta_l$ is the acquired phase shift that depends on the interaction potential, $P_l$ is the Legendre polynomial, and $|\mathbf{k}_i| = |\mathbf{k}_f| =$ k. The two-body wavefunction can then be written as [60],

$$\psi(r,\theta) = \frac{1}{(2\pi)^{3/2}}\sum_l (2l+1)\frac{P_l(\cos(\theta))}{2ik}\left[e^{2i\delta_l}\frac{e^{ikr}}{r} - \frac{e^{-i(kr-l\pi)}}{r}\right]|s\rangle\ . \tag{2.3}$$

To reflect the quantum mechanical nature of the colliders, the total spin and spatial wavefunction $\psi(r,\theta)$ must be antisymmetric. If two fermions interchange, $\theta \to \theta - \pi$. Under this exchange, the spatial part of the wavefunction is symmetric (antisymmetric) for even (odd) $l$. This implies that two fermions in the $s = 0$ spin singlet state can only interact through even partial waves, while two fermions in one of the $s = 1$ spin triplet states can only scatter through odd partial waves. Thus, elastic collisions between two fermions in the same spin state can occur through odd $l$, while fermions in different spin states can interact through even and odd $l$, based on whether the spin state is symmetric or antisymmetric. Two ground state atoms with low energy $k \to 0$ have a phase shift $\delta_l \propto k^4$ for $l > 1$, and $\delta_l \propto k^{2l+1}$ for $l = 0$ or 1 [61]. The phase shift is thus smaller as $l$ increases at ultralow temperatures where $k$ is small. Thus, the scattering amplitude given in Equation 2.2 is largely governed by low $l$ partial waves at ultralow temperatures. As a result, two cold fermions in the same spin state to a good approximation only undergo p-wave ($l = 1$) scattering. In contrast, two fermions in different spin states can undergo s-wave ($l = 0$) or p-wave scattering depending on if the spin is in a singlet or a triplet state. The proportionality factors of the phase shifts are called the scattering length for s-wave scattering, $a$, and the scattering volume for p-wave scattering, $b^3$.

The ratio $\delta_1/\delta_0 = k^2b^3/a$ is proportional to $T$ in the classical limit. P-wave scattering is thus suppressed at ultralow temperatures below the p-wave barrier. The threshold energy $E_{th}$ at which collisions occur can be approximated as

$$E_{th}(l) = \frac{\hbar^2 l(l+1)}{2mb^2} - \frac{C_6}{b^6}\,, \tag{2.4}$$

where $l$ is the corresponding partial wave, m is the mass of the atom, and

$$b^2 = \sqrt{\frac{6C_6 m}{\hbar^2 l(l+1)}}\,. \tag{2.5}$$

The $C_6$ coefficient for the $^1\mathrm{S}_0$ state is 3107(30) a.u and for the $^3\mathrm{P}_0$ state is 5360(200) a.u. [62], where 1 a.u. $= 1\ E_h a_0^6$, $E_h$ is the Hartree energy and $a_0$ is the Bohr radius. For $l = 1$, the centrifugal barrier is thus 35 $\mu$K in $^1\mathrm{S}_0$ and 26 $\mu$K in $^3\mathrm{P}_0$. Using narrow-line laser cooling we can reach temperatures of 1 $\mu$K. P-wave scattering, although small at $\mu$K temperatures, has been measured in both $^{87}$Sr and $^{171}$Yb optical lattice clocks in the excited clock states [63, 64, 25]. In the upcoming sections we will discuss the Fermi-degenerate regime, where $T$ is 100s of nK. P-wave scattering is negligible at these temperatures and only s-wave scattering is allowed.

The elastic scattering cross section is $\sigma = \int |f(\theta)|^2 d\Omega$, which can be simplified to $\sigma = 4\pi/k^2 \sum_l (2l+1)\sin^2\delta_l$. For fermions in different spin states that undergo s-wave scattering, this further simplifies to ($k \to 0$)

$$\sigma = 4\pi a^2\,, \tag{2.6}$$

where $a$ is the scattering length. However, for fermions in the same spin state, the s-wave scattering cross section is zero.

## 2.2 Noninteracting Fermi gases

S-wave collisions, the predominant collisions at ultralow temperatures, are forbidden for spin-polarized fermions. As a result, a spin-polarized ultracold Fermi gas can be described as an ideal Fermi gas consisting of noninteracting particles. Noninteracting theory is also a good first approximation for multi-component Fermi gases with small scattering lengths. This theory highlights the unique statistics of fermions and its consequences.

In this section, we first describe trapped Fermi gases in subsection 2.2.1. We subsequently describe the expansion of noninteracting Fermi gases after being released from the confining potential in subsection 2.2.2. Next we describe the structure factor, the response of the system to an external wavevector, in subsection 2.2.3, and the consequences of the Pauli exclusion principle on the structure factor, including Pauli blocking of collisions in subsection 2.2.4 and Pauli blocking of light scattering in subsection 2.2.5. We conclude with a discussion of a Fermi gas's correlation function, which is its response to spatial perturbations, in subsection 2.2.6 and the resulting suppression of density fluctuations in subsection 2.2.7.

### 2.2.1 Statistics of trapped Fermi gases

The thermodynamics of non-interacting Fermi gases can be described through statistical relations. The average number of fermions in a given spin state with energy $\epsilon$ is given by the Fermi-Dirac distribution [65]

$$\mathcal{F}(\epsilon) = \frac{1}{e^{\beta(\epsilon-\mu)}+1}\,, \tag{2.7}$$

where $\beta = 1/k_bT$, $k_b$ is the Boltzmann constant, and $\mu$ is the chemical potential. Non-interacting trapped Fermi gases can be described by the Hamiltonian

$$H = \frac{\mathbf{p}^2}{2m} + U(\mathbf{r})\,, \tag{2.8}$$

where $\mathbf{p}$ is the momentum, $m$ is the mass, $U(\mathbf{r}) = \frac{1}{2}m\sum_i \omega_i^2 x_i^2$ is the trapping potential, and $\omega_i$ are the trap frequencies due to the confinement along direction $x_i$. For a symmetric trap where $\omega_x = \omega_y = \omega_r$, we can rewrite the potential as $U(\mathbf{r}) = \frac{1}{2}m\omega_r^2(x^2+y^2+\lambda^2z^2)$ with $\lambda = \omega_z/\omega_r$. The total atom number is

$$\begin{aligned} N &= \int_0^\infty g(\epsilon)\mathcal{F}(\epsilon)d\epsilon \\ &= -\frac{\omega_r}{\omega_z}\left(\frac{k_bT}{\hbar\omega_r}\right)^3 Li_3(-\zeta)\,, \end{aligned} \tag{2.9}$$

where $\zeta = e^{\beta\mu}$ is the fugacity, $Li_n$ is the generalized polylogarithm of order $n$ and $g(\epsilon)$ is the density of states as a function of energy $\epsilon$, which in 3D is equal to [66]

$$g(\epsilon) = \frac{\epsilon^2}{2\hbar\bar{\omega}^3}\,, \tag{2.10}$$

where $\bar{\omega} = \left(\prod_j \omega_j\right)^{1/3}$. At $T = 0$, the occupation is one for each distinct energy state below $E_F$ and zero above $E_F$. The above equation can then be simplified to $N = \int_0^{E_F} g(\epsilon)d\epsilon$ and integrated to give $E_F = \hbar\bar{\omega}(6N)^{1/3}$. The total energy of the system is

$$\begin{aligned} E &= \int_0^\infty \epsilon g(\epsilon)\mathcal{F}(\epsilon) \\ &= -\frac{3}{\lambda}\frac{(k_bT)^4}{(\hbar\omega_r)^3} Li_4(-\xi)\,. \end{aligned} \tag{2.11}$$

At $T = 0$ the mean energy per particle is $\frac{3}{4}\,E_F$. The fugacity is related to the reduced temperature through

$$Li_3(-\zeta) = -\frac{1}{6(T/T_F)^3}\,. \tag{2.12}$$

For large numbers of atoms, a semiclassical phase space distribution can be used to describe the many-body wavefunction, where $f(\mathbf{r},\mathbf{p}) = (2\pi\hbar)^{-3}\mathcal{F}(H(\mathbf{r},\mathbf{p}))$. A semiclassical transport equation can be derived by assuming the phase space density is conserved, that is $df(\mathbf{r},\mathbf{p},t)/dt = 0$. Expanding this derivative gives us $\partial f/\partial t + \nabla_{\mathbf{r}} f \cdot \dot{\mathbf{r}} + \nabla_{\mathbf{p}} f \cdot \dot{\mathbf{p}} = 0$. This simplifies to

$$\left(\partial_t + \frac{\mathbf{p}}{m}\cdot\nabla_{\mathbf{r}} - \nabla_{\mathbf{r}}\,U(\mathbf{r})\cdot\nabla_{\mathbf{p}}\right) f = 0\,. \tag{2.13}$$

The above equation is called the Vlasov, or the collisionless Boltzmann, equation. We can see that the Fermi phase space distribution function, given by

$$f_0(\mathbf{r},\mathbf{p}) = \frac{1}{(2\pi\hbar)^3}\frac{1}{e^{\beta\left(\frac{\mathbf{p}^2}{2m}+U(\mathbf{r})-\mu\right)}+1}\,, \tag{2.14}$$

solves Equation 2.13 in equilibrium, when $\partial_t f = 0$. The real space density $n(\mathbf{r}) = \int d^3\mathbf{p} f(\mathbf{r},\mathbf{p})$ is then given by

$$n(\mathbf{r}) = -\frac{(k_b m T)^{3/2}}{(2\pi)^{3/2}\hbar^3} Li_{3/2}(-\zeta e^{-m\omega_r^2\beta\rho^2/2})\,, \tag{2.15}$$

where $\rho^2 = x^2 + y^2 + \lambda^2 z^2$.

### 2.2.2 Time of flight expansion

As is further discussed in Section 3.2, high-SNR images of the atomic cloud at high densities are best performed after the atoms are released from the confining potential and measured after long expansion times. The expanded gas can then be appropriately fit to extract $T/T_F$ and the atom number of the gas. For a noninteracting gas, atoms expand ballistically and thus the phase space density $f(t, \mathbf{r}, \mathbf{p}) = f_0(t, \mathbf{r} - \mathbf{p}t/m, \mathbf{p})$. This can be rewritten as [67]

$$f(\mathbf{r}, \mathbf{p}, t) = f_0 \left( \frac{r_i}{\lambda_i(t)}, \lambda_i(t) p_i - m\dot{\lambda}_i(t) r_i \right) , \tag{2.16}$$

where $f_0$ is the equilibrium distribution function given in Equation 2.14. The parameters $\lambda_i$ are scaling parameters that represent the dilution of the gas along the ith direction and can be solved to give the distribution function for different expansion times. We assume that before $t = 0$, the gas is in equilibrium with trap frequency $\omega_i$ where $i$ denotes the cardinal direction. The dynamics are then described by a sudden trap frequency change at $t = 0$ from $\omega_i$ to $\omega_f$ [67]. Multiplying Equation 2.13 by $r_i p_i$ and integrating in phase space, we find

$$\ddot{\lambda}_i + \omega_f^2 \lambda_i - \frac{\omega_i^2}{\lambda_i^3} = 0 \, , \tag{2.17}$$

To study the expansion after switching off the trap, $\omega_f$ in Equation 2.17 is set to 0. The differential equation is then solved for the scaling parameters, which yields $\lambda_i(t) = \sqrt{1 + \omega_i^2 t^2}$. This simple rescaling is unique for a harmonic trap. The scaling parameters can then be plugged into the scaling ansatz to yield the phase-space distribution after time-of-flight. We get that the density evolves according to

$$n(\mathbf{r}, t) = \frac{n(\mathbf{r}, 0)}{\prod_i \sqrt{1 + \omega_i^2 t^2}} \, . \tag{2.18}$$

That is, the 3D density is simply rescaled after expansion out of the trap.

The 3D density is hard to extract experimentally. Instead, the line-of-site integrated density is imaged along a particular direction (here integrated along y) which gives

$$n(x, z) = -\frac{1}{2\sqrt{1 + (\omega_r t)^2}\sqrt{1 + (\omega_z t)^2}} \frac{m (k_b T)^2}{\pi \hbar^3 \omega_r} Li_2(-\zeta e^{-x^2/2\sigma_x^2 - z^2/2\sigma_z^2}) \, , \tag{2.19}$$

where

$$\sigma_i^2(t) = \left\langle x_i^2 \right\rangle_0 (t) = \frac{k_b T}{m} \frac{1 + \omega_i^2 t^2}{\omega_i^2} \, . \tag{2.20}$$

Fitting the expanded gas cloud to the above equation after time of flight allows us to extract the fugacity. As the fugacity depends on the shape of the atomic cloud and not on other extracted parameters, it allows an accurate determination of $T/T_F$. The aspect ratio of the line-of-site integrated density is

$$\frac{\sigma_z}{\sigma_x} = \frac{\omega_x}{\omega_z}\sqrt{\frac{1+\omega_z^2 t^2}{1+\omega_x^2 t^2}}\,. \tag{2.21}$$

At long expansion times ($\omega_i t >> 1$), the aspect ratio approaches one. This reflects the fact that expansion occurs ballistically. After long time-of-flight, the cloud reflects the isotropic momentum distribution even if the confining potential is anisotropic.

### 2.2.3 Static structure factor

Fermi statistics has profound effects on the scattering behavior of particles. The static structure factor $S_{\mathbf{k}}$ describes the response of a system to a perturbation with wave vector $\mathbf{k}$. Perturbations can come from, for example, light, or from collisions with other non-identical particles. The consequences of the Pauli exclusion principle are evident in the static structure factor, given by

$$S_{\mathbf{k}} = \sum_{\mathbf{u}}\sum_{\mathbf{v}} n_i(\mathbf{v})\Big(1-n_f(\mathbf{u})\Big)|\left\langle \mathbf{u}\right| e^{i\mathbf{k}\cdot\hat{\mathbf{r}}} \left|\mathbf{v}\right\rangle|^2\,, \tag{2.22}$$

where the sums are over all energy eigenstates and $\hat{\mathbf{r}}$ represents the position operator. This equation states that the probability a fermion scatters from energy state $|\mathbf{v}\rangle$ into energy state $|\mathbf{u}\rangle$ is proportional to the occupation number of the initial state $n_i(\mathbf{v})$, times the probability that the final state $n_f(\mathbf{u})$ is empty. The product must be weighted by the probability that the fermion will scatter into state $|\mathbf{u}\rangle$ given a momentum transfer of $\mathbf{k}$. In a harmonic trap with many harmonic oscillator levels filled, the structure factor can be approximated with a semiclassical equation as

$$S(\mathbf{k}) = h^{-3}\int d^3\mathbf{r}\int d^3\mathbf{p} f_i(\mathbf{p},\mathbf{r})\Big(1-f_f(\mathbf{p}+\hbar\mathbf{k},\mathbf{r})\Big)\,, \tag{2.23}$$

where $f(\mathbf{p},\mathbf{r})$ is given in Equation 2.14.

### 2.2.4 Pauli blocking of collisions

The Pauli exclusion principle describes a fundamental phenomenon that gives rise to properties such as Fermi pressure, which causes the size of a Fermi gas to saturate as the temperature is lowered [68]. The above discussion demonstrates a consequence of the Pauli exclusion principle, that scattering is not allowed if the final momentum state is occupied by another identical fermion. The momentum transfer $\mathbf{k}$ during this process can be imparted for example through collision with another particle. This has a measurable consequence on the equilibrium thermodynamic properties and collisional dynamics of a multiple component Fermi gas. In the degenerate regime, Pauli exclusion reduces a gas's ability to perform binary collisions, which can be illustrated by noting the following: Imagine that the system consists of two equal $T = 0$ Fermi gases, so that all levels below $E_F$ are occupied, and where each Fermi sea has a different spin so that scattering between the seas is allowed. The initial energies of any scattered particles $E_1$ and $E_2$ must be less than $E_F$. In order for two particles to scatter, the final states with energies $E_3$ and $E_4$ must be greater than $E_F$, since all states below $E_F$ are occupied. That is, our conditions for scattering are $E_1, E_2 < E_F$ and $E_3, E_4 > E_F$. However, energy conservation requires that $E_1 + E_2 = E_3 + E_4$. This is in direct contradiction with the energy bounds we set. Thus, scattering between two Fermi seas is completely blocked at $T = 0$.

The elastic cross-section for a two-component Fermi gas goes from the classical value of $\sigma_{el} = 4\pi a^2$ to 0 at $T = 0$ [69]. The suppression of collisions causes a reduction in the evaporation efficiency at degenerate temperatures [70] and in the energy per atom in an imbalanced two-component Fermi gas [71]. In the latter case, different Fermi energies cause a disparate mean energy per particle between the two components. In a classical system, collisions between components would equalize the mean energy per particle, but those collisions are blocked for a Fermi gas. The more degenerate component has a larger Fermi sea, and collisions that cause a reduction in energy are blocked due to occupied final states.

### 2.2.5 Pauli blocking of light scattering

The momentum $\mathbf{k}$ imparted to an atom can additionally be caused by light. When an atom absorbs a photon, it receives a recoil of energy $E_r = \hbar^2 k^2/2m$, where $k$ is the light's wavevector. For a light scattering experiment where an atom undergoes a directed absorption followed by a dispersive spontaneous emission event, the total momentum transfer $\mathbf{k}$ can range anywhere from 0 to $2k_r$, where $k_r = \sqrt{2mE_r}$ is the recoil momentum. This has the striking consequence that if $T = 0$, $k$ is much less than the Fermi momentum radius $k_F$, and the Fermi sea is weakly excited such that the ground state Fermi sea remains unperturbed after absorption of the probe light, most excited atoms are prohibited from decaying. Only atoms near the edge of the Fermi sea, which can be excited to unoccupied states outside of the Fermi sea, will be able to decay. Experiments to observe this Pauli suppression of the spontaneous emission rate of an atom will be discussed in more detail in Chapters 5 and 6. Here we review the theory of Pauli suppression in light scattering experiments, focusing on the intuition gained from analyzing the case of a $T = 0$ spin-polarized Fermi gas.

Equation 2.23 can be compared to a Maxwell-Boltzmann distribution to give the relative scattering rate [72]

$$\frac{S_{FM}(\mathbf{k})}{S_{MB}} = \frac{h^{-3}\int d^3\mathbf{r}\int d^3\mathbf{p} f_i(\mathbf{p},\mathbf{r})\Big(1 - f_f(\mathbf{p}+\hbar\mathbf{k},\mathbf{r})\Big)}{h^{-3}\int d^3\mathbf{r}\int d^3\mathbf{p} f_i(\mathbf{p},\mathbf{q})}\,. \tag{2.24}$$

This integral can be simplified by making the variable substitutions $\tilde{r}_j = r_j\sqrt{\beta m\omega_j^2/2}$, $\tilde{p}_j = p_j\sqrt{\beta/2m}$ to give

$$\frac{S_{FM}(\mathbf{k})}{S_{MB}} = 1 - \frac{6}{\pi^3 E_F^3 \beta^3}\int d^3\tilde{\mathbf{r}}\int d^3\tilde{\mathbf{p}}\frac{1}{1+\zeta^{-1}e^{(\tilde{\mathbf{p}}^2+\tilde{\mathbf{r}}^2)}}\frac{1}{1+\zeta^{-1}e^{((\tilde{\mathbf{p}}+\sqrt{\beta E_F}\mathbf{k}/k_F)^2+\tilde{\mathbf{r}}^2)}}\,, \tag{2.25}$$

where $\bar{\omega} = (\omega_x\omega_y\omega_z)^{1/3}$ is the average trap frequency, and we used the fact that $\hbar k_F = (2mE_F)^{1/2}$ and $E_F = \hbar\bar{\omega}(6N)^{1/3}$. This makes the integral spherically symmetric. We can align our coordinate system such that the momentum transfer $\mathbf{k}$ is along the z-direction, that is $\mathbf{k} = k\hat{z}$. The position and two other momentum directions can be expressed in 5-dimensional spherical coordinates with radius $s$ to give

$$\frac{S_{FM}(\mathbf{k})}{S_{MB}} = 1 - \frac{16}{\pi E_F^3 \beta^3} \int dss^4 \int dp_z \frac{1}{1+\zeta^{-1}e^{s^2+p_z^2}} \frac{1}{1+\zeta^{-1}e^{s^2+(p_z+k_{scal})^2}} \,, \tag{2.26}$$

where we have used the fact that the volume element, integrated over the 4 angular directions, is equal to $8\pi^2/3s^4ds$ and $k_{scal} = \sqrt{\beta E_F}k/k_F$. Finally, we let $a = s^2$ to arrive at the formula

$$\frac{S_{FM}(\mathbf{k})}{S_{MB}} = 1 - \frac{8}{\pi E_F^3 \beta^3} \int daa^{3/2} \int dp_z \frac{1}{1+\zeta^{-1}e^{a+p_z^2}} \frac{1}{1+\zeta^{-1}e^{a+(p_z+k_{scal})^2}} \,. \tag{2.27}$$

This can be numerically solved for finite $T/T_F$ to extract the reduction factor of the scattering rate. Equation 2.27 can be explicitly solved at $T = 0$ to obtain [72]

$$\frac{S_{FM}(\mathbf{k})}{S_{MB}} = 1 - \frac{32}{5\pi}\chi(\frac{k}{2k_F})\Theta(2 - k/k_F)\,, \tag{2.28}$$

where $\Theta$ is the Heaviside step function and

$$\chi(x) = \frac{x\sqrt{1-x^2}}{48}(-8x^4 + 26x^2 - 33) + \frac{15}{48}\cos^{-1}(x)\,. \tag{2.29}$$

For a light scattering experiment, an atom first receives a momentum kick $\mathbf{k}_{abs}$ along a defined direction, and a second randomly oriented momentum kick $\mathbf{k}_{emi}$ upon spontaneous decay, where $|\mathbf{k}_{abs}| = |\mathbf{k}_{emi}| = k_R$. The total momentum transfer $\mathbf{k}$ is then given by $\mathbf{k} = \mathbf{k}_{abs} + \mathbf{k}_{emi}$ where $k = 2k_R sin(\alpha/2)$ and $\alpha$ is the angle between the absorbed and emitted photon. This is illustrated in Fig. 2.1 for the specific case of a single excited atom in the center of the Fermi sea in a $T = 0$ gas. Here, if $k_F > 2k_R$, complete suppression is achieved and $S_{FM}(\mathbf{k}) = 0$.

Equation 2.28 is plotted in Fig. 2.2 as a function of $\alpha$ and $k_F/k_R$. Decay can occur if the momentum transfer kicks the atom outside the Fermi sea. No suppression occurs when $k > 2k_F$, as is reflected in the Heaviside step function in Equation 2.28. This is because all atoms, regardless of their position within the Fermi sea, will get kicked outside it. For $k < 2k_F$, suppression is dominant in a cone near the absorption direction, where the total momentum transfer is small. Larger suppression can be achieved at all angles $\alpha$ when $E_F >> E_R$. However, even at large Fermi

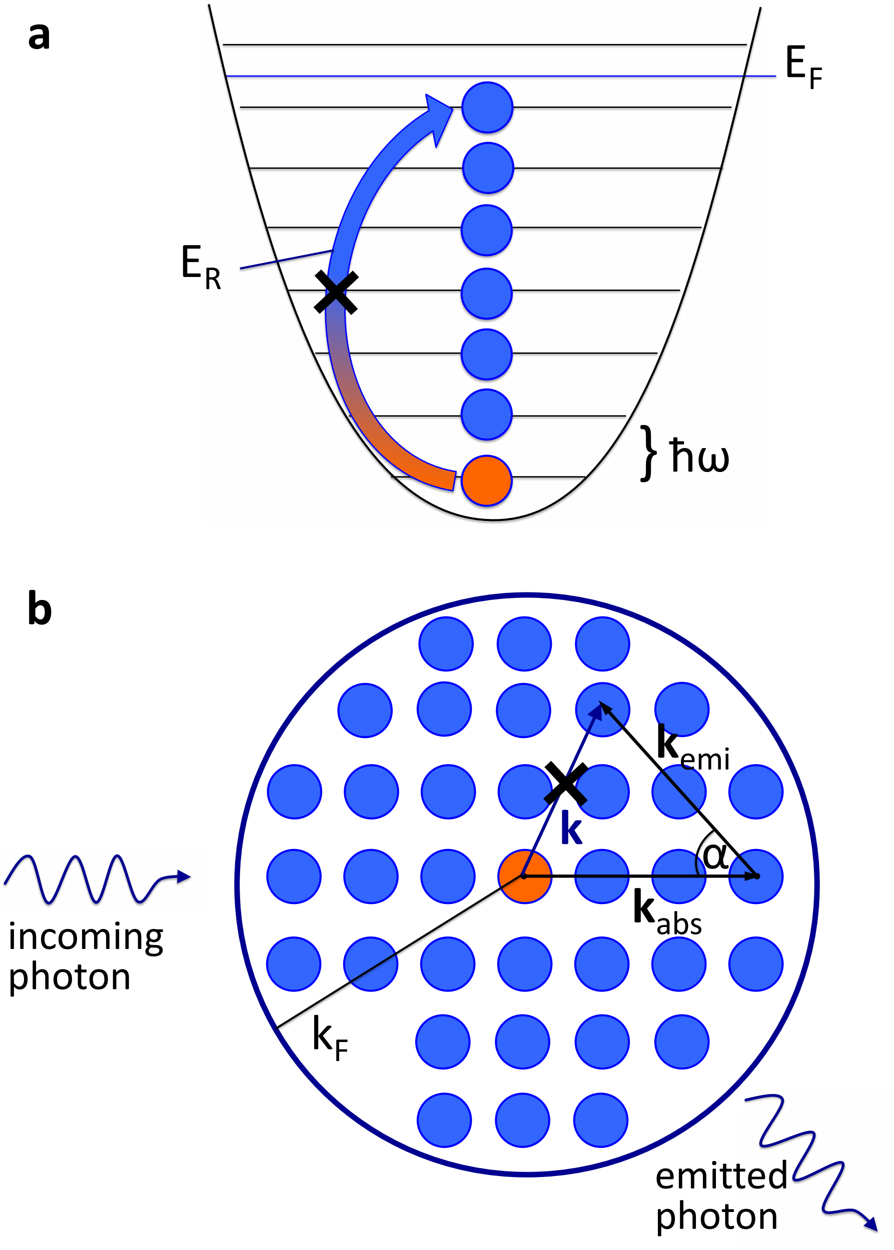

Figure 2.1: (a) In a $T = 0$ Fermi gas, all available harmonic oscillator states up to the Fermi energy $E_F$ are filled with unity occupation. An excited atom (orange) acquires a recoil energy $E_R$ when returning to its internal ground state (blue). (B) In momentum space, the atoms form a Fermi sea occupying all states up to the Fermi momentum $\hbar k_F$. Spontaneous decay of an excited atom with emission along $\alpha$ and total momentum transfer $\hbar k$ can happen only if the final momentum state is not occupied by another ground state fermion. If $k_F > 2k_R$, all final states are occupied and the atom cannot decay. The decay in both (a) and (b) is blocked since the final state is occupied.

energies, atoms near the edge of the Fermi sea can be excited to available decay channels outside

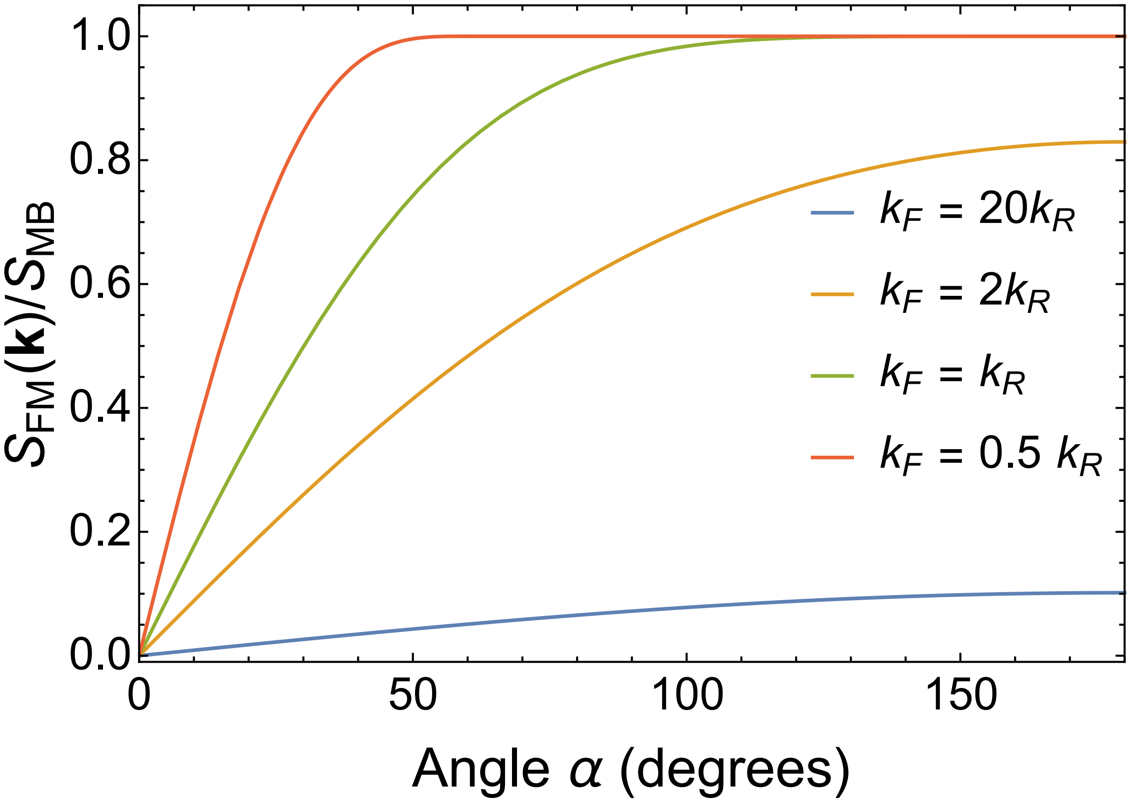

Figure 2.2: Suppression of the scattering rate for a Fermi versus classical gas for various angles $\alpha$ between the absorbed and emitted photons, and Fermi versus recoil momentum. When $k = 2k_R \sin(\alpha/2) > 2k_F$, no suppression occurs.

the Fermi sea. Complete suppression thus only occurs for $E_F >> E_R$ and when only the atoms near the center of the Fermi sea are excited. Note that Equation 2.28 only depends on the ratio $k/k_F = 2k_R/k_F \sin(\alpha/2)$. Thus, changing the ratio of $k_R/k_F$ or the angle $\alpha$ are equivalent. At finite temperature, holes within the Fermi sea provide additional paths for atoms to decay, and even with $E_F >> E_R$ only finite suppression is achieved at all angles.

### 2.2.6 Density-density correlation function

If Fermi statistics modify the response of a Fermi gas to a perturbation of wavevector $\mathbf{k}$, then it must similarly modify the response to perturbations at a distance scale of $\mathbf{r} = 1/\mathbf{k}$. This is reflected in the correlation function $\nu(\mathbf{r})$, which is the Fourier transform of $S_{\mathbf{k}}$ [73]:

$$\nu(\mathbf{r}) = \frac{1}{(2\pi)^3} \int d^3\mathbf{k} S_{\mathbf{k}} e^{i\mathbf{k}\cdot\mathbf{r}}\,, \tag{2.30}$$

where $\mathbf{r} = \mathbf{r}_1 - \mathbf{r}_2$ is the distance between two particles at positions $\mathbf{r}_1$ and $\mathbf{r}_2$. The idea to look at density-density correlations of ultracold atoms was originally proposed in Ref. [74], and was first measured between different spin states of a Feshbach molecule [75]. To further analyze $\nu(\mathbf{r})$, we take advantage of the local density approximation (LDA) [76] and absorb the spatial variation of the potential into a locally changing chemical potential $\mu_{LDA} \equiv \mu - U(\mathbf{r})$. This allows us to locally treat the trapped Fermi gas as a homogeneous gas. The density-density correlation function $C(\mathbf{r}) = n\nu(\mathbf{r})$, where $n$ is the density, can then be written as [77]

$$C(\mathbf{r}) = n\delta(\mathbf{r}) - \left[\frac{k_B T}{E_F}\frac{k_F^2}{2\pi^2 r}\int_0^\infty du \frac{u \sin(u\sqrt{k_B T/E_F}k_F r)}{e^{-\beta\mu_{LDA}}e^{u^2}+1}\right]^2 . \tag{2.31}$$

For a $T = 0$ gas, the correlation function further simplifies to [78]

$$\begin{aligned} C(\mathbf{r}) &= n\delta(\mathbf{r}) - n^2\frac{9}{(k_F r)^2}\left[\frac{\cos(k_F r)}{k_F r} - \frac{\sin(k_F r)}{(k_F r)^2}\right]^2 \\ &= n\delta(\mathbf{r}) - n^2(g^2(\mathbf{r}) - 1)\,, \end{aligned} \tag{2.32}$$

Equation 2.32 is divided into "auto-correlations", which associate the correlation of the particle with itself, and pair-wise correlations given by $g^2(\mathbf{r})$, which is the conditional probability of finding two particles separated by distance $\mathbf{r}$. $g^2(r)$ is plotted in Fig. 2.3 versus $k_F r$. From this figure, one can see for distances $r \sim 1/k_F$ that $g^2(r) < 1$ and approaches 0 as $r \to 0$. This reflects the reduced probability of finding two fermions closer than $\sim 1/k_F$ due to Pauli exclusion.

Combined with the autocorrelations, $C(\mathbf{r})$ is negative for fermions. This fermionic 'anti-bunching' was originally observed in a band insulator of $^{40}$K atoms released from an optical lattice [79], and in a gas of $^3$He [80]. Higher order correlations beyond second order lead to the formation of Pauli Crystals, geometrical structures that are formed in few-body systems [81, 82].

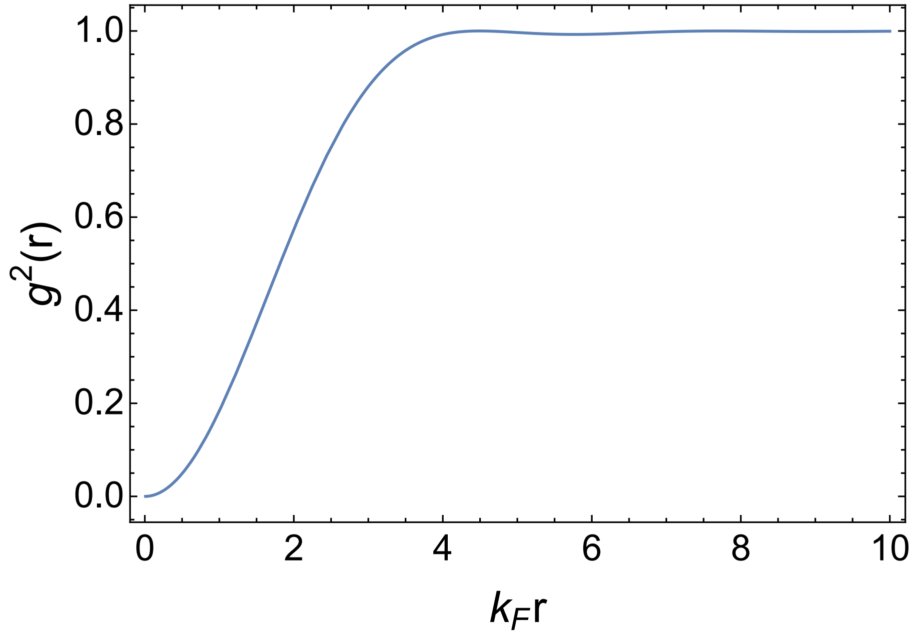

Figure 2.3: Pair distribution function versus scaled distance between the two particles.

### 2.2.7 Density fluctuations

The correlation function $C(\mathbf{r}) = \langle n(\mathbf{r}_1)n(\mathbf{r}_2)\rangle - \langle n(\mathbf{r}_1)\rangle \langle n(\mathbf{r}_2)\rangle$ is related to density fluctuations through

$$\left\langle (\delta n(\mathbf{r}))^2 \right\rangle = \int d^3\mathbf{r}_1 \int d^3\mathbf{r}_2 \, C(\mathbf{r})\delta(\mathbf{r}_1 - \mathbf{r}_2 - \mathbf{r}) \, , \tag{2.33}$$

where the notation $\langle \cdot \rangle$ represents the statistical mean, which is the result of a large number of independent realizations. In an experimental context, this implies the result of a large number of repeated measurements. The particle number fluctuations in a subvolume $V = 4/3\pi R^3$ of the Fermi gas can be expressed as

$$\left\langle (\delta N)^2 \right\rangle = \int_0^R C(r)h(r) \, 4\pi r^2 dr = \frac{1}{(2\pi)^3} \int d^3\mathbf{k} n S(\mathbf{k}) H(\mathbf{k}) \, , \tag{2.34}$$

where $h(\mathbf{r})$ is a geometrical overlap factor, given by

$$h(\mathbf{r}) = \int_V d^3\mathbf{r}_1 \int_V d^3\mathbf{r}_2 \delta(\mathbf{r}_1 - \mathbf{r}_2 - \mathbf{r}) \, . \tag{2.35}$$

Physically, this represents the overlap region between a subvolume $V$ and that subvolume shifted by $\mathbf{r}$, while $H(\mathbf{k})$ is its Fourier transform. To gain intuition about Equation 2.34, we first look at a $T = 0$ gas. In this limit, the number fluctuations can be rewritten for large $k_F R$ as [76, 83]

$$\left\langle (\delta N)^2 \right\rangle = \frac{(k_F R)^2}{2\pi^2} \ln\left[4e^{\gamma - 1/2} k_F R\right] + \mathcal{O}(1/k_F R)\,, \tag{2.36}$$

where $4e^{\gamma-1/2} = 4.32$. In a $T = 0$ gas, there are no thermal fluctuations since every state is always occupied below $E_F$. However, Equation 2.36 reveals an additional source of atom number noise. Upon measurement, atoms are projected into the subvolume with a probability given by the overlap of the particle's wavefunction inside $V$. This finite probability for small enough box sizes causes atom number fluctuations, similar in concept to quantum projection noise. For a box with many atoms, quantum projection noise is a particular problem on the edges of the subvolume, since projection noise puts these atoms either inside or outside the box [2] . Hence, the fluctuations depend on the surface area of the box which goes like $R^2$. Written in terms of the atom number, Equation 2.36 can be written as

$$\frac{\left\langle (\delta N)^2 \right\rangle}{N} = 3\left(\frac{3}{32\pi^4}\right)^{1/3} N^{-1/3} \ln\left[10.45 N^{1/3}\right]\,, \tag{2.37}$$

and thus the effect disappears in the thermodynamic limit, when a subvolume contains many particles and the projection noise tends towards zero.

In the thermodynamic limit at finite temperature, $H(\mathbf{k}) \to V\delta(\mathbf{k})$ so that Equation 2.34 simplifies to $(\delta N)^2 = NS(0)$, yielding the result of the fluctuation-response theorem [84] with generalized force $\mu$, which is the chemical potential:

$$\left\langle (\delta N)^2 \right\rangle = N k_B T n \kappa_T\,, \tag{2.38}$$

where $\kappa_T = -1/V(\partial V/\partial P)_{T,N}$ is the isothermal compressibility. This result can also be derived using the Grand partition function

$$\mathcal{Z} = \prod_p \sum_{n_p} e^{-\beta n_p(\epsilon_p - \mu)}\,, \tag{2.39}$$

---

[2] Technically, the same underlying source of projection noise exists for smaller boxes where there are only a few atoms, but it is difficult to accurately model the fluctuations in this case as it depends on the precise shape of the single-particle wavefunctions.

where the sum is over states $p$ with occupation per state $n_p$. For identical fermions, the occupation can be either zero or one so that

$$\mathcal{Z} = \prod_p (1 + e^{-\beta(\epsilon_p - \mu)})\,. \tag{2.40}$$

The average atom number $\langle N \rangle$ is related to the Grand Potential $\Omega = -k_B T \ln(\mathcal{Z})$ through $N = -\left(\partial\Omega/\partial\mu\right)_{V,T}$, which after making the sum continuous gives the familiar equation

$$N = 4\pi \frac{V}{h^3} \int_0^\infty dpp^2 \frac{1}{\zeta^{-1} e^{\beta\epsilon_p} + 1} = \frac{V}{\lambda^3} f_{3/2}(\zeta)\,, \tag{2.41}$$

where $f_n(\zeta) = -Li_n(-\zeta)$ and $\lambda = \sqrt{2\pi\hbar^2/mk_B T}$ is the thermal deBroglie wavelength. The variance is then [85]

$$\left\langle (\delta N)^2 \right\rangle = \left(k_B T \frac{\partial}{\partial\mu}\right)^2 \log(\mathcal{Z}) = k_B T \frac{\partial N}{\partial \mu}\,. \tag{2.42}$$

$\kappa_T$ can be expressed using Maxwell's relations as $\kappa_T = V/N^2 \left(\partial N/\partial\mu\right)_{T,V}$. Equation 2.42 thus reproduces Equation 2.38. Given the relation $\partial f_n(\zeta)/\partial\zeta = f_{n-1}(\zeta)/\zeta$, we find

$$\left\langle (\delta N)^2 \right\rangle = \frac{V}{\lambda^3} f_{1/2}(\zeta)\,, \tag{2.43}$$

and thus

$$\left\langle (\delta N)^2 \right\rangle /N = \frac{f_{1/2}(\zeta)}{f_{3/2}(\zeta)} = n k_B T \kappa_T\,. \tag{2.44}$$

Atom number fluctuations in the above equation are of purely thermal origin and can be understood as follows. Thermal fluctuations manifest on the Fermi surface, where the occupation number is not unity and the majority of holes lie. In real space, this corresponds to fluctuations delocalized equally over the whole homogeneous Fermi gas. As $T/T_F$ decreases, the width of the Fermi surface narrows and the number of holes decreases so that the thermal fluctuations correspondingly decline. Taken in light of the LDA, this implies that fluctuations on the edge of a trapped Fermi gas, where the local $T/T_F$ is larger, will experience increased fluctuations compared to the center of the Fermi gas where $\mu$ is maximum. To first order in $T/T_F$, Equation 2.44 becomes

$$\left\langle (\delta N)^2 \right\rangle /N = \frac{3}{2} T/T_F\,, \tag{2.45}$$

implying $\kappa_T = \frac{3}{2nE_F}$. In contrast, for a classical gas, $(\delta N)^2/N = 1$, reflecting the Poisson statistics of the gas [3] .

In the actual experiment, we do not measure the 3D atomic density but instead the column density, which is the 3D density integrated along the line-of-site (LOS) of the imaging camera. We can obtain the expected fluctuations by integrating the fugacity in Equation 2.44 through the imaging direction $x_3$ [4] :

$$\left[(\delta N)^2/N\right]_{LOS} = \frac{\int f_{1/2}(\zeta(x_1,x_2,x_3))dx_3}{\int f_{3/2}(\zeta(x_1,x_2,x_3))dx_3} = \frac{f_1(e^{-\beta(\mu-U(x_1,x_2))})}{f_2(e^{-\beta(\mu-U(x_1,x_2))})}\,. \tag{2.46}$$

To obtain $T/T_F$ from the experimental data, we look at $(\delta N)^2$ versus $N$ in the same subvolume across a series of images. We perform the noise analysis after time-of-flight to avoid any collective scattering processes that can occur when imaging an atomic cloud at high density. Because the density is simply rescaled after time-of-flight, the noise properties $(\delta N)^2/N = k_BT/n\,\partial n/\partial\mu$ are not altered. To account for shot-to-shot atom fluctuations due to imperfections in the experimental preparation, we high pass each image by fitting each atom cloud to a gaussian and looking at the residuals. In comparison to scaling each image, this also minimizes the effect of center-of-mass fluctuations on the results. Repeating this protocol for subvolumes in the center vs edge of the Fermi gas gives us $T/T_F$ as a function of the harmonic confinement, which we then fit with theory. The subvolume size is set by looking at $(\delta N)^2/N$ and observing when the fluctuations saturate as we vary the box size. Finally, photon shot noise must be subtracted to get an accurate calibration of the thermal fluctuations. This can easily be obtained for each subvolume by looking at the bright image in the absorption image analysis. See Chapter 3 for more details on our imaging methods.

Sub-Poissonian fluctuations were first measured by the groups of Ketterle [86] and Esslinger [87] in noninteracting trapped Fermi gases, showing up to around 50% of suppression compared to a classical gas. Reduced fluctuations have also been seen in the Mott-insulating and band-insulating regimes in an optical lattice, see for eg [88, 89, 90], and have been used as a complementary

---

[3] The number fluctuations for a classical gas follow a binomial distribution. For large atom numbers, this is approximately Poissonian and the probability of having atom number $N$ in subvolume $V$ is $p_N = \langle N\rangle^N e^{-\langle N\rangle}/N!$. The atom number variance is thus $(\delta N)^2 = \langle N\rangle$.

[4] We use the identity $\int_{-\infty}^{\infty} f_n(\zeta e^{-x^2})dx = \sqrt{\pi} f_{n+1/2}(\zeta)$

technique to confirm the degenerate temperatures that were extracted through global profile fits in KRb [91].

## 2.3 Interacting Fermi gases

When more than one spin component exists in a Fermi gas, s-wave collisions allow interactions between components with a strength that depends on the scattering length $a$. In this section, we outline the physics of interacting two-component Fermi gases, which are the simplest multi-component system to analyze and gain intuition. This will provide a theoretical basis which will be expanded on in Chapter 4 to describe interacting SU($N$) systems with $N = 10$ spin components. In subsection 2.3.1 we derive the Hamiltonian for an interacting Fermi gas, and in subsection 2.3.2 we discuss the expansion dynamics of interacting systems. We conclude with a discussion of density fluctuations in a repulsively interacting trapped Fermi gas in subsection 2.3.3.

### 2.3.1 Interaction Hamiltonian

The scattering potential between particles is complex at short-range, but can be simplified at long range into a Van-der Waals potential in the ground state, $V(r) \sim C_6/r^6$. For excited state atoms, dipole-dipole interactions are also important, with $V(r) \sim C_3/r^3$. Fermi discovered that a simpler pseudopotential can describe many properties correctly, including the energies and scattering phase shifts. The pseudopotential for s-wave scattering is given by [92]

$$V(\mathbf{r}) = \frac{4\pi a\hbar^2}{m}\delta(\mathbf{r})\,. \tag{2.47}$$

The use of a pseudopotential greatly simplifies the interaction potential between particles, and is accurate as long as the details of the short-range physics are not important.

Given the simplification granted by the Fermi pseudopotential, we will now derive the interaction potential in an ultracold two-component Fermi gas. As derived in Section 2.1, s-wave collisions are predominant at ultralow temperatures. Interactions thus largely occur between particles with different spins. The Fermi pseudotential allows us to write the total interaction energy as

$$\begin{aligned} H_{int} &= \int d^3\mathbf{r} d^3\mathbf{r}' \hat{\psi}^\dagger_\uparrow(\mathbf{r})\hat{\psi}^\dagger_\downarrow(\mathbf{r}')V(\mathbf{r}-\mathbf{r}')\hat{\psi}_\downarrow(\mathbf{r}')\hat{\psi}_\uparrow(\mathbf{r}) \\ &= g\int d^3\mathbf{r}\hat{\psi}^\dagger_\uparrow(\mathbf{r})\hat{\psi}^\dagger_\downarrow(\mathbf{r})\hat{\psi}_\downarrow(\mathbf{r})\hat{\psi}_\uparrow(\mathbf{r})\,, \end{aligned} \tag{2.48}$$

where we have identified the interaction strength $g = 4\pi\hbar^2 a/m$, and $\hat{\psi}_\sigma(\mathbf{r})$ ($\hat{\psi}^\dagger_\sigma(\mathbf{r})$) annihilates (creates) a fermion of spin $\sigma$ at point $\mathbf{r}$. We have labeled the two spin states as $|\uparrow\rangle$ and $|\downarrow\rangle$. The fermionic operators satisfy $\{\hat{\psi}_\sigma(\mathbf{r}), \hat{\psi}^\dagger_{\sigma'}(\mathbf{r}')\} = \delta_{\sigma,\sigma'}\delta(\mathbf{r}-\mathbf{r}')$. Given the density operator $\hat{n}_\sigma(\mathbf{r}) = \hat{\psi}^\dagger_\sigma(\mathbf{r})\hat{\psi}_\sigma(\mathbf{r})$, and assuming the density for both components is equal, that is $\hat{n}_\uparrow(\mathbf{r}) = \hat{n}_\downarrow(\mathbf{r}) = \hat{n}(\mathbf{r})$, the interaction energy can be further rewritten as

$$\begin{aligned} H_{int} &= g\int d^3\mathbf{r}\hat{n}_\uparrow(\mathbf{r})\hat{n}_\downarrow(\mathbf{r}) \\ &= g\int d^3\mathbf{r} n^2(\mathbf{r})\,. \end{aligned} \tag{2.49}$$

The total Hamiltonian for a single component can be written as

$$H_\sigma = \int d^3\mathbf{r}\,\hat{\psi}^\dagger_\sigma(\mathbf{r})\left(-\frac{\nabla^2}{2m} + U(\mathbf{r})\right)\hat{\psi}_\sigma(\mathbf{r}) + \int d^3\mathbf{r}\hat{\psi}^\dagger_\sigma(\mathbf{r})\Big(gn(\mathbf{r})\Big)\hat{\psi}_\sigma(\mathbf{r})\,, \tag{2.50}$$

where the first term describes the kinetic and potential energy of the fermions, which are confined by a harmonic trapping potential $U = m/2\sum_i \omega_i^2 x_i^2$. The above equation makes it apparent that the interaction energy looks like an additional effective potential with a strength given by the mean field energy:

$$V_{MF} = gn(\mathbf{r})\,. \tag{2.51}$$

The derived interaction Hamiltonian is accurate for a two-component Fermi gas. In general, interactions can exist between many spin components, and the interaction potential must take into account all possible two-body interactions, which in general have different scattering lengths $a$. Under SU($N$) symmetry, the nuclear spin degree of freedom is decoupled from the electronic angular momentum so that all scattering lengths $a$ are equal for atoms in different nuclear spin states, and the interaction Hamiltonian is greatly simplified. This allows enhanced interactions without inelastic spin loss that normally result when a gas has many-components. We will discuss SU($N$) interactions in more detail in Chapter 4.

### 2.3.2 Expansion dynamics

To solve for the expansion dynamics of the gas after switching off the harmonic confinement, we can use the same method as that used for noninteracting Fermi gases in subsections 2.2.1 and 2.2.2, but replace $U(\mathbf{r})$ with the effective potential $U(\mathbf{r})+gn(\mathbf{r})$. The Boltzmann equation becomes

$$\Big(\partial_t + \frac{\mathbf{p}}{m}\cdot\nabla_{\mathbf{r}} - \nabla_{\mathbf{r}}\left[U(\mathbf{r})+gn(\mathbf{r})\right]\cdot\nabla_{\mathbf{p}}\Big) f = 0\,. \tag{2.52}$$

Solving the equation in equilibrium ($\partial_t f = 0$) gives us the interacting equilibrium distribution function

$$f_0(\mathbf{r},\mathbf{p}) = \frac{1}{(2\pi\hbar)^3}\frac{1}{e^{\beta\left(\frac{\mathbf{p}^2}{2m}+U(\mathbf{r})+gn(\mathbf{r})-\mu\right)}+1}\,. \tag{2.53}$$

Due to the dependence of the distribution function on $n(\mathbf{r})$, the equilibrium distribution must be solved self-consistently [59]. First a zeroth order distribution function is calculated by assuming there are no interactions. The density is then calculated through $n(\mathbf{r}) = \int d^3\mathbf{p} f(\mathbf{r},\mathbf{p})$, and then using the calculated density, the next order distribution function is derived. This process is repeated several times until the distribution function converges. The time-of-flight expansion dynamics can then be solved for using the same scaling method as introduced for the non-interacting gas. The scaling ansatz is

$$f(\mathbf{r},\mathbf{p},t) = f_0\left(\frac{r_i}{\lambda_i(t)}, \lambda_i(t)p_i - m\dot{\lambda}_i(t)r_i\right)\,, \tag{2.54}$$

where $f_0$ is the equilibrium distribution function. The scaling parameters $\lambda_i$ satisfy the differential equation [93]

$$\ddot{\lambda}_i + \omega_f^2\lambda_i - \frac{\omega_i^2}{\lambda_i^3} + \xi_i\omega_i^2\left(\frac{1}{\lambda_i^3} - \frac{1}{\lambda_i\prod_j\lambda_j}\right) = 0\,, \tag{2.55}$$

where $\xi_i = g\langle n\rangle/(g\langle n\rangle + \langle p_i^2\rangle/2m)$. For a zero temperature Fermi gas, $\xi \sim k_F a$, where $k_F a$ is commonly referred to as the interaction parameter. It can be understood as the ratio of the scattering length to the interparticle distance, and characterizes the strength of interactions.

If we switch off the harmonic trap, $\omega_f$ is set to zero and we can numerically solve for $\lambda_i$. The aspect ratio of the gas after time $t$ is then $\sqrt{\langle r_z(t)\rangle^2/\langle r_r(t)\rangle^2} \equiv \sigma_z/\sigma_r = \lambda_z(t)\omega_r/\lambda_r(t)\omega_z$. For a repulsively interacting Fermi gas ($a > 0$), the cloud aspect ratio will invert for long time-of-flight. This can be understood as follows. Interactions provide an additional force during expansion that is proportional to $dn(\mathbf{r})/d\mathbf{r}$. A trap that is initially tightly confined in the z-direction will thus expand more after time-of-flight, since interactions will preferentially push atoms along the direction of the largest density gradient. This is in contrast to the non-interacting case, where the aspect ratio approaches one after long time-of-flight, as dictated by the initial homogeneous momentum.

#### 2.3.2.1 Collisions during expansion

An implicit assumption made thus far is that collisions do not occur during the expansion. Collisions change the momentum distribution and as a result can alter the expanded density distribution. While the mean-field force is non-dissipative, collisions are dissipative and the availability of the final momentum states as governed by Fermi statistics needs to be considered [94]. The Boltzmann equation, which can be derived by assuming unimpeded semiclassical motion of particles, needs to be modified. With collisions the Boltzmann equation becomes [95]

$$\Big(\partial_t + \frac{\mathbf{p}}{m} \cdot \nabla_{\mathbf{r}} - \nabla_{\mathbf{r}} \left[U(\mathbf{r}) + gn(\mathbf{r})\right] \cdot \nabla_{\mathbf{p}}\Big)\, f = I_c[f]\,, \tag{2.56}$$

where $I_c[f]$ is the collisional term. In general the collisional term describes two-body collisions and is given by [94]

$$I_c[f] = \frac{a^2}{h^3 m} \int d^3p_2 d\Omega |\mathbf{p}_1 - \mathbf{p}_2| \left[(1 - f_\sigma(\mathbf{p}_1))(1 - f_{\sigma'}(\mathbf{p}_2)) f_\sigma(\mathbf{p}_1') f_{\sigma'}(\mathbf{p}_2') - (\sigma \leftrightarrow \sigma')\right]\,, \tag{2.57}$$

where the last term refers to the first term with $\sigma$ and $\sigma'$ swapped. This equation can be simplified by using the relaxation time approximation [95, 94, 96]. Here, we assume that the distribution function relaxes to equilibrium over some timescale $\tau$:

$$I_c[f] = \frac{f - f_{le}}{\tau}, \tag{2.58}$$

where $f_{le}$ is the local equilibrium distribution function, which defines the distribution at a given point in time where collisions no longer change the temperature of the gas. The relaxation time $\tau$

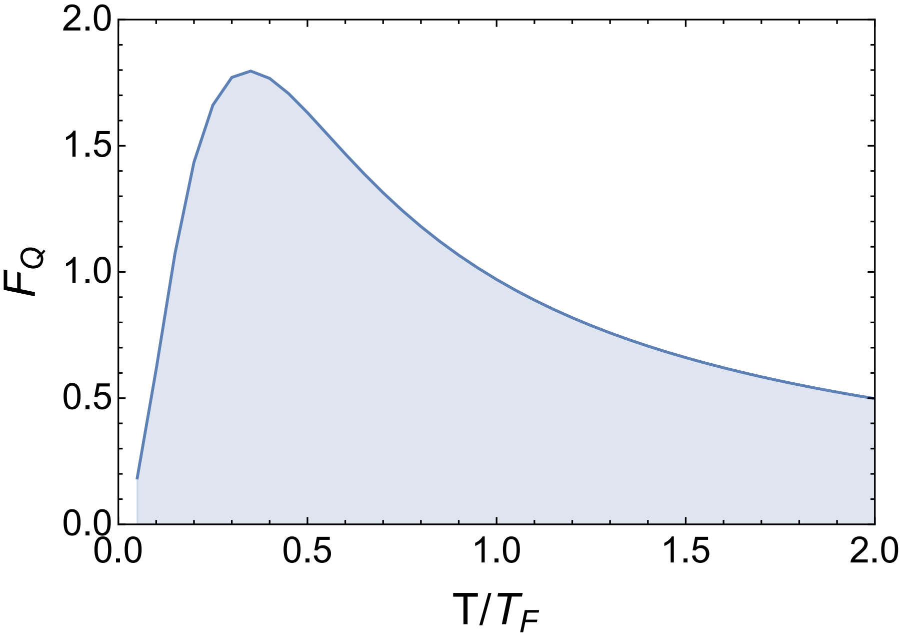

Figure 2.4: $F_Q$, an important parameter for the collisional term in the Boltzmann equation

can be defined as [94]

$$(\bar{\omega}\tau)^{-1} = \frac{4}{5\,3^{1/3}\pi}(N^{1/3}a/a_{ho})^2 F_Q(T/T_F)\,, \tag{2.59}$$

where $N$ is the number of atoms per species, $a_{ho} = \sqrt{\hbar/m\bar{\omega}}$ is the harmonic oscillator length, and $F_Q$ is a function that is only dependent on $T/T_F$, and whose precise form is given in Ref. [94]. Fig. 2.4 plots $F_Q$ and displays the important behavior. At very low temperatures, Fermi statistics suppresses the number of collisions between atoms and one finds that the gas is in the collisionless regime. At high temperatures, collisions are again less likely because for a fixed atom number, a higher temperature causes the density to decrease. However, at intermediate temperatures, collisions during expansion can be an important element of the dynamics.

To properly describe the expansion dynamics with collisions, the scaling parameters have to be modified. Collisions occur when the local temperature is not constant. As such, in addition to the parameters $\lambda_i$ that describe the spatial expansion of the gas, we introduce additional scaling parameters $\theta_i$ to describe when the temperature along all three axes are not equal. The distribution function can now be scaled as [96]

$$f(t, r_i, v_i) = \frac{1}{\prod_j (\lambda_j \theta_j^{1/2})} f_0 \left( \frac{r_i}{\lambda_i}, \frac{1}{\theta^{1/2}} \left( v_i - \frac{\dot{\lambda}_i}{\lambda_i} r_i \right) \right) , \tag{2.60}$$

and the scaling parameters to describe the expansion are solved using

$$\ddot{\lambda}_i + \omega_i^2 \frac{\theta_i}{\lambda_i} + \xi_i \omega_i^2 \left( \frac{\theta_i}{\lambda_i} - \frac{1}{\lambda_i \prod_j \lambda_j} \right) = 0 \tag{2.61}$$

$$\dot{\theta}_i + 2 \frac{\dot{\lambda}_i}{\lambda_i} \theta_i = -\frac{1}{\tau} \left( \theta_i - \frac{1}{3} \sum_j \theta_j \right) , \tag{2.62}$$

where we have already set the term that describes the harmonic confinement to zero. One can see from these equations that when the effective temperatures are equal ($\theta_i = \bar{\theta} = 1/3 \sum_j \theta_j$), collisions are effectively shut off and we get the corresponding scaling solutions without interactions with $\theta_i = \lambda_i^{-2}$. This is equivalent to sending $\tau \to \infty$. The aspect ratio can then be solved using $\sigma_z / \sigma_r = \lambda_z(t) \omega_r / \lambda_r(t) \omega_z$. Interestingly, while the mean-field interaction depends on the sign of the scattering length, $a$, the collisional term depends on $a^2$, and thus is not sensitive to whether the interactions are repulsive or attractive.

The first observation of anisotropic expansion was reported in Ref. [97]. Here, the two-component Fermi gas was prepared with large attractive interactions ($a \approx -10^4 a_0$) so that the gas was a superfluid. The mean-field treatment derived above is incorrect at these large interaction strengths, and instead the hydrodynamic equations of superfluids must be used as in Ref. [93].

### 2.3.3 Compressibility

Interactions also cause a change in the compressibility of a gas. Repulsive interactions, much like Pauli exclusion, create a pressure that resists a change in volume. The compressibility $\kappa_T = 1/n^2 \partial n / \partial \mu$ can be derived numerically using the equilibrium distribution function for an interacting gas, as given in Equation 2.53. To gain intuition about the results, we can look perturbatively at the compressibility for low temperatures and small interaction parameters. At finite temperature, we can take use of the Sommerfield expansion and arrive at for the chemical potential [98, 73]

$$\mu(T, a) = E_F \left[ 1 - \frac{\pi^2}{12} \left( \frac{T}{T_F} \right)^2 + \frac{4}{3\pi} k_F a \right] + \mathcal{O}((k_F a)^2) \, . \tag{2.63}$$

Given $T_F$ and $k_F$'s dependence on the density, we can then derive that the number fluctuations are

$$\frac{(\delta N)^2}{N} = \frac{3}{2}\frac{T/T_F}{1+\frac{2}{\pi}k_F a}\,, \tag{2.64}$$

showing that the fluctuations decrease for both lower temperature and larger interactions.

# Chapter 3

# Making, measuring and probing Fermi-degenerate clocks

This chapter discusses the experimental details of creating and probing a highly precise Fermi-degenerate optical lattice clock. In section 3.1, we describe the process to create a Fermi-degenerate gas of $^{87}$Sr atoms and load it into a 3D optical lattice. We then discuss the imaging techniques that we use to spatially resolve our sample in section 3.2. We finish the chapter in section 3.3 with a discussion of how we transfer the stability of our ultrastable laser based on a Si resonator to the $^{87}$Sr atoms.

## 3.1 Preparation

Here we review the experimental steps necessary to prepare a Fermi-degenerate 3D optical lattice. Many of these steps have been detailed in other theses[1] , and thus will only be discussed in brief here. Focus is put on the stages that are new as of this thesis, such as the transparency and the TenS4 lasers. First in subsection 3.1.1 we summarize our experimental sequence. In subsection 3.1.2 we describe the main experimental apparatus, including the optical layout for each laser used in the experiment. In subsection 3.1.3 we provide an overview of cooling $^{87}$Sr and trapping the atoms in an optical dipole trap, and describe how we measure trap frequencies in subsection 3.1.4. We then detail the transparency beam technique in subsection 3.1.5, which allows us to overcome light-assisted loss and increase the density of atoms before evaporation. In subsection 3.1.6 we discuss the TenS4 laser that allows us to spin-polarize a gas after evaporation with minimal heating. Finally,

---

[1] See mainly Ref. [99].

we detail loading the spin-polarized gas into the optical lattice in subsection 3.1.7.

### 3.1.1 Summary of experimental sequence

To create a Fermi-degenerate clock, we perform the following steps.

(1) A high flux of hot Sr atoms is created with an atomic beam oven that runs at a temperature of 480°C, which are then slowed using a Zeeman slower and directed into the main vacuum chamber with two 2D MOTS.

(2) Atoms are cooled to mK temperatures in a 'blue' MOT, which addresses the $^1\mathrm{S}_0 \rightarrow {}^1\mathrm{P}_1$ transition.

(3) Atoms are then transferred to a second-stage MOT on the $^1\mathrm{S}_0 \rightarrow {}^3\mathrm{P}_1$ transition that cools the atoms to $\mu$K temperatures.

(4) For evaporative cooling, the atoms are loaded into a crossed optical dipole trap (XODT).

(5) The transparency laser is applied to the dimple region of the XODT and a further stage of cooling with the single frequency red MOT occurs to cool atoms in the reservoir of the ODT while the density of atoms in the dimple is increased.

(6) Nuclear spin states $m_F = -9/2$ and $m_F = -7/2$ are optically pumped to other spin states.

(7) Evaporation with the remaining 8 spin states then proceeds to reach temperatures less than 0.1 times the Fermi temperature with about 50,000 atoms per spin state.

(8) The Tens4 laser is applied to spin-polarize the sample with minimal heating.

(9) Atoms are adiabatically loaded into the 3D optical lattice to form a band insulator.

(10) Clock spectroscopy is performed on the atoms to measure the atomic transition frequency.

Advances in atomic clocks hinge on optimizing, understanding, and harnessing the physics at each stage of the preparation process. In particular advances in quantum technology benefit from controlling and manipulating quantum properties of lab-made quantum platforms. Inspired by this idea, Chapters 4, 5, and 6 focus on studying, understanding, and manipulating Fermi gases. In these chapters, the above procedure is stopped after step (7). Frequently all 10 spin states are also used in these experiments.

### 3.1.2 Experimental apparatus

Numerous lasers are required to implement all the steps detailed above. Our experiment consists of three optics breadboards stacked vertically to create optical beam paths that can enter the vacuum chamber from one of the 15 different available viewports. Beam paths for the bottom, middle, and top optical breadboards are shown in Figs. 3.1, 3.2, and 3.3, respectively. Further details on the various beam paths in these drawings will be referred to in their corresponding sections later in the chapter.

Our experiment is surrounded by an Al enclosure to remove air currents and improve temperature stability, as shown in Fig. 3.4. The box has two 'garage doors' that open to allow optical access to the main parts of the experiment. Small holes on the sides of the box, far away from important optical beams, allow cables to escape easily. We found that adding this box significantly reduced fringe issues in our imaging system. The air currents caused by leaving panels of the box open were found to cause residual parasitic etalons to fluctuate. Dust is also reduced inside the box, which decreases the number of stationary fringes. The box is equipped with foam inside each of the panels to damp acoustic vibrations. We additionally temperature control the main optical table using water cooling that is hooked up to a 100 mK stable chiller. The chiller temperature is roughly 22 C so that when we open the garage doors there is no significant temperature perturbation. We also temperature control any significant heat sources inside such as AOMs, the oven,

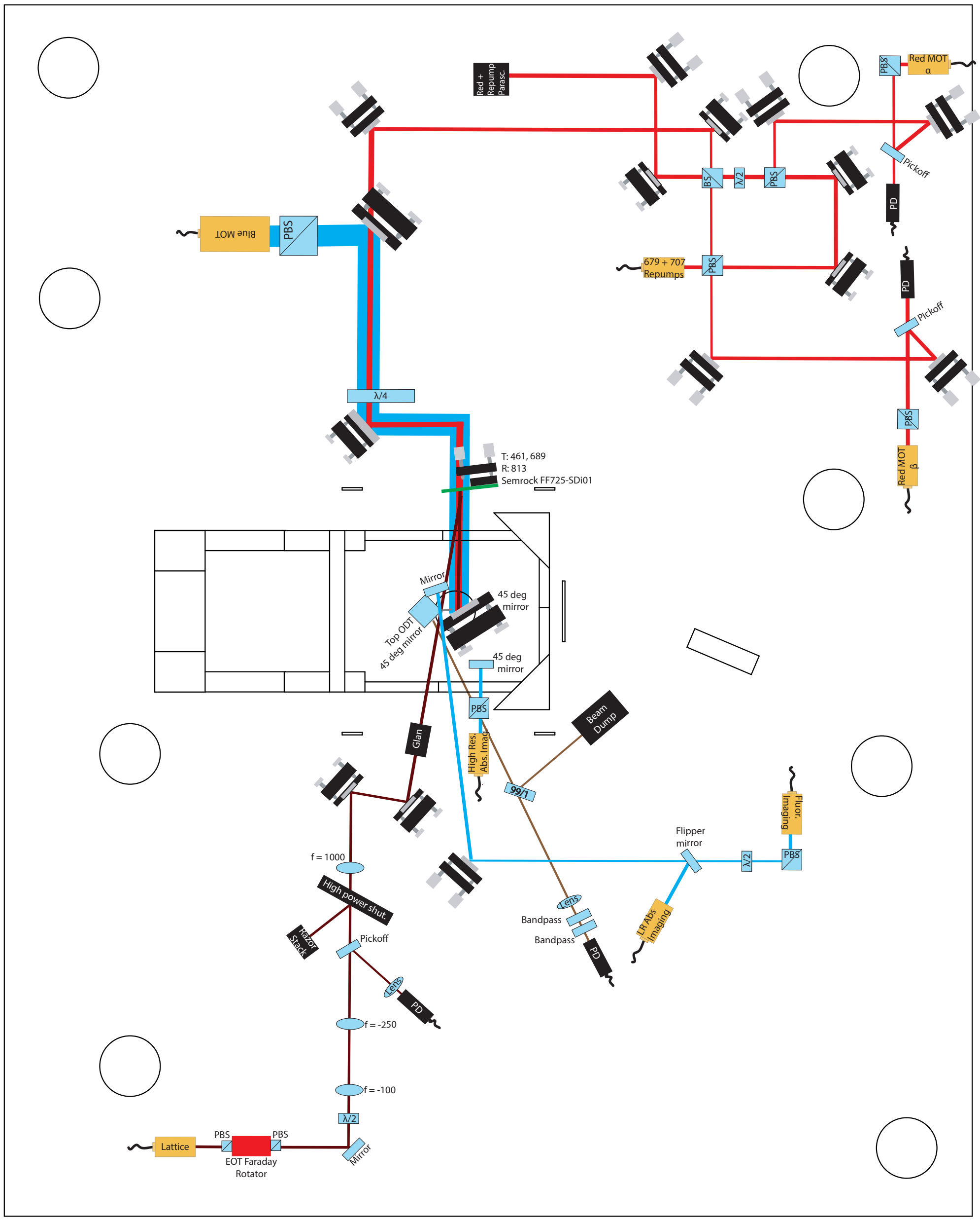

Figure 3.1: Optical layout of the lower optical breadboard. Optical beams are brought to the main mezzanine through 45 degree mirrors. The 45 degree mirrors in the center of the diagram are directed onto the atoms in the center of the vacuum chamber on the main mezzanine.

and beam dumps. With these implementations, the temperature stability inside the box is +/- 100 mK throughout the day and is relatively immune to larger temperature drifts in the main lab. We find that we have to realign our optical beams significantly less with this control. For ease, we use picomotor mirror mounts on optics mirrors that are frequently adjusted such as for the lattice

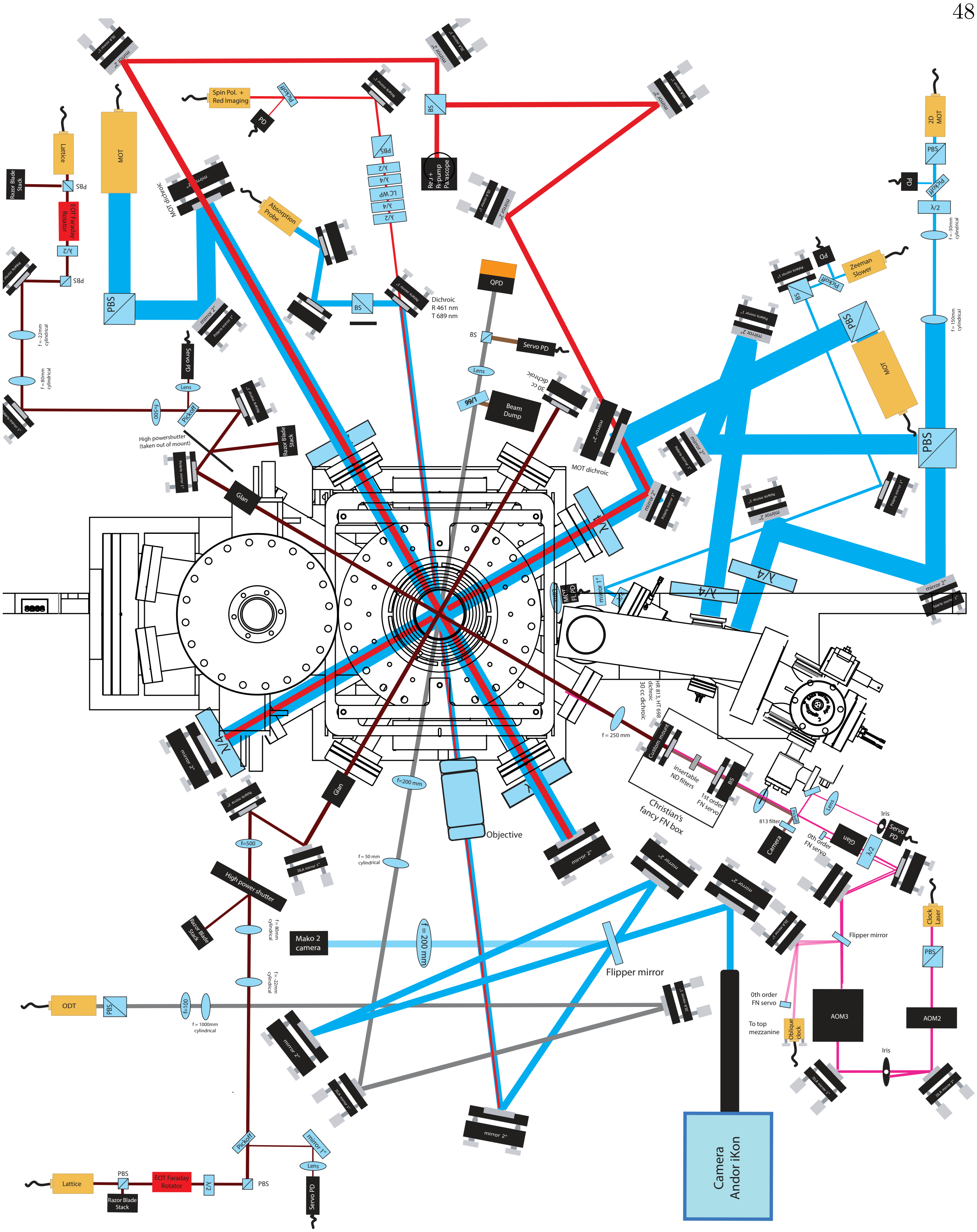

Figure 3.2: Optical layout of the middle optical breadboard. Atoms are trapped in the center of the vacuum chamber shown in the middle of the diagram.

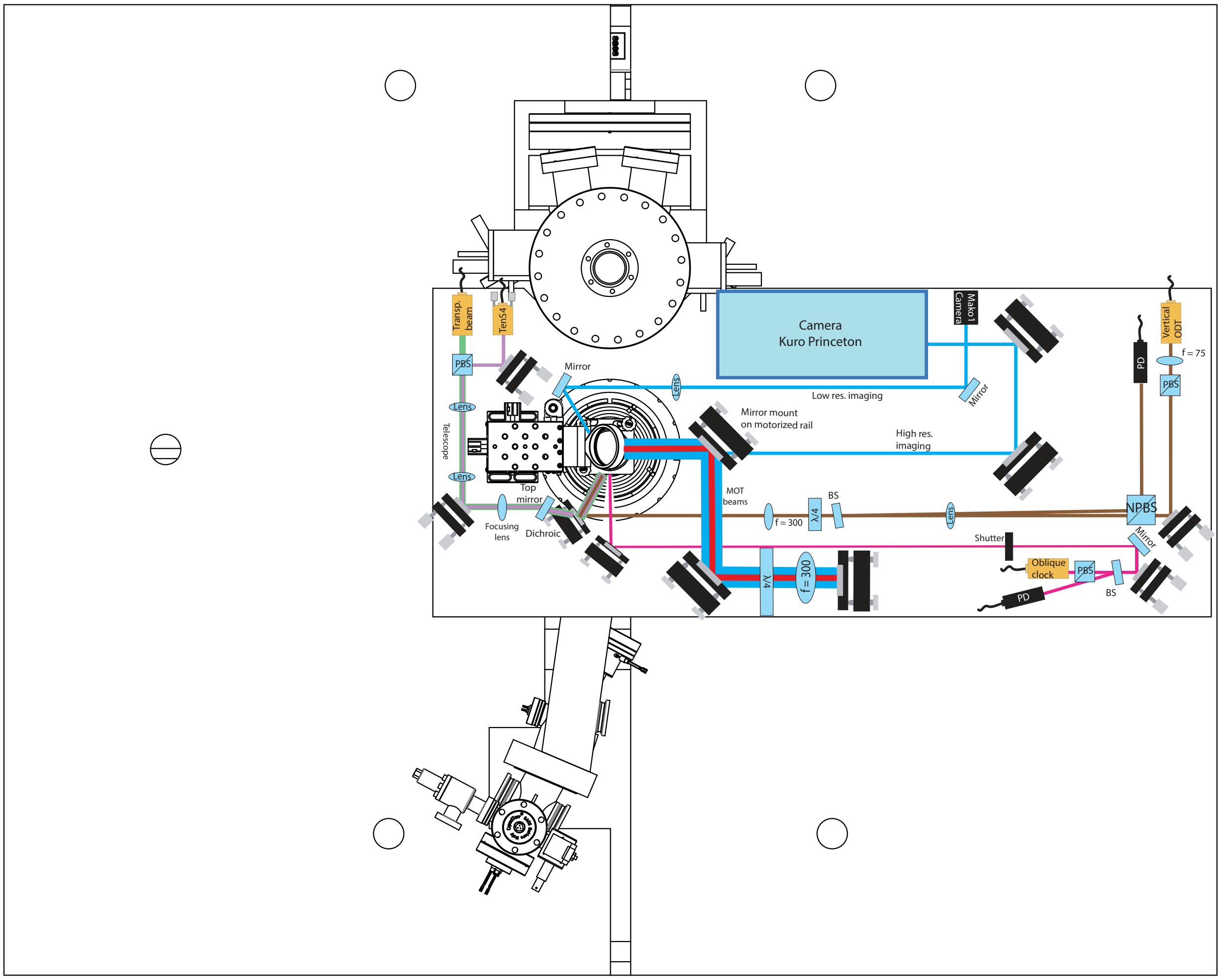

Figure 3.3: Optical layout of the top optical breadboard.

beams.

Figure 3.4: One side of the Al enclosure that surrounds the main experiment.

### 3.1.3 Overview of cooling and trapping $^{87}$Sr

Preparing a Fermi degenerate gas starts with cooling and trapping $^{87}$Sr. For a more detailed account of cooling $^{87}$Sr to $\mu$K temperatures using a two-stage MOT, see Refs. [100, 101]. Refs. [99, 102] discuss trapping Sr in a crossed optical dipole trap (XODT); the latter reference is not the JILA experiment but the preparation has many overlaps.

A simplified level diagram of $^{87}$Sr is shown in Fig. 3.5. The first stage of laser cooling begins on the 30.4 MHz $^1S_0 \rightarrow {}^1P_1$ transition. A high flux of hot atoms first leave a commercial AO Sense oven, and are slowed in an AO Sense Zeeman slower and transversely cooled in two 2D MOTs before entering the main chamber. We have had to replace the AO Sense oven multiple times over

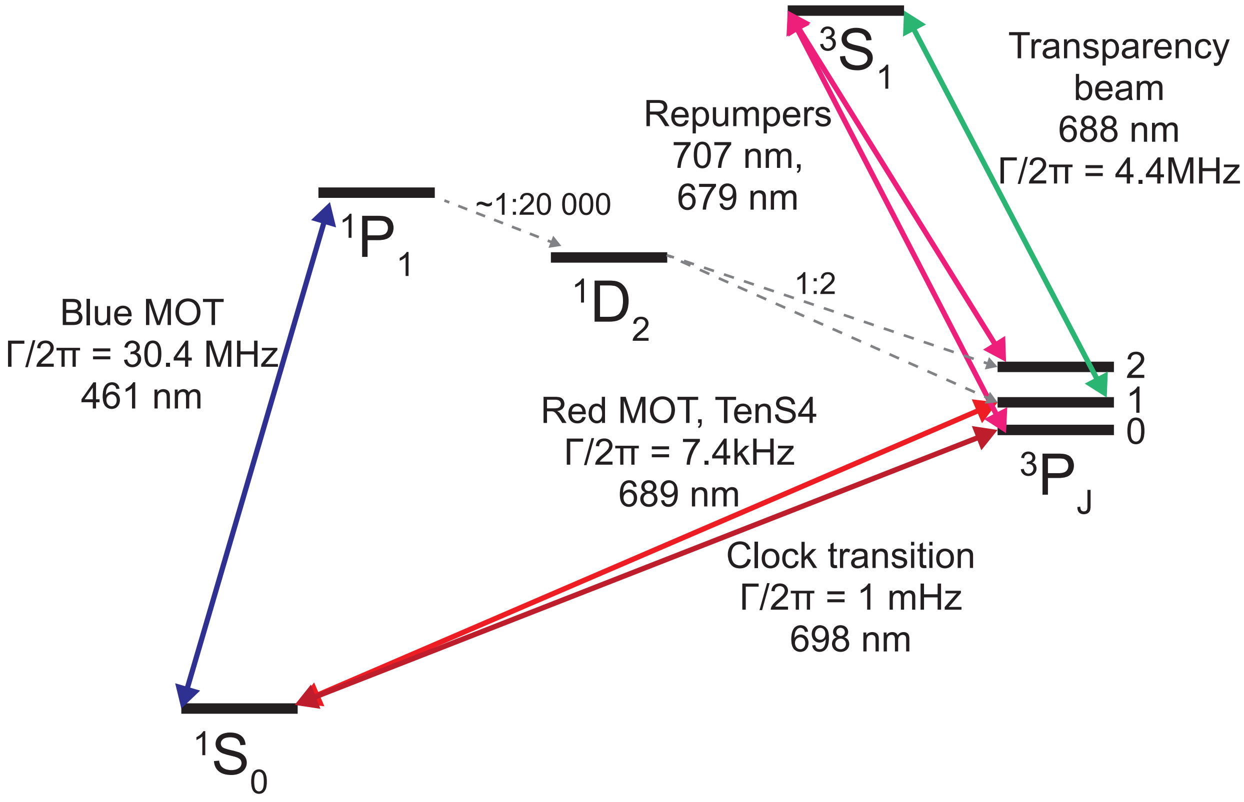

Figure 3.5: Simplified energy level diagram of $^{87}$Sr.

the course of my PhD. During replacement, we have frequently seen a ‘volcano’ of Sr on the exit aperture of the oven, where Sr sticks and accumulates. Eventually the Sr creates a bridge that shorts two disconnected pieces of the chamber, which degrades the temperature stability of the oven and significantly reduces the oven’s clear aperture. We recently replaced our oven with the more modern AO Sense oven that has improved temperature control and are hoping this fixes our intermittent issues.

After the atomic beam enters the chamber, atoms are trapped in a ‘blue’ MOT that has a 30 G/cm gradient. The $^1P_1$ transition is almost closed, with a 1:20,000 chance of decaying to the $^1D_2$ state [103], which then either decays to the $^3P_2$ state or the $^3P_1$ state with 1:2 odds. The atoms that decay to $^3$P$_2$ are then trapped in that state due to the 40 s lifetime of the state, which limits the lifetime of the MOT to a few 10s of ms. Multiple repumping transitions can be used; we historically pump atoms to the $^3$S$_1$ state, which requires two repumping lasers at 679 nm and 707 nm to pump atoms out of the $^3$P$_2$ and $^3$P$_0$ states; the latter becomes populated from decay out of the $^3$S$_1$ state.

Atoms are then loaded into a second stage 'red' MOT on the 7.4 kHz $^1$S$_0 \rightarrow {}^3$P$_1$ transition. Cooling on this narrow line transition with a $J = 0$ ground state requires two lasers to effectively cool the atoms and pump them out of nuclear spin states that are not trapped [104]. In the first broadband red MOT stage, the frequency of the red MOT cooling lasers is modulated to capture and cool more atoms from the blue MOT. The modulation is then gradually ramped down, as is the intensity of the lasers, until the red MOT is operated at a single frequency with an intensity below the saturation intensity. This allows us to achieve $\mu$K temperatures with roughly $10^7$ atoms.

We perform optical evaporation of the atoms which requires the atoms to be trapped inside an ODT. In particular, we employ two ODTs, one 'reservoir' horizontal ODT (HODT) that has a sheet-like geometry with waists of 340 $\mu$m and 20 $\mu$m in the horizontal and vertical directions, respectively. The second ODT is a 'dimple' vertical ODT (VODT) that is aligned at roughly 10° with respect to gravity and is circular with a 30 $\mu$m waist. While the reservoir ODT traps many atoms and sets the trap depth, the dimple ODT sets the density of atoms, which can be correspondingly higher than in the reservoir due to the small waist. The ODT is on during the broadband and single frequency red MOT, and we adjust the frequency of the MOT to cool directly into the ODT.

### 3.1.4 Measuring trap frequencies

Trap frequencies are measured using two different methods. In the first technique, we pulse on a second dipole trap that is slightly offset from the cloud and look at the center of mass oscillation frequency inside the dipole trap. In particular, we use a lattice laser with the retro-reflected beam blocked to form the extra dipole trap. The dipole trap is then extinguished at variable times and the center of mass position of the atoms is measured after a fixed time of flight.

Second, we parametrically heat the atoms by modulating the intensity of the dipole trap. This is achieved by modulating the RF power of an AOM. Since we have servos that stabilize our ODT intensity, we add the modulation either at the output of the servo or at the servo reference, depending on if the modulation frequency is outside or inside the servo bandwidth, respectively. The heating rate is maximized at twice the trap frequency [105]. We do not measure atom loss, which requires high modulation intensites that can lead to nonlinearities in the drive signal and the excitation of atoms beyond the minimum of the trap where the harmonic approximation holds. Instead we look at the width of the cloud after time of flight, which is sensitive to the temperature of the atoms in the trap. Minimal heating can be easily measured with this technique and small, clean modulation frequencies can be applied that result in high SNR heating resonances.

Examples of the dipole oscillations and parametric heating resonances are given in Fig. 3.6. Dipole oscillations are performed by exciting the gas along a particular direction and thus cannot separately measure trap frequencies along $x$ and $y$. In contrast, we clearly observe the asymmetry in our VODT through parametric heating measurements. The trap frequencies extracted using the two methods agree well, as shown in Fig. 3.7.

### 3.1.5 Transparency beam

A large density in the dimple of our ODT is advantageous for efficient evaporative cooling. For a ground state with SU($N$) symmetry, the evaporation rate is given by $\Gamma = (N-1)n\sigma v_{rel}$, where $N$ is the number of spin components, $n$ is the single-component density, $\sigma = 4\pi a^2$ is the s-wave collisional cross-section, and $v_{rel}$ is the relative velocity (see Chapter 4). Inelastic light-assisted collisions [106] and reabsorption of the cooling light, which leads to an effective repulsion between atoms [107], scale with the density, making it challenging to achieve high density samples.

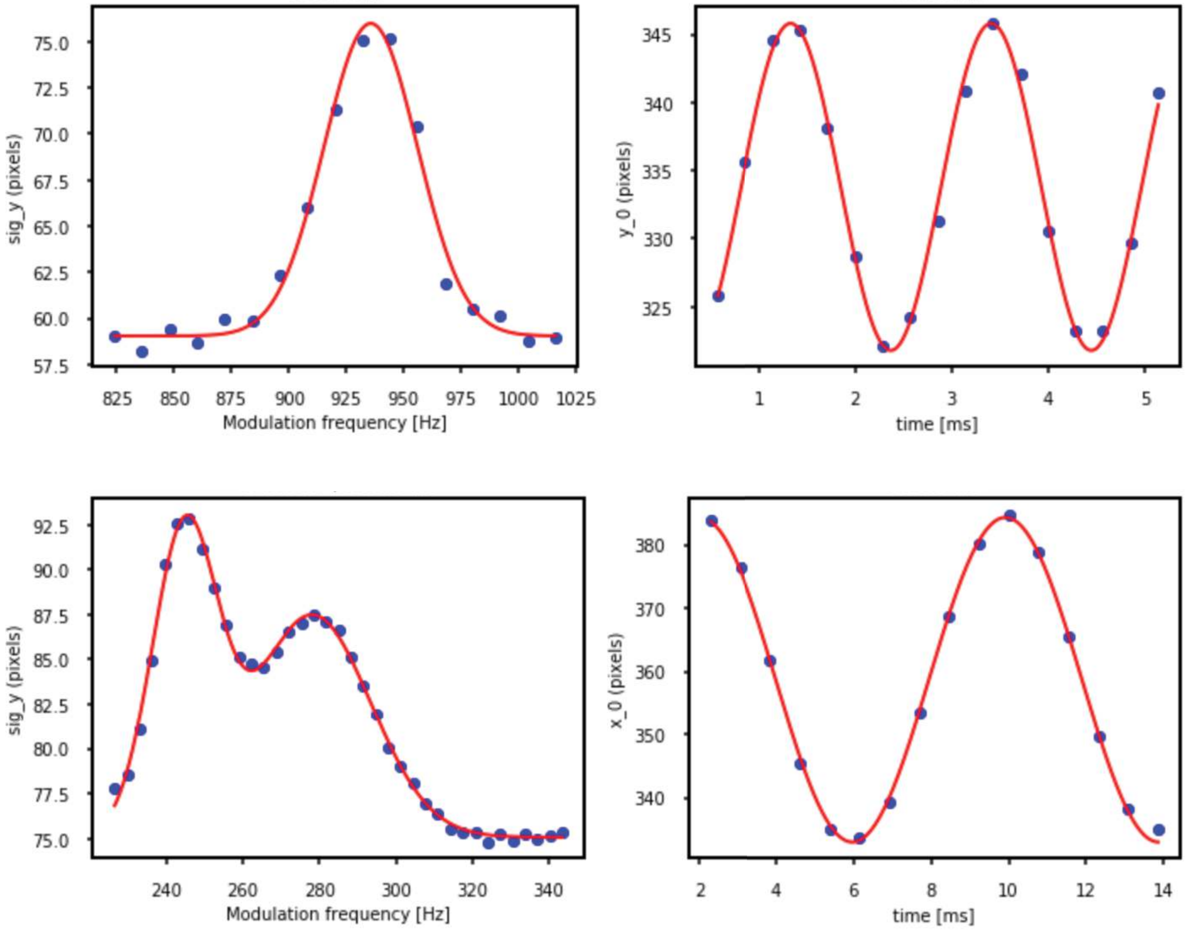

Figure 3.6: Left column: Parametric modulation of the ODT intensity leads to heating resonances at twice the trap frequency. The top figure shows the vertical trap frequency and the bottom the horizontal frequencies. Right column: Trap frequencies are extracted through dipole oscillations of the atomic cloud.

To overcome light-assisted loss, we render atoms inside the dimple transparent to the cooling light. This is achieved by applying an additional laser to atoms in the dimple that shifts the cooling light out of resonance, see Fig. 3.8. The large density of atoms that accumulate inside the dimple then thermalize with atoms in the surrounding reservoir.

Using a transparency beam to overcome light-assisted loss has been demonstrated in a low phase-space density MOT [108], and was used in bosonic $^{84}$Sr to reach the critical phase-space

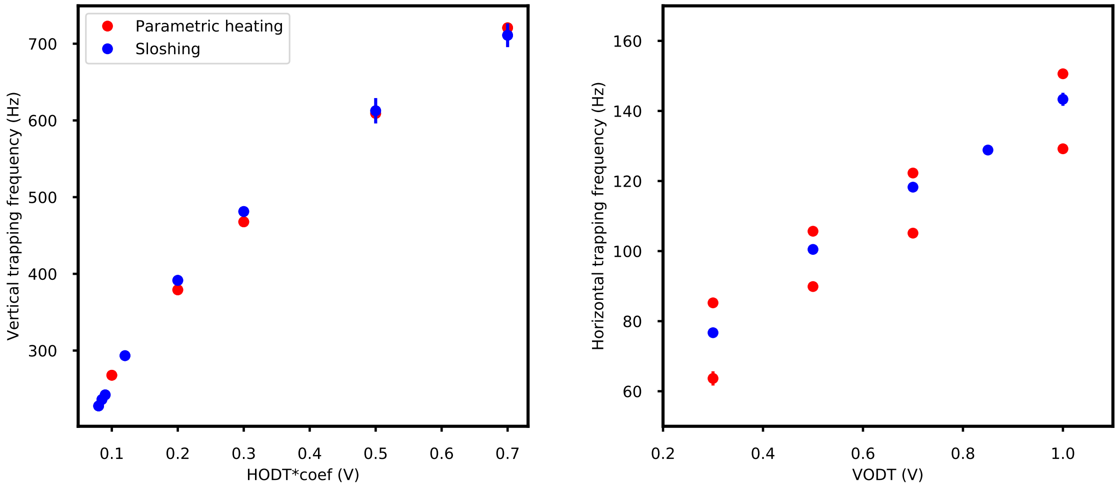

Figure 3.7: Trap frequency measurements for various intensity setpoints extracted using both parametric heating and dipole oscillations. The left shows the vertical trap frequency and the right the horizontal trap frequencies.

density for Bose-Einstein condensation without any evaporation [109]. The critical phase space density is reached when $n\lambda_{dB}^3 > 2.612$, where $\lambda_{dB}$ is the thermal de-Broglie wavelength and $n\lambda_{dB}^3 \propto nT^{-3/2}$. In comparison, Fermi-degeneracy does not have a critical point and the transition is instead continuous. While the effects of Fermi degeneracy begin when $n\lambda_{dB}^3 > 1$ $(T/T_F < 0.6)$, if one wants to reach deep degeneracy, say so that one can load a band-insulator state into an optical lattice with over 90% filling, the requirements are much more strict and one then needs $n\lambda_{dB}^3 > 20$ $(T/T_F < 0.1)$. This makes using the transparency beam alone as a replacement for evaporation in fermions more challenging. In addition, hyperfine structure creates additional complication, since a sufficient AC Stark shift needs to be created for each nuclear sublevel. Transparency from both the trapping and stirring second stage MOT lasers is also required [110].

Accordingly, the transparency beam is blue-detuned from the $^3\mathrm{P}_1$ to $^3\mathrm{S}_1$ transition by 25 GHz. The laser spatially overlaps with the VODT (see Fig. 3.3) but has a slightly larger waist to ensure all atoms in the dimple do not absorb cooling light, and delivers 5 mW of power to the

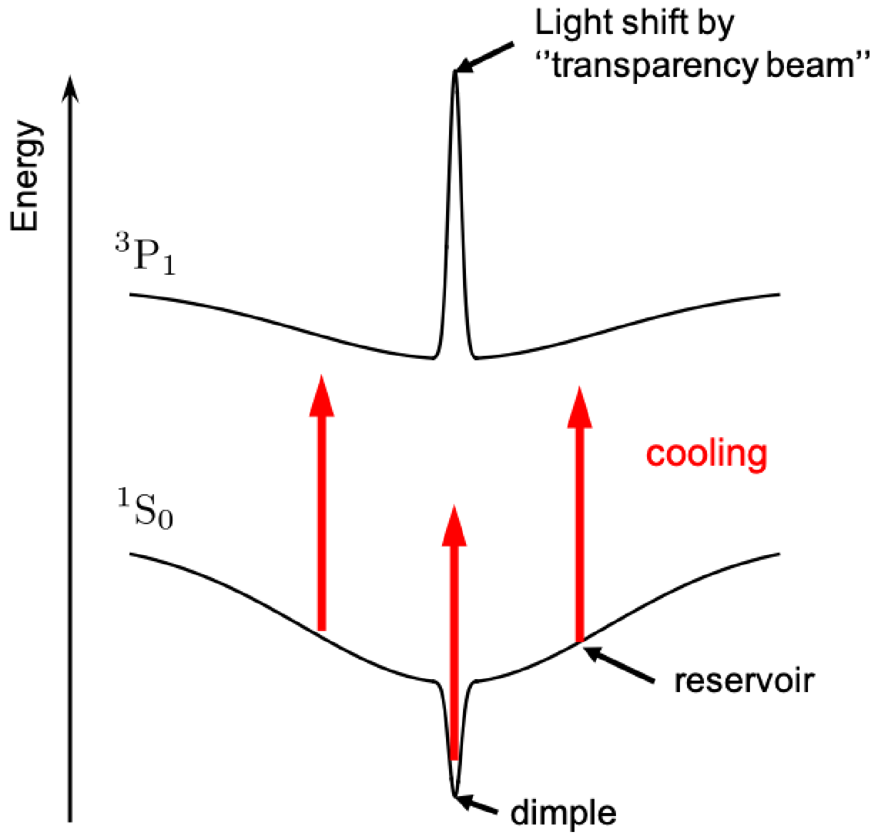

Figure 3.8: Potential energy of the $^1\mathrm{S}_0$ ground state atoms and $^3\mathrm{P}_1$ excited state atoms in the ODT. The transparency beam shifts the cooling light out of resonance for atoms in the dimple.

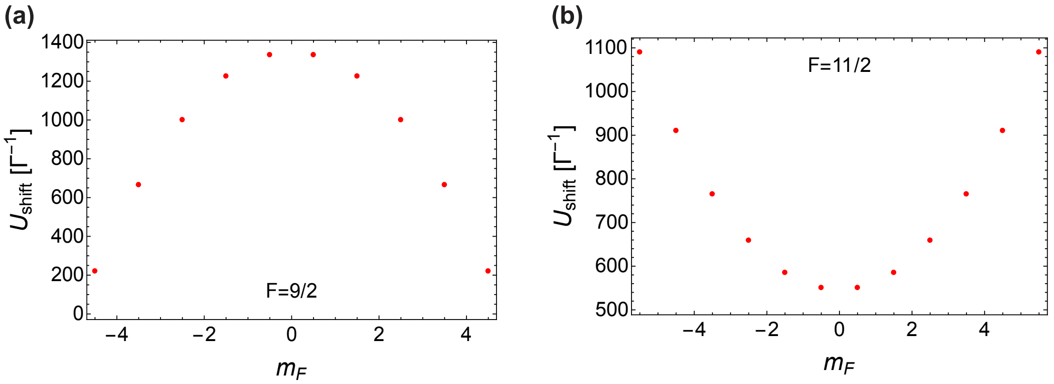

Figure 3.9: Calculated Stark shift of the excited $^3\mathrm{P}_1$ stirring/trapping states for different nuclear spin states. The linewidth of the $^3\mathrm{P}_1$ state is $\Gamma = 2\pi \times 7.5$ kHz.

experiment. The beam is linearly polarized along $x$, while a small magnetic field is applied along $z$ (see Fig. 3.10). In this configuration, the smallest Stark shift still detunes the excited state by $\sim$200

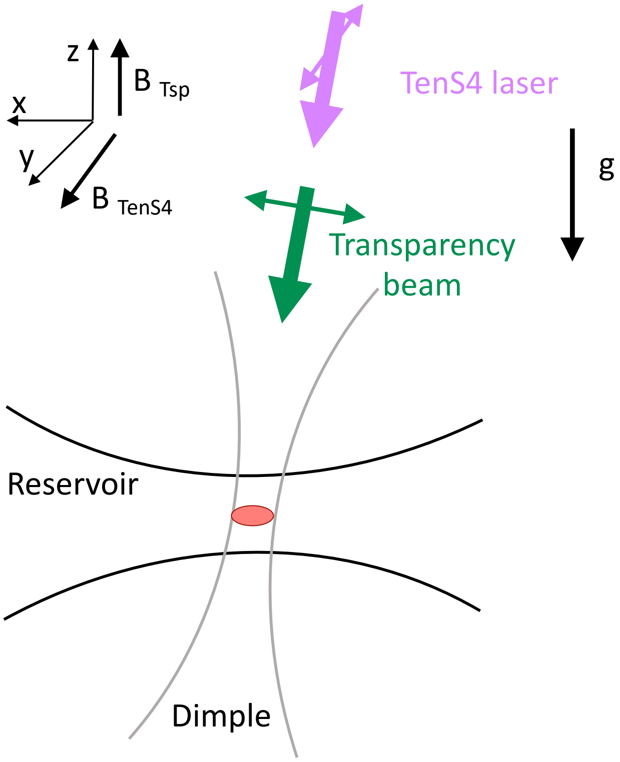

Figure 3.10: Schematic of the reservoir and dimple dipole traps, as well as the propagation direction (single arrows) of transparency beam and the TenS4 laser, and their polarization (double arrows). The magnetic field while the transparency beam is on is denoted by $B_{tsp}$ and the magnetic field while the TenS4 laser is on is represented by $B_{TenS4}$. The polarization of the TenS4 laser is along the magnetic field, so that the ellipticity is zero.

linewidths, see Fig. 3.9, and keeps spontaneous scattering events beyond relevant experimental time scales. In general the Stark shifts are sensitive to the transparency beam's polarization, and we calculate that circular light would not give a sufficient shift to all spin states for both cooling lasers.

The effect of the transparency beam on the sample is shown in Fig. 3.11. Here, we apply the transparency beam to the dimple part of the XODT and apply $^3P_1$ light to remove atoms from the reservoir. The atoms in the dimple do not absorb the $^3P_1$ light and thus remain in the trap after the pulse, as shown in the image on the right.

The transparency light is derived from an extended cavity diode laser (ECDL) that is filtered by a volume Bragg grating (VBG). Without the VBG, residual amplified spontaneous emission

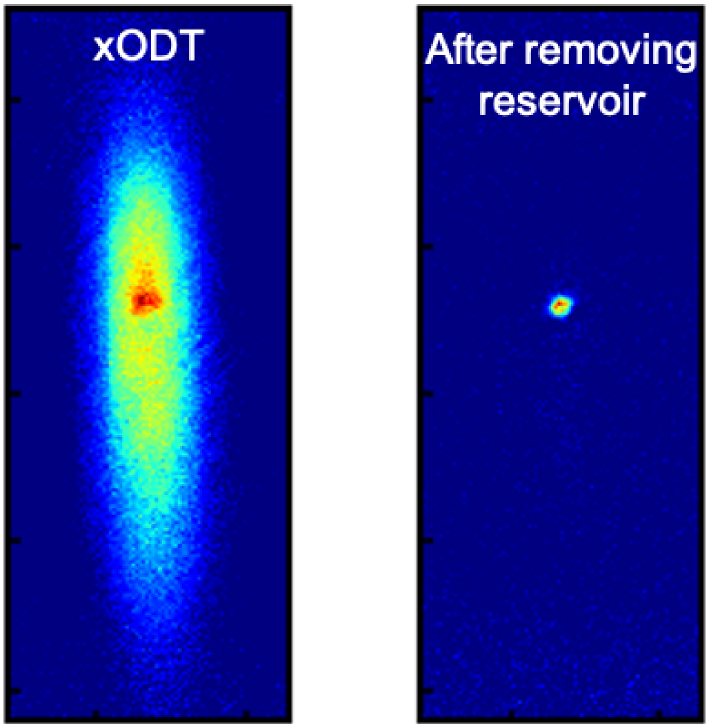

Figure 3.11: Atoms remaining in the xODT after applying a cleanup pulse to the xODT (left image) with the transparency beam on. Only atoms that don't absorb the cooling light remain.

(ASE) on-resonance with the ${}^1\mathrm{S}_0 - {}^3\mathrm{P}_1$ transition limits the lifetime of atoms in the dimple to 250 ms. With the filter, the lifetime is extended to 5 s.

To separately extract the number of atoms in the dimple and reservoir, the HODT is extinguished so that atoms fall under gravity. Atoms in the dimple are guided by the VODT which has a small angle with respect to gravity, while atoms in the reservoir undergo free expansion. This spatially separates the atoms in the dimple from atoms in the reservoir, and respective atom numbers are then measured using absorption imaging. The number of atoms in the dimple saturates at $5 \times 10^6$, i.e. about 50% of the total atom number, after 400 ms of cooling with the transparency beam. This leads to a total density of $2 \times 10^{14}$ atoms/cm$^3$, corresponding to a three-body lifetime around 10 s [54]. $T/T_F$ is then determined for atoms in the dimple by calculating $T_F$ and measuring the temperature. The latter is determined by fitting all atoms to a Gaussian after time-of-flight, and gives a temperature of $2\,\mu$K with $\mathrm{T}/\mathrm{T}_\mathrm{F} = 1.9$. Lower temperatures can be achieved by adjusting the MOT light, but without further improving the phase space density.

After the transparency beam is applied for 400 ms, we proceed with standard evaporation by lowering the trap depth of the HODT but keeping the VODT high to maximize the density throughout. We evaporate with all 10 spin states to maximize the evaporation efficiency, as discussed further in Chapter 4. For final trap depths of a few 100 nK and a vertical (radial) trap frequencies around 200 Hz (100 Hz), we can reach temperatures as low as 0.07 times the Fermi temperature, with roughly 50,000 atoms per spin state, after around 1 s of evaporation.

### 3.1.6 TenS4

After evaporation, the spin distribution is manipulated to subsequently load the optical lattice into a band-insulating state. Previous attempts to manipulate the spin distribution through optical pumping after evaporation resulted in light-induced heating of the atoms. Here we detail a method to manipulate the spin distribution of the gas where the atoms remain confined to the ground state so that there are no spontaneously emitted photons. This method can produce a spin-polarized gas with >90% spin purity with minimal heating.

#### 3.1.6.1 Stark shift

Our spin manipulation technique builds off of previous work that used optical beams to create differential spin forces in alkaline-earth atoms during time of flight [111, 112, 113]. In these previous experiments, atoms in different spin states could be separated after releasing them from the harmonic trap to image individual spin components. Our method, the Tensor Stark Shift Spin Selector (TenS4), creates a spin-selective repulsive force on the atoms from the tensor Stark shift of a laser while the atoms remain trapped in the XODT. This force can overcome the small confinement that holds the atoms after evaporation and can subsequently push the atoms out of the trap. In addition, our beam parameters have to be carefully chosen such that the spin state we

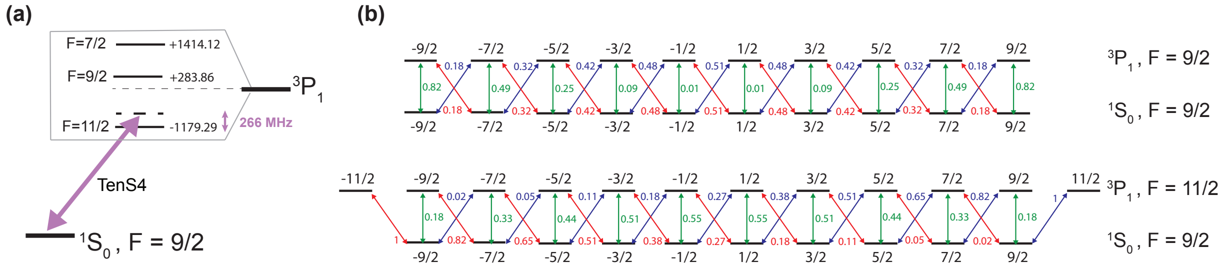

Figure 3.12: (a) $^3$P$_1$ hyperfine structure and TenS4 detuning. The TenS4 detuning is referenced to the zero magnetic field F=11/2 transition. (b) Clebsch-Gordan coefficients squared for transitions from the $^1$S$_0$ ground state to the $^3$P$_1$, $F = 11/2$ and $F = 9/2$ transitions. The $F = 11/2$ and $F = 9/2$ states have magnetic field sensitivities of 380 kHz $m_F$/G and 85 kHz $m_F$/G, respectively.

desire to keep in the trap feels no force. Any residual force on this state will heat the atoms in the trap. The ac Stark shift for a ground state atom with nuclear spin $m_F$ is given by [114]

$$\Delta\nu = \left(\Delta\kappa^s + \Delta\kappa^v m_F \xi \hat{e}_k \cdot \hat{e}_B + \Delta\kappa^t \beta\right) U_0 \,, \tag{3.1}$$

where $U_0$ is the trap depth, $\Delta\kappa^s$, $\Delta\kappa^v$, and $\Delta\kappa^t$ are the scalar, vector, and tensor shift coefficients, and $\xi$ is the beam ellipticity. The light propagation direction and quantization axis are given by $\hat{e}_k$ and $\hat{e}_B$, respectively. Finally, $\beta = (3|\hat{\epsilon} \cdot \hat{e}_B|^2 - 1)\left[3m_F^2 - F(F+1)\right]$, where $\hat{\epsilon}$ is the beam polarization vector [52, 114]. The TenS4 laser is detuned from the $^3$P$_1$, $F = 11/2$ state as shown in Fig. 3.12, and is offset from the atom cloud to create a spin-selective repulsive force on the atoms. The beam has a 30 $\mu$m waist with a peak intensity of 0.15 kW/cm$^2$, and is linearly polarized along the magnetic field ($\xi = 0$), which has a strength of 5 G. Due to the slight tilt of the beam, the magnetic field mostly points along $y$ but also has a small component along $z$ (see Fig. 3.10). The scalar shift provides an appreciable shift to all spin states, while the tensor shift, $\propto m_F^2$, produces a differential force between atoms with different $|m_F|$. A small differential shift between positive and negative $m_F$ states is further created with a magnetic field, which changes $\Delta\kappa^s$ and $\Delta\kappa^t$ due to a slightly different detuning from the atomic resonances.

The Stark shift cancels for atoms in a particular spin state at the proper detuning. For nuclear

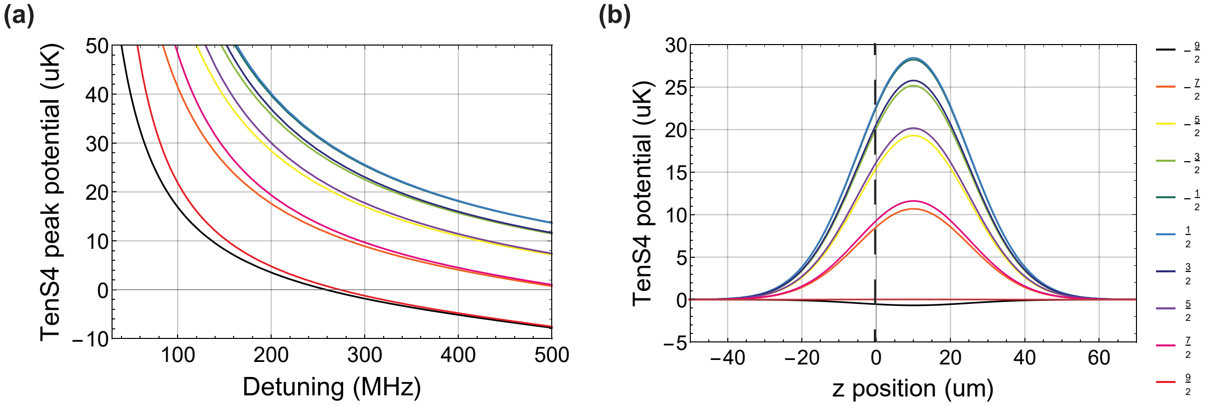

Figure 3.13: (a) Height of the TenS4 potential versus detuning. At 266 MHz, the TenS4 potential is zero for $m_F = +9/2$. (b) Potential of the TenS4 beam as a function of position at a detuning of 266 MHz. The beam is offset from the atoms by roughly 1/3 the trap waist (dashed line) to create a varying potential across the cloud. Plots are shown for a 5 G magnetic field.

spin state $\mathrm{m_F} = +9/2$, this occurs at 266 MHz, where the polarizability from $^3\mathrm{P}_1$, $F = 11/2$ cancels the polarizability from $^3\mathrm{P}_1$, $F = 9/2$. This is demonstrated in Fig. 3.13 (a). The spatial dependence of the TenS4 potential for the different spin components is shown in Fig. 3.13 (b).

#### 3.1.6.2 Experimental implementation

The TenS4 laser is overlapped with the VODT and the transparency beam, as shown in Fig. 3.3, which facilitates initial alignment. The TenS4 and transparency beam also share the same telescope to save space. The laser, which is at a 10° angle with respect to gravity, is then offset from the atomic cloud to provide a force both vertically and horizontally. The combined potential due to the ODT, the TenS4 laser and gravity is shown in Fig. 3.14. With only a 5 G applied magnetic field, a residual attractive potential remains for $\mathrm{m_F} = -9/2$ and $-7/2$. We thus conventionally remove these spins via optical pumping prior to evaporative cooling. Our optical pumping is performed using $\sigma^+$ light that is selectively tuned to the $^1\mathrm{S}_0 \rightarrow {}^3\mathrm{P}_1, F = 9/2$ resonance. First we apply a few ms pulse that is on resonance with the $^1\mathrm{S}_0, m_F = -9/2$ to $^3\mathrm{P}_1, m_F = -7/2$ transition. We then step the frequency and apply a second pulse on resonance with the $^1\mathrm{S}_0, m_F = -7/2$ to

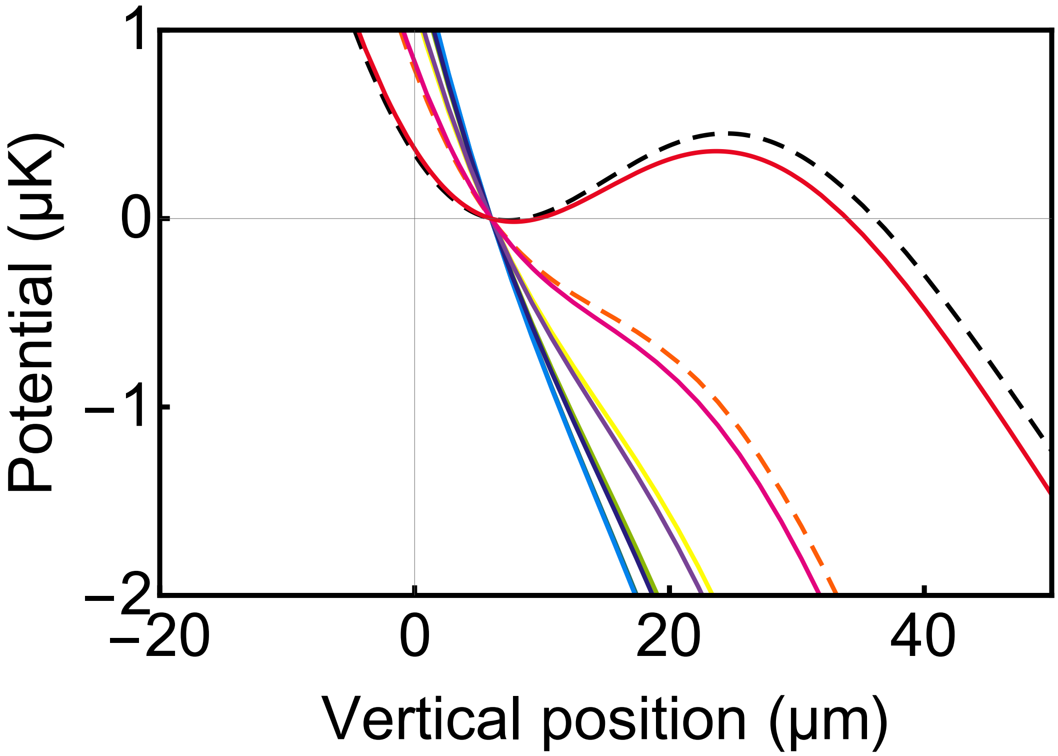

Figure 3.14: Combined potential due to the ODT, the TenS4 beam, and gravity. Dashed curves represent $m_F = -9/2$ and $m_F = -7/2$, which are removed through optical pumping.

${}^3\mathrm{P}_1, m_F = -5/2$ transition. This allows us to remove the $m_F = -9/2$ and $m_F = -7/2$ populations by 90%, as measured after evaporation Fig. 3.17. Going to a larger magnetic field and aligning the beam horizontally to provide maximum force along the vertical direction would remove the need to optically pump. A magnetic field of 50 G would more than satisfy this requirement. The spin-polarized gas can then be loaded into the lattice and coherently manipulated if one desires to work with a different spin state.

When we initially implemented the TenS4 laser, we measured an unexpected loss of atoms. Loss due to the TenS4 laser can be described by

$$\dot{n} = -n/\tau - 2Kn^2 - k_3 n^3 \,, \tag{3.2}$$

where the first term represents single-particle photon scattering with a lifetime of $\tau$, and the second term represents a two-body loss term with a loss rate of $K$. The vacuum-limited lifetime of the atoms was measured to be 120 s, significantly longer than any relevant experimental timescales. The last term represents three-body inelastic collisions with three-body loss coefficient $k_3$, which for $^{87}$Sr give us a lifetime around 10 s, much longer than the observed scattering lifetime [54].

Published photoassociation (PA) spectra on $^{87}$Sr is limited to $^1P_1$ [115], where the spectra is relatively simple due to the broad linewidth, which causes the hyperfine spectra to be unresolved. Narrow line photoassociation was measured on $^3P_1$ for bosonic $^{88}$Sr [116], but no published measurements on $^{87}$Sr exists. For $^{87}$Sr, the narrow linewidth $^3P_1$ transition is predicted to have a complex spectra due to the resolvable hyperfine structure and large nuclear spin [117]. To measure photoassociation spectra, we evaporate the atoms to a 500 nK trap depth and then ramp up the HODT to a few $\mu$K. The atoms are then exposed to the TenS4 laser at a power of 10s of $\mu$W for 100 ms - 1 s in a 5 G magnetic bias field. At this power and trap depth, the TenS4 does not modify the optical potential. The gas is then released from the dipole trap and the atom number is counted using absorption imaging. At a PA resonance, the atom number drops as hot molecules are formed that cannot be confined to the trap. Fig 3.15 shows the atom loss spectra for a variety of detunings near the $^3P_1$, $F = 11/2$ resonance. Due to the F = 9/2 and F = 7/2 states, resonances exist above and below F = 11/2. The TenS4 laser is referenced to our red MOT trapping laser, which is itself locked to a laser that has a ∼1 Hz linewidth. As such, the zero, which refers to the zero magnetic field value of the F=11/2 resonance, can be trusted to within 10s of kHz. Clear PA resonances exist around 80 MHz and 160 MHz and a broad loss feature consisting of many resonances is shown in the -400 MHz to -200 MHz region. The other peaks at -60 MHz, -100 MHz, -140 MHz, and 320 MHz consist of a single data point and thus need to be remeasured to confirm the existence of a resonance at these frequencies. The large intensities used for the measurements result in a large single-particle scattering rate near the $^3P_1$ resonance, and mask any PA resonances in this region. A more detailed scan at the TenS4 detuning, taken at a variety of powers, did not reveal a

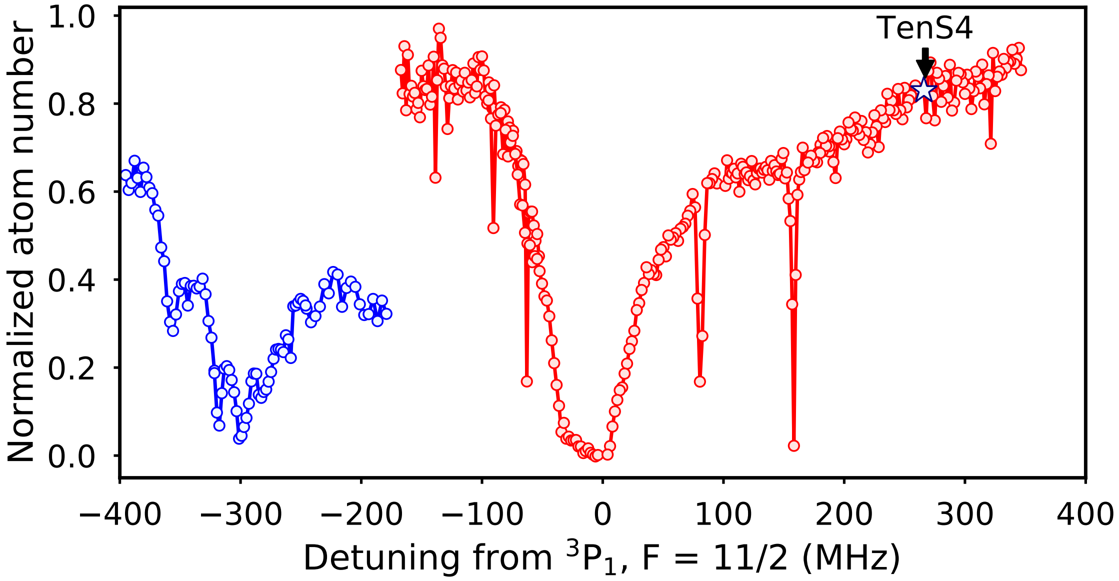

Figure 3.15: Photoassociation spectra. The blue data points were taken with 45 $\mu$W of power, and the red with 15 $\mu$W of power.

resonance.

Single-body loss is due to photon scattering with the TenS4 light. The predicted light scattering lifetime 266 MHz from resonance with the described beam parameters is 10s of ms, two orders of magnitude above the measured lifetime. However, the lifetime can be limited by amplified spontaneous emission (ASE) from the laser diode at the $^3P_1$ resonance frequencies. ASE can be suppressed through spectral filtering of the light using a Fabry-Perot cavity. In particular, we implemented a cavity with a 10 MHz linewidth and a finesse of 200 to suppress on-resonance scattering by 3 orders of magnitude. After installation of the cavity, the lifetime of atoms became consistent with the off-resonant scattering rate.

The optics of the TenS4 beam are shown in Fig. 3.16. The TenS4 laser is locked to an ultrastable laser (‘red master’) at 689 nm. This ultrastable laser is also used to lock our $^3P_1$ MOT beams. The light is then filtered with a Fabry-Perot cavity that has roughly 50% transmission before being sent to the main experiment. The Fabry-Perot cavity is locked to the TenS4 laser

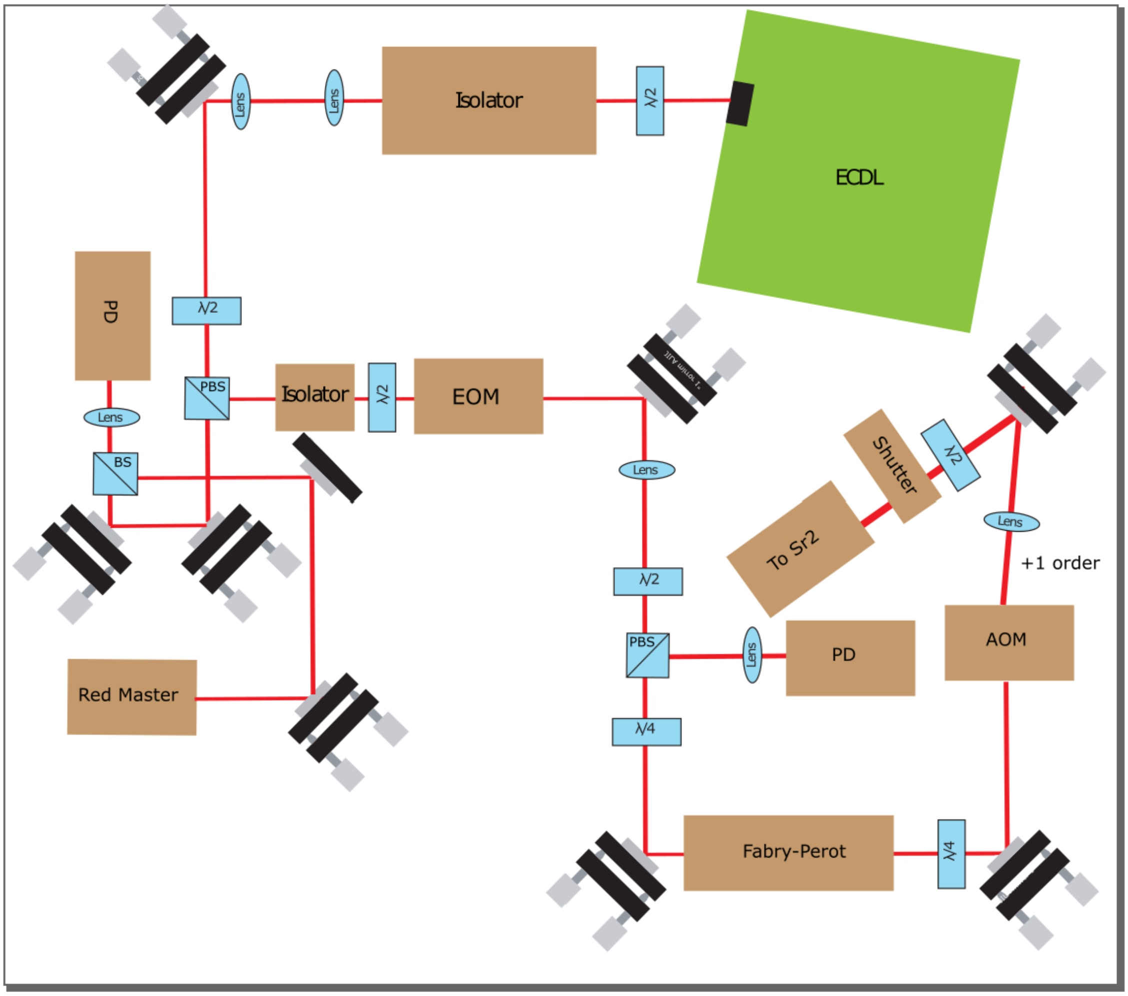

Figure 3.16: Optics setup for the TenS4 beam. Light from an ECDL is locked to an ultrastable laser with a roughly 1 Hz linewidth at 689 nm (red master). A Fabry-Perot cavity is used to filter the TenS4 light before being sent through a fiber to the experiment (to Sr2).

using PDH locking.

### 3.1.6.3 Spin purity measurements

To spin polarize the gas, we first evaporate down to a few 100 nK trap depth and then non-adiabatically turn on the TenS4 laser for a few ms. The TenS4 spin purity is measured by looking at the total atom number using blue absorption imaging, and by performing spectroscopy on the $^3P_0$ transition after the atoms are loaded into a 3D optical lattice. Fig. 3.17 (a) shows the total

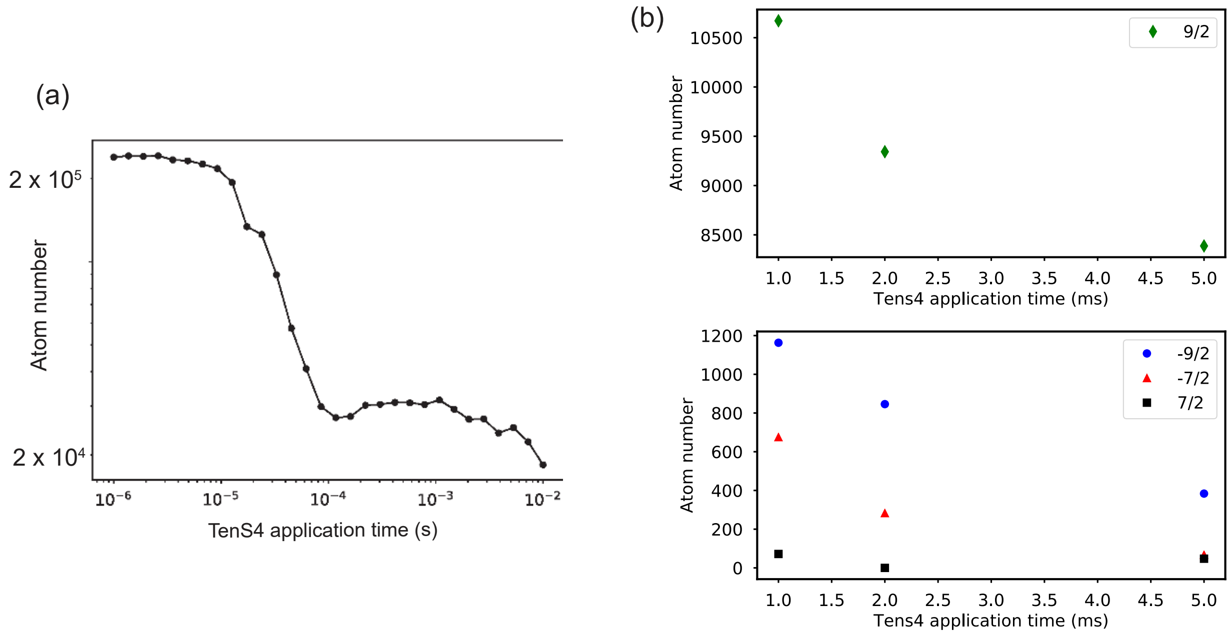

Figure 3.17: (a) Total atom number versus TenS4 application time. The majority of atoms are removed after 100 $\mu$s. (b) Spin-resolved measurements of the $m_F = +/-7/2$ and $m_F = +/-9/2$ states. After 1 ms, single-particle scattering is visible. Measurements in (a) and (b) were taken on different days with slightly different total atom numbers.

atom number after the TenS4 laser is applied for variable times. After 100 $\mu$s, most atoms in other spin states are removed. Spin-resolved measurements are shown in Fig. 3.17 (b), giving $> 90\%$ spin purity after 1 ms application time. For longer times, single particle scattering degrades the $m_F = +9/2$ population. At 5 ms, 96% spin purity is measured.

We also measure $T/T_F$ after applying the TenS4 laser for variable times, as shown in Fig. 3.18. The TenS4 laser does not change the temperature for short application times, since the atoms do not have time to change their momentum during the pulse. Around 10 $\mu$s, the pulse begins to heat the atoms but atoms do not have time leave the trap. With a pulse duration greater than 1 ms, the heated atoms have enough time to leave the trap and again cause minimal heating to the sample. Any single collision between an $m_F = 9/2$ atom and another atom leaving the trap would cause heating. However, this issue is avoided since the time for atoms to leave the trap is much less than

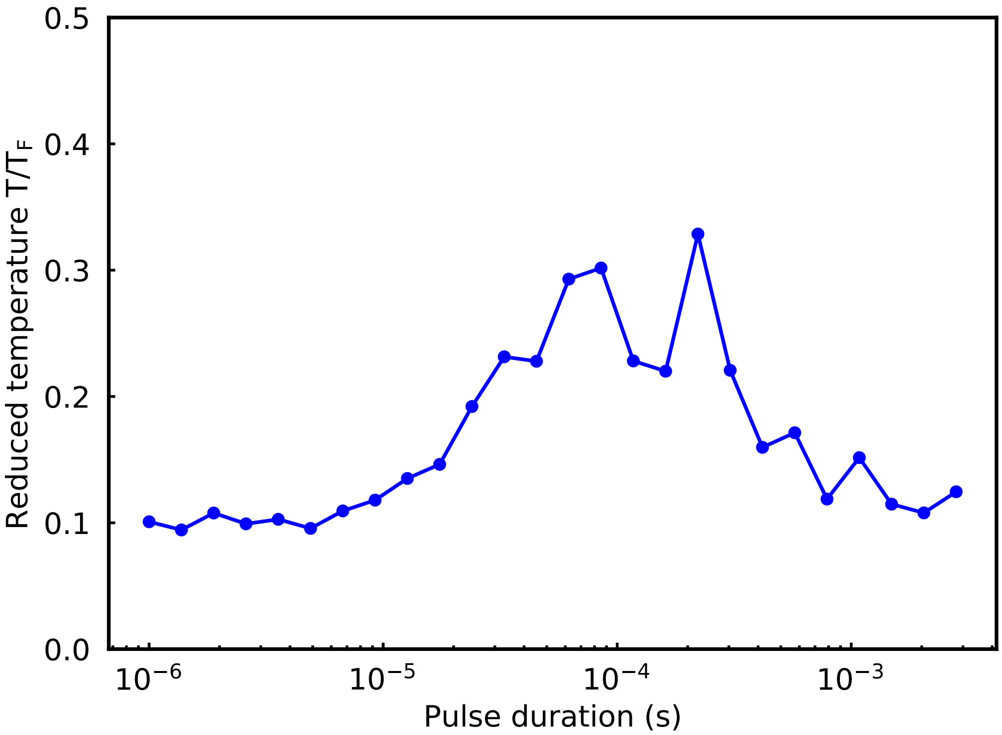

Figure 3.18: $T/T_F$ after switching on the TenS4 laser for variable amounts of time. After a long enough application time, the sample spin polarizes with minimal heating.

the collisional time after evaporation. If we do not optically pump $m_F = -9/2$ and $m_F = -7/2$ prior to evaporation, we notice residual heating after applying the TenS4 laser. Since a residual potential exists for these spin states, atoms undergo heating but not all atoms leave the trap; the atoms that remain in the trap heat the sample. With the TenS4 technique, we can demonstrate a $> 90\%$ spin polarized sample with minimal heating. The spin distillation technique enables us to load a single spin with $T/T_F = 0.1$ into a 3D optical lattice to create a band insulator.

### 3.1.7 Lattice loading

The spin-polarized, deeply degenerate gas is then adiabatically loaded into the 3D optical lattice. To measure the entropy increase after loading, we perform a round-trip measurement, first loading the atoms into the lattice and then back into the XODT. Afterwards, we extinguish the XODT and measure $T/T_F$ by fitting the expanded gas cloud after time-of-flight. We measure approximately 10% of heating throughout this process, confirming that the lattice is adiabatically loaded. We can reach trap depths above 100 $E_{rec}$ in each direction, sufficient to be in the Lamb-Dicke regime.

If the 3D lattice is loaded adiabatically from a low entropy Fermi gas, a band-insulator could be formed with one atom per lattice site. To check this, we perform high-resolution fluorescence imaging on the atoms while they are trapped in the optical lattice. We image atoms simultaneously with a high-resolution camera from the side (NA = 0.1) and from the top (NA=0.23). These images allow us to extract the 3D optical density in the center of the trap, and the results are confirmed using an inverse Abel transform from the image on the side [118]. Preliminary measurements show over an 85% filling fraction in the center of the gas, consistent with a roughly adiabatic lattice loading given the finite temperature of the gas before loading the lattice. More information on this measurement will be contained in an upcoming publication.

It's worth noting that the experiments discussed in Chapters 4, 5, and 6 study Fermi gases and thus do not include this lattice loading step. However, this step is crucial for creating a Fermi-degenerate 3D optical lattice clock.

## 3.2 Imaging techniques

High resolution imaging is a key tool in our experiment that allows us to look at the atomic density distribution and at locally varying frequency shifts. In this section, we detail the techniques we use to image the atomic density distribution in-trap and after time-of-flight. In subsection 3.2.1 we describe how we experimentally implement absorption imaging, which we use to image atomic clouds that have expanded to a low density after time-of-flight. When imaging in-situ clouds, we instead use high-intensity fluorescence imaging, which we discuss in subsection 3.2.2. We then detail our various imaging paths in subsection 3.2.3. In subsection 3.2.4 we describe how to measure camera parameters such as the read noise and the gain. Finally, in subsection 3.2.5 we discuss how relevant imaging parameters such as the magnification and the imaging resolution are extracted.

### 3.2.1 Imaging expanded gases

To image expanded gas clouds, we use the standard method of absorption imaging. Absorption imaging looks at the transmission of an atom cloud after it is exposed to on-resonance probe light. For low probe intensities, the transmitted intensity $I$ is given by the Beer Lambert law $I = I_0 e^{-\int \sigma_0 n dz}$, where $I_0$ is incident intensity, $\sigma_0$ is the low-intensity scattering cross section, $n$ is the atomic density, and $z$ is the imaging probe direction. Taking into account saturation at higher intensities and integrating along the atomic cloud gives us the more general formula for the number of atoms per pixel [119]

$$N = \frac{A}{\sigma_0} \log(S_b/S_a) + \frac{2}{\Gamma t_p g\, q}(S_b - S_a)\,, \tag{3.3}$$

where $A$ is the effective pixel area$^2$ , $S_b$ ($S_a$) is the number of counts in area $A$ without (with) atoms, $t_p$ is the imaging pulse time, $\Gamma$ is the spontaneous emission rate, $g$ is the camera gain, and $q$ is the detector quantum efficiency. Note that the above formula ignores higher order effects such as reabsorption, which will be discussed further later in this section.

The absorption imaging signal can be extracted using three images that are taken in succession. First, an imaging pulse is applied to the atomic cloud and the intensity transmission is imaged onto the camera, which gives counts $\tilde{S}_a$. A second 'bright' image is taken a few ms after the first (depending on the readout time of the camera) without atoms, so that the incident intensity can be measured with counts $\tilde{S}_b$. A final 'dark' image is then taken without the imaging probe light and without atoms, which measures the background counts due to dark counts and stray light, $S_{offset}$. This image is then subtracted from the bright ($S_b = \tilde{S}_b - S_{offset}$) and atom ($S_a = \tilde{S}_a - S_{offset}$) frames before calculating the number of atoms per pixel according to Equation 3.3. Fig. 3.19 shows an absorption image of our cloud after evaporation with roughly $5 \times 10^5$ atoms. Fitting this image to a Fermi-Dirac distribution allows us to extract the temperature of the gas according to

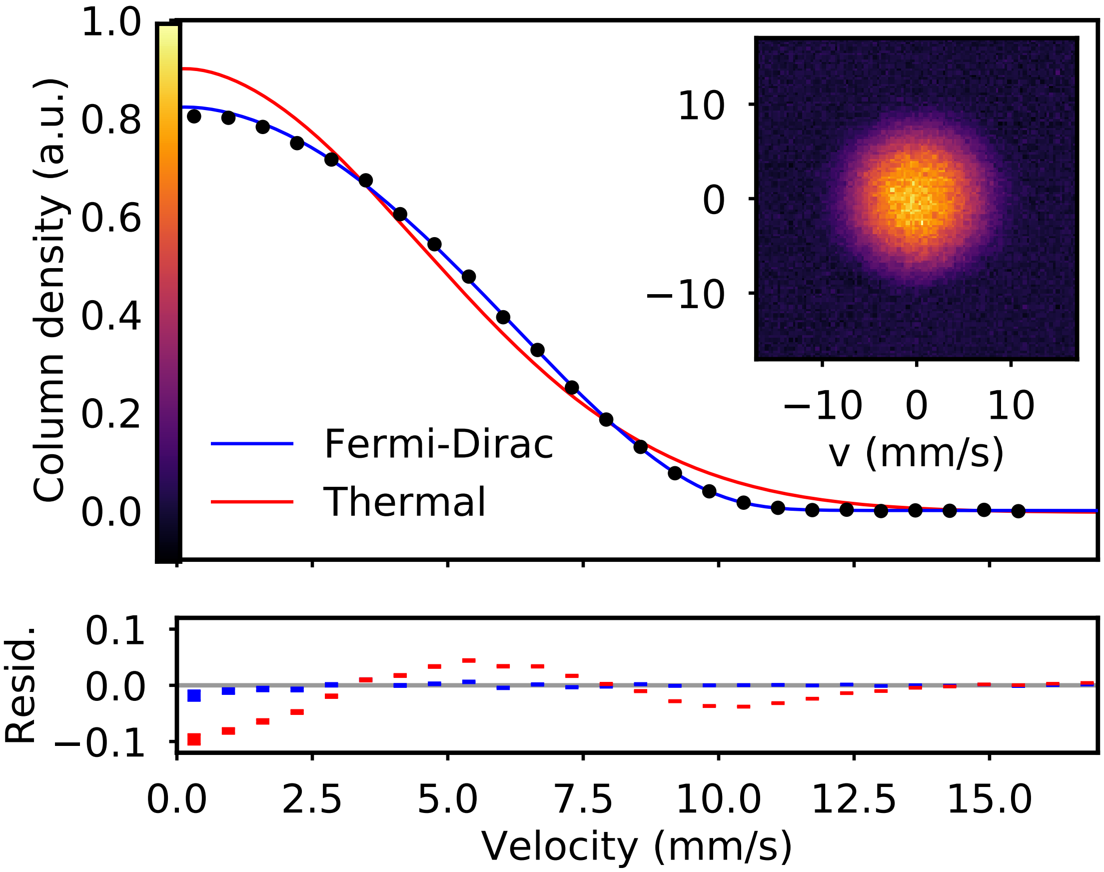

Figure 3.19: Fit of the atomic cloud to a Fermi-Dirac and a thermal distribution after the Fermi gas is released from the crossed optical dipole trap. The Fermi-Dirac distribution minimizes the residuals of the fit. The Fermi-Dirac fit extracts a $T/T_F = 0.08$. Inset: Absorption image of an expanded Fermi gas with a 10 ms time-of-flight.

Equation 2.19; here $T/T_F = 0.08$.

A calculation of the effective atomic cross-section must include the relevant hyperfine manifold of the ground and excited states, as well as the optical pumping dynamics throughout the imaging pulse. We perform imaging on the broad ($\Gamma = 2\pi \times 30.4$ MHz) $^1$P$_1$ state, where the large scattering rate allows high SNR images. We also have access to spin-resolved absorption imaging using the 'red' narrow $^3$P$_1$ transition. For $^1$P$_1$, the excited hyperfine manifold is unresolved so that all excited states are necessary to include in the calculation. Similar to Ref. [120], we calculate the effective cross section for $^1$P$_1$ using a rate equation model, and confirm its validity with a master equation

---

[2] The effective pixel area A is equal to the camera's pixel size multiplied by the imaging resolution.

calculation. For linearly polarized light on-resonance with the ${}^1\mathrm{P}_1$ $F = 11/2$ state, a saturation parameter of $s = 0.17$, and a 3 $\mu$s imaging pulse, the cross-section is 0.49 times the bosonic cross-section of $3\lambda^2/2\pi$, where $\lambda$ is the imaging probe wavelength. Imaging pulses of only a few $\mu$s ensure that blurring due to the directional absorption and diffusive emission of the imaging light is kept small. For a 1 $\mu$s pulse time, the atoms undergo a 500 nm displacement assuming a fully saturated transition.

Experimental imperfections such as polarization impurity can modify the effective cross section from the theoretical result. We perform two separate measurements to double check the calculation. First, we measure the local density fluctuations of a thermal gas. As detailed in Chapter 2, a thermal gas exhibits Poisson statistics, with $\Delta N^2/N = 1$. By analyzing the noise versus mean atom number in different regions of the gas, we can extract the atom number which provides a cross-check for the effective cross-section. A thermal gas can easily be created using for example parametric heating on evaporated samples. Additionally, quantum projection noise can be used to extract the atom number. Measuring the noise between two regions of the atomic cloud in a 3D optical lattice for a fixed pulse time and dead time provides a calibration of $N$. All of these methods agree on the effective cross-section within 20%. These measurements can be performed at low probe intensity, where only the first term in Equation 3.3 contributes to the result, so that $A/\sigma_0$ can be extracted. From a separate measurement of the effective pixel size $A$ (see subsection 3.2.5), the cross-section can be calculated. The probe intensity can then be varied and the coefficient in front of the second term adjusted so that the atom number remains fixed for different incident intensities.

### 3.2.2 In-situ imaging

In-situ, atomic densities are much higher and collective effects such as multiple scattering and dipolar shifts can distort the absorption imaging signal. Typically we think of emitters as being independent, so that the light scattered by individual atoms does not interact with the rest of the sample. This approximation breaks down at the high in-trap densities of over $10^{14}$ atoms/cm$^3$

we demonstrate after evaporation. Light that is scattered off single atoms can be reabsorbed by other atoms, which destroys the spatial information of the scattered photons and thus scrambles the imaging signal. Absorption imaging thus does not work well at high atomic densities, and other imaging techniques must be considered.

Phase contrast imaging as well as dark ground imaging [121] extract the atomic density distribution by looking at the phase change of highly detuned light across the atomic sample. These techniques prevent optical absorption of the imaging light and thus avoid the common pitfalls associated with absorption imaging. An alternative technique is high intensity fluorescence imaging. Here, a high intensity probe beam is applied to the cloud on-resonance, and the spontaneously emitted light is collected off-axis. If the number of probe photons is much higher than the number of atoms, atoms are much more likely to absorb a photon from the probe beam as opposed to a re-scattered photon from another atom. High-intensity fluorescence imaging has been used to accurately extract the density distribution of a MOT with densities as high as $10^{12}$ atoms/cm$^3$ [122]. We use it to accurately image in-situ Fermi-dirac density distributions with densities higher than $10^{14}$ atoms/cm$^3$.

An example of in-trap and time-of-flight density images extracted using absorption imaging (left column) and high-intensity fluorescence imaging (right column) are shown in Fig. 3.20. At central densities above $10^{14}$ atoms/cm$^3$, the optical depth is greater than 100 despite the apparent reduced optical depth shown in the absorption images. Collective effects such as superradiance along the probe beam cause the apparent optical depth to decrease. The apparent optical depth increases quickly as the atoms are released from the trap and the density decreases, but at 500 $\mu$s time-of-flight, the apparent optical depth only reaches 5. In contrast, high-intensity fluorescence imaging correctly models the in-situ optical depth of 150, and the expected decrease in the optical depth after time-of-flight. The intensity of the fluorescence beam is set by looking at the number of detected photons on a camera when the probe intensity is varied. Around 1000 I/I$_{\mathrm{sat}}$, the number

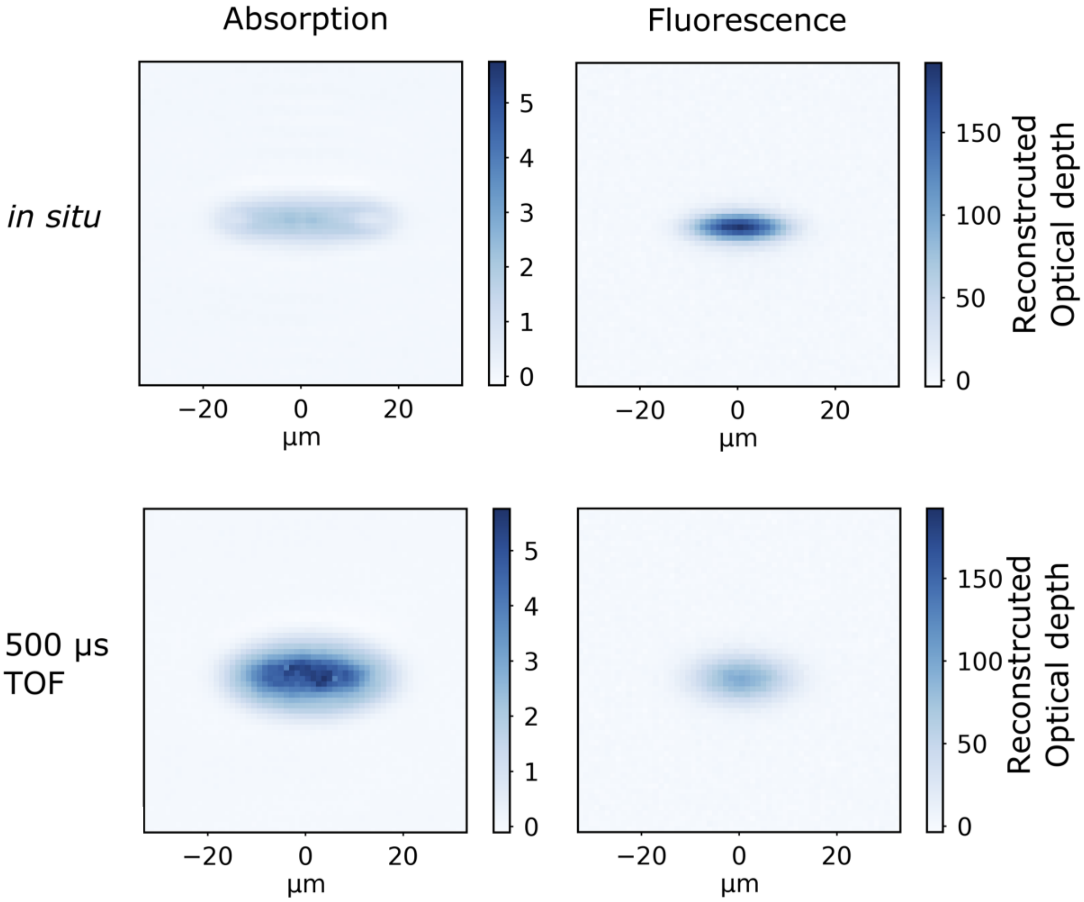

Figure 3.20: Measured optical depth of an atomic cloud with densities greater than $10^{14}$ atoms/cm$^3$, captured both in situ (top row) and after 500 $\mu$s time-of-flight (second row). Absorption imaging (left column) incorrectly extracts the optical depth due to collective effects such as superradiance. The optical depth is conversely accurately extracted using high-intensity fluorescence imaging (right column). The images are extracted using a high resolution side imaging setup with an NA = 0.1

of photons saturates. As expected, we additionally measure that the total fluorescence counts, integrated over the entire cloud, does not change after the cloud is expanded in time-of-flight.

The expected number of camera counts is given by

$$S = \frac{\Gamma}{2} \times t_p \times q \times g \times N \times SA \,, \tag{3.4}$$

where $t_p$ is the imaging pulse time, q is the quantum efficiency, $g$ is the camera gain, $N$ is the atom number, and $SA$ is the collection angle of the imaging system. Practically, it is challenging to precisely extract the solid angle of the camera. We alternatively calibrate the fluorescence signal by using absorption imaging on expanded gas-clouds, where atom numbers can be precisely determined. For a 5 $\mu$s pulse time, we expect 8 counts per atom on the Princeton camera (see subsection 3.2.3). The atom number we extract with this method agrees with Equation 3.4 using our calculated solid angle within 30%.

Fluorescence images are acquired in a single shot. However, background counts due to the camera offset and stray light need to be removed to accurately extract the number of counts. For a stable experiment where stray light does not drift over time, many 'dark' frames can be taken in a separate experimental run and averaged before subtracting it from individual fluorescence images. This allows greater SNR since it reduces the read noise of the processed image (see subsection 3.2.4). We have found that when trying to extract spatial density distributions with on average less than one photon per pixel, as will be shown in Chapter 5, it is necessary remove the average dark count on a pixel-by-pixel basis, since the mean dark count varies slightly across the CCD.

After time-of-flight, the imaged atoms are spread over many pixels and the fluorescence imaging signal is more affected by the camera's read noise. As such, it is easier to obtain high SNR images using absorption imaging after time-of-flight.

### 3.2.3 Imaging paths

Our experiment contains four different imaging paths to access a range of resolutions and field of views along different angles, as shown in Figs. 3.1, 3.2, and 3.3. Our highest-NA imaging axis is along the vertical direction, where the 90 mm distance between the atoms and the 2 inch wide objective lens provides us with an NA = 0.23 and a magnification of 13 (labeled 'Princeton Kuro'). We also have a low resolution camera with a wider field of view from the top ('Mako 1') that allows us to image for example the entire ODT prior to evaporation. The Princeton camera is a back-illuminated CMOS sensor with 1200 x 1200 pixels that are 11 $\mu$m $\times$ 11 $\mu$m with a quantum efficiency of 85% at 461 nm. It has a specified read noise of 2.1 $e^-$ at a conversion gain of 1.59 ADU/$e^-$ with a 200 MHz readout rate/12 bit mode (ADU means analog-digital-units, that is, the conversion from electrons to digital counts). This camera is quite fast because each row is simultaneously read out in parallel; the 200 MHz readout rate implies the one million pixels can be read out in around 10 ms. This makes it ideal for taking multiple images in fast succession, and reduces the amount of stray light that hits the detector during the readout.

From the side we have a high-resolution axis with an NA = 0.1 and a magnification of 11 ('Andor iKon'), while the low-resolution camera ('Mako 2') provides a wider field of view and more easily allows us to look at expanded gas clouds over a range of time-of-flights. The Andor iKon-M 934 is a CCD camera with 1024 x 1024 pixels that are 13 $\mu$m × 13 $\mu$m each. The quantum efficiency is 80% at 461 nm. At a readout speed of 1 MHz (1 full frame per second), it has a read noise of 8 $e^-$, and a conversion gain of 0.5 ADU/$e^-$ with a 16 bit ADU resolution.

All of these cameras are set up to perform absorption imaging or fluorescence imaging on the $^1P_1$ transition, where the fast decay allows many scattering events in $\mu$s timescales so that high SNR images can be obtained. We are also equipped with a red absorption path from the side so that we can perform spin-resolved measurements on the $^3P_1$ transition.

The high intensities we use for fluorescence imaging require a tightly focused imaging beam with a large power. We use a commercial Toptica system that delivers up to 30 mW of power to the experiment for this purpose. The probe beam we use for fluorescence imaging is shown in Fig. 3.1 (labeled 'flour. imaging'). The beam is focused onto the atoms with a waist of 100 $\mu$m and is on axis with the 'Mako 1' camera shown in Fig. 3.3. High-resolution fluorescence images can be taken using the horizontal imaging system labeled 'Camera Andor iXon' in Fig. 3.2 (NA = 0.1) and the vertical imaging system labeled 'Camera Kuro Princeton' in Fig. 3.3 (NA = 0.23).

To switch between absorption imaging and fluorescence imaging, we use a flipper mirror on the bottom mezzanine of our experiment. The small beam waist we use for fluorescence imaging is not suitable for absorption imaging over a wide field of view. We thus switch between this fiber port and a low resolution absorption imaging port with a flipper mirror. The low resolution fiber port has a mm beam waist so that it can image large atom clouds, for example in the XODT. Absorption imaging axes are also implemented for the high-NA side (labeled 'absorption probe') and vertical (labeled 'High. res. abs. imag.') axes. For the vertical path, care is taken to reduce the number of imaging fringes, as discussed in the following subsection.

#### 3.2.3.1 Imaging fringe mitigation

Fringes that show up in the imaging system can distort the atomic density distribution and add noise to the extracted atom number, and thus are essential to remove for accurate imaging. Because absorption imaging requires multiple shots to perform the analysis, the technique is sensitive to varying fringes in the imaging system. Vibrations that are on the order of 10s of Hz can cause fringes due to either dust particles, residual etalons, or pointing fluctuations of the probe beam to move between the atom and bright frames, such that the artifact remains in the analyzed image.

To ensure we have high quality images with few fringes, the optical beam path needs careful consideration. First, the high-resolution vertical beam path (labeled ‘high res. abs. imag.’) is made as short as possible, with no optics close to the edge of the optics table where there are more environmental perturbations. This helps minimize the influence of pointing fluctuations at the fiber tip. In addition, few optical elements are used to reduce the number of possible etalons and potential dust particles in the optics path. Etalons are particularly insidious in imaging systems, since even a 100:1 intensity ratio can produce a fringe contrast of 20%. AR coatings are thus not sufficient to completely remove this noise source. We tilt our imaging beam by 5 degrees with respect to the viewports to avoid reflection-induced interference. The CCD is also tilted and has an appropriate filter so that no stray light hits the camera. Care is taken in choosing the collimation package of the imaging fiber so that a Gaussian beam exits the fiber. Typically monochromatic lenses are better for this purpose than molded aspheres, which can cause residual structure in the emitted beam.

At the output of the imaging laser (not shown in the optical beam path diagrams), we use AOMs to switch on and off the imaging light and a shutter right before the fiber to block any unwanted light. The shutter is opened a few ms before the AOM is switched on to produce a clean pulse of imaging light at the atoms. During this time, zeroth order leakage of the AOM that is coupled into the fiber can heat the atoms. We have found that it is desirable to have two switching AOMs in series to reduce zeroth order light leakage to much less than a photon per atom over these few ms. RF electronics such as switches should also be properly terminated. Finally, if one is using an injection locked laser for the imaging light, it is desirable to have on hand a diagnostic tool such as a Fabry Perot cavity to ensure the seeding is adequate. We have found it is best to avoid this issue entirely by not using injection locked lasers for our imaging light.

### 3.2.4 Measuring camera parameters

To get an accurate calibration of the atom number and fluctuations, it is necessary to measure camera parameters such as the read noise and the gain. In a typical CCD camera, a two dimensional array of pixels measures the intensity distribution across the array. Photons are converted to electrons based on the quantum efficiency, $q$, and are then amplified by a gain factor $g$ and read out on a pixel by pixel basis. The camera is thermoelectrically cooled to reduce the dark current below other relevant noise sources. However, every camera has noise associated with the readout process of the electrons. For a good camera, the read noise $r$ is typically a few electrons. It can be measured by looking at the pixel counts in a dark image, that is an image without atoms and without light, where the standard deviation of pixel counts $S$ is given by $\Delta S_{read} = g\, r$.

The CCD is also subject to photon shot noise, given by $\Delta n_p^2/\bar{n}_p = 1$ with $\bar{n}_p$ average photons. The conversion of photons to electrons follows a binomial distribution with a success probability given by the quantum efficiency, so that $\Delta n_e^2 = \bar{n}_e$ where $\bar{n}_e = q\,\bar{n}_p$ is the average number of electrons. The electrons are then amplified deterministically by the gain, giving a variance in the number of counts due to shot noise $\Delta S_{shot}^2 = g\,\bar{S}$ where $\bar{S} = g\,q\,\bar{n}_p$. The camera gain can thus be measured by looking at the noise of an illuminated CCD. CCDs are not necessarily illuminated uniformly, so that the analysis requires two frames to be taken and subtracted. A difference image is calculated as $S_{diff} = S_a - S_b$, where both frames are without atoms but with equivalent light illumination[3] . The read noise and shot noise are independent, so that total noise in a given frame

---

[3] It is usually necessary to provide a normalization in the total counts between the two images to correct for slight

can be calculated as

$$\Delta S^2_{diff} = 2\Delta S^2_{read} + 2\Delta S^2_{shot} = 2g\,\bar{S} + 2(g\,r)^2\,, \tag{3.5}$$

where the factor of two is due to the independent noise from two separate images and $\bar{S} = \bar{S}_a = \bar{S}_b$. Note that if separate dark frames are subtracted from each image, the added read noise must be included in this equation. If the same dark frame is used, however, the frame cancels in the difference image. The camera gain thus appears as the slope of a line that plots $\Delta S^2_{diff}$ versus $\bar{S}$. Fitting the offset provides a consistency check of the read noise determined from the dark image measurement. An example of this is given in Fig. 3.21, where 700 images were used to extract a camera gain of $c = 1.63 \pm .002$ ADU/e$^-$ and a read noise of $r = 2.4 \pm .01$ e$^-$, consistent with the Princeton Kuro data sheet and an independent calibration of the read noise using a dark frame. Imaging artifacts such as residual fringes can increase the measured noise in the difference image. The data in Fig. 3.21 shows measurements for both coherent and incoherent light, demonstrating there is no added noise in the system due to interference effects. Data was taken for each gain setting, but for Princeton's 16 bit 'gain combining' mode, it was found that the gain was nonlinear.

### 3.2.5 Measuring imaging parameters

Two other parameters that must be measured are the imaging magnification and resolution. The magnification can be measured using Kapitza-Dirac scattering [123, 99]. Here, lattice light is quickly pulsed on which populates momentum states $2n\hbar k$, where $n$ is an integer and $k$ is the lattice wavevector. After time of flight, these momentum wavepackets separate, and the distance between them can be used to accurately calibrate the magnification. For our side imaging system, the magnification can also be calibrated by measuring the distance that the atomic cloud falls under gravity for a variable time-of-flight.

The imaging resolution can be extracted by measuring spatial correlations in a system with zero correlation length. This can be achieved by looking at the spatial correlation of independent

---

variations in the total intensity between the shots.

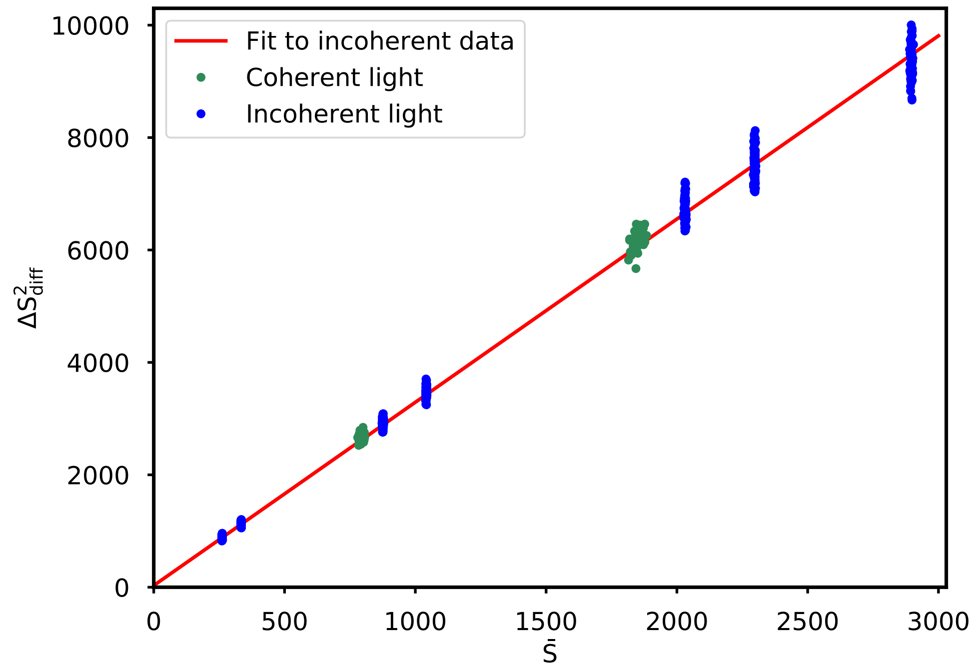

Figure 3.21: Variance of the difference image $\Delta S^2_{diff}$ versus the mean of the bright image $\bar{S}$. Fitting the data to a line allows one to extract the camera gain through the slope, and the read noise through the offset. Measurements are taken with both incoherent and coherent light to confirm the absence of excess noise when using coherent light.

atoms in a 3D optical lattice [32, 124]. In a lattice, correlations in the excitation fraction can be measured by performing Ramsey spectroscopy on the atoms. After measurement, the atoms are projected into either the ground or excited state which produces binomial noise given by the QPN. A finite imaging resolution creates spatial correlations in the image (not, of course, in the atoms), which can be calculated by looking at the average correlation between pixels that are a certain distance $j$ apart after standardizing the data: $\left\langle (p_e^i - \bar{p}_e)(p_e^{i+j} - \bar{p}_e) \right\rangle / \mathrm{var} p_e$, where $p_e^i$ is the excitation fraction at pixel $i$, $\bar{p}_e$ is the average excitation fraction over pixels $i$, and $\langle\rangle$ refers to an average over all pixels $i$. The resolution can then be extracted by plotting the correlation versus distance $j$ and fitting the 1/e$^2$ distance. A similar measurement can be performed by looking at the spatial dependence of the number of atoms in a thermal gas, where Poisson statistics dictates $\Delta N^2/N = 1$. In either case, it is crucial to double check that the resolution degrades as the image is defocused. If the imaging system is outside the depth of field, the correlation will produce the resolution defined by the NA of the imaging system, which is misleadingly given by the diffraction limit, and will be rather insensitive to changes in the focus.

## 3.3 Stability transfer

Our ultrastable laser locked to a Si resonator is centered at 1542 nm, where high quality telecom fiber components and fiber lasers exist. The transparency window of Si starts around 1 $\mu$m, preventing construction of the laser at the 698 nm $^1\mathrm{S}_0 \rightarrow {}^3\mathrm{P}_0$ clock transition. To bridge the frequency gap between 1542 nm and 698 nm while maintaining the high Q optical stability of the ultrastable laser, a frequency comb is used. In this section, we summarize our frequency comb architecture and stability transfer measurements from the ultrastable laser to the 3D optical lattice experiment. In subsection 3.3.1 we briefly introduce frequency combs. Subsection 3.3.2 details the stability transfer setup, and subsection 3.3.3 summarizes measurements of the frequency comb's instability. Finally, in subsection 3.3.4 we discuss measurements of the fiber noise that is introduced when the clock light is delivered to the 3D optical lattice experiment.

### 3.3.1 Frequency comb technology

A frequency comb is a phase-stabilized mode-locked laser. The series of optical pulses at the output of a mode-locked laser is the result of the coherent addition of many optical modes of a resonator over 10s of nm in bandwidth, which are locked together as a result of nonlinearity in the laser [125]. The series of pulses are not only regularly spaced, but are also phase coherent with one another. In the frequency domain, this corresponds to many 'comb' teeth, as shown in Fig. 3.22. Each comb tooth is defined by the equation [126, 127, 128]

$$\nu_n = n \times f_{rep} \pm f_0 \,, \tag{3.6}$$

where $n$ is an integer and $f_{rep} = 1/T = c/L$ is the repetition rate, $T$ is the time between pulses, and $L$ is the mode-locked laser round-trip cavity length. The carrier-envelope offset is given by $f_0$ and is related to the phase slip per pulse $\Delta\phi$, which arises due to a difference between the group

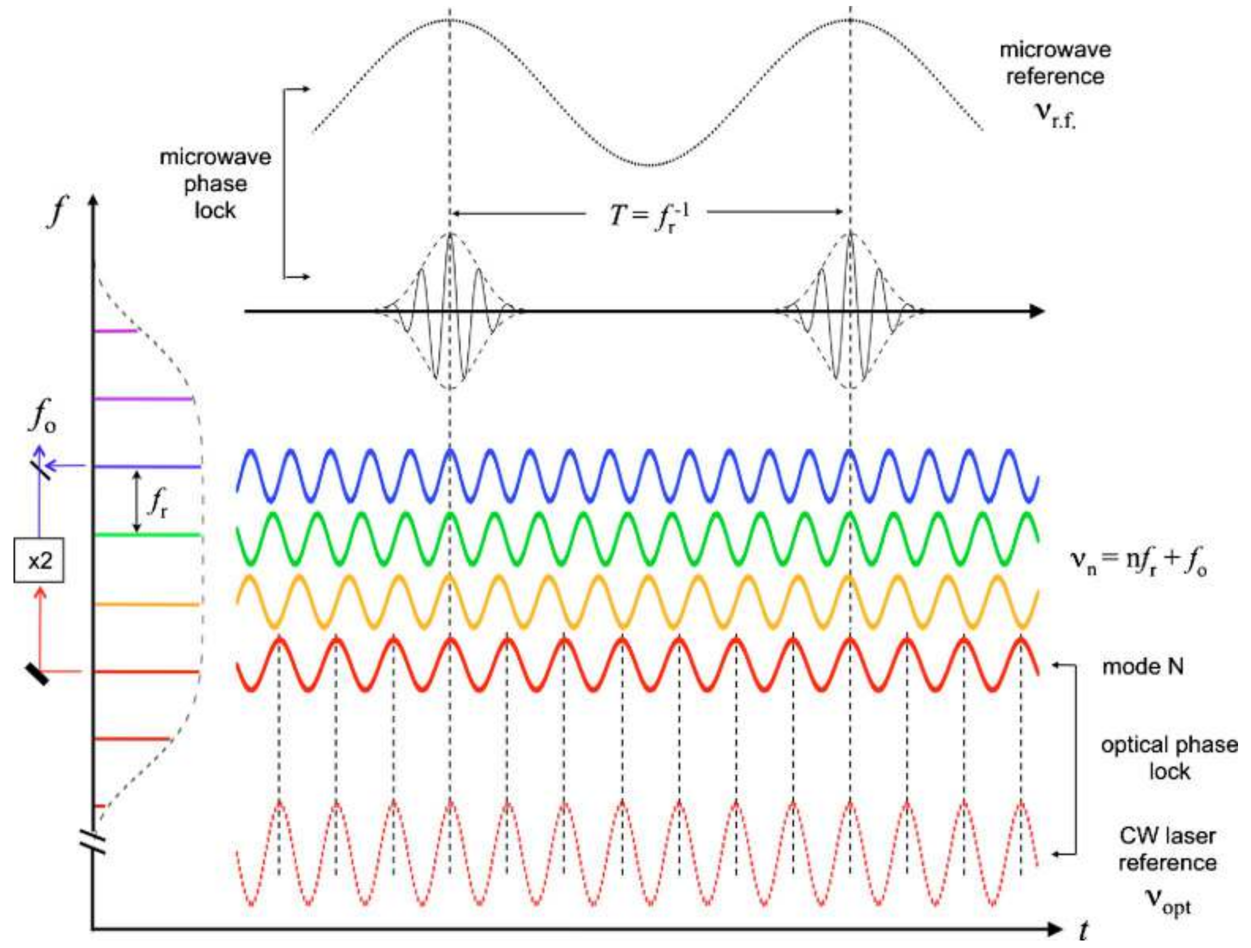

Figure 3.22: Time and frequency representation of a frequency comb. In the time domain, a series of pulses regularly spaced by time $T$ are generated from the output of a mode-locked laser. These pulses are the result of the coherent addition of many optical modes of a mode-locked laser. The carrier offset-frequency, defined as zero here, is due to a phase slip between the carrier and envelope each pulse. $f_{rep}$ can be locked to a microwave reference or a laser. The carrier-envelope offset $f_0$ must also be stabilized. Figure adapted from Ref. [1].

and phase velocity in the mode-locked resonator. The carrier-envelope offset is related to the phase slip per pulse through

$$f_0 = \frac{1}{2\pi} f_{rep} \Delta\phi \, , \tag{3.7}$$

where $\Delta\phi = (1/v_g - 1/v_p)L\omega_c$ where $v_g$ ($v_p$) is the group (phase) velocity, and $\omega_c$ is the carrier frequency. The difference between group and phase velocities arise from dispersion inside the mode-locked resonator.

The only two free parameters that describe every comb tooth are $f_{rep}$ and $f_0$. These two parameters can be robustly stabilized. Many applications that do not require state-of-the-art precision lock $f_{rep}$ directly to a microwave source. The repetition rate is generally an accessible microwave frequency between 100 MHz and 1 GHz. However, the noise on $f_{rep}$ gets amplified by $n$, which is on the order of $10^6$. As a result, it is more beneficial to lock a single comb tooth directly to a stable laser.

The carrier-offset phase is separately stabilized and can be detected using a self-referencing technique called an f-2f interferometer [129]. Here, a low frequency part of the optical spectrum is frequency doubled using second harmonic generation. A heterodyne beat is then formed between the doubled spectrum and a high-frequency portion of the comb spectrum to produce $f_0$, since

$$f_0 = 2v_N - v_{2N} = 2(Nf_{rep} + f_0) - (2Nf_{rep} + f_0)\,. \tag{3.8}$$

Self-referencing requires the comb to span an optical octave. Mode-lock laser bandwidths can only achieve 10s of nm bandwidth, meaning external frequency broadening must be performed. Frequency broadening is generally achieved in optical fiber through the process of self-phase modulation, which uses the intensity dependence of the nonlinear index of refraction (the Kerr effect). Optical fibers allow large intensities to be generated since they confine light in small mode-waists. However, chromatic dispersion gradually widens the pulse duration, reducing the peak intensity of the pulses and thus limiting the maximum achievable frequency broadening. Engineered photonic crystal fiber [130] circumvents this problem by providing zero dispersion near the carrier frequency while supporting a fundamental spatial mode. It was the introduction of these optical fibers that allowed the first demonstration of an optical octave and subsequent direct detection and locking of $f_0$ [131, 132].

With the repetition rate locked to an ultrastable laser and the carrier offset phase stabilized, the stability of the ultrastable laser is then transferred to the entire comb spectrum. One can think of this as converting an ultrastable laser at a single frequency into hundreds of thousands of ultrastable lasers that span frequencies of over 100 THz. The stability of the Si cavity can thus be transferred to the comb tooth at 698 nm, on resonance with the clock transition. A laser at 698 nm can then be phase-locked to the comb and delivered to the optical lattice clock through phase-stabilized optical fibers, as discussed in the following subsections.

### 3.3.2 Stability transfer frequency chain

We use a commercial Menlo Er:fiber frequency comb to transfer the stability of the ultrastable laser at 1542 nm to 698 nm. The comb is based on an Er-doped femtosecond all-PM fiber mode-locked laser [133] with a repetition rate of 250 MHz and a center wavelength around 1560 nm. The comb has over a 1 MHz bandwidth on both $f_0$ and $f_{rep}$ due to high-bandwidth EOM actuators that have minimal crosstalk [134]. The almost-independent control of the two actuators is achieved using an interferometer implemented with polarization optics, where the amplitude between the two arms is adjusted to achieve a change in the carrier envelope without altering the center frequency. The comb is equipped with additional low-bandwidth piezo and thermoelectric actuators that allow the comb to stay locked for multiple months.

The frequency comb is a multi-branch comb, where the output of the mode-locked laser is split between different ‘branches’ that serve different optical purposes as illustrated in Fig. 3.23. Each branch contains a separate Er:doped fiber amplifier (EDFA) and highly nonlinear fiber to maximize frequency broadening at a particular optical frequency. Our frequency comb contains three separate branches. The first arm is dedicated to detecting $f_0$ through an f-2f interferometer. A second arm is used to provide a frequency reference at 813 nm, which is our lattice wavelength. Approximately a 1 Hz frequency shift of the clock transition occurs if the lattice laser is off the magic wavelength by 1 GHz per $100E_{rec}$ lattice depth for a combined scalar and tensor Stark shift of an atom with $|m_F| = 9/2$. Stabilizing the lattice lasers to below a kHz is easily achievable with this system. Since the broadened comb spectrum spans roughly 1 $\mu$m to 2 $\mu$m, it is necessary to double the comb light using a periodically-poled lithium niobate (PPLN) crystal, and 25 mW of power is provided in a 3 nm bandwidth at the free-space output of the crystal. The light then goes into a home-built

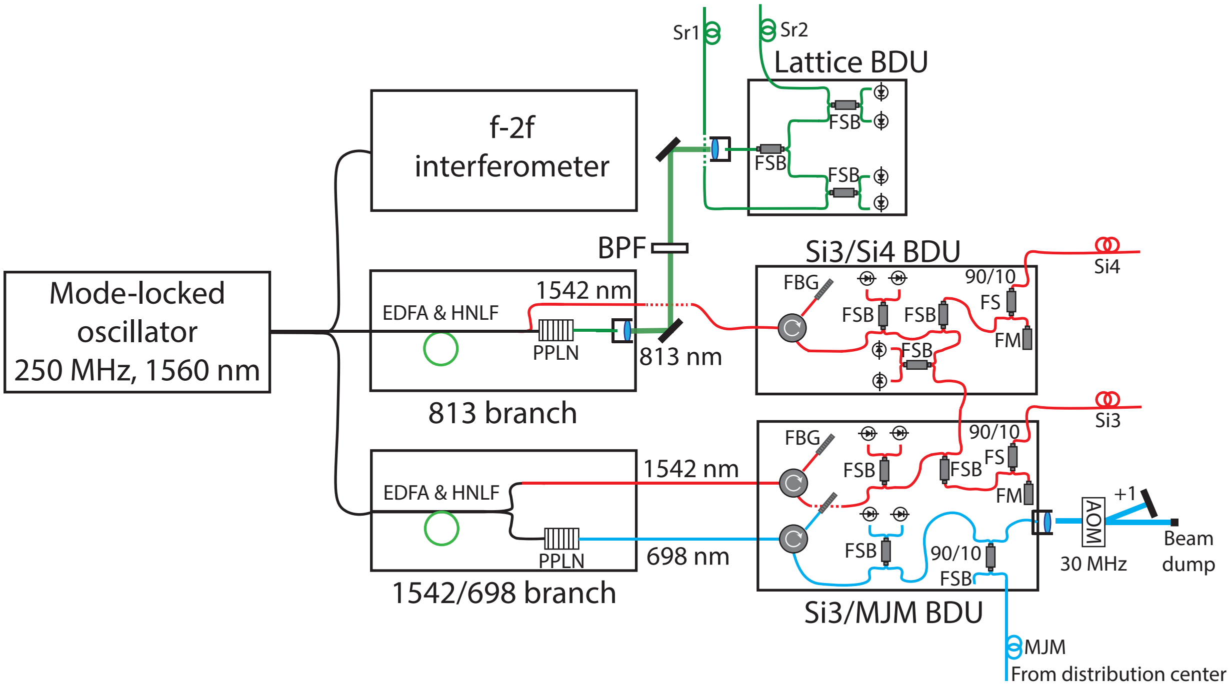

Figure 3.23: Outline of the Menlo frequency comb we use for stability transfer of the Si3 cavity to other wavelengths relevant for Sr. Separate branches are used for each desired frequency output. We have branches that stabilize $f_0$, our 813 nm lattice lasers, and a custom branch with minimal differential noise to transfer the stability of Si3 (the 124 K cavity) to 698 nm, the ${}^1\mathrm{S}_0 \rightarrow {}^3\mathrm{P}_0$ clock transition. Our frequency comb is locked to Si3, and the beat between the frequency comb and MJM (a pre-stabilized cavity at 698 nm) provides the error signal to phase-lock MJM to the comb. Heterodyne beats between Si3 and Si4 (the 4 K Si cavity), and between the frequency comb and Si4, also occur inside the Menlo comb box. Acronyms are: erbium-doped fiber amplifier (EDFA), highly nonlinear fiber (HNLF), periodically-poled lithium niobate (PPLN), bandpass filter (BPF), beat-detection unit (BDU), pm fiber splitter (FS), pm fiber splitter with fast axis blocked (FSB), fiber bragg grating (FBG), faraday mirror (FM), acousto-optic modulator (AOM). All fibers and fiber components are polarization-maintaining (PM).

beat detection unit (BDU), which contains PM fiber splitters to combine the comb light with the lattice lasers, and a high-bandwidth balanced detector to detect the heterodyne beat. Note that because of the doubler, the comb teeth follow the equation $\nu_n = 2nf_{rep} \pm 2f_0$. Heterodyne beats are generated separately with two different lattice lasers to provide a stable frequency reference for each Sr experiment. We achieve 30 dB - 40 dB SNR with 100 kHz resolution bandwidth for these beats.

The last branch is used generate beatnotes at both 1542 nm and 698 nm. Outputs centered at these two different wavelengths were implemented in a single branch to reduce the differential noise between the two spectral regions. The comb light around 1542 nm is split off right before the HNLF, while the output of the HNLF goes into a PPLN to generate 5 mW of power in a 3 nm bandwidth centered at 698 nm. In both cases, the comb light is then filtered with a 0.5 nm bandwidth fiber bragg grating (FBG) and combined on a beam splitter with a cw laser to generate a heterodyne beat that is detected using a balanced detector. The 1542 nm output of the branch forms a beat with the Si3 light (the 124 K Si cavity), which is transferred over to the Menlo optics table using a phase-stabilized fiber link. The fiber noise reference is provided by a PM Faraday mirror that is inside a metal, temperature-controlled box. The 698 nm comb light forms a beat with MJM, which is a pre-stabilized laser at 698 nm [35]. The fiber noise cancellation between MJM and the frequency comb uses two AOMs to form the beat. The first AOM before the fiber provides the actuator for the fiber stabilization. A unique frequency from the fiber noise reference is guaranteed using a second static AOM right before the fiber noise reference mirror. This ensures that the servo only sees the reflection from the mirror and is insensitive to spurious reflections from other micro-optics, fiber tips, or fiber splices. We are able to achieve 50 dB SNR at 100 kHz resolution bandwidth for both the Si3-comb beat and the MJM-comb beat.

We additionally take spare light from the comb at 1542 nm to generate a beat with Si4 (the 4 K Si cavity) in a separate Si3/Si4 BDU. The comb light is similarly filtered using a FBG before being combined with the fiber-stabilized Si4 light to generate a beat. We also create a second beat between Si4 and Si3 inside this BDU.

The full stability transfer schematic is shown in Fig. 3.24. Light from Si3 is delivered to the Er comb using a phase-stabilized link, and is used to lock the comb at 35 MHz by actuating on $f_{rep}$. We additionally lock $f_0$ to a referenced microwave signal at 35 MHz. This transfers the stability of Si3 to every comb tooth, providing a stable reference for our lattice lasers and our pre-stabilized

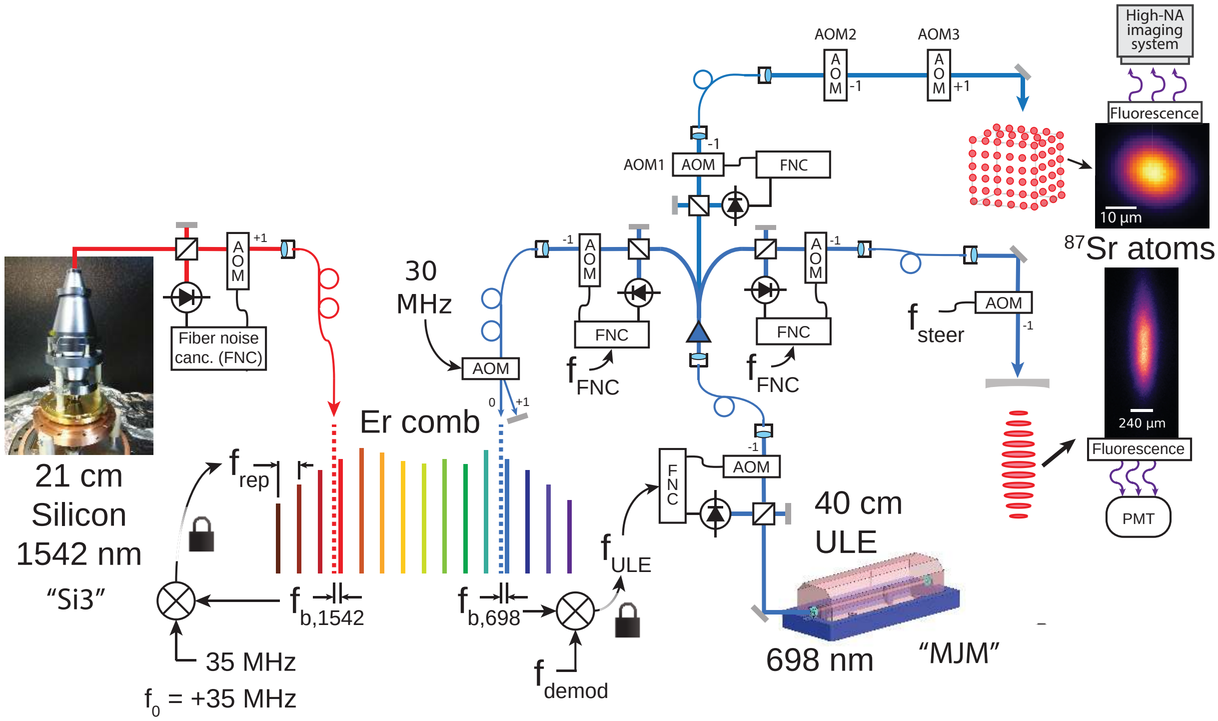

Figure 3.24: Stability transfer of the Si3 cavity to the 1D and 3D optical lattice clocks. A frequency comb is utilized to do the transfer. The comb is locked to Si3, and a pre-stabilized ULE cavity at 698 nm is locked to the comb. The stabilized light of the ULE cavity seeds two injection locked lasers (not shown) before being distributed to the Sr experiments and the frequency comb. The fiber links between the comb and the Si3/ULE laser, and the Sr experiments and the distribution center, are phase-stabilized.

laser at 698 nm. To complete the stability transfer process, the MJM laser is then phase-locked to the comb. The MJM ultrastable laser's output first goes to a distribution center with a phase-stabilized fiber link. The light is used as a seed to injection lock two different 30 mW diodes, which are then distributed to the various Sr experiments and to the frequency comb. The MJM laser has $1 \times 10^{-16}$ fractional frequency instability from 1 s to 10s of s [42], and good high frequency noise. Si3, on the other hand, has improved Brownian thermal noise which is the dominant noise source up to around 2 Hz. To maximize the noise performance between the two cavities, we lock MJM to the comb with a bandwidth around 1 Hz. This optimizes the noise performance of the combined Si3-MJM cavity as determined through simulations of the Dick Effect, described in Chapter 1. To actuate on the MJM laser, we sum the error signal from the MJM-comb beat into the fiber noise

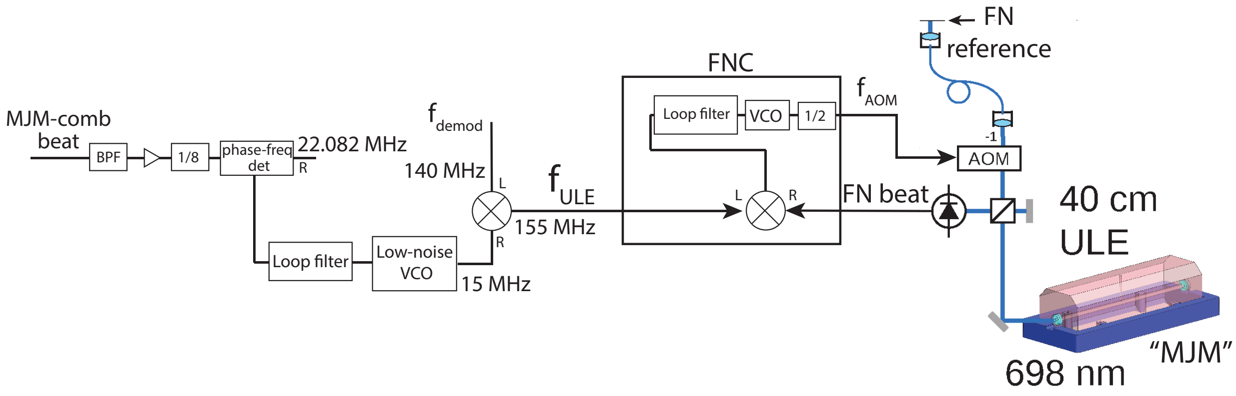

Figure 3.25: Electronics demonstrating how we lock MJM to the frequency comb. The MJM-comb beat provides an error signal which we use to steer the demodulation frequency of the MJM fiber noise servo. Both the fiber noise and the MJM-comb servo are closed feedback loops.

frequency reference, as shown in Fig. 3.25. The beat is bandpass filtered, amplified, and divided by a factor of 8 before being demodulated and sent into a loop filter. The output of the loop filter is then sent into a low-noise VCO, which is mixed with a local oscillator to provide the fiber noise frequency reference at the correct frequency. The fiber noise reference is mixed with the fiber noise beat and sent to a loop filter that drives an internal VCO, which powers the MJM fiber noise AOM. All of the fiber noise servos and the phase locks with the frequency comb are closed feedback loops so that the Si3 phase is properly transferred to MJM.

### 3.3.3 Differential noise

To not introduce additional noise in the stability transfer, it is essential to reduce differential noise between the 1542 nm path and the 698 nm path. Any noise added between the 1542 nm and 698 nm branches of the comb, in the distribution center, or in the transfer of the light to the Sr experiments, will degrade the pristine stability provided by the Si cavity. A critical potential noise source in the frequency comb is from unstabilized fiber, which can add noise caused by vibrations or temperature fluctuations. To reduce the amount of differential noise between the two paths,

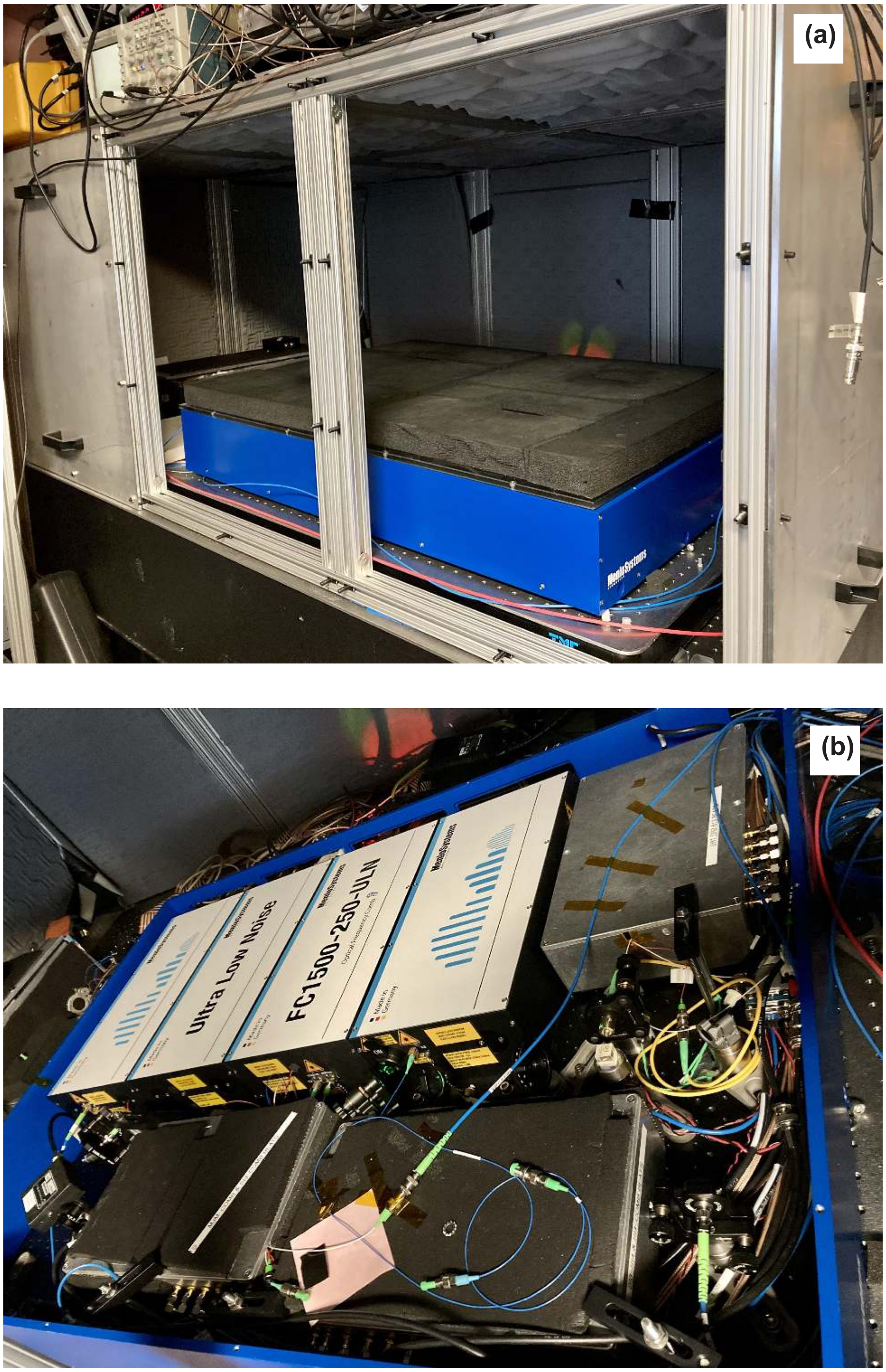

Figure 3.26: (a) Picture of the frequency comb, including the outer Al box, the 2 inch breadboard, and the inner box that goes around a smaller Al breadboard that is water-cooled and clamped to the middle-sized breadboard. (b) Optical components of the frequency comb, inside the inner box. Out-of-loop fiber components are housed in Al boxes that are thermo-electrically stabilized to within 10 mK.

the fiber lengths are made as short as possible. The 1542 nm path is picked off in the comb as close to the 698 branch as possible, so that the differential fiber path in the 1542/698 branch is only 10-15 cm. Fiber components in the Si3/MJM BDU are spliced with roughly 10 cm leads. In addition, all fiber components in the BDU are housed within a metal box that is temperature controlled with a 10 mK temperature stability. The fiber leads between the 1542/698 branch and the Si3/MJM BDU box are only a few cm long. Furthermore, all fibers in the frequency comb are polarization-maintaining (PM) to reduce fluctuations due to polarization rotation, and all fiber splitters have the fast axis blocked. The box has foam on top and the sides to reduce vibrational coupling.

The frequency comb sits on top of a water-cooled Al breadboard that is tightly clamped to a 2 inch breadboard that sits on top of the larger optical table with small viton feet. We use a low-noise Lauda ECO RE 415 S chiller at the minimum flow rate to provide the water cooling. We confirmed that the chiller did not add vibration noise by looking at the coherence between the Si3-MJM beat and an accelerometer placed on the comb table. The water-cooled breadboard is surrounded by a plastic box with foam on the lids. Furthermore, the 2 inch thick breadboard is surrounded by a large Al box with conical foam inside to damp vibrations. Temperature fluctuations inside the large Al box are sub-100 mK over the course of a day. The various boxes are shown in Fig. 3.26. The large Al box around the Sr2 (3D optical lattice) experiment was modeled after the box around the frequency comb. The Menlo comb is equipped with a number of heavy electrical cables to power the pump diodes, provide feedback to the repetition rate and the offset beat, etc. We clamp the cables with viton on the main large optical table to dampen their vibrations. We furthermore connect ribbon cables for the pump diodes and light flexible cables for the rest of the cables to lessen the impact of cable vibrations on the comb.

The added instability of the stability transfer process due to the frequency comb is assessed by performing a comb comparison with an identical reference system [135]. Each comb is locked to a common local oscillator at 1542 nm, and the repetition rates are set to the same value. The offset beat $f_0$ is also phase-locked but differs between the two combs by 5 MHz so that the heterodyne

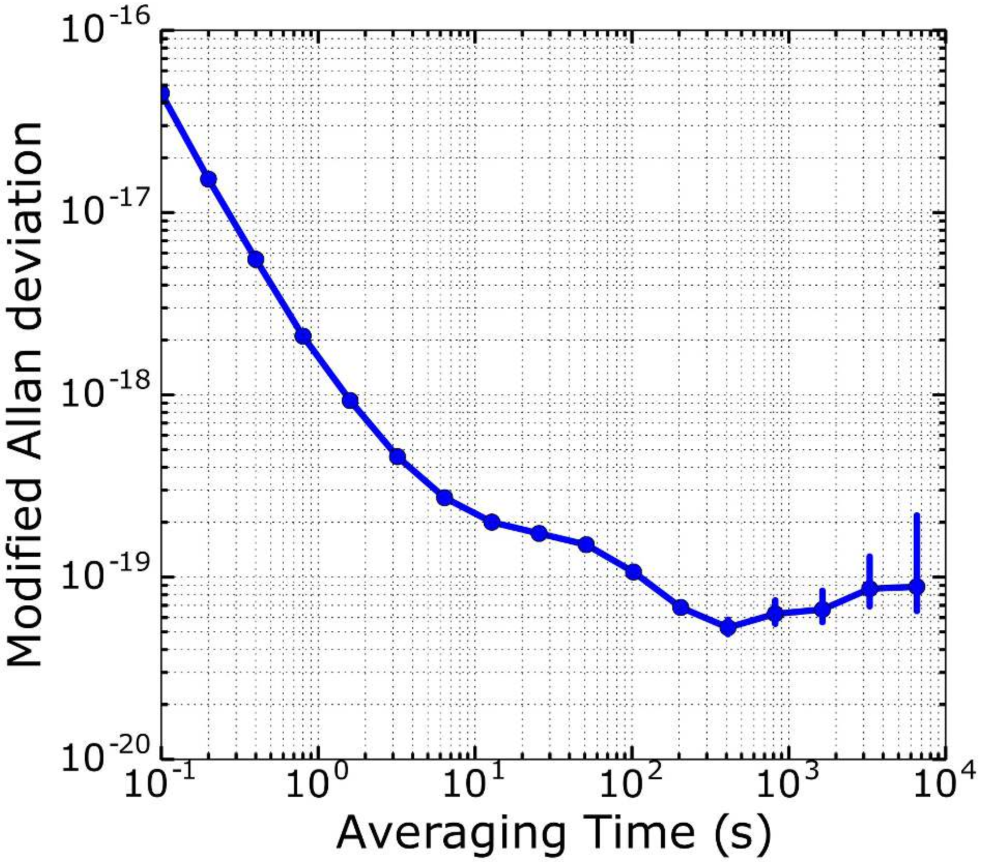

Figure 3.27: Differential noise between two identical frequency combs. Each comb is locked to a common reference at 1542 nm, and a heterodyne beat is formed at 698 nm that is then counted on a frequency counter.

beat at 698 nm is 10 MHz after the PPLN crystals. The heterodyne beat is then counted using a dead-time free lambda-type frequency counter with a 100 ms gate time. Because the repetition rates are equal for the two systems, all comb lines within the 2.5 nm output of the PPLN crystal contribute to the measured signal. The results of the measurement are shown in Fig. 3.27. The instability due to the frequency comb is $1.6 \times 10^{-18}$ at 1 s, well below the local oscillator noise, while the measured frequency offset of the beat is $1.5 \times 10^{-19}$.

This measurement was performed with Menlo's commercial BDU units. The instability of our home-built BDU units were measured separately. To measure the noise, the comb light is replaced so that a cw-cw beat is formed with the same local oscillator. To measure the noise in the 1542 nm out-of-loop fiber, Si3 light is split off before the fiber link and a separate phase-stabilized fiber link is sent to the comb input port of the 1542 nm BDU (prior to the circulator in Fig. 3.23). The fiber noise AOMs are offset in frequency so that a heterodyne beat is formed at 10 kHz, which is subsequently counted. The results, as seen in Fig. 3.28 (a), show an instability of $4 \times 10^{-18}$ at 1 s averaging time. We further measured the frequency offset over the course of a week, where we saw variations in the center frequency of $2 \times 10^{-19}$. A similar experiment is performed on the 698 nm out-of-loop fiber path in the BDU. A separate path on the distribution center is used, with a separate phase-stabilized link, to generate the cw-cw beat. Results are shown in Fig. 3.28 (b), where the instability is $5 \times 10^{-18}$ at 1 s averaging time. The frequency offset over the course of a week varied at $5 \times 10^{-19}$. The noise is well below the Si cavity, ensuring that any degradation of the stability transfer due to the frequency comb is negligible. Note that these measurements provide an upper bound of the instability of the home-built BDU, since the measurement includes noise from the phase-stabilized fiber links and any out-of-loop noise on the distribution center between the two 698 nm paths. The noise of the 698 and 1542 fiber paths in the BDU are measured independently, and thus does not take into account that some noise could be common-mode between the two fiber paths.

### 3.3.4 Optical path length stabilization

The 698 nm light, locked to the Si3 ultrastable laser, is transferred to the Sr experiments using phase-stabilized fibers [136]. The link operates in a pulsed fashion so that light is only delivered to the atoms throughout the coherent interrogation, and is extinguished during the dead time and readout time. This pulsed operation is a known source of phase transients [137]. To overcome this issue in previous work, the 0th order transmission of the switching AOM was used as the fiber noise reference, while the 1st order diffracted beam was directed to the atoms [36]. This ensured

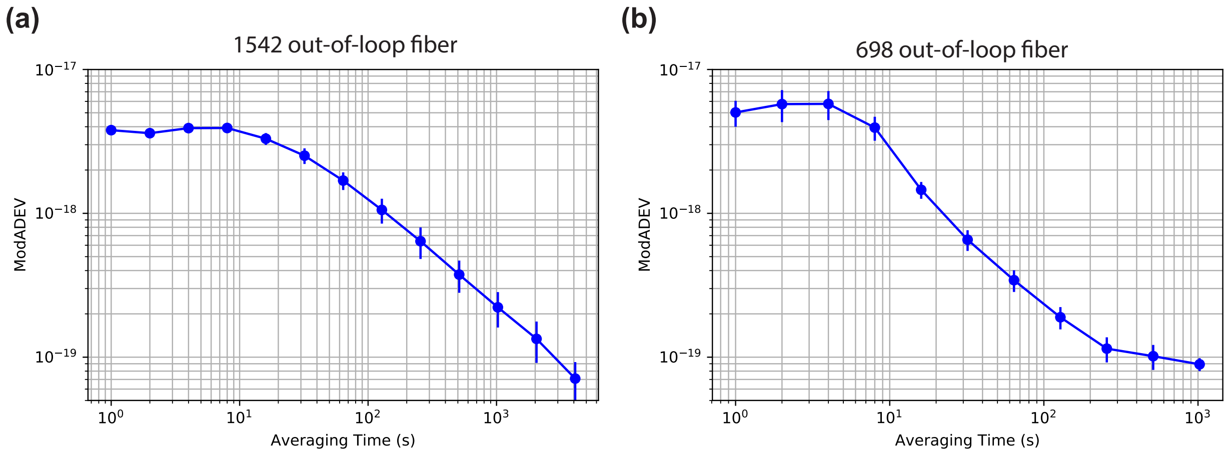

Figure 3.28: Instability of the out-of-loop fiber in the home-built BDU boxes. The measurements include fiber noise from the phase-stabilized links.

that RF-induced heating of the AOM was mostly common-mode, and that the fiber-noise servo was always engaged. The 0th order beam was reflected right before the lattice retro mirror so that both the 0th and 1st order beams sampled roughly the same optical path. This method reduced the frequency shift uncertainty to below $10^{-18}$ [138], and the out-of-loop path length between the 0th and 1st order was small enough to successfully transfer a clock with an instability of $1 \times 10^{-16}$ to the atoms.

However, we found that the differential noise between the 0th and 1st order paths was above the level of the Si3 clock laser instability despite the only 10 cm path length difference. The out-of-loop noise was made worse by the lack of a tight enclosure around the experiment during that time. Differential path length changes between the 0th and 1st order beams can be driven by thermal changes in the AOM and air currents. Furthermore, reflections from the fiber tip or the front surface of the AOM can add noise if the 0th order light is used as the phase reference. To test the out of loop noise, a heterodyne beat was formed between the 1st order paths of two separate phase-stabilized links with an out-of-loop path length difference of 10 cm. We saw a significantly reduced out-of-loop noise when the 1st order light of the AOM was used as the phase-reference as

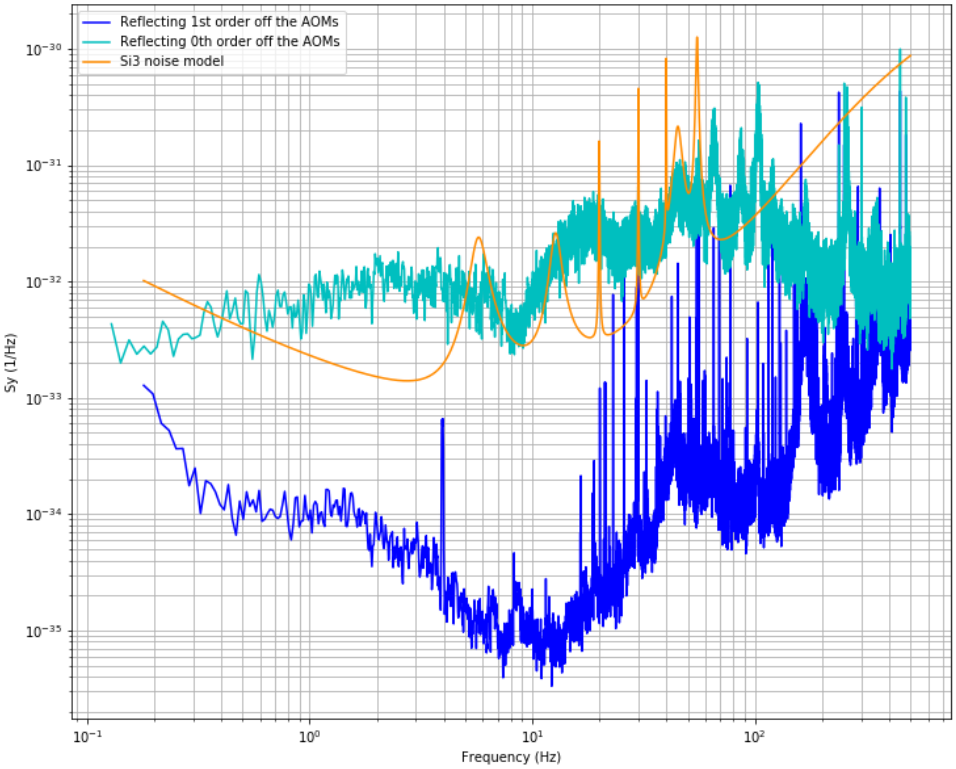

Figure 3.29: PSD of the out-of-loop fiber noise measurements. When using the 0th order as the fiber noise reflection but the 1st order to perform spectroscopy, the differential noise between the paths is above the Si3 noise floor. When using the 1st order to provide the phase reference and perform spectroscopy, the noise is much smaller.

opposed to the 0th order, as shown in Fig. 3.29.

To circumvent these issues, in Ref. [3] we used the first diffracted order of the AOM for both the fiber phase noise reference and for spectroscopy. A wedged beam sampler is placed before the lattice retro mirror to provide a 10% back-reflection for optical path length stabilization. A shutter is placed after the beam sampler to keep clock light from hitting the atoms while keeping the servo engaged. To prevent phase transients from impacting the clock interrogation, the clock light is detuned by 1 MHz 7 ms before the Rabi pulse and the shutter is opened. Any phase transients from re-engaging the servo occur while the clock light is detuned, that is when the atomic sensitivity

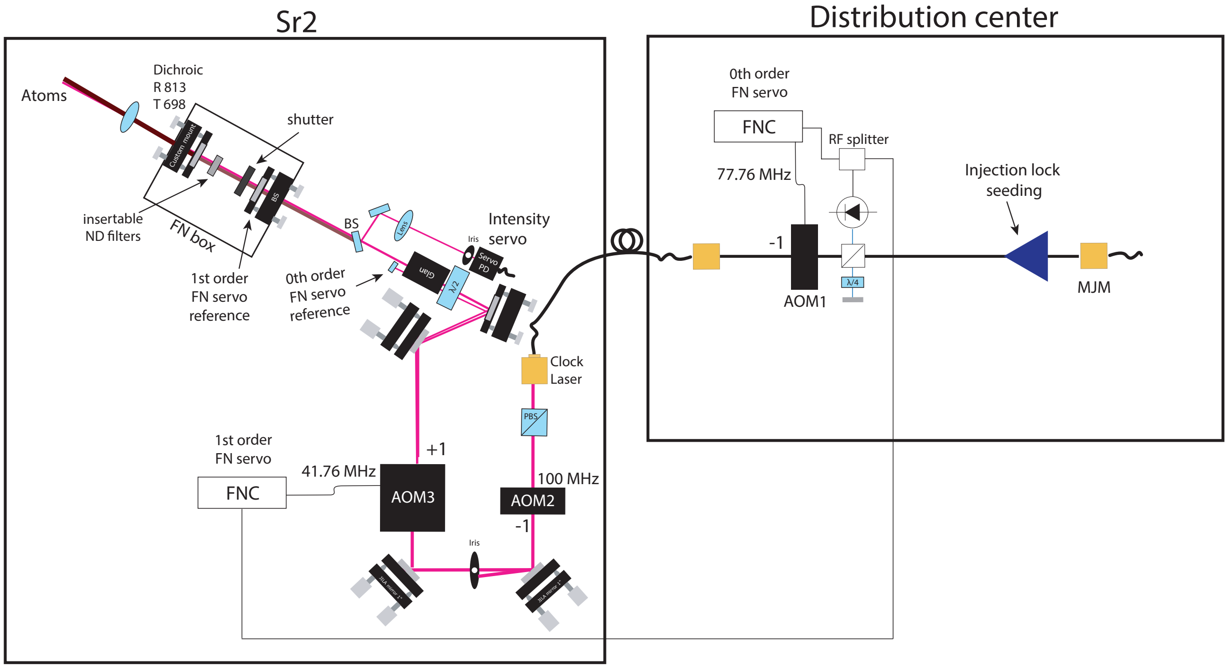

Figure 3.30: Schematic of the updated fiber noise stabilization setup. Both a 0th order and a 1st order servo are utilized. The 0th order servo, which provides actuation on the RF of AOM1, is continuously on, and provides phase-stabilization for the majority of the fiber link. The 1st order servo removes any differential noise between the 0th and 1st order paths. This servo is turned off (by shutting off AOM3) right before spectroscopy, while the shutter is opened.

function is negligible. After the servo settles, the frequency is then linearly swept onto resonance over 3.4 ms. The fractional frequency shift due to the sweeping of the light onto resonance is calculated to be below $2 \times 10^{-19}$ for a 600 ms pi pulse.

For Ramsey instead of Rabi spectroscopy, the clock light must be extinguished during the dark time to avoid a significant clock shift. We thus devise an alternative fiber noise locking scheme that A.) adds minimal phase noise to the clock light delivered to the atoms, B.) reduces phase transients when the clock light is pulsed on/off, and C.) provides maximal frequency agility on the Bloch sphere. The optics and general locking schematic are shown in Fig. 3.30. A fiber noise servo is implemented using the 0th order light of AOM3 as the fiber noise reference, and a separate servo takes care of the differential noise between the 0th order and 1st order paths. For this second servo, the diffracted 1st order light from AOM3 is used as the fiber noise reference. The 0th order servo steers the RF drive of AOM1, while the 1st order servo steers AOM3. We additionally add another AOM, AOM2, after the fiber so that the 0th order servo fiber noise reference is not at the same frequency as the reflection off the fiber tip. The 0th order servo is continuously on, providing phase-stable clock light at the $10^{-16}$ level.

The 1st order servo remains activated for the majority of the cycle by having the shutter closed so that the light does not hit the atoms. Before performing spectroscopy, AOM3 is shut off, the shutter is opened, and then AOM3 is switched on again to create a clean pulse of light for spectroscopy. Opening the shutter takes around 3 ms. During this time, AOM3 is off, and the 1st order fiber noise servo is disengaged. The key challenge is then to make sure that re-engaging this servo does not introduce significant phase transients. One may think that you could just use an integrator hold feature on the servo during this time, but we measured significant phase deviations with this method.

Instead, we feed in a synthetic fiber noise beat into the servo while AOM3 is turned off. The electronics, shown in Fig. 3.31, show how we provide a reference with the right phase and frequency to the servo box. The solution presented in Fig. 3.31 solves issues A.) and B.) discussed above. When AOM3 is on, the fiber noise beat is connected to the input of the servo, and is phase-locked to a reference ($f_{ref}$). The error signal steers an internal VCO that is used to drive AOM3 ('1F out'). The VCO output is centered at 77.76 MHz, so that we need to mix the signal with a function generator at 36 MHz to get to the right frequency for AOM3.

Right before the shutter is opened, a TTL shuts off the RF drive of AOM3 and simultaneously switches the input of the fiber noise servo to the synthetic beat signal. The correct frequency is provided by $f_{ref}$, but the phase needs to be locked so that it is not sensitive to environmental

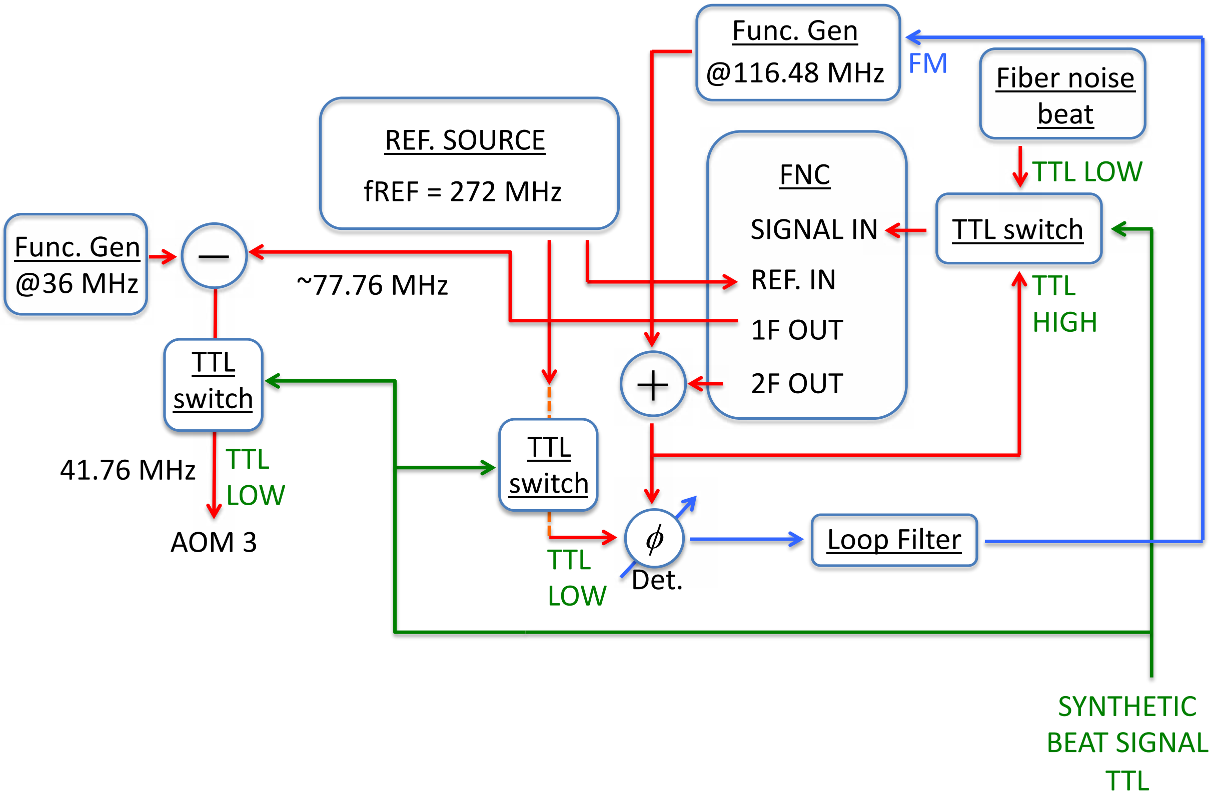

Figure 3.31: 1st order fiber noise servo electronics, which reduces phase excursions when the servo is re-engaged. While AOM3 is on, the 1st order diffracted beam provides a reference for the fiber noise beat, which actuates on the RF to AOM3. AOM3 is shut off before spectroscopy using a TTL. During this time, a synthetic beat signal is fed into the fiber noise input. To get the right phase and frequency input, a servo is used on the synthetic beat signal before AOM3 is extinguished to properly reference it to $f_{ref}$.

perturbations such as temperature changes. This is achieved using a phase lock loop. The reference is mixed with a function generator using a phase detector, and the output passes through a loop filter into the FM modulation port of the function generator. Temperature changes can also alter the mixer output inside the servo box. As a result, it is necessary to keep the fiber noise servo as part of the phase loop to prevent accrued error. We use the $2F$ output of the box for this purpose, which is derived from the internal VCO. The function generator is first mixed with the $2F$ output before being combined with the reference on the phase detector. The output of the mixer is then

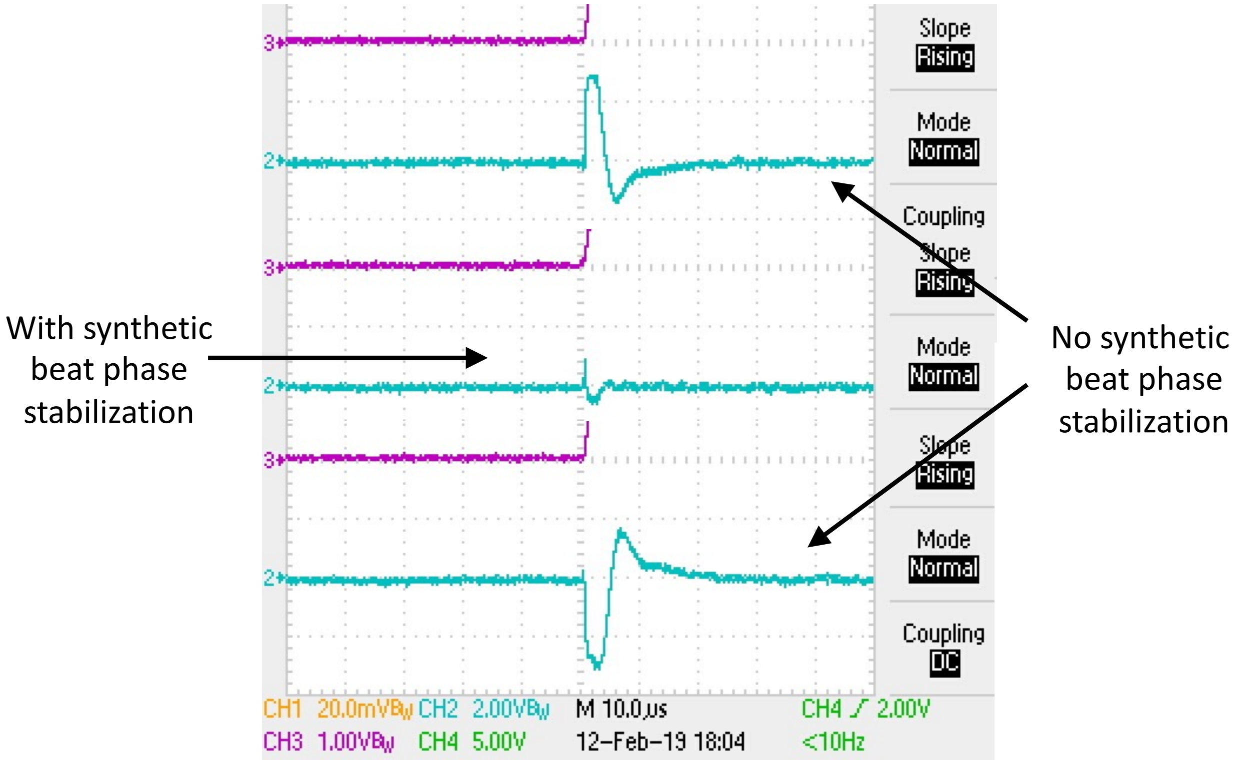

Figure 3.32: Phase transients of the 1st order fiber noise servo once AOM3 is powered and the fiber noise beat is connected to the servo. 3V corresponds to 90 degrees. Here, the purple traces show the TTL that turns AOM3 on, and simultaneously switches the servo input to the fiber noise beat. The blue traces show the in-loop error of the fiber noise servo. The top and bottom traces show the phase deviation without the feedback loop on the synthetic beat's phase. The center trace shows the reduced phase deviation when the loop is engaged. The magnitude of the phase transient with the synthetic beat phase stabilization enabled corresponds to an AOM phase chirp frequency shift of below $10^{-19}$ for a 450 ms Ramsey dark time and 15 ms $\pi/2$ pulses.

used as the synthetic beat signal while AOM3 is off.

To ensure the right phase is fed into the servo once AOM3 is extinguished, the phase lock loop is activated while AOM3 is on. To set the phase to the right value in the servo, the BNC cable length between $f_{ref}$ and the phase detector is varied to minimize the phase transients once the servo is reengaged with the real fiber noise beat. Finally, when AOM3 is off, we put an integrator hold on the clock light intensity servo to avoid integrator wind-up.

The phase transients that occur once AOM3 is re-activated with and without the phase stabilization of the synthetic beat signal are shown in Fig. 3.32. With the phase stabilization engaged, we numerically calculate that the deviations correspond to a sub-$10^{-19}$ clock shift assuming a 450 ms Ramsey dark time and 15 ms $\pi/2$ pulses.

The solution presented thus far in Fig. 3.31 solves issues A.) and B.) discussed above. However, the VCOs in the fiber noise servos have a limited bandwidth of +/- 100 kHz. To increase our scan range so that we have a solution that solves A.), B.) and C.), we simultaneously jump the AOM3 frequency and the reference frequency. This is accomplished, with a few additional electronics, by changing $f_{ref}$, as shown in Fig. 3.33. Instead of a single frequency synthesizer as shown in Fig. 3.31, the AOM3 frequency is mixed with $f_{ref}$ and another function generator. The synthetic beat signal phase lock also needs to be jumped, so $f_{gen}$ is split into two synthesizers - $f_{ref}$ and another signal generator. $f_{ref}$ is then common to the derived AOM3 frequency, the reference frequency for the fiber noise servo, and both inputs of the phase detector, so that a different spectroscopy frequency can be achieved by changing $f_{ref}$ without significantly disturbing the fiber noise servo. This also allows the clock light frequency to be quickly adjusted, since it mostly removes the change in $f_{ref}$ from the error signal.

Any vibrations from the dichroic onwards are common-mode between the lattice and the clock laser. Path length fluctuations between the 1st order FN reference and the dichroic however are uncompensated and must be minimized. To accomplish this, we implement a rigid mounting structure between the two mirrors, as shown in Fig. 3.34. The mirrors are mounted into the structure of the box and the box is hermetically sealed. Furthermore, ND filters can be inserted using a motorized actuator so that the intensity of the clock light at the atoms can be changed by many orders of magnitude without changing the fiber noise beat amplitude. An SRS shutter is implemented inside the box as well and is mounted on a translation stage for alignment purposes.

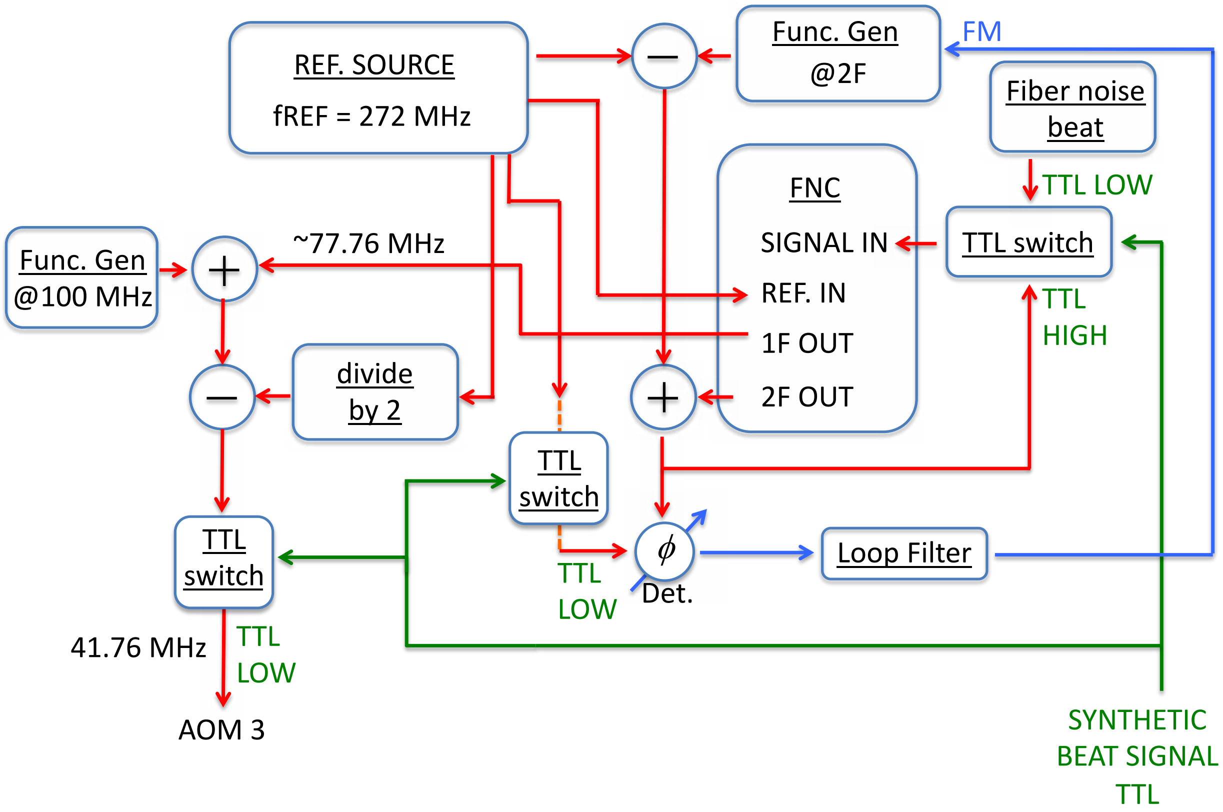

Figure 3.33: Full electronics for the 1st order fiber noise servo, that reduces phase transients when reengaging the servo and provides maximal frequency agility. The electronics feed in a synthetic beat signal with the right phase and frequency when AOM3 is shut off, right before spectroscopy. The electronics also include the ability to scan the beat frequency over a wide range by feeding forward on $f_{ref}$ and the beat signal.

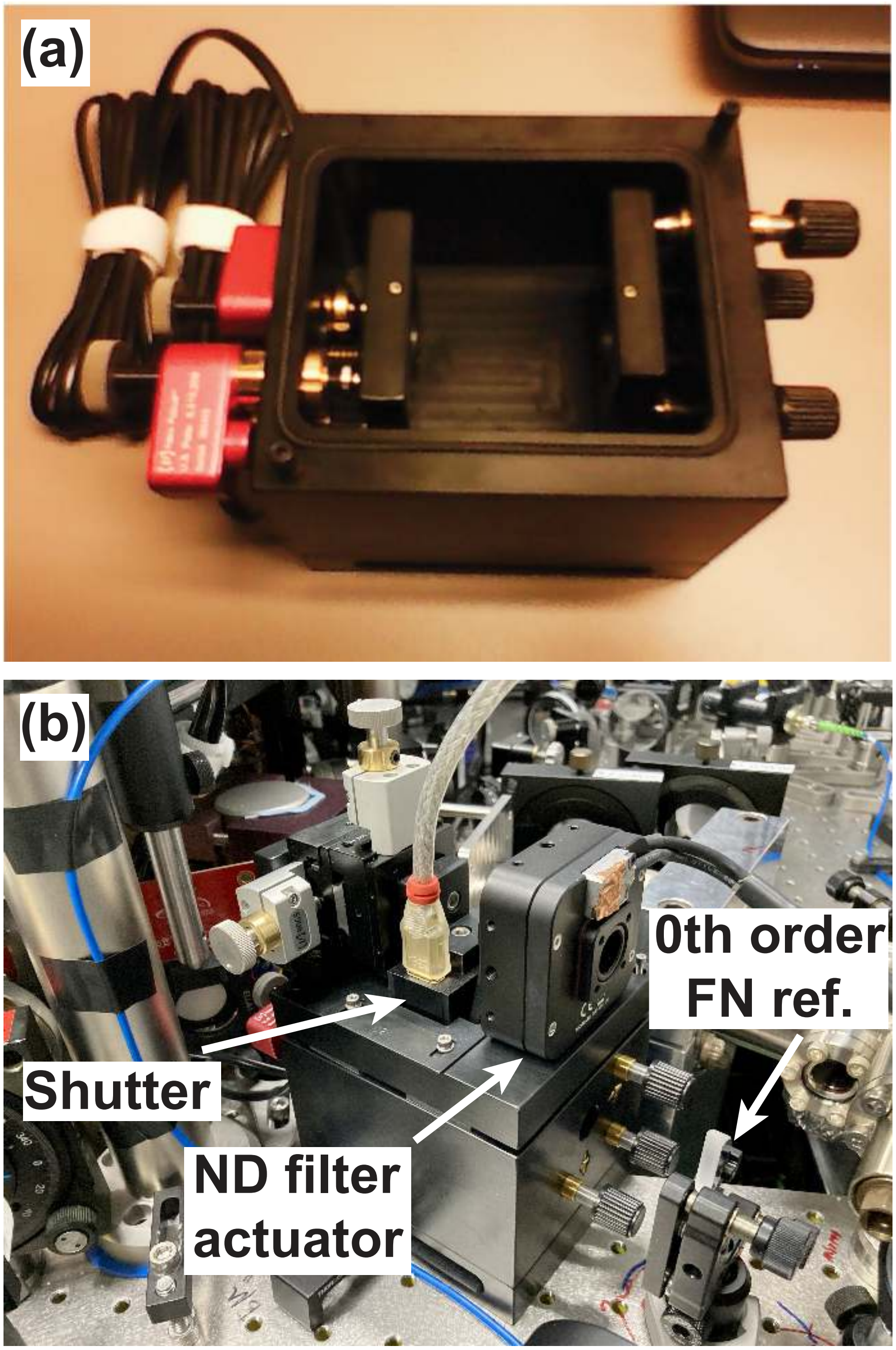

Figure 3.34: Fiber noise box. The first mirror of the box contains the 1st order FN reference, and the last mount contains the lattice retro mirror (a dielectric that reflects 813 nm, transmits 698 nm) that provides a common phase reference for the lattice light and the clock light. ND filters can be inserted inside the box with a motorized actuator, and an SRS shutter is also mounted to the top of the box.

# Chapter 4

# Thermodynamics of a deeply degenerate SU($N$)-symmetric Fermi gas

*The research described in this chapter has been reported in the following publication: Lindsay Sonderhouse*, Christian Sanner*, Ross B. Hutson, Akihisa Goban, Thomas Bilitewski, Lingfeng Yan, William R. Milner, Ana M. Rey and Jun Ye, "Thermodynamics of a deeply degenerate SU(N)-symmetric Fermi gas," Nat. Phys.* **16***, 1216–1221 (2020). * (these authors contributed equally)* [51].

A Fermi-degenerate 3D optical lattice clock has shown a record instrinsic QPN stability of $1.5 \times 10^{-17}/\sqrt{\tau}$. However, due to the extended time spent preparing a Fermi gas of more than 10 s, the corresponding laser noise is high - with the Si cavity's $4 \times 10^{-17}$ thermal noise floor and a few second pulse time, the Dick Effect stability is above $10^{-16}/\sqrt{\tau}$. To make the 3D lattice clock competitive as an independent clock, it is necessary to reduce the preparation time, which is dominated by the evaporative cooling step to reach degeneracy.

Pioneering work by Deborah Jin showed that Pauli blocking reduces the efficiency of evaporative cooling at low temperatures, making it challenging to reach deep degeneracy. As a result, realizing degeneracy in fermions has spurred numerous independent studies over the past two decades by exploiting two-component spin mixtures near a Feshbach resonance. In this chapter, we detail experiments to study SU($N$) interactions [139, 140] in a $^{87}$Sr Fermi gas with $N \leq 10$, and utilize the enhanced interactions for rapid evaporation. While recent studies have started to investigate the intriguing properties of SU($N$) quantum matter, most of the effort so far has been concentrated on the investigation of lattice-confined gases [141, 139, 142, 143, 144, 54, 145]. On the other hand, experiments probing the role of SU($N$) interactions in a regime where a Fermi liquid description is accurate have been limited to non-degenerate [62] or only slightly degenerate [146, 147, 148, 149] gases. Here, we explore a deeply degenerate regime where $N$ Fermi seas coexist and fundamentally modify the system's thermodynamics (Fig. 4.1).

We first outline the challenges of evaporating fermions and motivate using many components with SU($N$) symmetry during evaporation. We then detail our preparation scheme, and demonstrate an unprecedented short time to reach Fermi degeneracy with a temperature $T/T_F = 0.22$, where $T_F$ is the Fermi temperature, achieved in just 0.6 s of evaporation with a laser-cooled sample. Our preparation scheme concludes with a new technique to spin-polarize degenerate Fermi gases without causing light-induced heating, allowing efficient preparation of a low entropy spin-polarized Fermi gas. We then characterize the enhanced interactions caused by a many-component SU($N$)-symmetric gas. In the deeply degenerate regime, we show through precise measurements of density fluctuations and expansion dynamics that the large number $N$ of spin states under SU($N$) symmetry leads to pronounced interaction effects in a system with a nominally negligible interaction parameter. We conclude with a technique to extract $T/T_F$ in an interacting gas by fitting the full density profile of the gas, and with it are able to demonstrate thermometry accurate to one-hundredth of the Fermi energy using a single experimental image.

## 4.1 Cooling fermions to degeneracy

Cooling fermions to degeneracy has historically been more challenging than cooling bosons due to the reduced interaction between identical fermions at low temperatures. Evaporation, a workhorse technique that is used to achieve quantum degeneracy in atomic gases [150, 151], requires atoms to rethermalize through collisions at each step of the evaporation process. As outlined in Chapter 2, the dominant interactions at ultralow temperatures in quantum gases occur via $s$-wave contact scattering, which, for identical fermions, vanishes due to the anti-symmetry of fermionic wavefunctions. As a result, spin-polarized fermions predominantly interact through higher order

$p$-wave interactions. At low temperatures these interactions are suppressed by the height of the centrifugal barrier (10s of $\mu$K in the $^1$S$_0$ state of $^{87}$Sr). Fermi-degeneracy requires temperatures of 100s of nK. Identical fermions can thus not be evaporatively cooled to degeneracy.

### 4.1.1 Common techniques

Thermalization throughout evaporation requires collisions between distinguishable atoms. There are two common techniques to achieve this. First, multi-component fermionic gases can be used. $S$-wave collisions are then allowed between different components. This was first achieved in 1999 in the group of Debbie Jin using a Fermi gas consisting of atoms in two magnetic sublevels of $^{40}$K [70]. However, they observed that the cooling efficiency decreased when the gas became sufficiently degenerate, since rethermalizing collisions were blocked if the final states were occupied by another atom. This limited the efficiency of evaporative cooling at degenerate temperatures. Many cold fermion clouds are also created through sympathetic cooling with a bosonic atom. If bosons are co-loaded into the optical or magnetic trap, they can efficiently evaporate and the fermions will sympathetically cool through collisions with the bosons. Popular combinations include $^7$Li and $^6$Li [68], $^6$Li and $^{23}$Na [152, 153] and $^{40}$K with $^{87}$Rb [154]. There is no Pauli blocking of collisions with a Bose-Fermi mixture, which may improve the evaporation efficiency. However, additional loss can arise due to three body recombination. Extra experimental complexity is also required to create both a Fermi and Bose gas in the same apparatus. Furthermore, the spatial overlap between the BEC and Fermi gas can be poor due to Fermi pressure, which increases the size of the Fermi gas compared to BEC [68]. At this time, Fermi degeneracy has been achieved through evaporation in a range of other atoms and molecules, including but not limited to $^6$Li [155], $^{173}$Yb [156], $^{171}$Yb [112], $^{87}$Sr [157, 158, 49], $^{167}$Er [159], $^3$He [160] and KRb [161].

Although these techniques have allowed systems to reach Fermi degeneracy, evaporation is typically slow, 10s of seconds. This is because rethermalization, which requires a few collisions per particle, is still limited despite the described increase in the $s$-wave collisional parameter. For a two-component gas of equal densities, the elastic collision rate is given by $\Gamma = n\sigma v_{rel}$, where $n$ is the single component density, $\sigma = 4\pi a^2$ is the collision cross section, $a$ is the $s$-wave scattering length, and $v_{rel}$ is the relative velocity between the two colliding particles. The latter, of course, decreases as the temperature is reduced. For a 3D Gaussian distribution, $v_{rel} = \sqrt{16k_BT/\pi m}$. To increase the collision rate (and thus the rethermalization rate), one can increase the scattering length $a$, through for example a Feshbach resonance. However, in alkaline-earth atoms such as Sr, only optical Feshbach resonances exist which are known to be lossy [162]. As a result, one relies on increasing the density of atoms. This however has its own limits - light-assisted collisions limit the attainable initial density [106]. In addition, once degeneracy is reached, Fermi pressure reduces the attainable density per component.

### 4.1.2 Exploiting SU($N$) symmetry for cooling

Binary mixtures are commonly used to reach degeneracy. They are well studied and versatile platforms for quantum simulation capable of exploring a wide parameter space [163, 164]. However, the additional freedom in choosing the number of spin components, $N$, offers unique, largely unexplored opportunities. Using more components enhances the collision rate, and in the limit of large $N$, the gas should behave like a boson [147]. The collision rate, given by $\Gamma = (N-1)n\sigma v_{rel}$, increases linearly with the number of components, $N$. In the $^1S_0$ state, $^{87}$Sr has 10 nuclear spin components. Compared to a 2 component mixture, where each atom only interacts with 50% of the gas, an atom interacts with 90% of the particles in a 10 component gas. This increase in the number of collisional partners enhances the collision rate.

Alkaline-earth fermionic atoms have SU($N$) symmetry in the nuclear spin states of the $^1S_0$ ground and $^3P_0$ clock state, where $N$ can be as large as 10. This symmetry arises from the decoupling between the nuclear and electronic degrees of freedom ($I \cdot J = 0$) intrinsic to the atom's internal ground state manifold and gives rise to SU($N$)-symmetric two-body interactions, characterized by a single nuclear-spin-independent scattering length, $a$ [139, 140]. SU($N$) symmetry is an untapped resource for cooling [142, 165, 166, 167]. Absent of SU($N$) symmetry, a 10 component gas would experience spin changing collisions, which cause heating and loss of atoms. Inelastic spin

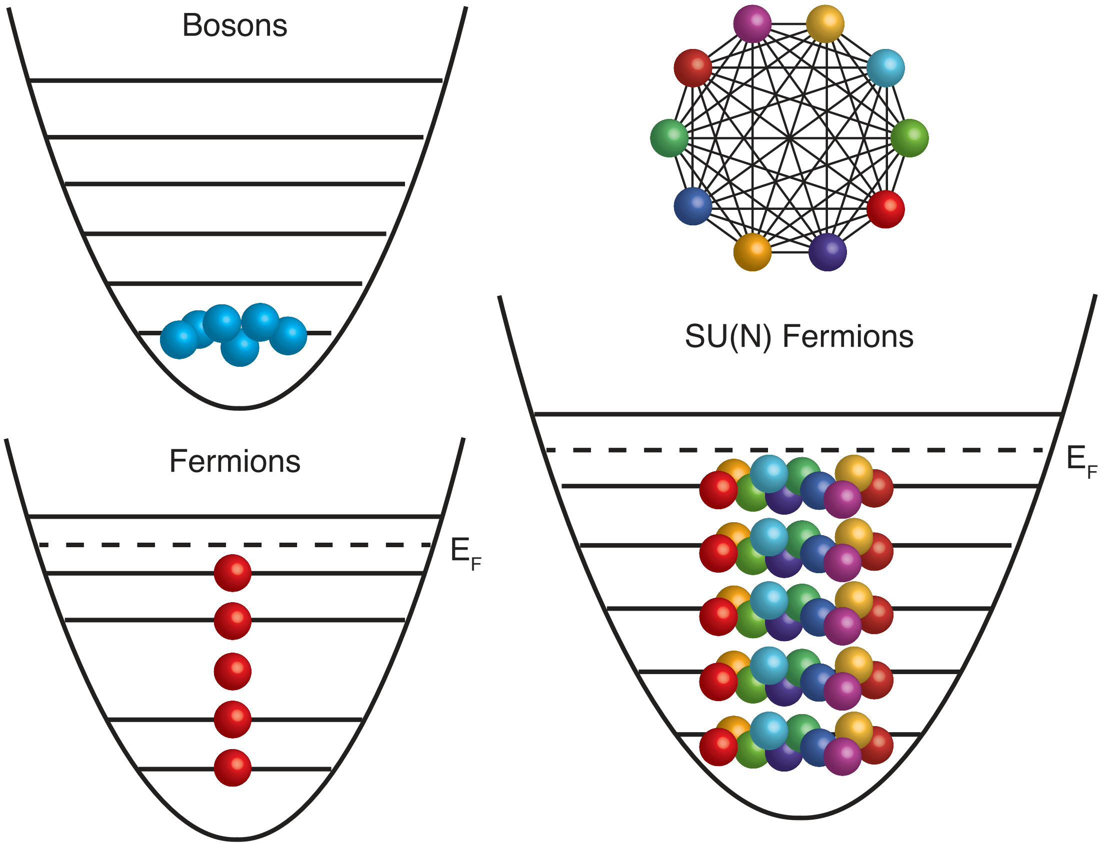

Figure 4.1: Unlike bosons which can occupy the same state, indistinguishable fermions must separate into different energy levels. SU($N$) fermions, on the other hand, can have $N$ particles per state. In a given level, each particle has $(N-1)$ distinct partners, as shown in the top right, and interactions are correspondingly enhanced.

changing collisions are forbidden under SU($N$) symmetry, and thus the enhanced collision and thermalization rate provided by the increased number of components can be fully taken advantage of. SU($N$) symmetry thus provides a tool to efficiently remove entropy from the system.

## 4.2 Rapid cooling of fermions to degeneracy

Our preparation scheme (Fig. 4.2a) begins with standard laser cooling techniques developed for alkaline-earth atoms, as described in [104] and in Chapter 3. After two stages of laser cooling, roughly $10^7$ atoms are cooled to 2 $\mu$K in a far-off-resonant crossed optical dipole trap (XODT) with

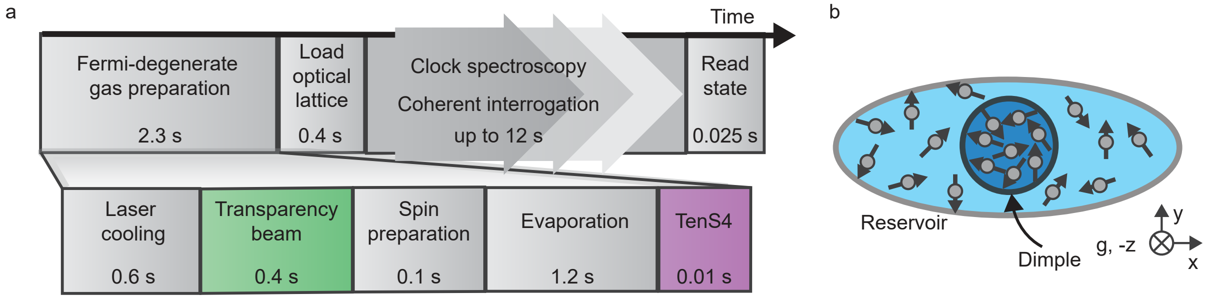

Figure 4.2: **a,** Timing diagram showing stages of the experimental sequence. The times are optimized for clock operation in the band insulating regime. Single spin samples with 20,000 atoms at $T/T_F = 0.2$ are prepared in a 3D optical lattice in under 3 s. **b,** Atoms are confined in a crossed optical dipole trap consisting of a reservoir and dimple trap, and accumulate in a dimple after a "transparency" laser is applied. The transparency and TenS4 lasers overlap with the dimple, and form a 10° angle with respect to gravity.

a sheet-like geometry [49, 157]. A vertically oriented round optical dipole trap (VODT) forms a dimple in a horizontal optical sheet potential that is provided by an elliptically shaped horizontal optical dipole trap (HODT) (Fig. 4.2b). The HODT provides support against gravity and therefore determines the effective trap depth. The stronger confinement in the horizontal plane afforded by the dimple and the large vertical trap frequencies provided by the HODT provide a high initial atomic density, which is ideal for efficient evaporation.

### 4.2.1 Transparency beam

Here we provide a brief summary of the transparency beam, which is discussed in detail in Chapter 3. The density obtainable in a MOT is generally limited by inelastic light-assisted collisions [106] and reabsorption of the cooling light, which leads to an effective repulsion between atoms [107]. To further increase the density inside the dimple beyond these limits, we locally apply an additional laser that renders atoms inside the dimple region transparent to MOT light, a method that was adapted from bosonic $^{84}$Sr [109]. The beam spatially overlaps with the VODT but has a slightly larger waist. This "transparency" laser shifts the cooling light out of resonance, and a high density can then be reached inside the dimple, where atoms collect. Atoms in the dimple

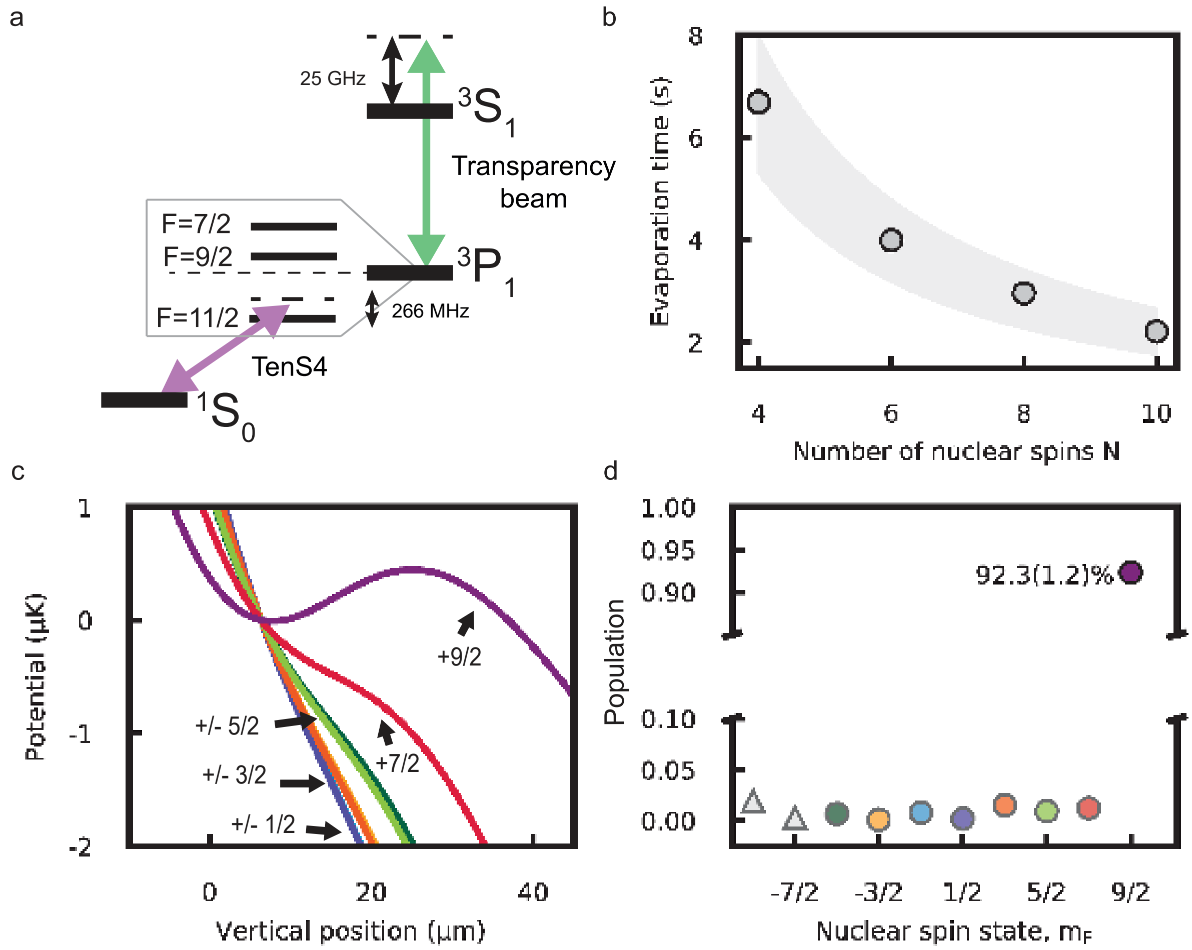

Figure 4.3: **a,** Level diagram depicting the energy transitions for the transparency beam and Tensor Stark Shift Spin Selector (TenS4). **b,** Time to reach $T/T_F = 0.12$ for different numbers of nuclear spin states $N$ participating in evaporation. Each trajectory is prepared with $9.6(8) \times 10^5$ atoms per spin state and $T/T_F = 2.0(1)$. The gray band denotes a $1/(N-1)$ scaling based on the number of initial collisional partners, given a ±20% change in the atom number. The error bars are upper bounds, reflecting the resolution of the sampling grid. **c,** Combined optical and gravitational potential after application of the TenS4 laser. The beam creates a spin-dependent modification of the potential, and only atoms in spin state $\mathrm{m_F} = +9/2$ (purple line) are supported against gravity. Atoms in $\mathrm{m_F} = -9/2$ and $-7/2$ are removed through optical pumping. **d,** Spin purity after application of the TenS4 laser for 10 ms. Atoms are loaded into a 3D optical lattice and the spin state population is determined using selective excitation on the ultranarrow $^1\mathrm{S}_0 - {}^3\mathrm{P}_0$ transition. Gray triangles correspond to spin states that are removed through optical pumping. The error bars denote the standard error of the mean (s.e.m.) and are smaller than the marker size.

thermalize with atoms in a large reservoir part of the trap, which are continually being cooled by the MOT light.

The transparency beam has allowed the production of Bose-Einstein condensation without additional evaporation [109]. However, for fermions additional complications can arise. Compared to bosonic strontium, $^{87}$Sr has additional hyperfine structure, creating a different AC Stark shift for each nuclear sublevel. Transparency from both the trapping and stirring second stage MOT lasers is also required [110]. Accordingly, we use transparency light that is blue-detuned by 25 GHz from the $^3\mathrm{P}_1 - {}^3\mathrm{S}_1$ transition (Fig. 4.3a). This provides an ample shift for all nuclear spin states and keeps spontaneous scattering events beyond relevant experimental time scales. After 400 ms of cooling with the transparency beam, the number of atoms in the dimple saturates with $5 \times 10^6$ atoms, i.e. about 50% of the total atom number, a temperature of $2\,\mu$K, and $\mathrm{T/T_F} = 1.9$. Lower temperatures can be achieved by adjusting the MOT light, but without further improving the phase space density.

### 4.2.2 The SU($N$) edge

The very dense and almost degenerate sample can then be further cooled via forced evaporation. Spin relaxation is absent due to the SU($N$)-symmetric nature of $^{87}$Sr in the $^1\mathrm{S}_0$ ground state; however, over the timescale of seconds we observe a decay of the sample which is well described by a 3-body loss process. The lack of spin relaxation and the small 3-body loss coefficient are further advantageous features of cooling using $^{87}$Sr atoms in comparison to alkalis.

To determine the three-body loss coefficient $k_3$, we load a thermal gas with temperature $T = 1.45\,\mu$K into the dimple part of the recompressed dipole trap. Starting from an initial central density of $n = 3.9 \times 10^{14}$ cm$^{-3}$ we measure over the next ten seconds a decay of the total atom number $\tilde{N}(t)$ as a function of the holding time $t$. The observed atom loss is modeled as

$$\tilde{N}(t) = \tilde{N}(0) - k_3 \int_0^t d\tau \int n^3(\mathbf{r}, \tau) dV \,, \tag{4.1}$$

where $n(\mathbf{r}, t)$ is the total atomic density at position $\mathbf{r}$ and time $t$. The data and corresponding fit are given in Fig.4.4. We find a three-body loss coefficient of $k_3 = 4.7(1.2) \times 10^{-30}\,\mathrm{cm}^6/\mathrm{s}$.

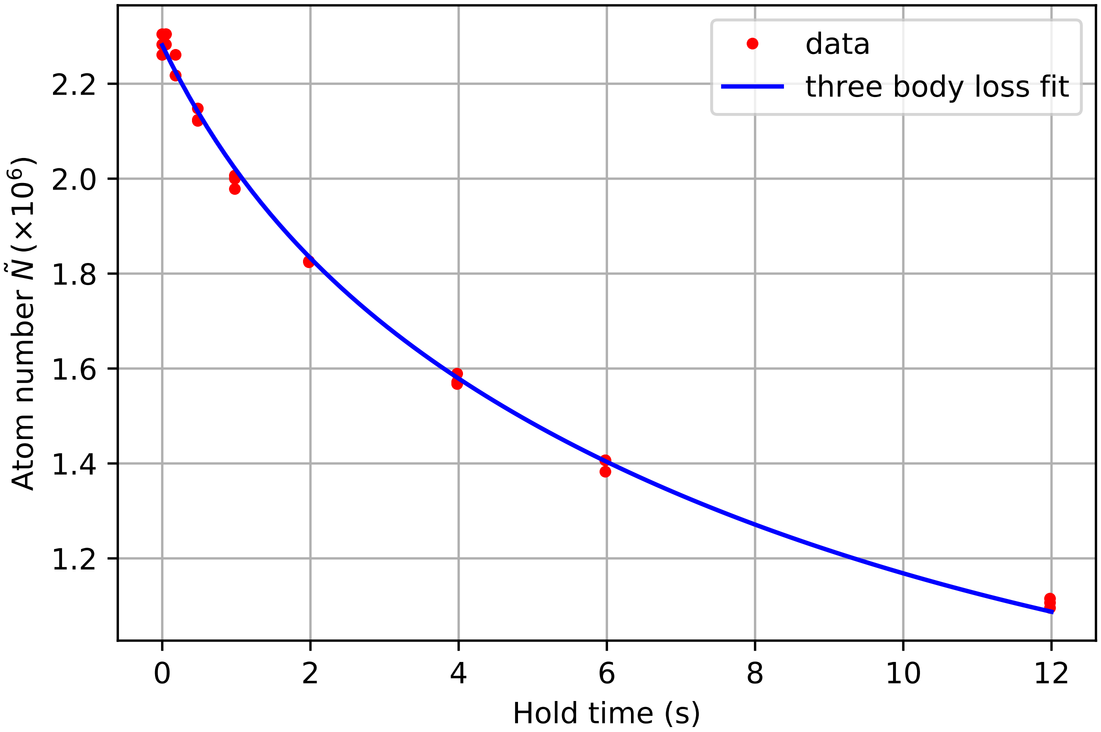

Figure 4.4: Three-body loss measurement, which is used to extract $k_3$.

Interestingly, this is a factor of 2 larger than the recent lattice-based 3-body measurement that showed agreement with a universal Van der Waals model [54]. Discrepancies in 3-body loss between bulk gas measurements and predictions have been seen before [168, 169]. These discrepancies indicate the challenge of accounting for inhomogeneous density profiles in a bulk gas measurement. Under our experimental conditions, single and two-body contributions are expected to be negligible over a time interval of ten seconds. Using a corresponding multivariate model, we find both to be statistically insignificant.

Before quantum degeneracy, the elastic collision rate [156] for a balanced spin mixture with a spatially averaged single-spin density $\bar{n}_\sigma$ is proportional to $(1-1/N)\, N\bar{n}_\sigma$. Assuming a constant atom number per spin state, it is thus advantageous to have all 10 spin states populated. We reach

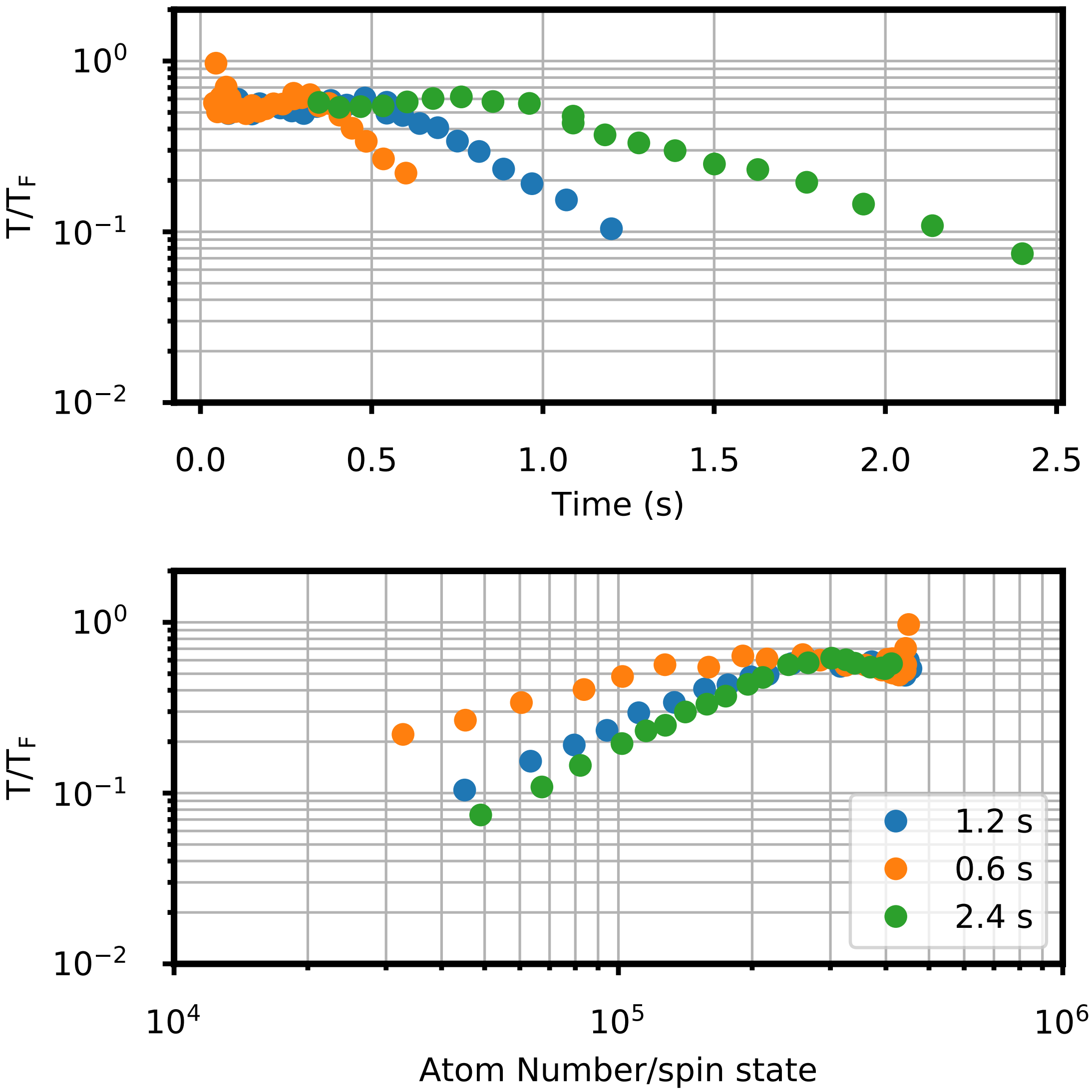

Figure 4.5: Evaporation trajectories for three different total times, 0.6 s (orange), 1.2 s (blue), and 2.4 s (green). The time constant of the ramps are adjusted to increase the total evaporation length while maintaining the same final trap depth. The top plot shows $T/T_F$ as a function of time, and the bottom $T/T_F$ versus atom number per spin state.

an initial collision rate of $1000\,\mathrm{s}^{-1}$ with $N = 10$. Evaporation begins at a trap depth of $20\,\mu$K with trap frequencies in the dimple of $(\nu_\mathrm{r}, \nu_\mathrm{z}) = (100, 800)\,$Hz. The HODT intensity is then reduced in a two-stage ramp down to a final trap depth of a few 100 nK with trap frequencies of $(100, 200)\,$Hz.

After 600 ms of evaporation, we reach $T/T_F = 0.22$ with $3 \times 10^4$ atoms per spin state. Slower evaporation leads to lower temperatures, and we achieve $T/T_F = 0.07$ with $5 \times 10^4$ atoms per spin

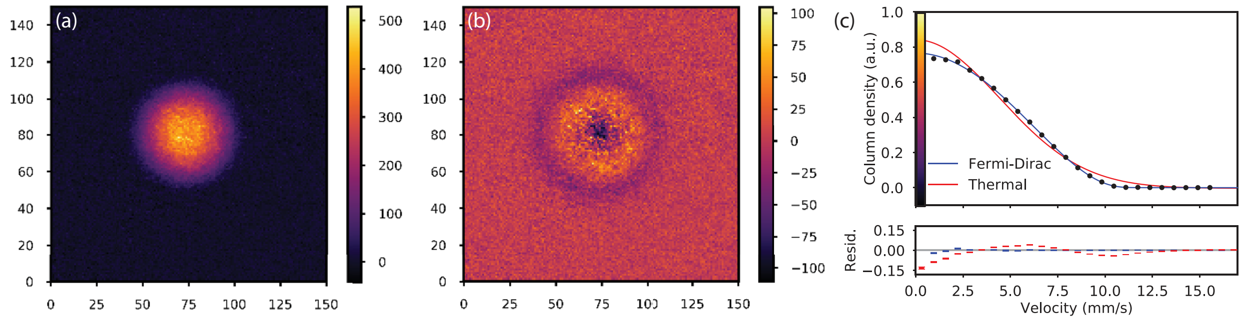

Figure 4.6: **a,** Density profile of a Fermi-degenerate gas after 10 ms time-of-flight with 10 spin states and $T/T_F = 0.07$. **b,** Residuals after fitting the cloud to a Maxwell-Boltzmann distribution. Color bars in each subplot correspond to the number of atoms per 1.37 $\mu\text{m}^2$. **c,** Radially averaged fit of the density profile given in **a** to a Maxwell-Boltzmann distribution and a Fermi-Dirac distribution. The thermal distribution has larger residuals than the Fermi-Dirac fit.

state after evaporating for 2.4 s. Trajectories of three different lengths are given in Fig. 4.5 [1] . At such low temperatures, the normally modest deviation from a thermal distribution is striking, see Fig. 4.6. Such fast trajectories mark a considerable improvement over previous evaporation results, where evaporation stages took around 10 s [49].

We observe an approximate $1/(N-1)$ scaling of the total evaporation time with the number of spin states participating in evaporation as shown in Fig. 4.3b, reflecting the reduction in collisional partners for smaller $N$. Here, each sample is prepared with the same atom number per spin state and $T/T_F$, and is measured after reaching $T/T_F = 0.12$. The final atom number per spin state is reduced by roughly a factor of two as $N$ is decreased.

## 4.3 Spin Manipulation

Here we summarize the TenS4 technique, which is discussed in more detail in Chapter 3. In order to manipulate the spin composition of the atom sample and prepare a spin-polarized gas, we apply a spin-selective optical potential to the atoms after evaporation. While past procedures

---

[1] The data shown in Fig. 4.3 (b) and Fig. 4.5 are extracted using a full density profile fit that includes a mean-field interaction term, as described later in this chapter. Corrections to $T/T_F$ are around 20% at the lowest temperatures. Using a non-interacting fit, our minimum extracted $T/T_F$ is 0.05.

have used optical Stern-Gerlach techniques to separate out spin states during time-of-flight [111, 112, 113], our method, the Tensor Stark Shift Spin Selector (TenS4), creates a spin-selective force on the atoms from the tensor Stark shift of a laser while the atoms remain trapped in the XODT. Atoms with the same $|\mathrm{m_F}|$ experience a small differential force due to an applied magnetic field of 5 G. This magnetic field is too small to fully remove $\mathrm{m_F} = -9/2$ and $-7/2$. We thus conventionally remove these spins via optical pumping prior to evaporative cooling. For the SU($N$) measurements in the following section, however, we always use all 10 nuclear spins. The TenS4 beam is offset from the atoms such that the AC Stark shift varies across the atomic sample by hundreds of nK, which causes a spin-dependent modification in the combined optical and gravitational potential of the atoms (Fig. 4.3c). The TenS4 laser is blue-detuned from the $^3\mathrm{P}_1$, F = 11/2 transition by 266 MHz (Fig. 4.3a), where the polarizability from $^3P_1$, F = 11/2 cancels the polarizability from $^3\mathrm{P}_1$, F = 9/2 for nuclear spin state $\mathrm{m_F} = +9/2$. As a result, atoms with $\mathrm{m_F} = +9/2$ are unaffected by the TenS4 laser while all other spin states feel a repelling force.

The spin purity after applying the TenS4 laser for 10 ms is measured by loading the atoms into a deep 3D optical lattice. The spin population for each nuclear spin state is then read out through selective $\pi$-pulse excitations on the clock transition. We measure 92% of the atoms in the target $\mathrm{m_F} = +9/2$ state, as shown in Fig. 4.3d, and an atom number of $3.3 \times 10^4$ after application of the TenS4 beam, in rough agreement with $1/8^{\mathrm{th}}$ of the initial atom population of $2.5 \times 10^5$. The temperature of the sample heats by only ∼10%. Our technique provides spin-state selectivity without optical excitation and as a result does not cause light-induced heating, overcoming issues typically associated with optical pumping schemes. The spin distillation technique enables us to load a single spin with $T/T_F = 0.2$ into a 3D optical lattice with a total preparation time under 3 s (Fig. 4.2 a).

## 4.4 Characterization of SU($N$)-enhanced interactions

Having prepared a high-density deeply degenerate SU(10) gas, we demonstrate in this section that a nominally very weakly interacting quantum system with interaction parameter $k_F a \ll 1$, where $k_F$ is the Fermi wave vector, can develop striking interaction effects due to SU($N$) enhancement. The nuclear spin degree of freedom substantially modifies the character of the gas towards an interacting multi-component Fermi liquid with subtle consequences for correlation analysis and thermometry. We first describe our experimental measurements of the compressibility, the expansion dynamics, and anisotropic features of expanded gas clouds, and conclude with a summary of the interacting theoretical model we use to describe the measurements.

### 4.4.1 Isothermal compressibility

In order to investigate this intriguing quantum system and illuminate the role of SU($N$) symmetry, we perform measurements that characterize the system's thermodynamics. A key quantity in this context is the isothermal compressibility $\kappa = \frac{1}{n^2}\frac{\partial n}{\partial \mu}$, where $n = N\, n_\sigma$ denotes the particle density and $\mu$ the chemical potential. For $^{87}$Sr with $a = 97 a_{\mathrm{Bohr}}$, the contact interactions are repulsive and one expects a decreased compressibility compared to an ideal Fermi gas with compressibility $\kappa_0$. For a homogeneous gas in the zero temperature limit, $\kappa_0 = 3/(2 N n_\sigma E_F)$ with Fermi energy $E_F$ and Fermi wave vector $k_F = (6\pi^2 n_\sigma)^{1/3}$. One finds to first order in $k_F a$ that [170]

$$\kappa_0/\kappa = 1 + (N-1)\, 2 k_F a/\pi\,. \tag{4.2}$$

Therefore, the symmetric $N$-component system is effectively $(N-1)$-fold more repulsive than a typical two spin component Fermi liquid [171]. The favorable scaling with number of internal levels has to be contrasted with the weak dependence of the compressibility on the atom number per spin state in a harmonically trapped gas, where $k_F \propto N_\sigma^{1/6}$. All experiments reported in the following were carried out with spin-balanced 10-component samples. By focusing on this maximum N-limit, we achieve the most pronounced interaction effects and can perform the most sensitive experiment-theory comparisons.

Experimentally, we access the compressibility of the gas by measuring its local density fluctuations. Fluctuations, either thermal or quantum, are the drivers of phase transitions, and are

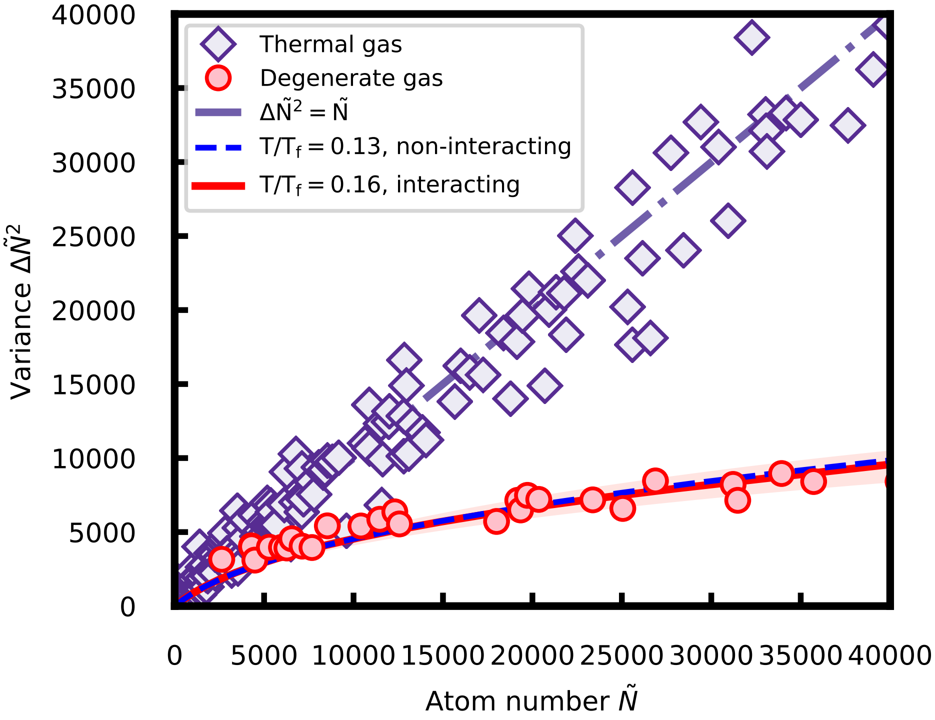

Figure 4.7: Density fluctuations after 11.5 ms time-of-flight for a degenerate cloud with $N = 10$ nuclear spin states (red circles). The data is fit using an SU($N$) interacting model to extract $T/T_F = 0.16$ (red solid line), with shading representing a $2\sigma$ uncertainty of $\pm 0.02\,T/T_F$. Fitting the data instead to a non-interacting ideal Fermi gas gives $T/T_F = 0.13$ (blue dashed line), showing an interaction-induced suppression of ~20%. The difference between the interacting and non-interacting fits is much less than the scatter in the data, highlighting the indistinguishability between interacting and non-interacting systems by measuring density fluctuations alone at the given signal-to-noise ratio. The total density fluctuations are 25% of that of the thermal gas. A thermal cloud (purple triangles) reproduces Poisson statistics with $\Delta\tilde{N}^2/\tilde{N} = 1$ (purple dot-dashed line). Each data point is obtained by looking at the atom number variation and mean in a subregion of the cloud for a series of images.

sensitive to the underlying phase of matter, its quasi-particles and interactions. The fluctuation-dissipation theorem states that the thermally driven fluctuations of a thermodynamic variable are fundamentally related to the conjugate external force through the susceptibility [84]. Considering a small subvolume of the gas cloud containing on average $\tilde{N}$ atoms, the corresponding generalized force is the local chemical potential $\mu$. The fluctuation response theorem then states that

$$\partial\tilde{N}/\partial\mu = \frac{1}{k_B T}(\Delta\tilde{N})^2 \,. \tag{4.3}$$

Through Maxwell's relations we can arrive at $\partial\tilde{N}/\partial\mu = \kappa\tilde{N}^2/V$ [85]. The relative number fluctuations $\eta = \Delta\tilde{N}^2/\tilde{N}$ are therefore related to the susceptibility $\partial\tilde{N}/\partial\mu$ via $\eta = nk_BT\kappa$, where $k_B$ is the Boltzmann constant. The compressibility elucidates the underlying statistics of the gas. The equation of state of a classical ideal gas dictates $\eta = 1$, reflecting the Poisson statistics of a thermal sample. A Fermi gas on the other hand is incompressible due to Fermi pressure. As a result, one expects a reduced compressibility compared to a thermal sample; for a deeply degenerate ideal Fermi gas, $\eta = 3/2\; T/T_F$. These sub-Poissonian fluctuations reflect the degeneracy pressure in the gas.

#### 4.4.1.1 Virial expansion

To theoretically derive the compressibility under SU($N$) interactions at finite temperature, a virial expansion technique can be used in addition to directly calculating the density distribution of the gas (see Section 4.4.4) [172, 173, 174]. Here, the grand partition function of a many-body quantum system is expressed using a series of perturbative functions that depend on the statistics of the gas. We start with the expression for the chemical potential of a homogeneous Fermi gas at low temperature and with weak interactions [175]:

$$\begin{aligned}\mu(n,T,a) = E_F \bigg[ 1 - \frac{\pi^2}{12}(T/T_F)^2 + \frac{4}{3\pi}(N-1)k_Fa \\ + \frac{4(11-2\ln(2))}{15\pi^2}(k_Fa)^2(N-1)\bigg] + CT^2a^2\,,\end{aligned} \tag{4.4}$$

where $C$ is a constant independent of $n$. The compressibility, $\kappa = \frac{1}{n^2}\frac{\partial n}{\partial \mu}$, can then be evaluated from the dependence of $n$ on the Fermi parameters.

For simplicity we only keep terms up to first order, to obtain for the number fluctuations

$$\Delta\tilde{N}^2/\tilde{N} = k_BTn\kappa = \frac{3}{2}\frac{T/T_F}{1+\frac{2}{\pi}(k_Fa)(N-1)}\,. \tag{4.5}$$

This suggests that even in the $k_Fa \ll 1$ limit the interaction effects become non-negligible due to the $(N-1)$-fold SU($N$) enhancement.

#### 4.4.1.2 Density fluctuation measurements

Our density fluctuation measurements are performed on expanded gas clouds. After abruptly turning off the harmonic confinement ($\nu_r = 130\,\mathrm{Hz}, \nu_z = 240\,\mathrm{Hz}$) the quantum degenerate sample that contains in total $10 \times 59000$ atoms such that $k_F a = 0.07$ freely expands over 11.5 ms. We then obtain line-of-sight integrated density profiles via absorption imaging. Following the protocol described in [86, 87] we run this experiment in a repeated fashion. Each image is broken up into small subregions, and the images are normalized such that the total atom number is equal for each image. For each projected subregion of the cloud containing on average $\tilde{N}$ atoms we can measure the statistical variance $\Delta\tilde{N}^2$. Fig. 4.7 shows the results obtained from 400 individual images together with a calibration line derived from noise measurements on a thermal gas. Pronounced noise suppression down to about 25% of thermal noise in the center of the sample indicates that the gas is deeply in the quantum regime.

To quantitatively interpret the noise data beyond first order including both Fermi pressure and SU($N$)-enhanced interactions, we calculate the expected line-of-sight integrated number fluctuations based on a kinetic approach [176, 177], using the collisional Boltzmann-Vlasov equation with a mean-field interaction term (see Section 4.4.4 for more details). The Boltzmann-Vlasov equation describes the evolution of the semi-classical phase-space distribution $f(\mathbf{r}, \mathbf{p})$ with position $\mathbf{r}$ and momentum $\mathbf{p}$:

$$\left(\partial_t + \frac{\mathbf{p}}{m} \cdot \nabla_{\mathbf{r}} - \nabla_{\mathbf{r}} \left[U(\mathbf{r}) + V_{\mathrm{MF}}(\mathbf{r})\right] \cdot \nabla_{\mathbf{p}}\right) f = I_c(f)\,. \tag{4.6}$$

The phase-space distribution evolves due to ballistic motion of particles (second term), the forces due to the harmonic trapping potential, $U = m/2 \sum_i (2\pi\nu_i)^2 r_i^2$, the mean field interactions, $V_{\mathrm{MF}} = g(N-1)n$ with $g = 4\pi\hbar^2 a/m$, and the collisional integral, $I_c(f)$ [177, 96]. Solving the Boltzmann-Vlasov equation in equilibrium and for finite temperature allows us to obtain the real space density, $n(\mathbf{r})$, from which we can compute the compressibility, and thus the number fluctuations in trap and after time of flight. By fitting this model to the observed fluctuations, we extract a temperature $T/T_F = 0.16 \pm 0.01$. At these low temperatures, $I_c(f)$ plays no role.

To illustrate the interaction-induced compressibility change we additionally fit a noninteracting model to the noise data, which gives an apparent $T/T_F = 0.13 \pm 0.01$, indicating a ∼20% compressibility reduction due to interactions. More precisely, we find that the compressibility in the center of the trap is reduced by 18% compared to a non-interacting gas at the same density and temperature. This percentage is comparable to the ratio of 21% between the interaction energy in a small volume $V$ at the centre of the cloud, $g/2\,(N-1)n_\sigma^2 V$, and the total energy of a noninteracting Fermi gas at the same density, $3/5\,E_F n_\sigma V$. Clearly, without prior knowledge of the interaction parameter, one cannot distinguish between a colder or more repulsively interacting system. Repulsive interactions mimic Fermi statistics, each acting to reduce the density where it is highest, in the center of the gas. Having a full thermodynamic description at hand we also perform global profile fits of the acquired images to numerically calculated density distributions and find $T/T_F = 0.17 \pm 0.01$. That is, using the self-consistent solution of Equation 4.13 after time of flight provides us with a density distribution, which we can use to fit the full density profile of the gas with $T/T_F$ as a free parameter. This approach, which we discuss in more detail later in Section 4.4.3 (and as shown in Fig. 4.9), allows measurement of the temperature in the presence of interactions in a single measurement. This is in contrast to measuring local density fluctuations, which requires taking hundreds of images to get good statistics. The temperature derived by fitting the full density profile is in good agreement with the temperature derived from density noise measurements. We want to emphasize again that even though the two underlying physical mechanisms that lead to the observed suppression of density fluctuations are fundamentally different, it is impossible to distinguish these two contributions by performing density noise measurements alone at the given signal-to-noise ratio.

### 4.4.2 Expansion dynamics

To unambiguously distinguish between temperature and interaction effects, we study the expansion dynamics of the cloud after being released from the trap. Interactions provide an ad-

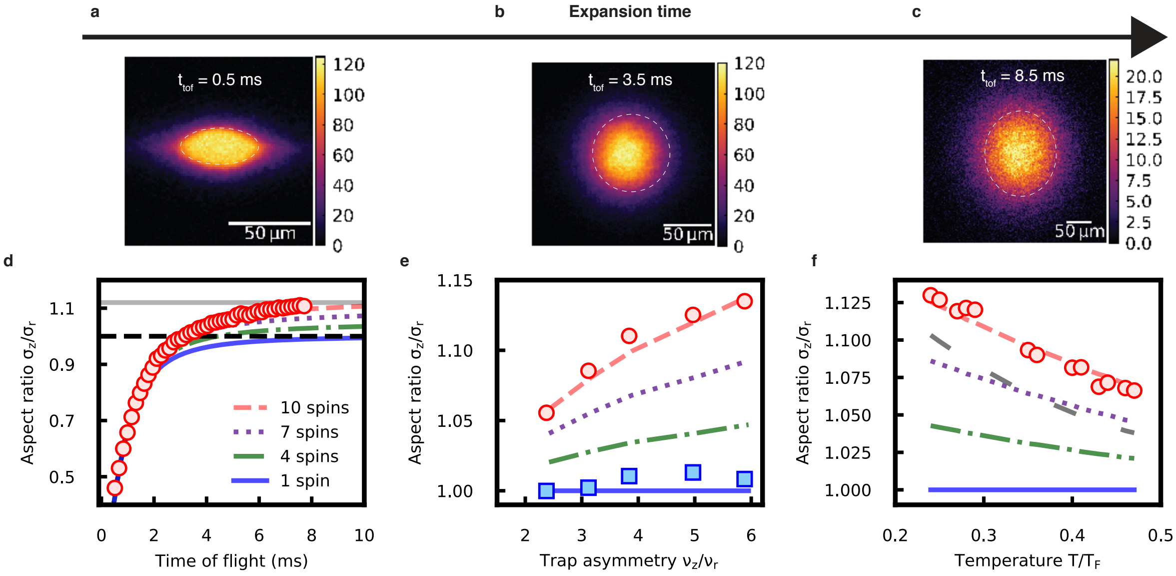

Figure 4.8: **a, b, c,** Line-of-sight integrated atomic density for 0.5 ms, 3.5 ms, and 8.5 ms time-of-flight ($t_{tof}$) expansion times. The colorbar's unit corresponds to the number of atoms per 1.37 $\mu$m$^2$. **d,** Aspect ratio of a cloud of cold atoms with N = 10 nuclear spin states released from an optical dipole trap for variable expansion times (red circles). After $\sim$3 ms, the aspect ratio passes through unity (black dashed line), a clear signature of interactions in the gas. At long times, the sample approaches an aspect ratio of 1.12 (grey line). The sample has an initial trap asymmetry of $\nu_z/\nu_r = 6.4$. In panels **d - f**, the expected aspect ratio is shown for N = 10 (red dashed line), N = 7 (purple dotted line), N = 4 (green dash-dotted line), and N = 1 (blue solid line) nuclear spin states. **e,** Aspect ratio versus initial trap asymmetry of a degenerate gas for N = 10 (red circles) and N = 1 (blue squares) spin states after time-of-flight expansion for 15.5 ms. **f,** Aspect ratio versus temperature. Data is shown with roughly the same atom number per shot. The data is fit using an interacting model that includes both a mean-field interaction and an additional collisional term. Neglecting the collisional term fails to explain the results (gray dashed line). All error bars represent the s.e.m. and are smaller than the marker size.

ditional release energy during expansion that is mapped to momentum after long time-of-flight. Interactions preferentially push atoms along the direction of the largest density gradient. As a result, the initial trap asymmetry is inverted and this conversion produces an anisotropic distribution after long time-of-flight, see Fig. 4.8a-c. The expansion can be described via scaling solutions of the time-dependent Boltzmann–Vlasov equation (see Section 4.4.4) [178, 179, 76, 180]. Unlike in trap, the effect of interactions on the density after expansion cannot be partly captured by a lower temperature, and result in a non-unity aspect ratio at long times. This is in contrast to a non-interacting gas, where expansion occurs ballistically so that at after long time-of-flight, the cloud reflects the isotropic momentum distribution even if the confining potential is anisotropic.

Fig. 4.8d displays the aspect ratio of a SU(10) atom cloud measured after variable expansion times $t_{\text{tof}}$ out of a harmonic trap with $\nu_r = 125$ Hz and $\nu_z = 800$ Hz. The sample contains 50,000 atoms per spin component at $T/T_F = 0.16$. Initially, the atom cloud reproduces the trap's asymmetry. As $\nu_{r,z}t_{\text{tof}}$ becomes larger than one, the spatial density distribution is more and more determined by the momentum distribution in the gas. Observing an inversion of the aspect ratio beyond 1 is an unambiguous signature that interactions have modified the isotropic momentum distribution during time-of-flight [97].

To further explore this behavior, in Fig. 4.8e we present measurements of the expanded cloud aspect ratio ($t_{\text{tof}} = 15.5$ ms) as a function of the confinement asymmetry for a 10-component gas and a spin-polarized gas, both at $T/T_F = 0.16$. In the non-interacting case $N = 1$ (blue data points), the aspect ratio is always 1 as expected in the long time-of-flight limit. Finally, in Fig. 4.8f we show the dependence of the observed cloud aspect ratio on $T/T_F$ for a fixed initial confinement with $\nu_r = 130$ Hz and $\nu_z = 725$ Hz at a fixed $t_{\text{tof}} = 15.5$ ms. Atomic interactions add a mean field term $\propto a$ and a collision term $I_c(f) \propto a^2$, see Equations 4.10 and 4.12. The latter, however, is only relevant in the presence of high collision rates, and, in fact, its pronounced effect is observed when the gas is relatively hot (Fig. 4.8f). In comparison, at low temperatures the interaction energy and kinetic energy become comparable, and the collisional rate is suppressed by Fermi statistics.

All measurements are well reproduced by our quantitative model, see Section 4.4.4. Since our model allows us to extract the density distribution of the gas, we can also easily extract the aspect ratio. To emphasize the role of $N$ in modifying the dynamics, we also plot in Fig. 4.8d-f the behavior expected for $N = 1$, 4, 7, 10 spin states using the validated theoretical model. Because the aspect ratio measurements, which are extracted through Gaussian fits, are fairly immune to most imaging artifacts, they can be exploited to perform precise thermometry of the interacting

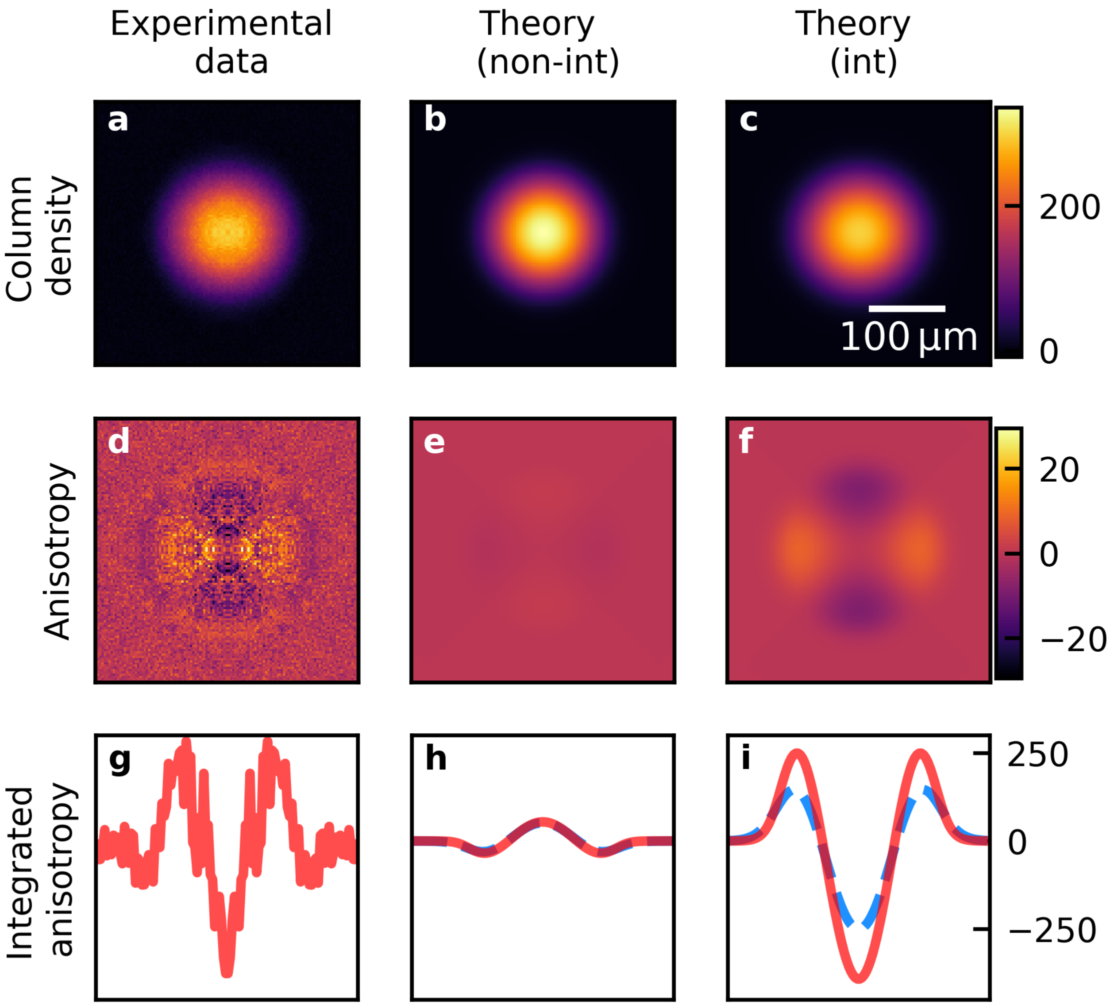

Figure 4.9: **a,b,c,** Line-of-sight integrated atomic density $n(x,z)$ after time-of-flight for a single shot of the experimental data, non-interacting theory, and interacting theory, respectively. The colorbar's units represent the number of atoms per 1.37 $\mu$m$^2$. Images are shown with an initial trap asymmetry of $\nu_z/\nu_r = 1.8$ and $T/T_F = 0.17$. **d,e,f,** The anisotropy of the cloud, defined as $n(x,z) - n(z,x)$, is shown in the second row, where lobes are clearly visible for clouds with interactions. To improve the signal-to-noise ratio the experimental image is first symmetrized by reflection along the $x$ and $z$-axes. **g,h,i,** If the anisotropy is integrated along one direction, peaks symmetric to the center of the gas appear for the interacting distribution that are sensitive to temperature, while the non-interacting signal shows a different signature that displays only weak temperature dependence. Here, the red lines show the integrated anisotropy of the images in (d-f), while the blue dashed lines in (h) and (i) show the integrated profile for a 50% higher temperature.

Fermi gas.

### 4.4.3 Anisotropic density features

Beyond their directly visible manifestation through cloud ellipticity one can also identify interaction-modified expansion dynamics in the full density profile of the gas by carefully inspecting high-signal-to-noise absorption images. Fig. 4.9 illustrates that a presumably round line-of-sight integrated density profile $n(x, z)$ still contains a systematic interaction signature. After a time-of-flight time of 11.5 ms, we observe density profiles that at first sight appear circularly symmetric (first row) for the experimental data (first column), and the noninteracting (second column) and the interacting (third column) model. Interactions are revealed in the transpose-anisotropy of the density distribution, defined as $n(x, z) - n(z, x)$, shown in the second row. The transpose anisotropy removes any common mode features between the two axes. Both the experimental data and the interacting model exhibit pronounced lobes that are not visible in the non-interacting case. Finally, a one-dimensional measure of this anisotropy can be defined by integrating over one of the axes ($\int dz(n(x, z) - n(z, x))$) as shown in the third row. In the integrated transpose-anisotropy we observe peaks symmetric to the centre of the cloud whose height are sensitive to $T/T_F$ for the experimental data and the interacting model, whereas in the noninteracting case this anisotropy is significantly reduced, inverted and insensitive to temperature. The small residual anisotropy in the non-interacting theory reflects the initial asymmetric trap, whose effect on the cloud after long time-of-flight is minimal. These results reveals the interacting nature of the Fermi gas in a single absorption image and can serve as a precise temperature probe. In practice, to extract $T/T_F$ in an interacting gas, we minimize the least squares residuals between the integrated anisotropy of an experimental image and the simulated image with $T/T_F$ used as a single free parameter.

### 4.4.4 SU($N$) interacting model

In this section, we detail the theoretical model used to describe the density fluctuation and anisotropic expansion measurements. Study of a multi-component interacting system with SU($N$) symmetry is a logical extension of studying interacting two-component systems, as detailed in

Chapter 2. To study the collective behaviour of the quantum gas, we use a kinetic approach [176, 177]. Interactions can be approximated as two-body s-wave contact interactions. The total interaction energy is given by

$$\begin{aligned} H_{int} &= \frac{g}{2}\sum_{\sigma,\sigma'}\int d^3\mathbf{r}\hat{\psi}^\dagger_\sigma(\mathbf{r})\hat{\psi}^\dagger_{\sigma'}(\mathbf{r})\hat{\psi}_{\sigma'}(\mathbf{r})\hat{\psi}_\sigma(\mathbf{r}) \\ &= \frac{gN(N-1)}{2}\int d^3\mathbf{r}n^2_\sigma(\mathbf{r})\,, \end{aligned} \tag{4.7}$$

where $g = 4\pi\hbar^2 a/m$, the sum includes all $N$ spin components, and in the final step we assume the single component density $n_\sigma(\mathbf{r}) = \hat{\psi}^\dagger_\sigma(\mathbf{r})\hat{\psi}_\sigma(\mathbf{r})$ is the same for each component. Note that this equation is drastically simplified compared to a general multi-component interaction Hamiltonian due to SU($N$) symmetry[2] .

The total Hamiltonian for a single component is then

$$H_\sigma = \int d^3\mathbf{r}\,\hat{\psi}^\dagger_\sigma(\mathbf{r})\left(-\frac{\nabla^2}{2m} + U(\mathbf{r})\right)\hat{\psi}_\sigma(\mathbf{r}) + \int d^3\mathbf{r}\hat{\psi}^\dagger_\sigma(\mathbf{r})\Big(g(N-1)n_\sigma(\mathbf{r})\Big)\hat{\psi}_\sigma(\mathbf{r})\,, \tag{4.8}$$

where the first term describes the kinetic and potential energy of the fermions, which are confined by a harmonic trapping potential $U = m/2\sum_i(2\pi\nu_i)^2x_i^2$. The above equation looks like the Hamiltonian for a single species in an external potential with an additional effective potential given by the mean field energy:

$$V_{MF} = g(N-1)n_\sigma(\mathbf{r})\,, \tag{4.9}$$

which is $(N-1)$ more repulsive than a two-component gas (see Chapter 2).

To look at the dynamics, we use the semiclassical transport Boltzmann-Vlasov equation:

$$\Big(\partial_t + \frac{\mathbf{p}}{m}\cdot\nabla_\mathbf{r} - \nabla_\mathbf{r}\left[g(N-1)n_\sigma(\mathbf{r}) + U(\mathbf{r})\right]\cdot\nabla_\mathbf{p}\Big)\,f = I_c[f]\,. \tag{4.10}$$

The single component phase-space distribution $f$ evolves due to ballistic motion (second term), and from forces due to the harmonic trapping potential $U(\mathbf{r})$ and the mean-field interactions with strength $V_{MF} = g(N-1)n_\sigma(\mathbf{r})$. Finally, collisions during expansion are described by the integral $I_c[f]$ [177].

---

[2] For a theoretical description of a multi-component Fermi gas without SU($N$) symmetry, see Ref. [181].

Collisions can be approximated using the relaxation time approximation as [96]

$$I_c[f] = -\frac{f - f_{le}}{\tau} \,, \tag{4.11}$$

where $f$ approaches the local equilibrium state $f_{le}$ over a characteristic relaxation time $\tau$. We can follow [94, 182] and approximate the relaxation time as

$$(2\pi\nu\tau)^{-1} = (N-1)\frac{4}{5\,3^{1/3}\pi}\left(\tilde{N}^{1/3}\frac{a}{a_{ho}}\right)^2 F_Q(T/T_F)\,, \tag{4.12}$$

where $F_Q(T/T_F)$ is a universal function given by an integral [94]. At low temperatures, collisions are Pauli blocked and thus $F_Q$ vanishes as $(T/T_F)^2$, a signature of Fermi statistics. $F_Q$ is of order 1 in the intermediate temperature regime, and vanishes as $(T/T_F)^{-1}$ at higher temperatures. It is thus only in the intermediate temperature region where collisions play a significant role.

To obtain the phase space density in-trap, we solve the Boltzmann-Vlasov equation in equilibrium (i.e. with $I_c[f] = 0$ and $\partial f/\partial t = 0$). This gives us

$$f(\mathbf{r}, \mathbf{p}) = \frac{1}{e^{\beta\left(\frac{p^2}{2m} + U(\mathbf{r}) + g(N-1)n_\sigma(\mathbf{r}) - \mu\right)} + 1} \,. \tag{4.13}$$

However, since this equation depends on the single component density $n_\sigma(\mathbf{r}) = \int \frac{d^3\mathbf{p}}{(2\pi\hbar)^3} f(\mathbf{r}, \mathbf{p})$, it has to be solved self-consistently to get a closed-form solution. This is achieved iteratively. First, we ignore the interaction term which gives us $f_0$. Since for a given atom cloud, $\mu$ is unknown, $\mu_0$ is then determined from $\int \frac{d^3r d^3p}{(2\pi\hbar)^3} f_0(\mathbf{r}, \mathbf{p}) = N_\sigma$ where $N_\sigma$ is the number of atoms per spin species. The atom number can be measured through standard absorption imaging. For iteration number $i$, $n_i$ can then be computed from $f_{i-1}$ to update $V_{MF,i}$. This defines $f(\mu_i, V_{MF,i})$, where at each step $\mu_i$ is determined through normalization to the atom number. We then set $f_i = \alpha f(\mu_i, V_{MF,i}) + (1-\alpha) f_{i-1}$ with $\alpha = 0.9$. Iterating this procedure leads to convergence in 5-10 iterations for the parameters we consider. From Equation 4.13 we can then calculate, given the mean-field interaction, the full density profile $n(\mathbf{r}) = N n_\sigma(\mathbf{r})$ and the corresponding $T/T_F$ of the gas. However, due to higher order dipolar interactions caused by the absorption imaging probe beam, the density profile cannot be accurately fitted in-trap. As a result, we expand the gas before measurement.

#### 4.4.4.1 Time of flight expansion

To study the dynamics, we make a scaling ansatz for the distribution function [183, 96, 93, 184, 180]. Our ansatz is

$$f(\mathbf{r},\mathbf{p},t) = \frac{1}{\prod_j(\lambda_j\theta_j^{1/2})} f_0\left(\frac{r_i}{\lambda_i}, \frac{1}{\theta_i^{1/2}}(p_i - m\dot{\lambda}/\lambda_i r_i)\right) . \tag{4.14}$$

The parameters $\lambda_i$ and $\theta_i$ are scaling parameters along the ith direction that vary in time. Following [96], we take the moments of $r_i p_i$ and $p_i^2$ to obtain a closed set of differential equations for the scaling parameters $\lambda_i$, $\theta_i$:

$$\ddot{\lambda}_i + (2\pi\nu_i)^2\lambda_i - (2\pi\nu_i)^2\frac{\theta_i}{\lambda_i} + (2\pi\nu_i)^2\xi_i\left(\frac{\theta_i}{\lambda_i} - \frac{1}{\lambda_i\prod_j\lambda_j}\right) = 0\,, \tag{4.15}$$

and

$$\dot{\theta}_i + 2\frac{\dot{\lambda}_i}{\lambda_i}\theta_i = -\left(\theta_i - \bar{\theta}\right)/\tau\,, \tag{4.16}$$

where $\xi_i = \frac{g/2(N-1)\langle n_\sigma\rangle}{g/2(N-1)\langle n_\sigma\rangle + \langle p_i^2\rangle/m}$ accounts for the mean-field interaction with $\langle\cdots\rangle$ being phase-space averages with respect to the equilibrium distribution and $\bar{\theta} = 1/3\sum_i\theta_i$.

To study the expansion after switching off the trap, the second term in Equation 4.15 is set to 0. The differential equations are then solved for the scaling parameters, which when plugged into the scaling ansatz yield the phase-space distribution after time-of-flight. With the phase distribution distribution, we can then calculate the full density profile of the gas. The compressibility can be computed directly from the density profiles. In a harmonic trap the chemical potential varies as $\mu(\mathbf{r}) = \mu - U(\mathbf{r})$. Thus, to calculate the compressibility, the derivative with respect to $\mu$ can be replaced by a derivative with respect to one of the spatial directions, giving $\frac{\partial n}{\partial\mu} = \frac{-1}{m(2\pi\nu_i)^2 r_i}\frac{\partial n}{\partial r_i}$.

## 4.5 Concluding remarks

We have demonstrated that SU($N$) symmetry substantially enhances interaction dynamics in a quantum degenerate Fermi gas. The many-body problem for the dilute repulsively interacting Fermi gas can be solved exactly, and we have shown with high precision how the additional spin degree of freedom systematically modifies thermodynamic properties in the bulk gas. This opens the path for future quantum simulators to systematically explore SU($N$)-symmetric Fermi systems in periodic potentials.

The enhanced SU($N$) interactions allow us to reach ultralow temperatures in record speed. Rapidly creating a spin-polarized degenerate sample is an important milestone for the realization of a band-insulator atomic clock [55]. With a total preparation time under 3 s, Dick effect contributions are in the mid-$10^{-17}/\sqrt{\tau}$, and are thus on-par with the most stable intercomparisons to date [3]. This work sets the stage to prepare a low-entropy 3D band insulator with a spin-polarized Fermi gas. Ongoing work is expected to push the lattice clock coherence time to 10s of seconds.

# Chapter 5

## Pauli blocking of atom-light scattering

*The research described in this chapter has been reported in the following publication: Christian Sanner*, Lindsay Sonderhouse*, Ross B. Hutson, Lingfeng Yan, William R. Milner, and Jun Ye, "Pauli blocking of atom-light scattering," Preprint at https://arxiv.org/abs/2103.02216 (2021). * (these authors contributed equally)* [185].

Radiative relaxation of an excited quantum system is a ubiquitous phenomenon: it makes fireflies glow, underlies the radiative recombination of electrons and holes in light-emitting diodes, and can be observed as gamma decay of nuclear isomers. The intimately related phenomenon of light scattering involves minimally populated excited states that often assume a virtual character [60, 186]. The blue sky is a direct manifestation of such a second-order excitation-emission process with air molecules scattering sunlight. What all these light-matter interactions have in common is that the radiative decay depends on the final density of states for the joint emitter-photon system. In particular, for the photon channel it has been demonstrated [187, 188, 189] that manipulation of the density of vacuum modes through the use of an electromagnetic resonator modifies the emission and scattering of light. This Purcell effect is now widely used in nanostructured devices [190].

More than 30 years ago it was suggested [191] that constraints imposed by quantum statistics on an atomic medium could also modify spontaneous emission and light scattering. Fermi statistics requires the total wavefunction of a fermionic system to be antisymmetric, giving rise to the Pauli exclusion principle that forbids indistinguishable fermions from occupying the same internal and external quantum states. Accordingly, if a sufficient number of ground state fermionic atoms occupy all available external motional states into which an internally excited fermionic atom has to decay, this decay process will be blocked. The prospect to manipulate light scattering properties and to quantum engineer the natural lifetime of an excited atomic state by embedding it inside a Fermi sea has triggered many theoretical studies and proposals [192, 193, 194, 195, 196, 197, 72, 198, 199], but up to now this fundamental modification of atom-light scattering by Fermi statistics has not been observed, complicated by atomic properties and competing collective radiative behavior.

Spontaneous emission and light scattering are not synonymous. Even though the usual descriptions [186] of both processes involve the relaxation of an excited state (a populated atomic energy eigenstate and a virtual intermediate state, respectively), their properties and decay dynamics are different. In a noninteracting Fermi gas, however, the unavailability of final momentum states is the sole cause for single-particle modifications of radiative (re)emission properties and therefore equally affects all atom-light processes that transfer randomly directed recoil momentum to the atom [197].

In the following, we report the first direct observation of Pauli suppression of light scattering using a quantum degenerate Fermi gas of strontium atoms. We confirm that the suppression becomes stronger as degeneracy is increased and when the Fermi energy approaches the photon recoil energy. By angularly resolving the photon scattering rate, we measure up to a factor-of-two reduction in comparison to the natural value determined from a thermal ensemble. This striking manifestation of Fermi statistics connects for the first time the fundamental radiative property of atoms to their motional degrees of freedom subject to quantum statistics. The consequences of Pauli blocking of atomic motion have been demonstrated earlier, including the suppression of collisions [71], the direct observation of Fermi pressure [68], the onset of Hanbury Brown-Twiss anticorrelations [79, 80], local antibunching [200, 19, 88], the suppression of chemical reactions between molecules [201], and the formation of Pauli crystals [81].

In this chapter, we reintroduce the concept of Pauli blocking in section 5.1. In section 5.2 we explain our experimental strategy to observe Pauli blocking using a light scattering experiment with a weakly excited Fermi gas. We then detail our experimental results in section 5.3, and finally conclude in section 5.4.

## 5.1 Pauli blocking in a large Fermi sea

Fig. 5.1 illustrates the key concept of the experiment and introduces the relevant energy scales [178]. An ensemble of $N$ harmonically confined identical fermions of mass $m$ forms a quantum degenerate Fermi sea with close to unity occupation of the oscillator states if the thermal energy $k_B T$ is small compared to the Fermi energy $E_F = (6N)^{1/3}\hbar\omega$. The three-dimensional confinement is characterized by the mean trap frequency $\omega = (\omega_x \omega_y \omega_z)^{1/3}$, and $k_B$ and $\hbar$ denote the Boltzmann and reduced Planck constants, respectively. The Fermi temperature $T_F$ and Fermi wavevector $k_F$ are defined via $E_F = (\hbar k_F)^2/(2m) = k_B T_F$. If an atom inside the Fermi sea absorbs a photon carrying momentum $\hbar k_{abs}$, it gains a corresponding recoil energy $E_R = (\hbar k_{abs})^2/2m$. Here, we consider the case of weak confinement with $\hbar\omega << E_R$ and treat Rayleigh scattering as a two-step momentum transfer process [72, 202]. Upon photon re-emission the atom experiences a randomly directed second momentum kick $\hbar k_{emi}$ where $|k_{emi}| = |k_{abs}| = k_R$, resulting in a total momentum transfer $\hbar\mathbf{k} = \hbar\mathbf{k}_{abs} + \hbar\mathbf{k}_{emi}$. If, however, the corresponding motional state is already occupied by another atom within the Fermi sea, this decay channel is blocked, and light scattering will be suppressed. The relative temperature $T/T_F$ and the wavevector ratio $k/k_F$, where $\hbar k_F = (2mE_F)^{1/2}$ is the momentum space radius of the Fermi sea, determine the density of available final momentum states and hence the degree of blockade. Following Fermi's golden rule one finds using a local density approach [195, 72] a relative scattering rate of[1]

$$S(\mathbf{k}) = \frac{\int d^3\mathbf{p}\, d^3\mathbf{q}\, n_i(\mathbf{p},\mathbf{q})\,[1 - n_f(\mathbf{p},\mathbf{q})]}{\int d^3\mathbf{p}\, d^3\mathbf{q}\, n_i(\mathbf{p},\mathbf{q})}\,. \tag{5.1}$$

Here the integrals cover the six-dimensional phase space spanned by three momentum dimensions $\mathbf{p}$ and three real space dimensions $\mathbf{q}$. The initial and final state phase space cell occupations

---

[1] This equation simplifies to Equation 2.27 for a harmonically trapped gas.

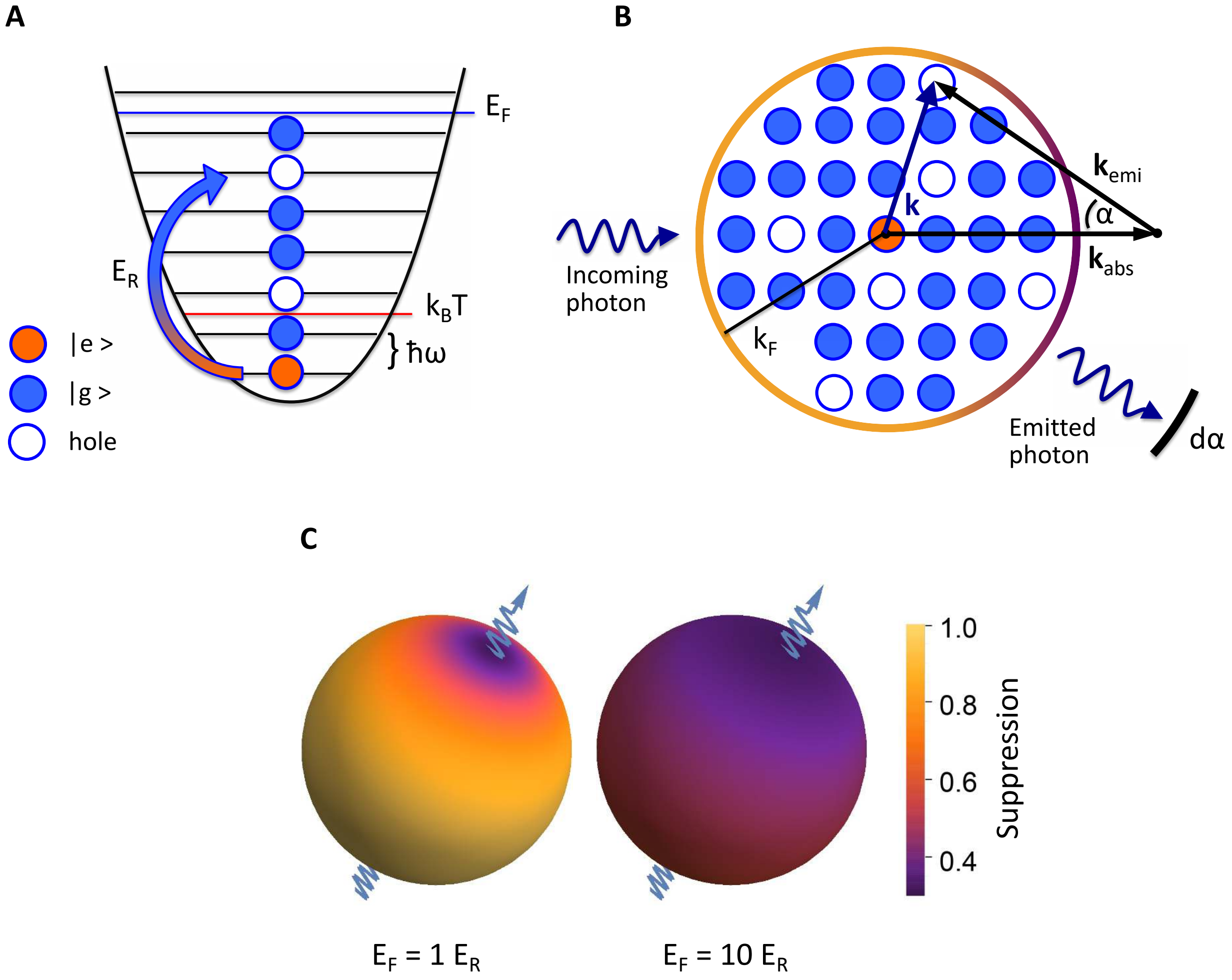

Figure 5.1: **Light scattering on atoms embedded inside a Fermi sea.**
(**A**) Indistinguishable fermions obey the Pauli exclusion principle. If the thermal energy $k_BT$ is sufficiently low they fill almost all available harmonic oscillator states up to the Fermi energy $E_F$ with near-unity occupation. An excited atom (orange) acquires a recoil energy $E_R$ when returning to its internal ground state (blue). (**B**) In momentum space, the atoms form a Fermi sea occupying most states up to the Fermi momentum $\hbar k_F$. Light scattering with re-emission along $\alpha$ and total momentum transfer $\hbar\mathbf{k}$ can happen only if the final momentum state is not occupied by another ground state fermion. A detector covering a solid angle $d\alpha$ registers the emitted photon. (**C**) Pauli blocking leads to a characteristic angular distribution of scattered photons in the deeply degenerate regime (here $T/T_F = 0.1$). For $E_F \sim E_R$ (left sphere) scattering is preferentially suppressed in a small cone around the forward direction, while $E_F >> E_R$ (right sphere) causes strong suppression for all scattering angles $\alpha$. The suppression factor specifies the scattering rate relative to a non-Pauli-blocked sample.

are given by $n_i = n_{FD}(\mathbf{p}, \mathbf{q})$ and $n_f = n_{FD}(\mathbf{p} + \hbar\mathbf{k}, \mathbf{q})$, where $n_{FD}$ is the Fermi-Dirac distribution for a harmonically trapped gas, that is

$$n_{FD}(\mathbf{p}, \mathbf{q}) = \frac{1}{1 + \xi^{-1} exp[\left(\Sigma_i \, p_i^2/(2m) + \Sigma_i m\omega_i^2 q_i^2/2\right)/k_B T]} \, . \tag{5.2}$$

The index $i$ runs over all three dimensions and $\xi$ is the fugacity related to $T/T_F$ through $1/Li_3(-\xi) = -6(T/T_F)^3$, where $Li_3$ is the trilogarithm function. The expression for $S(\mathbf{k})$ counts all available final momentum states for a given momentum transfer $\hbar\mathbf{k}$ and averages over all initial states within the Fermi sea.

## 5.2 Light scattering experimental strategy

The above analysis suggests two pathways to observe pronounced Pauli suppression of light scattering. One can either prepare a Fermi gas with $E_F >> E_R$ so that a significant decay blockade is obtained for all emission directions, that is, for any momentum transfer up to the maximum $2\hbar k_R$ (homogeneously colored right sphere in Fig. 5.1 C). Or one can relax this requirement and selectively observe only scattering events with a small momentum transfer so that $E_F \sim E_R$ is sufficient. The second approach, which we take here (gradient-colored left sphere in Fig. 5.1 C), is straightforwardly realized in a small-angle light scattering configuration where a small number of atoms within the Fermi sea are optically excited and a subset of the scattered photons is collected under a shallow angle $\alpha$ with respect to the excitation beam corresponding to a momentum transfer of $\hbar k = 2\hbar k_R \sin(\alpha/2)$.

A multitude of effects besides quantum statistics can influence radiation dynamics in a dense ensemble of emitters. Coherence, either externally imprinted or spontaneously established, can lead to super- and subradiant collective states that correspondingly exhibit super- and subnatural radiative lifetimes. Dicke superradiance [203, 204], radiation trapping [205], multiple scattering [206], and other forms of coherent or incoherent collective scattering [207] all critically depend on the integrated optical density $OD = \int \sigma n dl$ of the atomic gas. This attenuation parameter, derived from the single-atom scattering cross section $\sigma$ and density $n$, where $l$ is measured along the direction of the incoming light, defines a parameter region where the gas is optically thin ($OD << 1$) and single-particle scattering dominates over collective effects. Given that on resonance, $\sigma$ is on the order of the squared optical wavelength $\lambda^2 = (2\pi/k_R)^2$, and $k_F$ is tied to the 3D peak density via $n = k_F^3/6\pi^2$, it is not possible to satisfy the Pauli blocking criterion $k_F \sim k_R$ without violating the small OD requirement. Indeed, typical optical densities encountered in atomic Fermi gas experiments easily exceed 100. In this optically thick regime multiple photon scattering strongly affects the light propagation inside the sample, as evidenced with the resonant fluorescence image displayed in Fig. 5.2 B. Using off-resonant light reduces the effective scattering cross section and renders the atom cloud weakly absorbing for the incoming probe light at sufficient detuning. This, combined with differential observation strategies and avoiding light detection in the forward direction, minimizes the influence of collective scattering dynamics. Furthermore, unlike Pauli blocking, these competing effects are not dependent on quantum statistics and can therefore be observed using a thermal gas [26], instead of a quantum degenerate gas, to provide a baseline.

Our experiment starts with the preparation of a $^{87}$Sr Fermi gas as described in reference [54]. The $^1\mathrm{S}_0$, $F = 9/2$ ground state is split into ten magnetic spin states $m_F = -9/2, ..., 9/2$. Here $F$ is the total angular momentum of the nuclear spin. This fully thermalized 10 component sample [51] contains 18 000 atoms per spin state confined in a crossed optical dipole trap with maximum radial trap frequencies of $\omega_x = \omega_y = 2\pi \times 120$ Hz and an axial confinement with $\omega_z = 2\pi \times 506$ Hz. This leads to a Fermi energy of $E_F = 440$ nK for each of the ten Fermi seas and we reach temperatures down to $0.1T_F$. The small inter-component s-wave scattering length $a = 97a_0$, where $a_0$ is the Bohr radius, makes the Fermi gas weakly interacting with $k_F a = 0.06$, which is scaled by the number of spin states, increasing the total energy of the gas by less than 7%. These weak repulsive interactions in principle affect $S(\mathbf{k})$, but their differential effect is negligible [51] at the measurement precision achieved in this study. Under suitable conditions, any optical excitation returning to the ground state should experience a decay blockade. We perform specific measurements on the $^1\mathrm{S}_0 - {}^1\mathrm{P}_1$

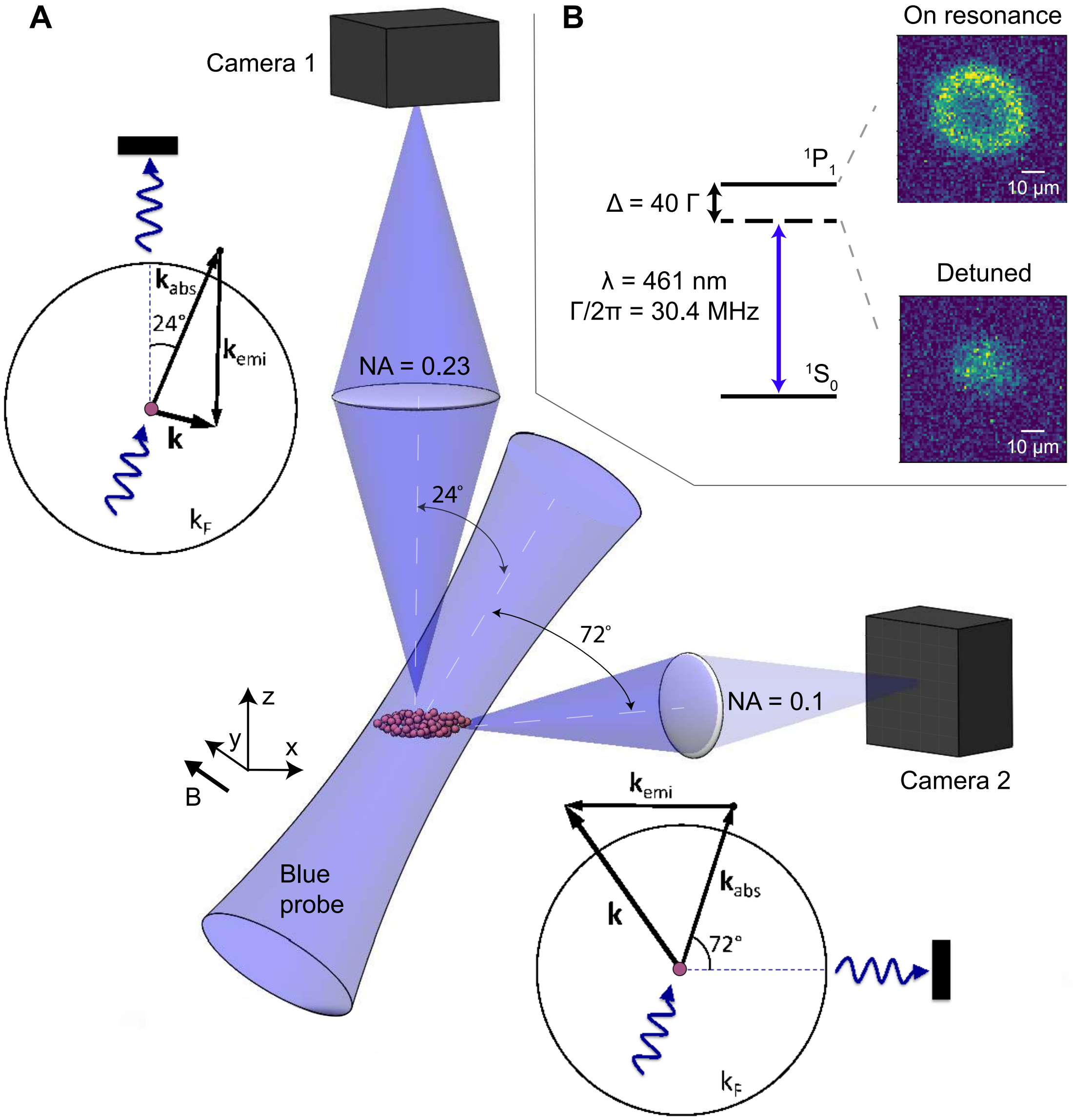

Figure 5.2: **Experimental Setup.**
(**A**) Off-resonant probe light excites $^{87}$Sr atoms inside a Fermi sea. Spontaneously re-emitted photons are collected simultaneously along two imaging axes under angles of 24° and 72°, with their numerical apertures ($NA$) shown respectively. Small scattering angles correspond to a small momentum transfer with $k/k_F < 1$, whereas the transversal observation detects photons from scattering events with $k/k_F > 1$. The circularly polarized probe beam has an intensity of $5I_{sat}$ where the resonant saturation intensity is $I_{sat} = 41$ mW/cm$^2$. (**B**) On resonance the atomic cloud is optically thick for the probe beam and the image formed on Camera 1 displays a hole in the cloud center due to multiple scattering. At a detuning of $\Delta = 40\Gamma$ the atom cloud is optically thin and the corresponding image resembles the atomic density distribution. The detuned frequency is used in the Pauli blocking experiment. A magnetic bias field of 3 Gauss applied in the horizontal plane along the y-direction defines the atomic quantization axis.

transition at 461 nm with a natural linewidth of $\Gamma = 2\pi \times 30.4$ MHz [208] and a recoil energy of $E_R = 520$ nK. Employing a continuous weak-drive Rayleigh scattering scheme, the Fermi gas is exposed for 1 $\mu$s to a 1.2 GHz detuned drive beam that causes on average $< 10\%$ of the atoms to undergo an excitation cycle. No evidence for inelastic scattering is observed.

For the given drive beam and atom cloud parameters the sample is optically thin with an effective OD of 0.02, corresponding to a forward transmission of 98%. As illustrated in Fig. 5.2, two detectors collect scattered photons simultaneously under off-axis angles of $\alpha_1 = 24°$ and $\alpha_2 = 72°$. These operational parameters are chosen to simplify the interpretation of our measurements. First, as discussed above, the detuning from resonance by $40\Gamma$ eliminates multiple scattering dynamics and furthermore avoids refractive lensing contributions [121] far off-axis. Second, the low excitation rate keeps the Fermi sea intact throughout the probe pulse exposure. Third, operating in the weak-drive limit ensures that there is no inelastic scattering contribution beyond the recoil-induced energy shift, i.e., Mollow triple-peaked fluorescence spectra and other strong-drive effects are negligible [186].

## 5.3 Experimental results

To systematically explore how quantum degeneracy affects light scattering, we start with a deeply degenerate gas of $T/T_F = 0.1$ and gradually heat it up to $T/T_F = 0.7$ through parametric confinement modulation while keeping the atom number and Fermi energy constant. Under these conditions photons scattered off of the weak probe pulse are counted. To satisfy the requirement to minimally disturb the Fermi gas by the probe, the number of collected photons along the two detection axes is correspondingly low. Even for the axis with a high $NA = 0.23$ objective lens fewer than 200 photons are collected at full quantum efficiency. By operating the gated CCD detectors in a hardware binning mode that maps all detected photons into a 3x3 superpixel array, we spatially and temporally isolate the signal from background contributions and maintain low readout noise. The measured photon counts are compatible with ab-initio estimates within 30% based on the reported drive parameters and detection efficiencies. All relevant thermodynamic parameters are independently assessed through measurements on expanded gas clouds after time of flight.

### 5.3.1 Temperature and Fermi energy dependence

The results of Pauli-suppressed scattering are shown in Fig. 5.3A. Under the shallow off-axis angle of 24°, where $k/k_F = 0.45$ for our Fermi sea, we find a strong dependence of the photon counts on $T/T_F$. To properly normalize the detector signal, i.e., to convert the registered photon counts to a suppression ratio without introducing an arbitrary scaling factor, it is necessary to prepare an equivalent reference sample that is not Pauli-blocked. Because the weak optical confinement does not maintain a constant atom number for $T/T_F > 1$, we devise an alternative method to eliminate Pauli blocking: At 10 $\mu$s before applying the actual probe pulse we expose the Fermi gas to a 5 $\mu$s long pre-pulse that destroys the Fermi sea by randomly exciting atoms to momentum states beyond $k_F$. Consequently, light scattering is no longer Pauli suppressed during the subsequent probe pulse. All blue round data points in Fig. 5.3A/B are normalized to a common reference photon count obtained from a single pre-pulse exposed sample (see below). Numerically integrating the expression for $S(\mathbf{k})$ at all probed temperatures reveals good agreement between experiment and theory. The simultaneously acquired measurements at an observation angle of 72° do not show a pronounced suppression and only exhibit a weak temperature dependence, as expected for $k/k_F = 1.27$ since most final momentum states lie outside of the Fermi sea.

To further verify that Pauli blocking is the mechanism responsible for the observed scattering behavior, we study the dependence on $k_F/k_R$ by varying the confinement while keeping atom number and $T/T_F = 0.13$ constant, as displayed in Fig. 5.3B. Even at the shallowest confinement with $k_F/k_R = 0.57$ ($E_F/E_R = 0.32$), the momentum transfer along the 24° axis amounts to only $k/k_F = 0.74$ so that we still observe substantial suppression of light scattering. This is in contrast to the 72° case, where $k/k_F = 2.07$ at $k_F/k_R = 0.57$. If $k/k_F > 2$ Pauli blocking is negligible at any temperature so that we normalize all photon counts acquired under 72° (red data points in Fig. 5.3A/B) with respect to this reference point (solid red circle in Fig. 5.3B).

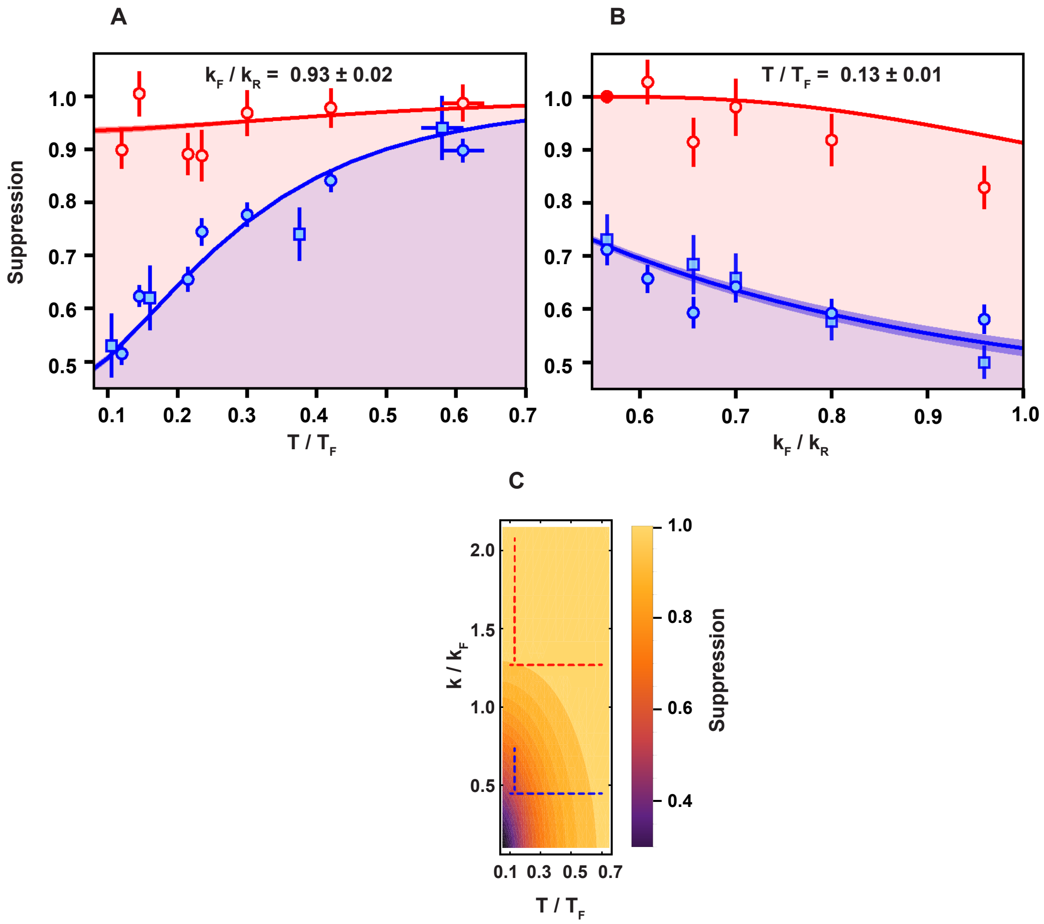

Figure 5.3: **Suppression of light scattering in a** $^{87}$Sr **Fermi gas over a range of temperatures and Fermi momentums.**
All measurements are performed with a 10-component Fermi gas containing 18 000 atoms per spin state. The scattering behavior is distinctly different for the two observation angles of 24° (blue circles and squares) and 72° (red circles). Raw photon counts are normalized with respect to measurements on non-Pauli-blocked reference samples (see main text). Each circle data point is derived from 150 iterations of the experiment, while each square point results from 50 experimental runs. Solid theory curves are calculated with no free parameters. The widths of the theory lines reflect the experimental uncertainties of Fermi energy and temperature. The error bars are purely statistical and indicate one-standard-deviation confidence intervals. (**A**) At a constant Fermi wavevector of $k_F/k_R = 0.93$ ($E_F/E_R = 0.86$), the atom ensemble's scattering cross section decreases as the gas approaches deep quantum degeneracy. The suppression observed under 24° is pronounced and reaches 50% at $T/T_F = 0.13$. In contrast, under 72°, the suppression is negligible. (**B**) At constant $T/T_F = 0.13$, $k_F$ is varied by adiabatically changing the confinement. A larger $k_F$ results in a stronger suppression. (**C**) The data reported in **A** and **B** are measured along 4 trajectories (dotted lines) through the parameter space spanned by $k/k_F$ and $T/T_F$. Depending on the scattering angle $k$ varies between 0 and $2k_R$. Light collected under an off-axis angle of 24° corresponds to a momentum transfer $\hbar k < \hbar k_F$ for the given Fermi gas, leading to substantial reduction of the density of available final states. On the contrary, for the 72° collection angle, the corresponding momentum transfer $\hbar k > \hbar k_F$. Thus most final states are not blocked and scattering is not suppressed.

### 5.3.2 Pre-pulse application

The additional blue square data points displayed in Fig. 5.3 were normalized by applying a pre-pulse separately for each data point and are in good agreement with the common-mode normalized measurements. In particular, with a 10 $\mu$s wait time before the probe pulse, the atomic density remains essentially the same with or without the pre-pulse. This ensures common-mode cancelation of collective scattering dynamics. Below we present light scattering measurements with variable pre-pulse durations for a deeply degenerate ($T/T_F = 0.11$) and heated ($T/T_F = 0.58$) Fermi gas. This data confirms the scattering-induced destruction of the Fermi sea over the course of the pre-pulse application.

The suppression factors reported in Fig. 5.3 as red and blue circles were obtained by normalizing the measured photon counts against a common reference count value. Residual total atom number and probe pulse intensity fluctuations were below 10% over the course of the data acquisition. For the 72° detection axis (red circles) the measurement at $k_F/k_R = 0.57$ (red solid circle), which is outside the Pauli-blocking regime with $S > 0.99$, directly provided the reference count. The photon counts detected along the 24° axis were normalized against a reference count measured by exposing the Fermi gas to a 1.2 GHz detuned pre-pulse to create holes in the Fermi sea before applying the actual probe pulse. Precise detection gating with an interline transfer CCD (Camera 1) and a short dark time of 10 $\mu$s between the two pulses avoided contamination of the probe signal with pre-pulse fluorescence while keeping the atomic density distribution unaffected. The pre-pulse intensity was calibrated such that each atom scattered on average more than one photon during a 5 $\mu$s long pulse. To directly verify that this exposure destroyed the Fermi sea and eliminated the Pauli blockade, we systematically varied the pre-pulse duration and observed for two samples at $T/T_F = 0.11$ and $T/T_F = 0.58$ how the probe signal saturated at the non-blocking reference level for longer pre-pulses (Fig. S1). A pre-pulse duration of 5 $\mu$s was chosen to obtain the reference count along the 24° detection axis.

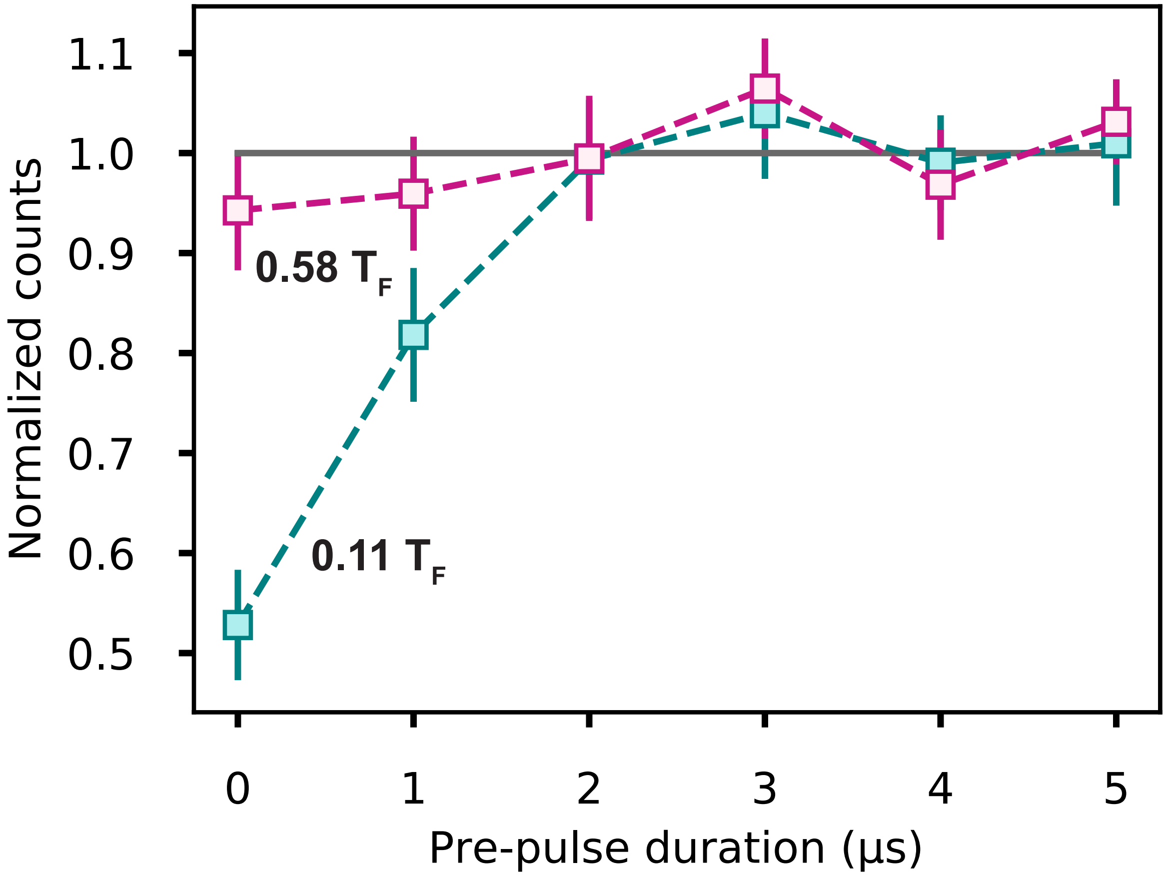

Figure 5.4: **Photon scattering from a Fermi gas after exposure to a pre-pulse of variable duration.**
For the chosen pre-pulse detuning and intensity, the Pauli blockade is destroyed after exposure for a few $\mu$s. The scattering signal from the deeply degenerate sample (green squares) increases by almost a factor of 2 while the barely degenerate sample (purple squares) shows only minimal increase, as expected for a Fermi sea with $k_F/k_R = 0.93$ under an observation angle of 24°. Data in the plot is normalized relative to the mean counts detected for 4 and 5 $\mu$s pre-pulse durations.

### 5.3.3 Spatially resolved scattering rate

Spatially resolving the origin of the scattered photons within the Fermi gas, in addition to counting the total number of scattered photons along a given direction, provides a picturesque revelation of the Pauli blocking mechanism. For this purpose, we modify the 24° high-NA axis to deliver magnified images of the atom cloud and employ a non-binning CMOS camera with a low readout noise of 2 photoelectrons. The cylindrically symmetric atomic cloud at $T/T_F = 0.12$ with a diameter of about 20 $\mu$m is projected along the z-axis into a 2D image with 0.9 $\mu$m wide pixels. Because a single pixel collects on average less than 1 photon, it is necessary to average hundreds of frames in order to derive a finely resolved scattering profile. Furthermore, we radially average the mean image to obtain the radial profile (blue data points) shown in Fig. 4. Residual optomechanical drifts in the optical setup cause small displacements of the center of mass position of the cloud during the frame averaging period. This, together with the finite resolution of the imaging system, leads to an effective $1/e^2$ pixel blurring on the order of 3 $\mu$m. To compare the observed scattering profile to theory predictions without introducing a free scaling parameter, we independently acquire in-situ density profiles of the Fermi gas through the same imaging setup via high intensity fluorescent imaging [122][2] . Using the frame-wide summed total photon counts and the measured global suppression ratio at $T/T_F = 0.12$ (Fig. 5.3A), we then properly scale the radial density profile to reflect the scattering profile expected without Pauli blockade for the weak probe beam (purple curve). Momentum space integration plus one-dimensional line-of-sight integration of $S(\mathbf{k})$ yields a radially resolved suppression ratio for us to determine the expected scattering profile with Pauli blockade (blue curve). Except at the center of the cloud, where radial averaging does not significantly improve the signal-to-noise ratio, we find good agreement between calculated and measured profiles. Towards the outer rim of the cloud the local Fermi energy drops so that light scattering is not suppressed anymore; the local suppression ratio will approach the thermal gas limit of 1. This happens, as seen with the blue theory curve, only in the outermost region where the density is so low that the signal-to-noise level is insufficient to reliably determine a suppression ratio.

---

[2] Also see Chapter 3. A separate manuscript is in preparation to further describe our high intensity fluorescence imaging method.

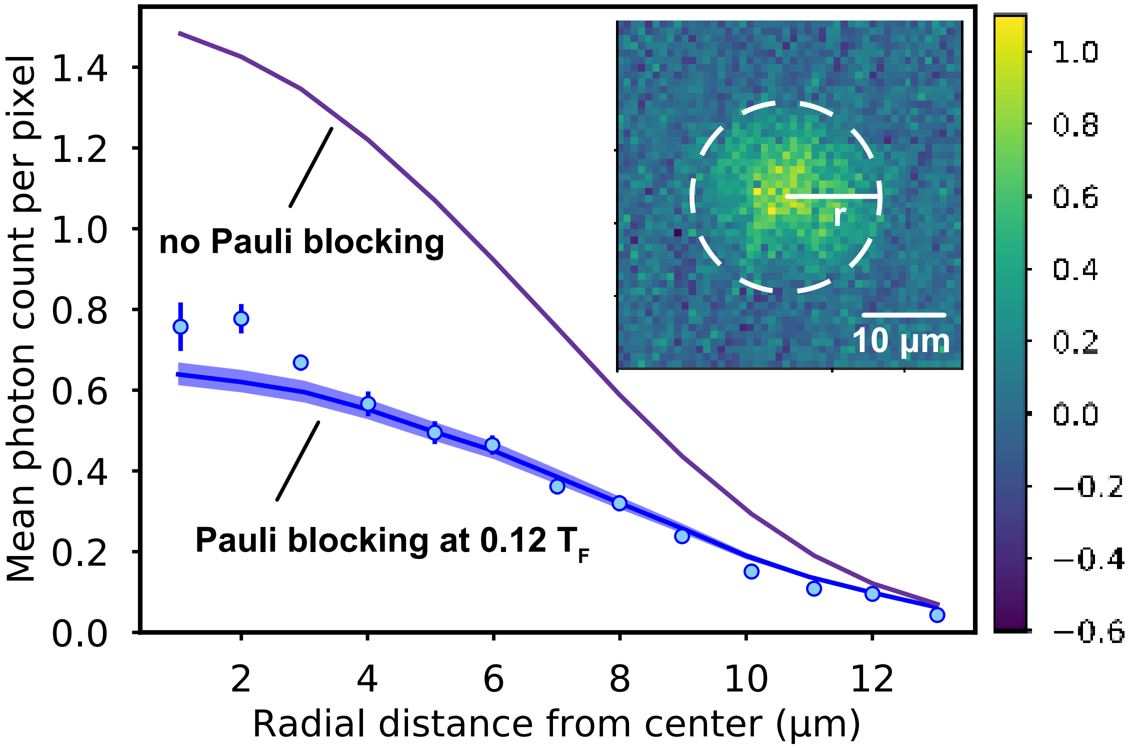

Figure 5.5: **Spatially resolved light scattering from a trapped Fermi gas at $\mathbf{T/T_F = 0.12}$.** Radially averaging the spatially resolved mean signal (inset) from 1100 individual images obtained along the z-axis yields a radial light scattering profile (blue data points). In-situ column density images, separately obtained using a high intensity fluorescent imaging technique, are used to predict the scattering signal for a non-degenerate gas (purple curve). The spatial profile of light scattering calculated for the $T/T_F = 0.12$ ensemble (blue curve) agrees well with the measured data.

## 5.4 Conclusion

In conclusion, we have reported a clear demonstration that Fermi statistics leads to strongly modified light scattering in a quantum degenerate system. The presence of a Fermi sea alters the final atomic motional mode spectrum and enables a direct observation of Pauli blockade of light scattering. Interpreted from a many-body system perspective, this experiment probes the structure factor [73] of a quantum degenerate Fermi gas. Defined as the Fourier transform of the spatial density-density correlation, the static structure factor $S(\mathbf{k})$ characterizes the linear response of a system to a perturbation with wavevector $\mathbf{k}$. Accordingly, the suppression of light scattering and the suppression of density fluctuations [86] in a Fermi gas are two interrelated manifestations of the same fundamental many-body physics.

It will be exciting to go beyond the regime of Rayleigh scattering and directly measure a prolonged excited state lifetime using properly prepared quantum states. The capability to alter a fundamental decoherence mechanism will open new avenues for quantum engineered atom-light interfaces. In particular, custom designed Fermi reservoirs can protect optical qubits at local nodes while facilitating cavity-free directional photon emission for efficient network connectivity. In the context of optical atomic clocks this work could enable spectroscopic interrogation times exceeding the natural lifetime of the excited clock state and investigation of novel radiative properties of atoms.

# Chapter 6

# Attempts to measure Pauli blocking of the natural lifetime using coherent control on a narrow-linewidth transition

Quantum information science strives to use well-controlled, artificial quantum systems to advance scientific understanding and foster the growth of new technology. Pauli blocking is a quantum tool that lies at the heart of this idea. A large Fermi gas made out of ultracold atoms is built using a tabletop experiment to quantum engineer an atomic transition with a lifetime longer than what nature would provide alone. Spontaneous emission causes information to escape into the environment and can thus destroy optical qubit states and ultimately limit spectroscopic resolution. As a result, this tool could have tremendous applications in quantum technologies such as precision metrology and quantum information processing.

The first observations of Pauli blocking of light scattering, which has now been measured in multiple experiments [185, 209], demonstrated the ability to realize this long-sought theoretical idea and established a scientific understanding of the fundamental and competing radiative mechanisms. This was a crucial first step towards implementing Pauli blockade as a practical tool, but the steady-state scattering regime these experiments were performed in is not suitable for modern atomic clocks and quantum information platforms, which require arbitrary coherent control of the atomic state.

In this chapter, we detail experiments that attempt to observe Pauli blocking of the natural lifetime of an atomic state after atoms in a Fermi gas are coherently driven to the excited state. We directly detect the lifetime of the atomic state by time-resolving the number of excited atoms, as opposed to angularly detecting the scattered photons as was done in Chapter 5 [185], and in Refs. [209, 210]. Measurements are performed on the 7.4 kHz linewidth $^3\text{P}_1$ transition in a multi-spin component Fermi gas of $^{87}$Sr atoms. In Section 6.1, we discuss our technique to create pronounced suppression using imbalanced Fermi gases. We then outline our experimental setup in Section 6.2. In Section 6.3 we detail a systematic study of the competing radiative effects present in this coherent-drive scheme by measuring the lifetime of a thermal gas of atoms. We then present lifetime measurements at degenerate temperatures. Although we measure an angle-averaged lifetime that is up to 20% longer than the natural lifetime at ultralow temperatures, as shown in Section 6.4, we will show that we could not fully rule out other systematic effects that come with coherently driving a system with a high optical depth (OD). An intriguing alternative is to use systems with different geometries. In Section 6.5 we detail initial measurements performed in two-dimensional systems formed in a 1D optical lattice, where collective radiative properties are designed to be different than in a 3D gas. In fact, here the experimental results are consistent with theory predictions based on Pauli blocking. However, we cannot fully support Pauli blocking with experimental results alone just yet. Finally, in Section 6.6 we present an outlook.

## 6.1 Pauli blocking with imbalanced Fermi gases

The key concept of Pauli suppression is illustrated in Fig. 6.1 (a), which shows the Fermi sphere in momentum space. A photon with initial momentum $\hbar\mathbf{k}_{abs}$ and final momentum $\hbar\mathbf{k}_{emi}$ transfers momentum $\hbar\mathbf{k} = 2\hbar k_R \sin(\alpha/2)$ to an atom, where $k_R = |\mathbf{k}_{abs}| = |\mathbf{k}_{emi}|$ and $\alpha$ is the angle between $\mathbf{k}_{abs}$ and $\mathbf{k}_{emi}$. For a zero-temperature gas with a Fermi energy much larger than the recoil energy, atoms in the center of the Fermi sea cannot decay since all available final states are occupied. Decay can only occur if an atom is within $\hbar|\mathbf{k}|$ of the Fermi surface. At finite temperature, the number of holes in the Fermi sea increases, and thus also does the number of unoccupied states that an atom can decay to. As the density of holes is greater near the surface, atoms within roughly $\hbar|\mathbf{k}| + \sqrt{2mk_bT}$ can decay.

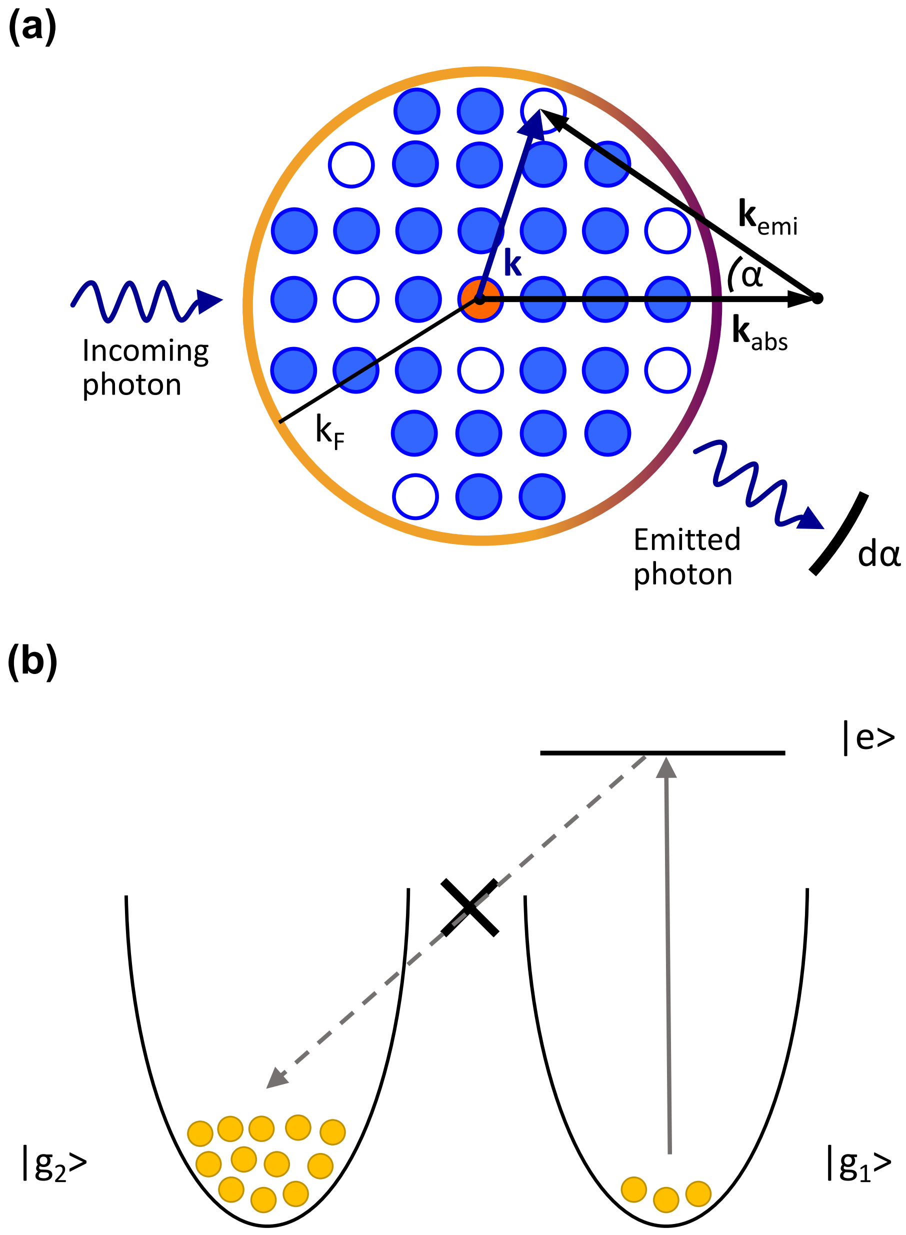

Figure 6.1: (a) Pauli blocking is maximized for atoms in the center of the Fermi sea. Atoms get a directional momentum kick $\hbar\mathbf{k}_{abs}$ from the absorbed light, and a diffusive momentum kick $\hbar\mathbf{k}_{emi}$ from the emitted light, giving a net momentum kick $\hbar\mathbf{k}$ in the center of the Fermi sea. An atom in the center has the maximal suppression since it is least likely to find an unoccupied final state. (b) Exciting atoms in the center of the Fermi sea can be approximated using a three-level scheme with imbalanced Fermi gases. Two ground states with an imbalanced atom number are created and the minor Fermi gas is excited so that it predominantly decays into the major Fermi gas. Under the optimal conditions this decay channel is blocked.

For maximal suppression, it is thus desirable to only excite atoms in the center of the Fermi sea. As suggested in Ref. [72], this could be achieved with an excitation laser that is focused much more tightly than the atomic cloud. Alternatively, one can create scattering between two imbalanced Fermi gases, where the atom number in one gas is much less than in the other, as shown in Fig. 6.1 (b). The two Fermi gases can be created for example by having two different spin states with unequal population that co-exist in the same optical trap. Their corresponding optical transitions are connected by the relevant Clebsch-Gordan coefficients. The minor Fermi sea, which only samples the smallest energies of the major sea, can then be excited and made to predominantly decay to the major Fermi sea. Compared with the tight probe beam technique, this has the further advantage that the ground state Fermi sea is not perturbed during the excitation. In this three-level scheme where the minor Fermi sea with fugacity $\xi_i$ is excited and only decays to the major sea with fugacity $\xi_f$, the scattering rate relative to a non-Pauli blocked sample is (see Equation 2.27)

$$S(k(\alpha)) = \frac{S_{FM}(\mathbf{k})}{S_{MB}} = 1 - \frac{8}{\pi E_{Fi}^3 \beta^3} \int da\, a^{3/2} \int dp_z \frac{1}{1+\xi_i^{-1} e^{a+p_z^2}} \frac{1}{1+\xi_f^{-1} e^{a+(p_z+k_{scal})^2}}\,, \tag{6.1}$$

where $k_{scal} = 2\sqrt{\beta E_{Fi}}\, k_R \sin(\alpha/2)/k_{Fi}$.

If the atomic population is detected, the total decay rate as opposed to the angle-dependent decay rate is measured. In contrast to the Purcell effect, where the solid angle of the cavity is too small to measurably change the atom's total decay rate, for large Fermi energies and low temperatures, Pauli blocking has the capability of changing the total decoherence rate of the atom (see the right sphere in Fig 5.1 (c) ). The total relative decay rate $M$ is given by integrating over all emission angles

$$M = \int S(k(\theta)) P(\theta) d\Omega = 2\pi \int_0^\pi S(k(\theta)) P(\theta) \sin\theta d\theta \tag{6.2}$$

where $\theta$ is the angle between the quantization axis and $\mathbf{k}_{emi}$, and $P(\theta)$ is the dipole emission pattern. For linear polarization $P(\theta) = 3/8\pi \sin^2\theta$, and for circular polarization $P(\theta) = 3/16\pi\,(1+\cos^2\theta)$. Note that with these definitions, $\theta$ is not necessarily the same angle as $\alpha$. The direction of the quantization axis can change the amount of suppression you get. If the maximum of the dipole emission pattern happens to coincide with the smallest k-vectors, more suppression will be achieved. Extending this to a three-level system where decay from the excited state can either occur to the major Fermi sea with blockade $M$ or back to the initial state (which is unblocked), the total suppression has to be weighted by the Clebsch-Gordan coefficients of the two possible decay paths, that is the suppression

$$M_{tot} = |\langle F_{g_{min}}, m_{g_{min}}; 1, q | F_{g_{min}}, 1; F_e, m_e \rangle|^2 + M_{maj} * |\langle F_{g_{maj}}, m_{g_{maj}}; 1, q | F_{g_{maj}}, 1; F_e, m_e \rangle|^2 . \tag{6.3}$$

## 6.2 Experimental setup

The preparation of our Fermi gas is described in Chapter 3. $^{87}$Sr atoms in all 10 nuclear spin states are evaporated to temperatures as low as $T/T_F = 0.1$ with radial confinement as high as $\omega_r = 2\pi \times 100$ Hz and a maximum axial confinement of $\omega_z = 2\pi \times 700$ Hz. Imbalanced Fermi gases are achieved by using atoms in two different nuclear spin states, $m_F = 9/2$ and $m_F = 7/2$, of the $^1$S$_0$ ground state, as shown in Fig. 6.2. The number of atoms with spin $m_F = 9/2$ is a factor of 10 smaller than the number of atoms in $m_F = 7/2$, which is achieved using optical pumping to remove most of the atoms in the $m_F = 9/2$ state. At $T/T_F = 0.1$, the final atom numbers give a maximum Fermi energy of 450 nK for the major component.

In order to directly measure the spontaneous emission lifetime of the excited state, we then coherently excite the $m_F = 9/2$ atoms on the $\Gamma = 2\pi \times 7.4$ kHz linewidth $^3$P$_1$ transition at 689 nm, where the 21.8 $\mu$s natural lifetime can be easily time-resolved. This leads to a recoil energy of 230 nK. An applied magnetic bias field of 1 G splits the excited state's sublevels so that the atoms can be coherently excited to the $F = 11/2$, $m_F = 9/2$ state using a 5 $\mu$s $\pi$ pulse with $\pi$-polarized light. Due to the Clebsch-Gordan coefficients, without Pauli blocking, the excited atoms would decay to the $m_F = 7/2$ ground state with an 82% probability. However, the large ground state Fermi sea

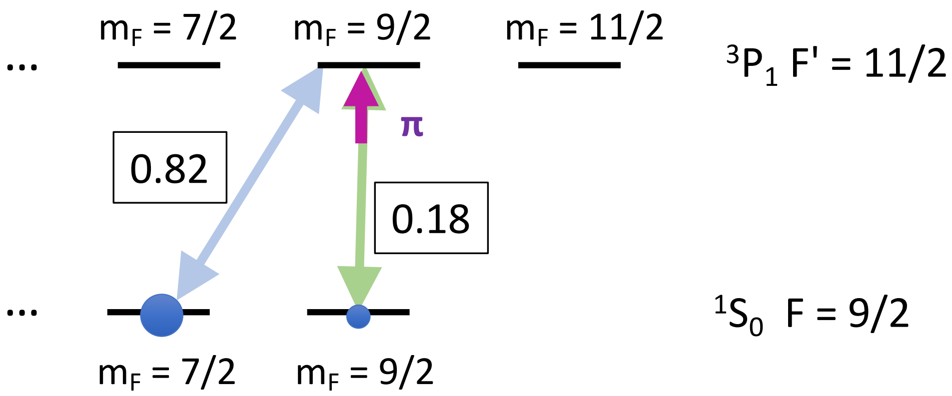

Figure 6.2: $^3$P$_1$ level scheme. Imbalanced Fermi gases with a 10:1 atom number ratio are created using two nuclear spin states of the ground $^1$S$_0$ state. Atoms in $\mathrm{m_F} = 9/2$ are then excited to the $^3$P$_1$, $F = 11/2$, $\mathrm{m_F} = 9/2$ excited state using a $\pi$ pulse with $\pi$ polarized light. The excited atoms are Pauli blocked from decaying to the $\mathrm{m_F} = 7/2$ ground state. The numbers in boxes refer to the Clebsch-Gordan coefficients squared.

largely blocks that decay channel for the minor excited Fermi gas.

The $F = 11/2$ state is used since it is the most magnetically sensitive $^3$P$_1$ hyperfine state, which reduces the probability of off-resonant excitation. The combined effects of off-resonant excitation and polarization impurity are measured by varying the Rabi detuning of the probe, as shown in Fig. 6.3. At -0.5 MHz, the probe is on-resonance with the $\mathrm{m_F} = 9/2$ to $\mathrm{m_F} = 11/2$ transition. These measurements give us an upper bound of the two effects of 2%. Given the 10:1 atom number ratio, this implies a worst-case scenario where we excite 5 times more 9/2 atoms than 7/2 atoms.

The prediction given in Equation 6.3 is shown in Fig. 6.4 for variable $T/T_F$ and $E_F/E_R$. Here it is assumed that the atom number ratio is 10:1 and that the Clebsch-Gordan coefficients are as shown in Fig. 6.2. Given our incoming light is $\pi$-polarized so that $\mathbf{k}_{abs}$ is perpendicular to the quantization axis, $\alpha = \pi/2 + \theta$. All of the $\mathrm{m_F} = 9/2$ population is excited so that no blockade occurs when atoms decay back to the $m_F = 9/2$ ground state. As a result the optimal suppression is determined by the Clebsch-Gordan coefficients; in this case the optimum $M_{tot} = 0.18$. For the

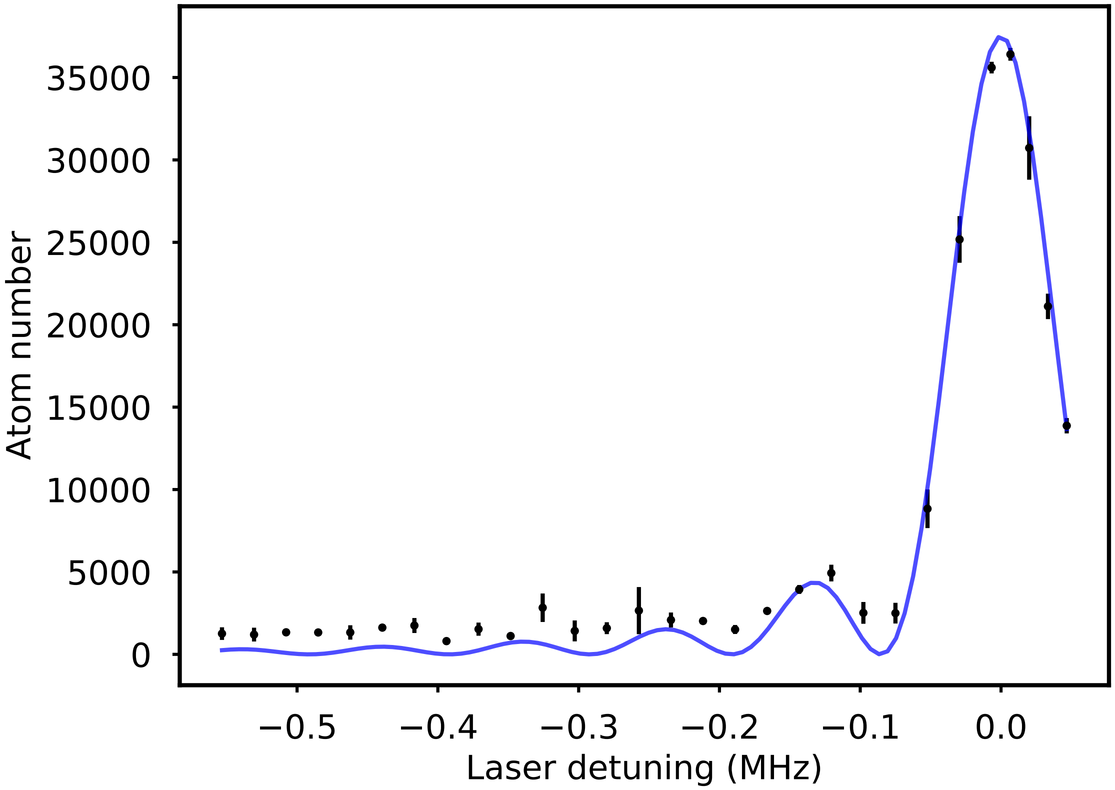

Figure 6.3: Rabi scan as the frequency of the excitation laser is changed. Zero corresponds to the $\mathrm{m_F} = 9/2$ to $^3\mathrm{P}_1$, $F = 11/2$, $\mathrm{m_F} = 9/2$ transition. Given the magnetic field of 1 G, the $\mathrm{m_F} = 11/2$ transition is on resonance at -.5 MHz.

Fermi energies and temperatures in our sample, we can expect a optimum $M_{tot} = 0.4$. The benefit of going to an imbalanced Fermi sea is shown in Fig. 6.5. At $T/T_F = 0.1$ and $E_F/E_R = 2.0$, two equally populated Fermi gases have a total suppression of 0.6, compared to 0.4 for an atom number imbalance of 10:1.

In this coherent excitation, 3-level scheme, multiple observables exist to measure Pauli suppression. The lifetime of the atomic state can be determined by time-resolving the population of excited atoms. In addition, if decay of excited atoms to the 7/2 ground state is blocked, more atoms will decay to the 9/2 ground state. Pauli blocking can thus be thought of as modifying the

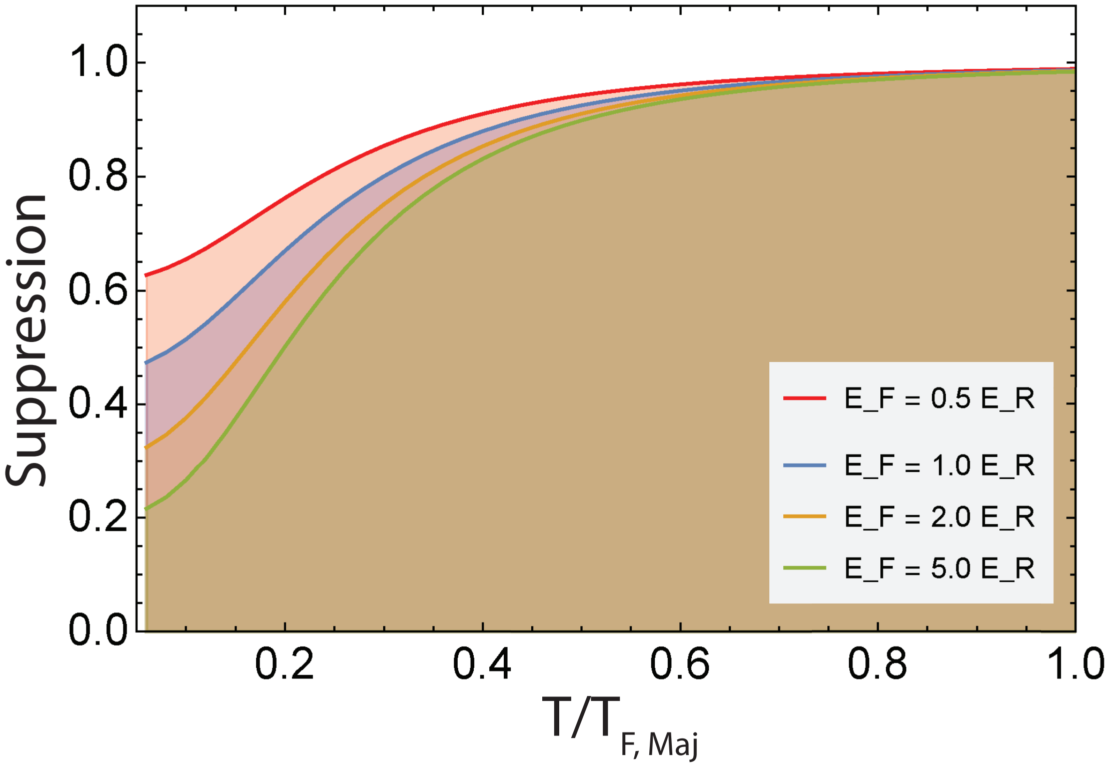

Figure 6.4: Prediction of Pauli blocking suppression for a three-level scheme where the atom number ratio between the two ground state Fermi gases is 10:1 and the Clebsch-Gordan coefficients for the decay are 0.82:0.18. Suppression is shown for various temperatures $T/T_F$ and Fermi energies $E_F/E_R$, quoted for the majority component.

branching ratio of the excited state. The number of atoms decaying to 9/2 as opposed to 7/2 can provide a separate confirmation of the blockade process. Finally, the decoherence rate of the atoms due to spontaneous emission can be measured by looking at the decay of Rabi oscillations. Below we discuss how we measure each of these observables.

To achieve fast, high SNR measurements, atomic state readout is performed using the 30.4 MHz broad $^1P_1$ transition, where roughly 100 photons can be scattered in 1 $\mu$s per atom. Around 1% of the fluoresced photons are subsequently detected using a high resolution imaging axis with an $NA = 0.23$. The experimental sequence to measure the lifetime is shown in Fig. 6.6 (a). First, the $m_F = 9/2$ atoms are excited to the $^3P_1$, $F = 11/2$, $m_F = 9/2$ state using a $\pi$ pulse. After a variable time $t_{wait}$, a 10 $\mu$s pulse of high intensity $^1P_1$ light causes significant recoil heating to the

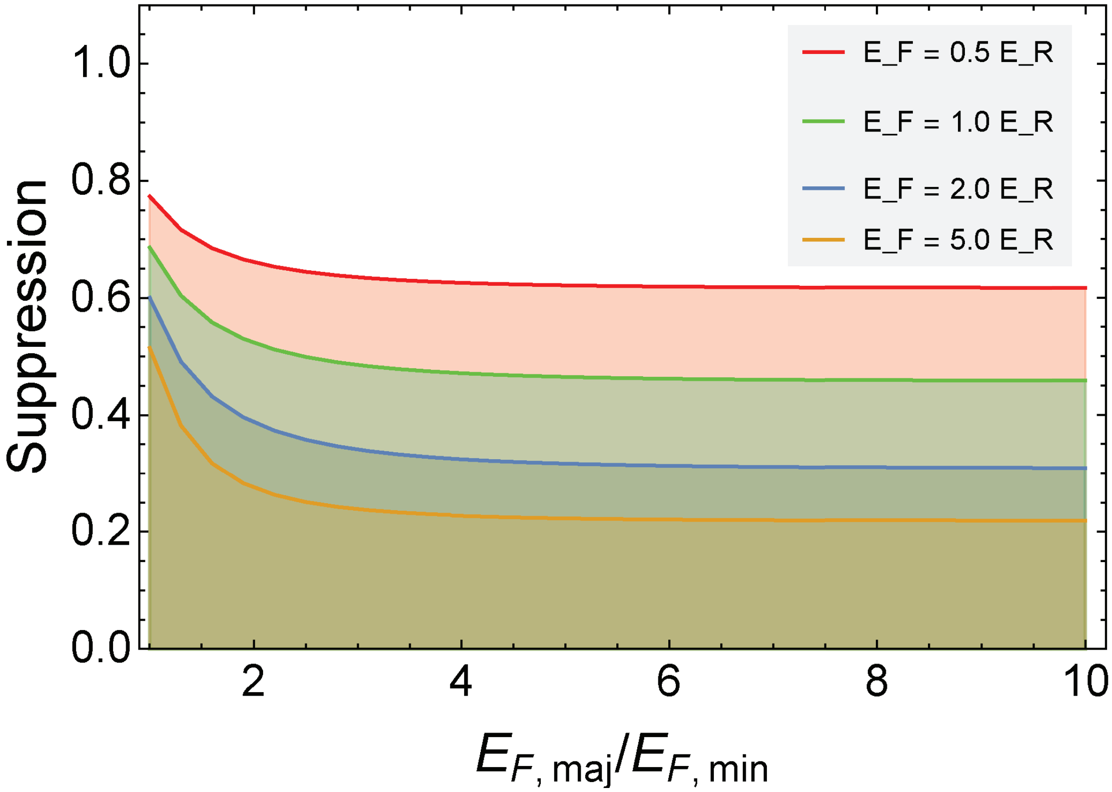

Figure 6.5: Total suppression for a three-level scheme where the Clebsch-Gordan coefficients for the decay are 0.82:0.18, and $T/T_F = 0.1$ with variable $E_F/E_R$ for the major component. Here the suppression is shown for different atom number imbalances for the major component and minor component ($E_F$ is quoted for the majority component in the legend).

ground state atoms, which are as a result removed from the trap. After a further 1 ms, all excited atoms have decayed and the ground state atoms are removed from the image. A fluorescence image is then taken during a 2 $\mu$s long $^1\mathrm{P}_1$ readout pulse, where light is collected using a vertical camera axis with an $NA = 0.23$. Wait times are varied from 1 $\mu$s to 200 $\mu$s, and 200 measurements are recorded over 20 different wait times. The wait time is randomized for each run. The lifetime is then extracted from the time constant, which is determined by fitting the entire data set to a single exponential. This allows us to time-resolve the decay of atoms out of the excited state. We originally used an alternative differential measurement technique that allowed us to measure the excitation fraction every shot so that we were immune to fluctuations in the total atom number. However, we found that our experiment was stable enough that this differential technique was

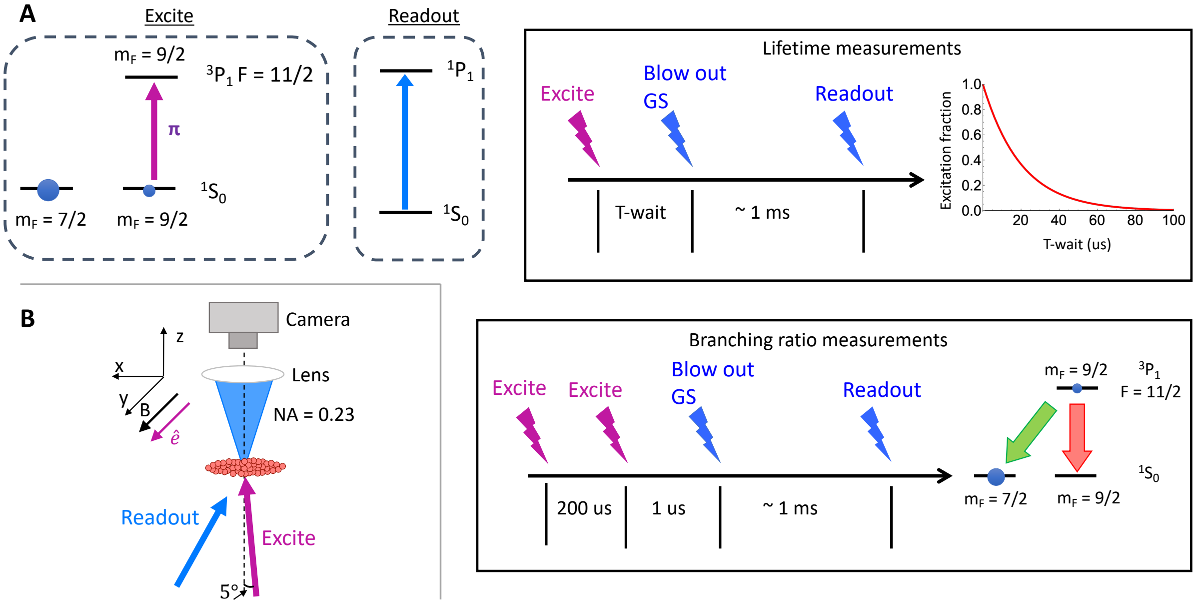

Figure 6.6: (a) Strategy to measure the excited state lifetime and the branching ratio from the $m_F = 9/2$ excited state. Atoms are excited on the narrow linewidth $^3P_1$ transition using a $\pi$ pulse and the excited atoms are read out using the broad $^1P_1$ transition. The upper and lower right panels describe how we measure the lifetime of excited atoms and the branching ratio of excited atoms back to $m_F = 9/2$, respectively, and are discussed in the main text. (b) Experimental setup. Excitation light probes a Fermi gas on-resonance with the $^1S_0$, $m_F = 9/2$ to $^3P_1$, $F = 11/2$, $m_F = 9/2$ transition. The ground state population is read out by taking a fluorescence image using the $^1P_1$ state, where the fluorescence is measured using a high NA imaging system.

unnecessary. To measure the decoherence rate (not shown), the same experimental procedure is used with $t_{wait} = 1\mu$s and a variable excitation time.

To measure the number of 9/2 atoms, the lifetime measurement can be repeated with T-wait = 1 $\mu$s, before any atoms have decayed. The branching ratio is then measured by first exciting all the atoms to 9/2 with a first $\pi$ pulse, waiting 200 $\mu$s for these atoms to decay, and then measuring the number of atoms that have decayed to 9/2 with another $\pi$ pulse (see Fig. 6.6 a). Comparing the total number of atoms that decay to $m_F = 9/2$ before and after the initial excitation pulse provides a measurement of the branching ratio on the $9/2 \rightarrow 9/2$ transition.

## 6.3 Optical depth considerations

We first measured a 28 $\mu$s lifetime of the excited state at $T/T_F = 0.1$, 30% longer than the natural lifetime. We soon discovered however that the longer-than-natural lifetime was insensitive to the temperature of the sample, indicating that other mechanisms were governing the radiative behavior. We also observed a faster-than-expected decoherence rate when Rabi flopping between the $\mathrm{m_F} = 9/2$ ground state and excited state. At the high central densities over $10^{14}$ atoms/cm$^3$ and on-axis optical depths (ODs) around 10 for each spin component, collective effects such as super and sub-radiance as well as multiple scattering influence the radiative properties of the atoms [205, 26]. In Chapter 5, we suppressed rescattering by detuning the drive frequency from the atomic resonance. This was a steady-state scattering experiment where atoms act like driven dipoles and light is scattered at the drive frequency. In contrast, here we are coherently driving atoms to the excited state and then extinguishing the drive. Atoms consequently spontaneously emit at the natural non-AC Stark shifted resonance frequency, and the probability of reabsorption is no longer reduced for a detuned drive. We thus sought to systematically study the competing mechanisms as the OD was changed for the different components, with the hope that we could find a parameter regime where we weren't sensitive to collective effects but still had an appreciable Pauli blocking signal.

Despite the long lifetime measured at thermal temperatures, we found evidence for superradiance in numerous measurements. By gating the camera on axis with the excitation laser within 1 $\mu$s of when the excitation pulse ends, we detected $> 10$ times more photons than what was expected through spontaneous emission alone. In addition, we measured a lifetime as short as 8 $\mu$s after exciting 9/2 atoms if the 7/2 component was first removed. With the 7/2 component in place, we also measured that up to 70% of the atoms returned to the $\mathrm{m_F} = 9/2$ ground state for a thermal gas with $T/T_F = 2.0$ despite a branching ratio of only 18%. By systematically varying the confinement and atom number of the $\mathrm{m_F} = 9/2$ component, we found that fractionally fewer atoms returned to the 9/2 ground state as the OD decreased, as shown in Fig. 6.7. The OD shown in this plot is

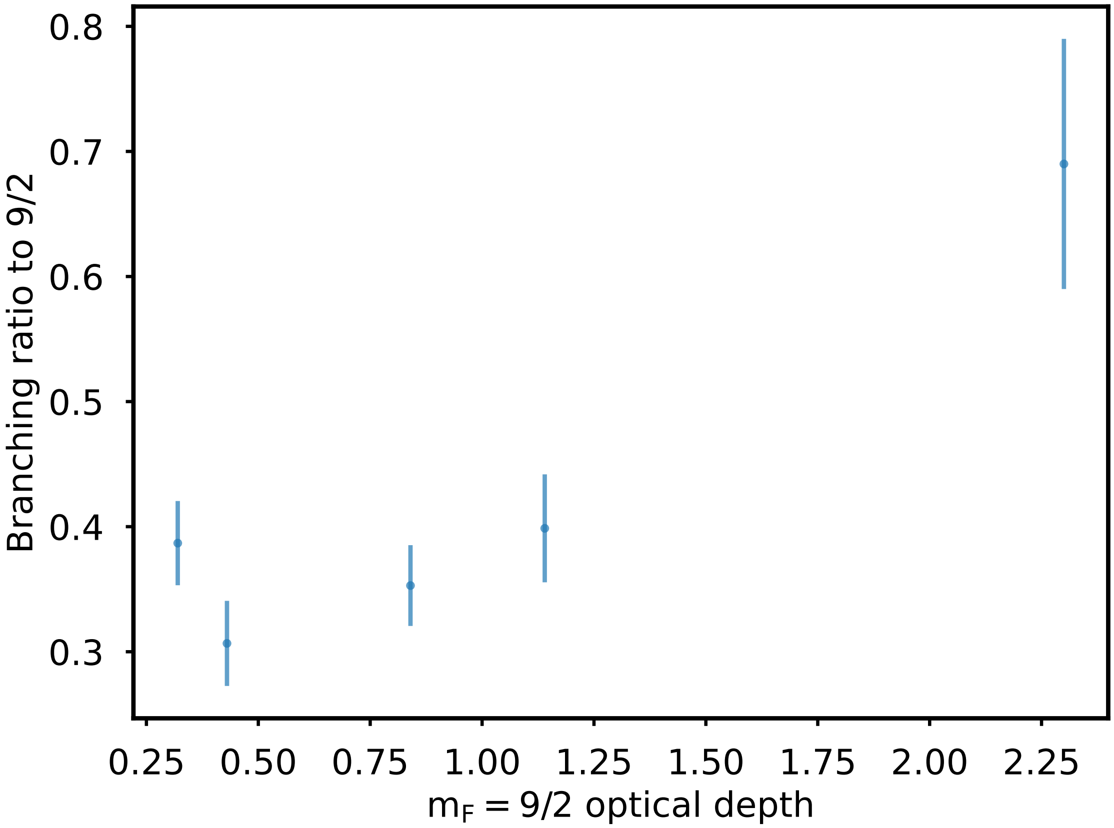

Figure 6.7: Fraction of atoms that return to the $m_F = 9/2$ ground state after the $m_F = 9/2$ atoms are excited to the $^3P_1$, $F = 11/2$, $m_F = 9/2$ state. Measurements are performed with a thermal sample where $T/T_F = 2.0$.

measured by counting the number of atoms in a central region of the Fermi gas and multiplying it by the cross-section, that is $OD = 3\lambda^2/2\pi \int n(0,0,z)dz$. We measured that the branching ratio approached a constant value for an $OD < 1$. The offset from 0.18, as expected from the Clebsch-Gordan coefficients, can be explained by residual excitation of the 7/2 atoms. Residual excitation of 7/2 atoms can occur through off-resonant excitation of the $\pi$-polarized probe light and due to polarization impurity, which can cause on-resonant excitation of 7/2 atoms to 9/2.

Once we reduced the $m_F = 9/2$ OD below 1, all measurable superradiant behavior disappeared. Coherent Rabi flopping on the 9/2 atoms in a thermal sample reproduced the expected profile given by the Rabi frequency and the spontaneous decay of the excited state, shown in Fig. 6.8,

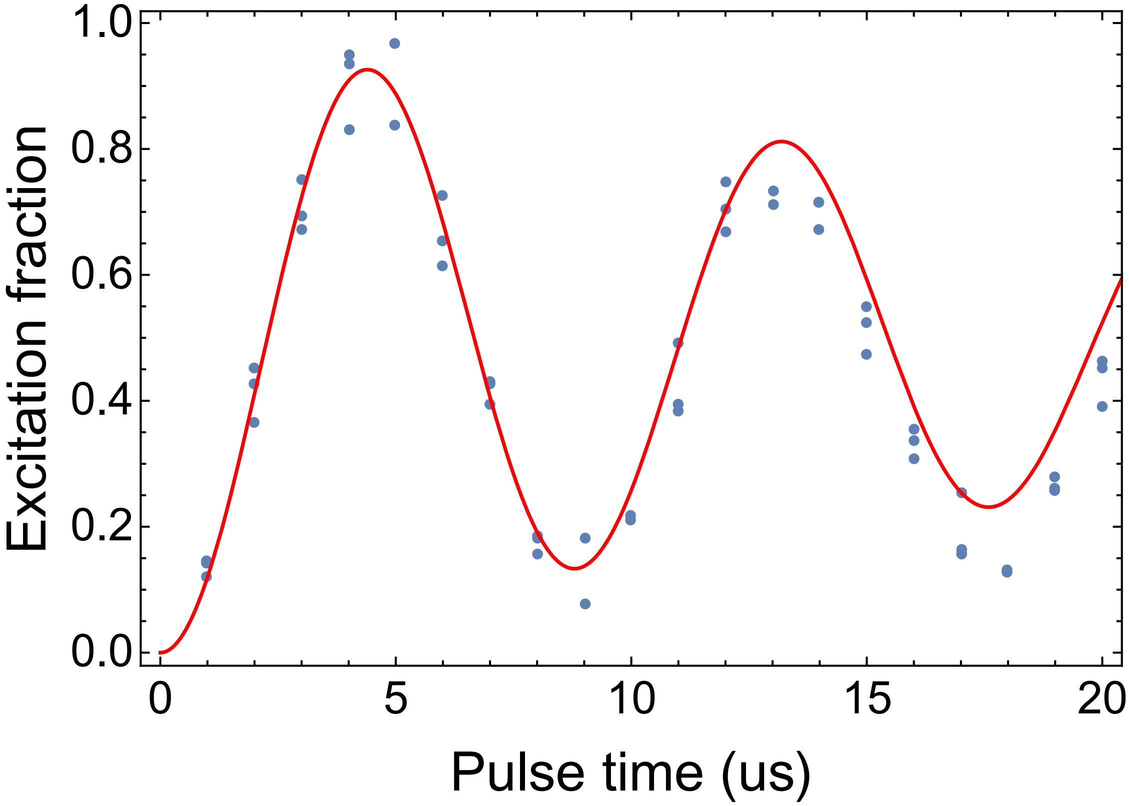

Figure 6.8: Rabi flopping on $^1\mathrm{S}_0$, $\mathrm{m_F} = 9/2 \rightarrow {}^3\mathrm{P}_1$, $\mathrm{m_F} = 9/2$ transition, measured on a thermal Fermi gas. The red line represents a fit using no free parameters and assuming the 21.28 $\mu$s natural lifetime for the excited state.

where the theory line is plotted for a two-level system with no free parameters. This experimental evidence suggests that superradiance predominantly occurs on the $9/2 \rightarrow 9/2$ transition, given by the phase imprint from the driving field.

Creating a sample with an OD $< 1$ for the $\mathrm{m_F} = 9/2$ atoms can easily be achieved by using fewer than 5000 atoms in 9/2 and by making our Fermi gas into a pancake, with tight axial frequencies of $\omega_z = 2\pi \times 700$ Hz and loose radial trap frequencies of $\omega_r = 2\pi \times 30$ Hz. The cloud is then probed along the z-direction for the minimal OD.

Despite the measured branching ratios at low 9/2 ODs that are close to the theory expectation, we still observed long lifetimes in non-degenerate Fermi samples. While superradiance seemed

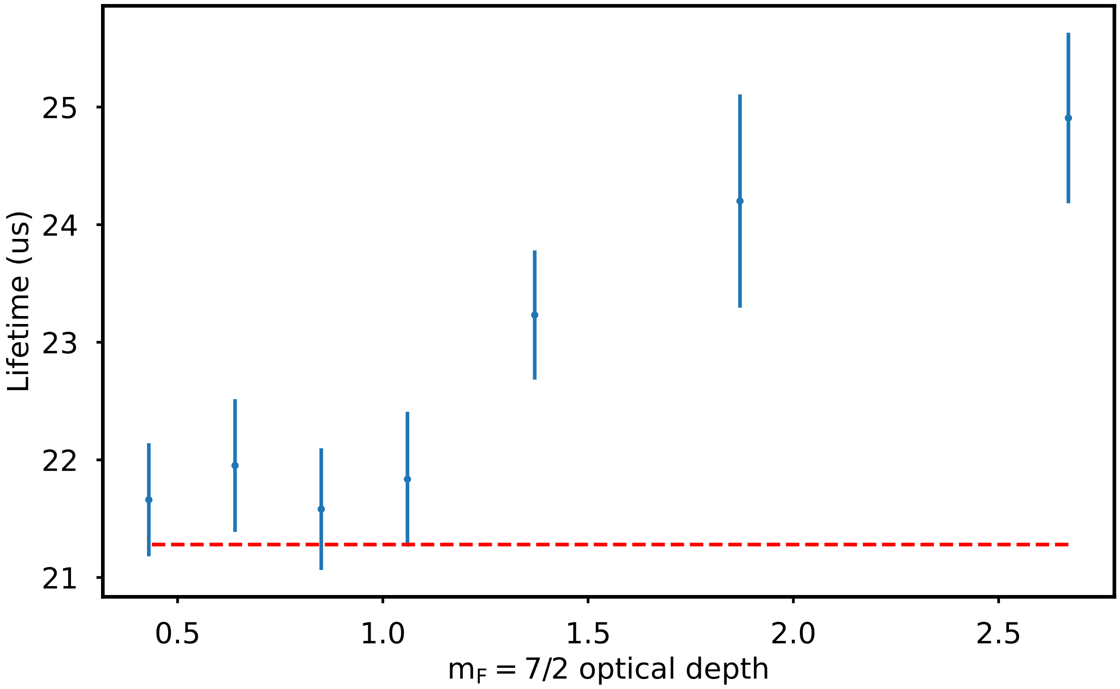

Figure 6.9: Lifetime versus $m_F = 7/2$ OD. Measurements are performed with a thermal sample where $T/T_F = 0.75$ at a 7/2 OD of 2.7. The 9/2 OD is fixed at 0.7 for all measurements.

to be removed by creating a sample with a 9/2 $OD < 1$, collective effects can still occur along the 7/2 channel, where the large Fermi sea creates an OD up to 5 at low temperatures. In particular, we suspect that multiple scattering is a dominant collective mechanism along the 7/2 channel. The lifetime was systematically measured in a thermal sample for various 7/2 ODs, as shown in Fig. 6.9. Here, the OD was changed by reducing the number of 7/2 atoms using optically pumping. We observed that the lifetime approached the natural lifetime as the 7/2 OD was reduced below 1.

Here is where we run into a challenge for observing Pauli blocking of the spontaneous emission rate on the $^3\mathrm{P}_1$ transition without any collective radiative effects that obscure the signal. Reducing the 9/2 OD removes collective effects on the 9/2 channel and simultaneously improves the Pauli blocking signal since fewer atoms in 9/2 creates a larger Fermi sea imbalance. In contrast, reducing the 7/2 OD reduces the major component's Fermi energy, which in turn degrades the Pauli blocking

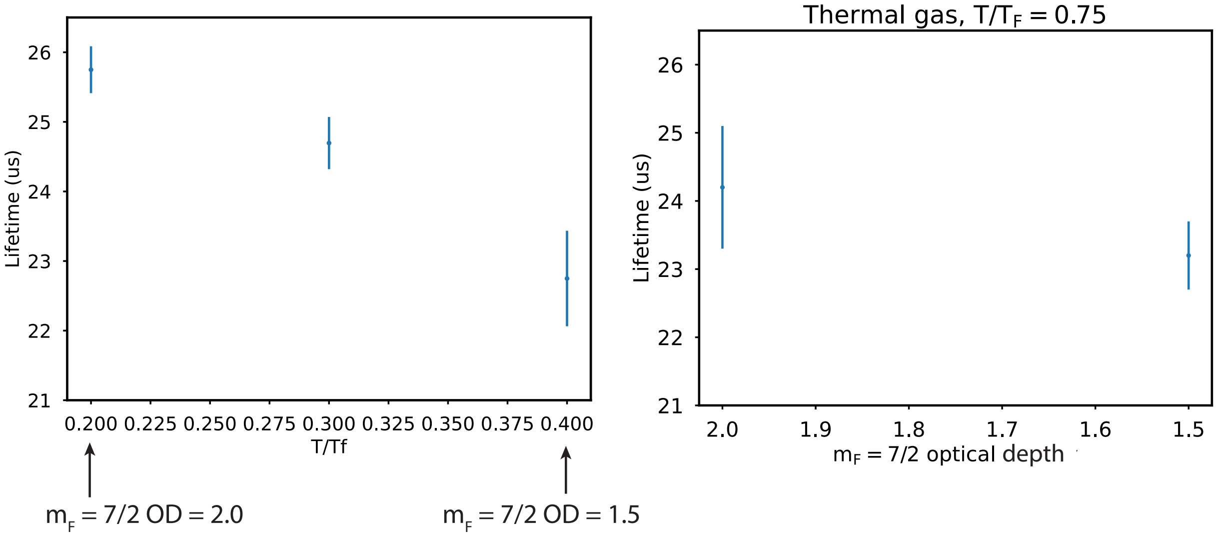

Figure 6.10: Measurements of the excited state lifetime for variable temperatures (here quoted for the majority component) while the OD is kept relatively constant. The 7/2 OD varies from 2.0 to 1.5 as $T/T_F$ is increased. Here the 9/2 OD is 0.7, and $T/T_F$ is quoted for the 7/2 component. Measurements of the lifetime performed for a thermal ($T/T_F = 0.75$) gas at equivalent ODs yield shorter lifetimes.

suppression.

## 6.4 Measurements with a cold sample

Given the measured dependence of collective radiative effects on the optical depth, we took differential measurements where we compared the lifetime at low and high temperatures with a fixed OD. Fig. 6.10 shows the lifetime as $T/T_F$ is increased, where the 7/2 OD changes from 2.0 to 1.5 across the measurement, and the maximum 9/2 OD is 0.7. The sample temperature is increased using parametric heating of the optical dipole trap. Measurements at the same 7/2 and 9/2 ODs but at a higher temperature show a reduced dependence on the OD, suggesting that the large differential effect we see at low temperatures is influenced by Pauli blocking. For the thermal samples, the 7/2 OD is varied by adjusting the number of atoms in $\mathrm{m_F} = 7/2$ using optical pumping. The measured decay curves from the excited state closely follow a single exponential at

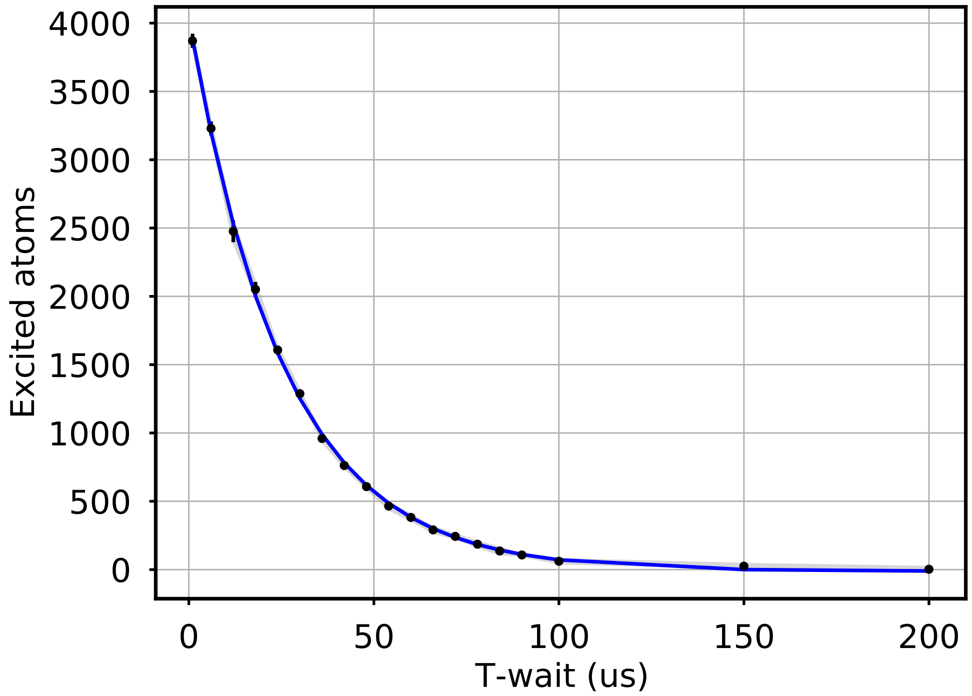

Figure 6.11: Full lifetime curve for a Fermi gas with a 7/2 OD of 2, a 9/2 OD of 0.7, and $T/T_F = 0.2$ for the major component. The blue line is an exponential fit to the data, which gives a $1/e$ lifetime of 25.7 ± 0.3 $\mu$s. Data points reflect the mean, and error bars are 1 standard deviation.

degenerate temperatures, as shown in Fig. 6.11 where a $1/e$ lifetime of 25.7 ± 0.3 $\mu$s is extracted.

We additionally measured the branching ratio from the $m_F = 9/2 \rightarrow m_F = 9/2$ transition for variable $T/T_F$, where the 7/2 OD and 9/2 OD was kept fixed by adjusting the number of atoms in each spin state using optical pumping. As shown in Fig. 6.12, as $T/T_F$ increased, we observed that fewer atoms return to the 9/2 ground state, which is consistent with Pauli blocking on the 7/2 channel causes more atoms to return to the 9/2 ground state at cold temperatures.

These measurements are suggestive that Pauli blocking is influencing the lifetime of excited atoms, but they rely on the assumption that the OD is the only important parameter for determining how much the lifetime is influenced by collective effects. To collect stronger evidence to claim the observation of Pauli blocking on $^3P_1$, we looked into alternative methods to observe Pauli blocking.

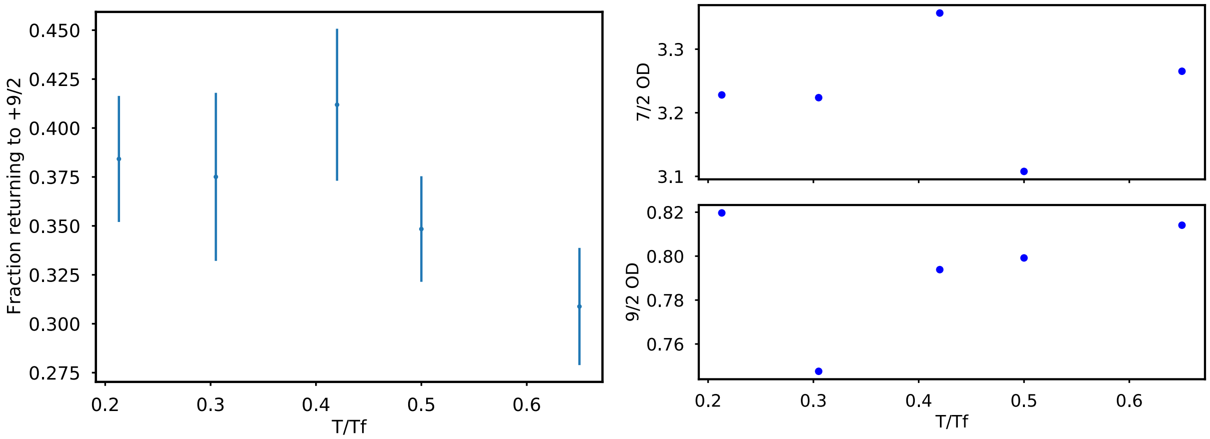

Figure 6.12: Fraction of atoms returning to $m_F = 9/2$ while the 7/2 and 9/2 optical depth are kept fixed. The temperature is quoted for the 7/2 component. As the sample is heated, the ratio decreases towards the non-Pauli blocked ratio. Here $T/T_F$ is quoted for the major component.

## 6.5 Measurements in a 1D optical lattice

Going to 2D has intriguing benefits for observing Pauli blocking in a coherent drive scheme as described here. First off, if the drive beam is along the tightest direction where the lattice confinement is large, the initial recoil associated with absorbing a photon is taken up by the trap instead of the atom, increasing the degree of suppression. Second, due to a change in the Fermi energy and the density of states in 2D, enhanced Pauli blocking is expected for a fixed atom number and radial trap frequency compared to 3D, and Pauli blocking can be observed at higher temperatures. Third, multiple scattering may be reduced. Even though the OD can be large along the radial direction, the probability that a photon will be spontaneously emitted along this direction is small - that is, the angle-averaged OD is quite small. Initial theory results that include the effects of both Pauli blocking and collective dynamics using a master equation suggest that multiple scattering is in fact reduced in a 2D geometry[1] . Doing measurements in a 1D optical lattice offers an alternative to a true 2D geometry if an experiment does not have immediate access to the required lattice setup. In a 1D optical lattice, it is desirable to load as few layers as possible.

---

[1] See an upcoming publication with Thomas Bilitewski and Ana Maria Rey.

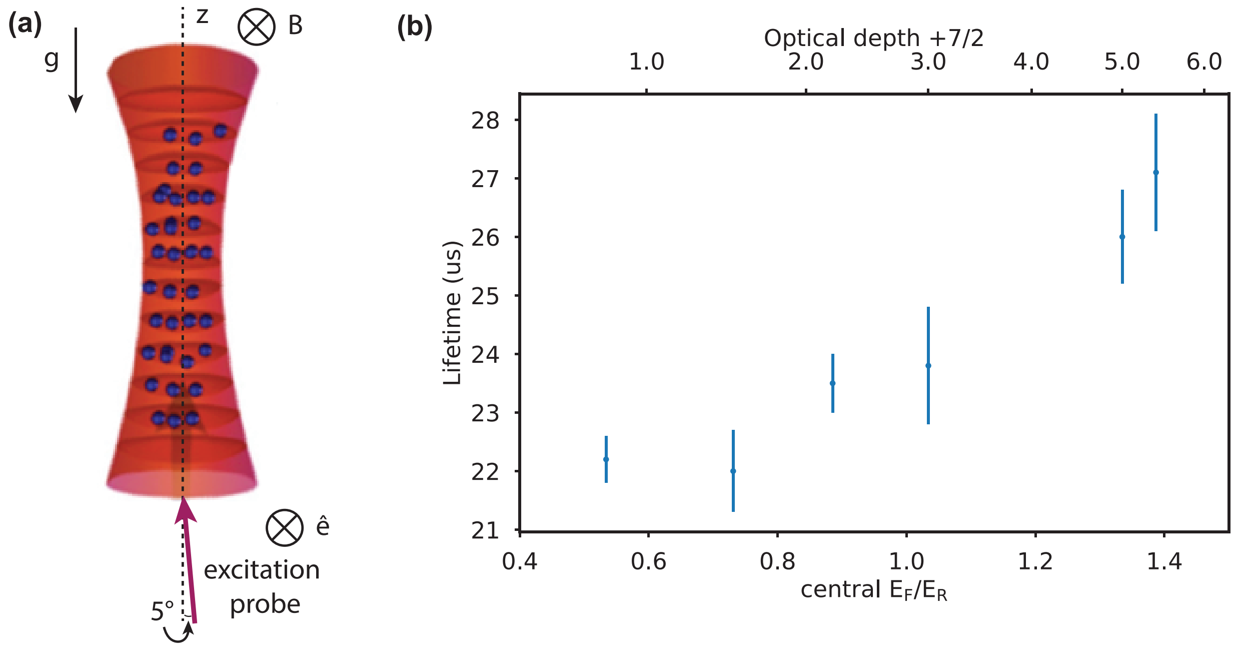

Figure 6.13: (a) Experimental setup to measure the lifetime in a 1D optical lattice. The optical lattice is formed along gravity, $g$, and the excitation probe polarization ($\hat{e}$ is along the magnetic field, which points into the page. (b) Lifetime of excited atoms in the 1D optical lattice versus $E_F/E_R$. The 9/2 OD is 0.8, and the temperature is $T/T_F = 0.6$ in the XODT when the 7/2 OD is 5.5.

For $E_F = 1E_{rec}$, a single layer has an OD of 1.5 along the tightly confined direction. However, how collective effects depend on the optical depth in a 2D gas and in a 1D optical lattice have not been studied.

Here we show measurements performed in a 1D optical lattice formed along the z direction, where the probe beam is incident with 5 degrees with respect to z, as shown in Fig. 6.13 (a). The axial trap frequency is $\nu_z = 44$ kHz, giving a Lamb-Dicke parameter along z of $\eta = \sqrt{\nu^p_{rec}/\nu_z} = 0.33$, where $\nu^p_{rec}$ is the recoil frequency of the probe laser. We use the scheme described in Fig. 6.6 (a) to measure the lifetime of the excited atoms. For these measurements, the 9/2 OD is 0.8 and $\omega_r = 2\pi \times 150$ Hz. The vertical extent of the cloud is 4 $\mu$m so that roughly 10 pancakes are loaded with 1000 atoms in 7/2 in the central pancake at $E_F/E_R = 1.4$. The temperature is $T/T_F = 0.6$ for

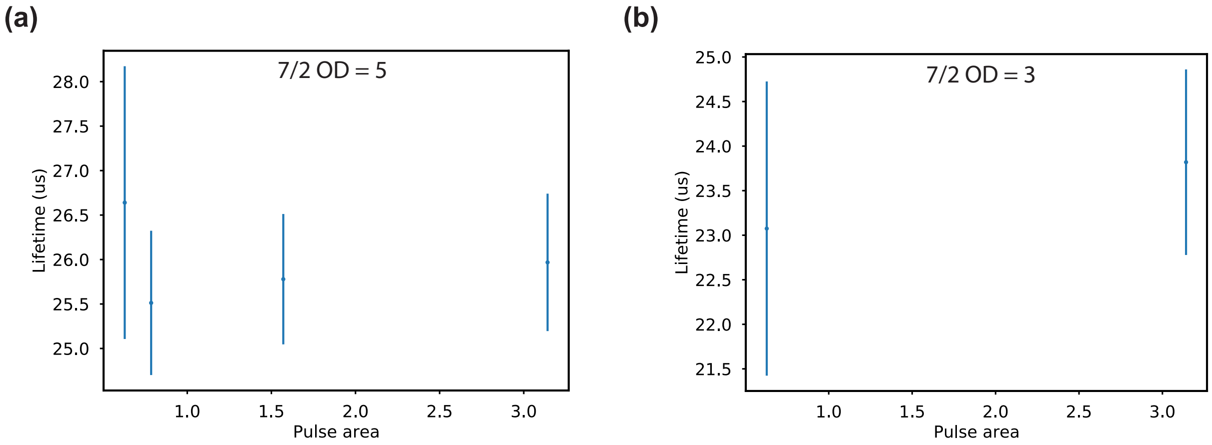

Figure 6.14: (a) Lifetime as the excitation pulse area is varied for a fixed 7/2 OD of 5 and a fixed 9/2 OD of 0.8 (b) Lifetime as the excitation pulse area is varied for a 7/2 OD of 3 and a 9/2 OD of 0.8

the 7/2 component. To achieve a temperature of $T/T_F = 0.6$, the Fermi gas is loaded into the 1D lattice and parametrically heated. The temperature is measured by fitting the expanded the Fermi gas in time-of-flight after the lattice is adiabatically decreased to 0 $E_{rec}$ and atoms are transferred to the XODT.

Fig. 6.13 (b) shows the measured lifetime as $E_F/E_R$ is varied for the 7/2 component. The 7/2 Fermi energy is varied by changing the number of 7/2 atoms using optical pumping. Similar to the 3D case, we observe that the lifetime increases as $E_F/E_R$, or equivalently the 7/2 OD, is increased. Contrary to the single 2D pancake case, in a 1D optical lattice, multiple scattering could still occur between pancakes, which makes interpreting the results more difficult. However, at $T/T_F = 0.6$, a Pauli suppression factor of 0.8 is expected in 2D. We measured the lifetime while varying the excitation pulse area at a fixed 7/2 $OD$ of 3, and separately for a fixed 7/2 $OD$ of 5, as shown in Fig. 6.14. In both cases the 9/2 OD was 0.8. Interestingly, we observe no difference in the lifetime as the pulse area is varied, suggesting that superradiance is absent in our system. This observation agrees with our measurements in a 3D gas, where we observed that superradiance disappeared once the 9/2 OD was less than 1.

While superradiance and multiple scattering have been extensively studied in 3D [205, 26], little research has been performed in 2D. Initial theory results suggest that multiple scattering is also suppressed in a 1D optical lattice.[2] More systematic measurements at a variety of temperatures and Fermi energies would be a fruitful future study to clarify the role of Pauli blocking and collective dynamics in this system.

## 6.6 Outlook

To observe the effects of Pauli blocking with an excitation scheme that coherently controls the atomic state, as discussed here, it is desirable to go to a 2D gas with a single layer. Here, the on-axis OD can be quite small and the Fermi energies large so that significant Pauli suppression is expected without the influence of competing collective radiative mechanisms. The three-level system we outline here has the advantage of having multiple observables to confirm Pauli blocking. In addition to measuring the lifetime of the excited state, the branching ratios between the two ground states and the excite state provide a new angle to observe the suppression. The technique presented in this chapter to measure the branching ratio was associated with systematic effects that caused residual excitation of 7/2 atoms, which limited us from observing the natural branching ratio of 0.18 at low ODs and thermal temperatures. A larger magnetic field would help with off-resonant excitation, but polarization impurity, which can excite 7/2 atoms to the 9/2 excited state, will always be on-resonance with the probe. Reducing the impurity below a percent is difficult. It would thus be optimal to devise an alternative strategy to measure the branching ratio, perhaps using optical Stern-Gerlach separation to measure the ground state spin population [113]. However, the spin states need to be spatially well-separated since small changes in the minority component need to be detected at high SNR, which can be technically difficult since this component has significantly fewer atoms than other spin states. Additionally, it is intriguing to think of measuring Pauli blocking by looking at the coherence time after continuously Rabi flopping on the desired

---

[2] See an upcoming publication by Thomas Bilitewski, Ana Maria Rey, and others.

state. While effects such as multiple scattering can change the lifetime as atoms spend more time on average in the excited state, it should not increase the coherence time. Our initial measurements of the coherence time did not lead to obvious results but more study into this effect could be fruitful. Finally, to use Pauli blocking in 3D optical lattice clocks, it is desirable to measure Pauli blocking in a 3D optical lattice as opposed to a Fermi gas [198]. This could be demonstrated using a similar three-level scheme with two atoms per lattice site.

# Chapter 7

# Conclusion

In this thesis, we present multiple results that highlight how quantum gas engineering can enhance the performance of Fermi-degenerate optical atomic clocks. Here, we provide a brief summary of the results reported in this thesis and provide an outlook on future research directions.

## 7.1 Summary

To improve the dead time of Fermi-degenerate atomic clocks, we described an experiment that used multiple nuclear spin states with SU(N) symmetry during evaporation to increase cooling rates. The compressibility and expansion dynamics of the SU(N)-interacting Fermi gas were studied in detail. This new cooling scheme allows us to significantly reduce the preparation time of Fermi-degenerate 3D optical lattice clocks, in turn reducing the Dick Effect for such systems to mid-$10^{-17}/\sqrt{\tau}$ if coherently interrogated for a few seconds using a state-of-the-art ultrastable laser.

We additionally showed that Fermi-degenerate gases can be used to reduce the spontaneous emission and light scattering rates using Pauli blocking. Pauli blocking exploits Fermi statistics to prohibit decay of an excited atom to states already occupied by an identical fermion. By embedding excitations within a degenerate Fermi sea, we measured up to a factor of two reduction in the light scattering rate along a direction where the net momentum transfer from the excitation light was reduced. Our method employed multiple precautionary measurements, including simultaneous observation of the fluoresced light under different angles (with different net momentum transfer) and measurements with hole-poked Fermi gases at the same density, to conclusively rule out potential competing radiative mechanisms. Our results agreed with a simple semiclassical model with no free parameters besides a single common scaling factor for the data.

We also presented results from an experiment that attempted to observe Pauli blocking using coherent spectroscopy on the $^3\mathrm{P}_1$ narrow linewidth transition. We presented a series of measurements in a bulk 3D Fermi gas and initial measurements in a 1D optical lattice. In the former we carefully explored the dependence of the lifetime on the optical depth.

The work presented in this thesis showcases a common theme in atomic physics: improvements in our fundamental understanding of quantum science goes hand in hand with advancing quantum technology. This connection between the very fundamental and the very practical is a cornerstone of our advances in AMO physics, and highlights the interlaced connections between academia, industry, and society at large.

## 7.2 Outlook

In the future, engineered light-matter interfaces could provide a new means to create next-generation optical lattice clocks. Contrary to what is practical using common light-matter interfaces such as an optical cavity, Pauli blocking provides an avenue to change the total decoherence rate of an atom. For large Fermi energies and low temperatures, the spontaneous emission rate can be reduced for all emission angles, resulting in a measurable change in the total (angle-averaged) spontaneous emission rate. Suppression larger than what we demonstrated can be achieved using a higher Fermi energy, or if instead the gas is loaded into a deep optical lattice. If Pauli blocking is implemented in a 3D optical lattice, it could be used to increase the coherence time of current optical atomic clocks beyond the limit given by the natural lifetime of an atomic transition.

One could even imagine using this technique to provide more flexibility in the chosen atomic clock transition. Instead of optimizing for insensitivity to a range of environmental parameters and simultaneously a long natural lifetime for narrow spectroscopy purposes, one could pick an atomic transition that is optimally insensitive to the environment, perhaps at the cost of a slightly shorter natural lifetime. Pauli blocking (or other cooperative techniques) could then be used to push the system into spectroscopic competitivity. In order to use Pauli blocking for practical devices, it is necessary to do a bit more homework on how the physical mechanism can be realized using coherent spectroscopy as would be necessary in a real quantum device. Of course the challenge with this mechanism is to find a way to remove cooperative scattering while still keeping other important quantities such as atom numbers high.

One could also use these competing radiative mechanisms as the dominant means for creating next-generation atomic clocks. A subradiant array of atoms is an alternative means to engineer longer lifetimes, the promise of which has been demonstrated using a 2D array of $^{87}$Rb atoms [211]. Avenues to observe subradiance in fermionic atoms with a multilevel internal structure such as $^{87}$Sr have also been discussed theoretically [212].

Superradiant lasers [213] reference the linewidth of the laser to an atomic transition, for the case of the clock transition in $^{87}$Sr, 1 mHz. A continuous superradiant laser has the potential to reduce the reliance of local oscillators on length standards, which could be advantageous as creating ultrastable resonators is a significant technical challenge. This system may one day allow the local oscillator and atomic reference to be combined into one device, removing the need for a distributed clock system.

By combining atomic clocks with optical cavities, one could demonstrate non-destructive detection of the atomic state, reducing dead time substantially. The combination of non-destructive measurement and spin squeezing using an optical cavity could create an atomic clock whose stability that surpasses the state-of-the-art and is better than the Standard Quantum Limit [214]. In the end, creating a system where each degree of freedom can be controlled and manipulated for the optimal conditions will only provide more opportunities and competitive avenues for quantum devices.

On the accuracy front, it will be interesting to study dipole-dipole interactions in the 3D optical lattice clock. The same physics that gives rise to cooperative scattering also implies the existence of dipole-dipole coupling between emitters. A spin-polarized 3D optical lattice clock removes contact interactions by making doubly occupied sites energetically suppressed by the bandgap. However, there are still higher order long-range interactions due to dipole-dipole interactions, which could be enhanced given the regularity of the atom array and the sub-wavelength spacing between emitters. At first glance, you might assume that such an interaction effect is very small given the strength roughly scales like the linewidth, in this case only 1 mHz. However, even frequency shifts at a fraction of the linewidth are now measurable in modern clocks. Diagnosing the spatial dependence of the dipole-dipole shift using our high-resolution imaging system will provide a deterministic avenue to ensure the minute shifts are due to dipole-dipole interactions instead of a number of other potential systematics such as AC Stark shifts, BBR gradients, and Zeeman shifts. After measuring the shift we can explore different lattice geometries [215] or spin components [216] to reduce this shift below a measurable quantity.

A Fermi-degenerate 3D optical lattice clock could also offer a clean way to measure higher-order ac Stark shift coefficients, since the trapping potential occupation number is well-controlled in all three directions. One challenge is that the hyperpolarizability coefficient changes for lattice beams that have a different polarization. Measuring the spatial dependence of such shifts could provide a sensitive detection method.

Engineering longer lifetimes also requires us to actually be limited by the natural lifetime of the excited clock state, which is 118 s for $^3\mathrm{P}_0$ [58]. Reducing the lattice depth along all three axes to below 4 $E_{rec}$ is necessary to not be limited by Raman scattering, but one then needs to find a means to have low tunneling rates [55]. An optical lattice with a larger lattice spacing can reduce the tunneling rate, which was used in an optical tweezer experiment with $^{88}\mathrm{Sr}$ to demonstrate a coherence time of 20 s for an 150 atom tweezer array [57]. Tweezer clocks are an intriguing avenue for future metrology but will need to solve scaling to a competitive number of atoms, as well as demonstrate a robust systematic evaluation. Alternatively lattices can be formed by interfering two beams at an angle to create a large lattice spacing that still operates at the magic wavelength necessary for state-independent trapping. A near-unity filled optical lattice could significantly relax the lattice spacing requirement as it suppresses tunneling between occupied lattice sites, although distinguishability created through the clock excitation will continue to be an issue unless the lattice spacing is made to be commensurate with the clock light.

The future of quantum precision metrology is quite bright — the combination of better control over atomic systems and further improvements in measurement stability and accuracy promises many exciting discoveries. Clock performance will one day reach the limit where new physics is limiting our measurements. This new physics could be fluctuating fundamental constants [16], dark matter [23], or a tantalizing idea, maybe even one day gravitational waves [24]. Moving atomic clocks outside the laboratory, and potentially into outer space, will provide even more opportunities for discovery. Regardless, the scientific attitude of understanding fundamentally the underlying system and its current limits will allow us to propose new solutions to better improve our devices, which in turn will lead to new scientific discoveries and to practical technologies for society.

# Bibliography

[1] Scott A. Diddams. The evolving optical frequency comb *Invited*. J. Opt. Soc. Am. B, 27(11):B51–B62, Nov 2010.

[2] `https://www.bipm.org`. Accessed: 2021-06-01.

[3] E. Oelker, R. B. Hutson, C. J. Kennedy, L. Sonderhouse, T. Bothwell, A. Goban, D. Kedar, C. Sanner, J. M. Robinson, G. E. Marti, D. G. Matei, T. Legero, M. Giunta, R. Holzwarth, F. Riehle, U. Sterr, and J. Ye. Demonstration of 4.8e-17 stability at 1 s for two independent optical clocks. Nature Photonics, pages 1–6, July 2019.

[4] M. Schioppo, R. C. Brown, W. F. McGrew, N. Hinkley, R. J. Fasano, K. Beloy, T. H. Yoon, G. Milani, D. Nicolodi, J. A. Sherman, N. B. Phillips, C. W. Oates, and A. D. Ludlow. Ultrastable optical clock with two cold-atom ensembles. Nature Photonics, 11(1):48–52, January 2017.

[5] Thomas Parker. The uncertainty in the realization and dissemination of the si second from a systems point of view. Rev. Sci. Instrum., 83:021102, 2012.

[6] Tobias Bothwell, Dhruv Kedar, Eric Oelker, John M. Robinson, Sarah L. Bromley, Weston L. Tew, Jun Ye, and Colin J. Kennedy. JILA SrI optical lattice clock with uncertainty of $2.0 \times 10^{-18}$. Metrologia, 56:065004, October 2019.

[7] N. Huntemann, C. Sanner, B. Lipphardt, Chr. Tamm, and E. Peik. Single-ion atomic clock with $3 \times 10^{-18}$ systematic uncertainty. Phys. Rev. Lett., 116(6):063001, February 2016.

[8] S.M. Brewer, J.-S. Chen, A.M. Hankin, E.R. Clements, C.W. Chou, D.J. Wineland, D.B. Hume, and D.R. Leibrandt. $^{27}Al^{+}$ quantum-logic clock with a systematic uncertainty below $10^{-18}$. Phys. Rev. Lett., 123(3):033201, July 2019.

[9] W. F. McGrew, X. Zhang, R. J. Fasano, S. A. Schäffer, K. Beloy, D. Nicolodi, R. C. Brown, N. Hinkley, G. Milani, M. Schioppo, T. H. Yoon, and A. D. Ludlow. Atomic clock performance enabling geodesy below the centimetre level. Nature, 564(7734):87–90, December 2018.

[10] L. von der Wense and B. Seiferle. The 229th isomer: prospects for. nuclear optical clock. Eur. Phys. J. A, 56:277, 2020.

[11] I. Pupeza, C. Zhang, M. Högner, and J. Ye. Extreme-ultraviolet frequency combs for precision metrology and attosecond science. Nat. Photonics, 15:175–186, 2021.

[12] Fritz Riehle. Towards a redefinition of the second based on optical atomic clocks. Comptes Rendus Physique, 16(5):506–515, 2015. The measurement of time / La mesure du temps.

[13] Tetsushi Takano, Masao Takamoto, Ichiro Ushijima, Noriaki Ohmae, Tomoya Akatsuka, Atsushi Yamaguchi, Yuki Kuroishi, Hiroshi Munekane, Basara Miyahara, and Hidetoshi Katori. Geopotential measurements with synchronously linked optical lattice clocks. Nature Photonics, 10(10):662–666, October 2016.

[14] C. W. Chou, D. B. Hume, T. Rosenband, and D. J. Wineland. Optical clocks and relativity. Science, 329(5999):1630–1633, 2010.

[15] Jacopo Grotti, Silvio Koller, Stefan Vogt, Sebastian Häfner, Uwe Sterr, Christian Lisdat, Heiner Denker, Christian Voigt, Ludger Timmen, Antoine Rolland, Fred N. Baynes, Helen S. Margolis, Michel Zampaolo, Pierre Thoumany, Marco Pizzocaro, Benjamin Rauf, Filippo Bregolin, Anna Tampellini, Piero Barbieri, Massimo Zucco, Giovanni A. Costanzo, Cecilia Clivati, Filippo Levi, and Davide Calonico. Geodesy and metrology with a transportable optical clock. Nature Phys, 14(5):437–441, May 2018.

[16] T. Rosenband, D. B. Hume, P. O. Schmidt, C. W. Chou, A. Brusch, L. Lorini, W. H. Oskay, R. E. Drullinger, T. M. Fortier, J. E. Stalnaker, S. A. Diddams, W. C. Swann, N. R. Newbury, W. M. Itano, D. J. Wineland, and J. C. Bergquist. Frequency ratio of al+ and hg+ single-ion optical clocks; metrology at the 17th decimal place. Science, 319(5871):1808–1812, 2008.

[17] N. Huntemann, B. Lipphardt, Chr. Tamm, V. Gerginov, S. Weyers, and E. Peik. Improved limit on a temporal variation of $m_p/m_e$ from comparisons of yb$^+$ and cs atomic clocks. Phys. Rev. Lett., 113:210802, Nov 2014.

[18] R. M. Godun, P. B. R. Nisbet-Jones, J. M. Jones, S. A. King, L. A. M. Johnson, H. S. Margolis, K. Szymaniec, S. N. Lea, K. Bongs, and P. Gill. Frequency ratio of two optical clock transitions in $^{171}$yb$^+$ and constraints on the time variation of fundamental constants. Phys. Rev. Lett., 113:210801, Nov 2014.

[19] Christian Sanner, Nils Huntemann, Richard Lange, Christian Tamm, Ekkehard Peik, Marianna S. Safronova, and Sergey G. Porsev. Optical clock comparison for Lorentz symmetry testing. Nature, 567(7747):204–208, March 2019.

[20] P. Delva, J. Lodewyck, S. Bilicki, E. Bookjans, G. Vallet, R. Le Targat, P.-E. Pottie, C. Guerlin, F. Meynadier, C. Le Poncin-Lafitte, O. Lopez, A. Amy-Klein, W.-K. Lee, N. Quintin, C. Lisdat, A. Al-Masoudi, S. Dörscher, C. Grebing, G. Grosche, A. Kuhl, S. Raupach, U. Sterr, I. R. Hill, R. Hobson, W. Bowden, J. Kronjäger, G. Marra, A. Rolland, F. N. Baynes, H. S. Margolis, and P. Gill. Test of special relativity using a fiber network of optical clocks. Phys. Rev. Lett., 118:221102, Jun 2017.

[21] A. Derevianko and M. Poselov. Hunting for topological dark matter with atomic clocks. Nat. Phys., 10:933–936, 2014.

[22] Asimina Arvanitaki, Junwu Huang, and Ken Van Tilburg. Searching for dilaton dark matter with atomic clocks. Phys. Rev. D, 91(1):015015, January 2015.

[23] Colin J. Kennedy, Eric Oelker, John M. Robinson, Tobias Bothwell, Dhruv Kedar, William R. Milner, G. Edward Marti, Andrei Derevianko, and Jun Ye. Precision metrology meets cosmology: Improved constraints on ultralight dark matter from atom-cavity frequency comparisons. Phys. Rev. Lett., 125:201302, Nov 2020.

[24] S. Kolkowitz, I. Pikovski, N. Langellier, M.D. Lukin, R.L. Walsworth, and J. Ye. Gravitational wave detection with optical lattice atomic clocks. Phys. Rev. D, 94(12):124043, December 2016.

[25] M. J. Martin, M. Bishof, M. D. Swallows, X. Zhang, C. Benko, J. von Stecher, A. V. Gorshkov, A. M. Rey, and Jun Ye. A quantum many-body spin system in an optical lattice clock. Science, 341(6146):632–636, August 2013.

[26] S. Bromley, B. Zhu, M. Bishof, X. Zhang, T. Bothwell, J. Schachenmayer, T.L. Nicholson, R. Kaiser, S.F. Yelin, M.D. Lukin, A.M. Rey, and J. Ye. Collective atomic scattering and motional effects in a dense coherent medium. Nat. Commun., 7:11039, 2016.

[27] S. Kolkowitz, S.L. Bromley, T. Bothwell, M.L. Wall, G.E. Marti, A.P. Koller, X. Zhang, A.M. Rey, and J. Ye. Spin–orbit-coupled fermions in an optical lattice clock. Nature, 542:66–70, 2017.

[28] S.L. Bromley, S. Kolkowitz, T. Bothwell, D. Kedar, A. Safavi-Naini, M.L. Wall, C. Salomon, A.M. Rey, and J. Ye. Dynamics of interacting fermions under spin–orbit coupling in an optical lattice clock. Nat. Phys., 14:399–404, 2018.

[29] W. M. Itano, J. C. Bergquist, J. J. Bollinger, J. M. Gilligan, D. J. Heinzen, F. L. Moore, M. G. Raizen, and D. J. Wineland. Quantum projection noise: Population fluctuations in two-level systems. Phys. Rev. A, 47(5):3554–3570, May 1993.

[30] G. J. Dick. Local oscillator induced instabilities in trapped ion frequency standards. Technical report, CALIFORNIA INST OF TECH PASADENA JET PROPULSION LAB, December 1987.

[31] Ali Al-Masoudi, Sören Dörscher, Sebastian Häfner, Uwe Sterr, and Christian Lisdat. Noise and instability of an optical lattice clock. Phys. Rev. A, 92(6):063814, December 2015.

[32] E.G. Marti, R.B. Hutson, Goban A., Campbell S.L., N. Poli, and J. Ye. Imaging optical frequencies with 100$\mu$Hz precision and 1.1$\mu$m resolution. Phys. Rev. Lett., 120:103201, March 2018.

[33] M. Takamoto, T. Takano, and H. Katori. Frequency comparison of optical lattice clocks beyond the dick limit. Nat. Photon., 5:288–292, 2011.

[34] D.G. Matei, T. Legero, S. Häfner, C. Grebing, R. Weyrich, W. Zhang, L. Sonderhouse, J.M. Robinson, J. Ye, F. Riehle, and U. Sterr. 1.5$\mu m$ lasers with sub-10 mhz linewidth. Phys. Rev. Lett., 118(26):263202, June 2017.

[35] M. Bishof, X. Zhang, M. J. Martin, and Jun Ye. Optical spectrum analyzer with quantum-limited noise floor. Phys. Rev. Lett., 111:093604, Aug 2013.

[36] M. J. Martin. Quantum metrology and many-body physics: pushing the frontier of the optical lattice clock. PhD thesis, University of Colorado Boulder, 2013.

[37] Sebastian Häfner, Stephan Falke, Christian Grebing, Stefan Vogt, Thomas Legero, Mikko Merimaa, Christian Lisdat, and Uwe Sterr. $8 \times 10^{-17}$ fractional laser frequency instability with a long room-temperature cavity. Opt. Lett., 40(9):2112–2115, May 2015.

[38] T. Kessler, C. Hagemann, C. Grebing, T. Legero, U. Sterr, F. Riehle, M.J. Martin, L. Chen, and J. Ye. A sub-40-mhz-linewidth laser based on a silicon single-crystal optical cavity. Nat. Photon., 6:687–692, 2012.

[39] J.E. Gray and D.W. Allan. A method for estimating the frequency stability of an individual oscillator. In 28th Annual Symposium on Frequency Control, pages 243–246, 1974.

[40] William R. Milner, John M. Robinson, Colin J. Kennedy, Tobias Bothwell, Dhruv Kedar, Dan G. Matei, Thomas Legero, Uwe Sterr, Fritz Riehle, Holly Leopardi, Tara M. Fortier, Jeffrey A. Sherman, Judah Levine, Jian Yao, Jun Ye, and Eric Oelker. Demonstration of a timescale based on a stable optical carrier. Phys. Rev. Lett., 123:173201, Oct 2019.

[41] E. Rubiola and F. Vernotte. The cross-spectrum experimental method. arXiv preprint arXiv:1003.0113, 2010.

[42] T. L. Nicholson, M. J. Martin, J. R. Williams, B. J. Bloom, M. Bishof, M. D. Swallows, S. L. Campbell, and J. Ye. Comparison of two independent sr optical clocks with $1 \times 10^{-17}$ stability at $10^3$ s. Phys. Rev. Lett., 109:230801, Dec 2012.

[43] Stefan Seel, Rafael Storz, Giuseppe Ruoso, Jürgen Mlynek, and Stephan Schiller. Cryogenic optical resonators: A new tool for laser frequency stabilization at the 1 hz level. Phys. Rev. Lett., 78:4741–4744, Jun 1997.

[44] W. Zhang, J. M. Robinson, L. Sonderhouse, E. Oelker, C. Benko, J. L. Hall, T. Legero, D. G. Matei, F. Riehle, U. Sterr, and J. Ye. Ultrastable silicon cavity in a continuously operating closed-cycle cryostat at 4 k. Phys. Rev. Lett., 119:243601, Dec 2017.

[45] John M. Robinson, Eric Oelker, William R. Milner, Wei Zhang, Thomas Legero, Dan G. Matei, Fritz Riehle, Uwe Sterr, and Jun Ye. Crystalline optical cavity at 4 k with thermal-noise-limited instability and ultralow drift. Optica, 6(2):240–243, Feb 2019.

[46] G. D. Cole, W. Zhang, M. J. Martin, J. Ye, and M. Aspelmeyer. Tenfold reduction of brownian noise in high-reflectivity optical coatings. Nat. Photon., 7:644–650, 2013.

[47] Garrett D. Cole, Wei Zhang, Bryce J. Bjork, David Follman, Paula Heu, Christoph Deutsch, Lindsay Sonderhouse, John Robinson, Chris Franz, Alexei Alexandrovski, Mark Notcutt, Oliver H. Heckl, Jun Ye, and Markus Aspelmeyer. High-performance near- and mid-infrared crystalline coatings. Optica, 3(6):647–656, Jun 2016.

[48] Andrew D. Ludlow, Martin M. Boyd, Jun Ye, E. Peik, and P. O. Schmidt. Optical atomic clocks. Rev. Mod. Phys., 87:637–701, Jun 2015.

[49] S. L. Campbell, R. B. Hutson, G. E. Marti, A. Goban, N. Darkwah Oppong, R. L. McNally, L. Sonderhouse, J. M. Robinson, W. Zhang, B. J. Bloom, and J. Ye. A Fermi-degenerate three-dimensional optical lattice clock. Science, 358(6359):90–94, October 2017.

[50] Tomoya Akatsuka, Masao Takamoto, and Hidetoshi Katori. Three-dimensional optical lattice clock with bosonic $^{88}$Sr atoms. Phys. Rev. A, 81:023402, Feb 2010.

[51] L. Sonderhouse, C. Sanner, R.B. Hutson, A. Goban, T. Bilitewski, L.F. Yan, W.R. Milner, A.M. Rey, and J. Ye. Thermodynamics of a deeply degenerate su($n$)-symmetric fermi gas. Nat. Phys., 16:1216–1221, 2020.

[52] P. G. Westergaard, J. Lodewyck, L. Lorini, A. Lecallier, E. A. Burt, M. Zawada, J. Millo, and P. Lemonde. Lattice-induced frequency shifts in sr optical lattice clocks at the $10^{-17}$ level. Phys. Rev. Lett., 106:210801, May 2011.

[53] S. G. Porsev, M. S. Safronova, U. I. Safronova, and M. G. Kozlov. Multipolar polarizabilities and hyperpolarizabilities in the sr optical lattice clock. Phys. Rev. Lett., 120:063204, Feb 2018.

[54] A. Goban, R. B. Hutson, G. E. Marti, S. L. Campbell, M. A. Perlin, P. S. Julienne, J. P. D'Incao, A. M. Rey, and J. Ye. Emergence of multi-body interactions in a fermionic lattice clock. Nature, 563(7731):369–373, November 2018.

[55] Ross B. Hutson, Akihisa Goban, G. Edward Marti, Lindsay Sonderhouse, Christian Sanner, and Jun Ye. Engineering quantum states of matter for atomic clocks in shallow optical lattices. Phys. Rev. Lett., 123:123401, September 2019.

[56] Sören Dörscher, Roman Schwarz, Ali Al-Masoudi, Stephan Falke, Uwe Sterr, and Christian Lisdat. Lattice-induced photon scattering in an optical lattice clock. Phys. Rev. A, 97:063419, June 2018.

[57] A.W. Young, W.J. Eckner, W.R. Milner, D. Kedar, M.A. Norcia, E. Oelker, N. Schine, J. Ye, and A.M. Kaufman. Half-minute-scale atomic coherence and high relative stability in a tweezer clock. Nature, 588:408–413, 2020.

[58] Juan A. Muniz, Dylan J. Young, Julia R. K. Cline, and James K. Thompson. Cavity-qed measurements of the $^{87}$sr millihertz optical clock transition and determination of its natural linewidth. Phys. Rev. Research, 3:023152, May 2021.

[59] B.H. Bransden and C.J. Joachain. Physics of atoms and molecules. Prentice-Hall, Harlow, 2003.

[60] J. Sakurai. Modern Quantum Mechanics. Addison-Wesley, New York, 1994.

[61] John Weiner, Vanderlei S. Bagnato, Sergio Zilio, and Paul S. Julienne. Experiments and theory in cold and ultracold collisions. Rev. Mod. Phys., 71:1–85, Jan 1999.

[62] X. Zhang, M. Bishof, S. L. Bromley, C. V. Kraus, M. S. Safronova, P. Zoller, A. M. Rey, and J. Ye. Spectroscopic observation of SU(N)-symmetric interactions in Sr orbital magnetism. Science, 345(6203):1467–1473, September 2014.

[63] M. Bishof, M. J. Martin, M. D. Swallows, C. Benko, Y. Lin, G. Quéméner, A. M. Rey, and J. Ye. Inelastic collisions and density-dependent excitation suppression in a $^{87}$sr optical lattice clock. Phys. Rev. A, 84:052716, Nov 2011.

[64] N. D. Lemke, J. von Stecher, J. A. Sherman, A. M. Rey, C. W. Oates, and A. D. Ludlow. $p$-wave cold collisions in an optical lattice clock. Phys. Rev. Lett., 107:103902, Aug 2011.

[65] W. Greiner, L. Neise, and H. Stöcker. Thermodynamics and Statistical Mechanics. Springer-Verlag, New York, 1995.

[66] D. A. Butts and D. S. Rokhsar. Trapped fermi gases. Phys. Rev. A, 55:4346–4350, Jun 1997.

[67] Georg M. Bruun and Charles W. Clark. Ideal gases in time-dependent traps. Phys. Rev. A, 61:061601, May 2000.

[68] Andrew G. Truscott, Kevin E. Strecker, William I. McAlexander, Guthrie B. Partridge, and Randall G. Hulet. Observation of fermi pressure in a gas of trapped atoms. Science, 291(5513):2570–2572, March 2001.

[69] M. J. Holland, B. DeMarco, and D. S. Jin. Evaporative cooling of a two-component degenerate fermi gas. Phys. Rev. A, 61:053610, Apr 2000.

[70] B. DeMarco and D. S. Jin. Onset of Fermi Degeneracy in a Trapped Atomic Gas. Science, 285(5434):1703–1706, September 1999.

[71] B. DeMarco, S. B. Papp, and D. S. Jin. Pauli blocking of collisions in a quantum degenerate atomic fermi gas. Phys. Rev. Lett., 86:5409–5412, Jun 2001.

[72] B Shuve and J H Thywissen. Enhanced pauli blocking of light scattering in a trapped fermi gas. Journal of Physics B: Atomic, Molecular and Optical Physics, 43(1):015301, dec 2009.

[73] D. Pines and P. Nozieres. The Theory of Quantum Liquids. W. A. Benjamin, Inc., 1966.

[74] Ehud Altman, Eugene Demler, and Mikhail D. Lukin. Probing many-body states of ultracold atoms via noise correlations. Phys. Rev. A, 70:013603, Jul 2004.

[75] M. Greiner, C. A. Regal, J. T. Stewart, and D. S. Jin. Probing pair-correlated fermionic atoms through correlations in atom shot noise. Phys. Rev. Lett., 94:110401, Mar 2005.

[76] Y. Castin. Basic theory tools for degenerate fermi gases. arXiv preprint arXiv:0612613, 2007.

[77] M. Klawunn, A. Recati, L. P. Pitaevskii, and S. Stringari. Local atom-number fluctuations in quantum gases at finite temperature. Phys. Rev. A, 84:033612, Sep 2011.

[78] S.-K. Ma. Statistical Mechanics. World Scientific Publishing, 1985.

[79] T. Rom, T. Best, D. van Oosten, U. Schneider, S. Fölling, B. Paredes, and I. Bloch. Free fermion antibunching in a degenerate atomic fermi gas released from an optical lattice. Nature, 444:733–736, 2006.

[80] T. Jeltes, J.M. McNamara, W. Hogervorst, W. Vassen, V. Krachmalnicoff, M. Schellekens, A. Perrin, H. Chang, D. Boiron, A. Aspect, and C. I. Westbrook. Comparison of the hanbury brown-twiss effect for boson and fermions. Nature, 445:402–405, 2007.

[81] Marvin Holten, Luca Bayha, Keerthan Subramanian, Carl Heintze, Philipp M. Preiss, and Selim Jochim. Observation of pauli crystals. Phys. Rev. Lett., 126:020401, Jan 2021.

[82] M. Gajdal, J. Mostowskil, T. Sowinskil, and M. Zaluska-Koturl. Single-shot imaging of trapped fermi gas. EPL, 115:20012, 2016.

[83] G. E. Astrakharchik, R. Combescot, and L. P. Pitaevskii. Fluctuations of the number of particles within a given volume in cold quantum gases. Phys. Rev. A, 76:063616, Dec 2007.

[84] H.B. Callen and Welton T.A. Irreversibility and generalized noise. Phys. Rev., 83:34–40, Jul 1951.

[85] L.D. Landau, E. M. Lifshitz, and L. P. Pitaevskii. Statistical Physics, Part 2 (Course of Theoretical Physics; Vol. 9). Pargamon Press, 1980.

[86] Christian Sanner, Edward J. Su, Aviv Keshet, Ralf Gommers, Yong-il Shin, Wujie Huang, and Wolfgang Ketterle. Suppression of Density Fluctuations in a Quantum Degenerate Fermi Gas. Phys. Rev. Lett., 105(4):040402, July 2010.

[87] Torben Müller, Bruno Zimmermann, Jakob Meineke, Jean-Philippe Brantut, Tilman Esslinger, and Henning Moritz. Local observation of antibunching in a trapped fermi gas. Phys. Rev. Lett., 105:040401, Jul 2010.

[88] Ahmed Omran, Martin Boll, Timon A. Hilker, Katharina Kleinlein, Guillaume Salomon, Immanuel Bloch, and Christian Gross. Microscopic observation of pauli blocking in degenerate fermionic lattice gases. Phys. Rev. Lett., 115:263001, Dec 2015.

[89] Daniel Greif, Maxwell F. Parsons, Anton Mazurenko, Christie S. Chiu, Sebastian Blatt, Florian Huber, Geoffrey Ji, and Markus Greiner. Site-resolved imaging of a fermionic Mott insulator. Science, 351(6276):953–957, February 2016.

[90] Lawrence W. Cheuk, Matthew A. Nichols, Katherine R. Lawrence, Melih Okan, Hao Zhang, and Martin W. Zwierlein. Observation of 2d fermionic mott insulators of $^{40}$K with single-site resolution. Phys. Rev. Lett., 116:235301, Jun 2016.

[91] William G. Tobias, Kyle Matsuda, Giacomo Valtolina, Luigi De Marco, Jun-Ru Li, and Jun Ye. Thermalization and sub-poissonian density fluctuations in a degenerate molecular fermi gas. Phys. Rev. Lett., 124:033401, Jan 2020.

[92] Immanuel Bloch, Jean Dalibard, and Wilhelm Zwerger. Many-body physics with ultracold gases. Rev. Mod. Phys., 80(3):885–964, July 2008.

[93] C. Menotti, P. Pedri, and S. Stringari. Expansion of an interacting fermi gas. Phys. Rev. Lett., 89:250402, Dec 2002.

[94] L. Vichi. Collisional damping of the collective oscillations of a trapped fermi gas. Journal of Low Temperature Physics, 121(3/4):177–197, 2000.

[95] N.W. Ashcroft and N.D. Mermin. Solid state physics. Thomson Learning, Inc., 1976.

[96] P. Pedri, D. Guéry-Odelin, and S. Stringari. Dynamics of a classical gas including dissipative and mean-field effects. Phys. Rev. A, 68:043608, Oct 2003.

[97] K. M. O'Hara, S. L. Hemmer, M. E. Gehm, S. R. Granade, and J. E. Thomas. Observation of a strongly interacting degenerate fermi gas of atoms. Science, 298:2179–2182, Dec 2002.

[98] T. D. Lee and C. N. Yang. Many-body problem in quantum mechanics and quantum statistical mechanics. Phys. Rev., 105:1119–1120, Feb 1957.

[99] Sara Campbell. A Fermi-degenerate three-dimensional optical lattice clock. PhD thesis, University of Colorado Boulder, 2017.

[100] Martin M. Boyd. High Precision Spectroscopy of Strontium in an Optical Lattice: Towards a New Standard for Frequency and Time. PhD thesis, University of Colorado Boulder, 2002.

[101] Andrew D. Ludlow. The Strontium Optical Lattice Clock: Optical Spectroscopy with Sub-Hertz Accuracy. PhD thesis, University of Colorado Boulder, 2002.

[102] S. Stellmer. Degenerate quantum gases of strontium. PhD thesis, University of Innsbruck, 2013.

[103] M. A. Norcia, A. W. Young, and A. M. Kaufman. Microscopic control and detection of ultracold strontium in optical-tweezer arrays. Phys. Rev. X, 8:041054, Dec 2018.

[104] T.H. Loftus, T. Ido, A.D. Ludlow, M.M. Boyd, and J. Ye. Narrow line cooling: finite photon recoil dynamics. Phys. Rev. Lett., 93:073003, August 2004.

[105] T. A. Savard, K. M. O'Hara, and J. E. Thomas. Laser-noise-induced heating in far-off resonance optical traps. Phys. Rev. A, 56:R1095–R1098, Aug 1997.

[106] P. S. Julienne, A. M. Smith, and K. Burnett. Theory of Collisions between Laser Cooled Atoms. In David Bates and Benjamin Bederson, editors, Advances In Atomic, Molecular, and Optical Physics, volume 30, pages 141–198. Academic Press, January 1992.

[107] D. W. Sesko, T. G. Walker, and C. E. Wieman. Behavior of neutral atoms in a spontaneous force trap. J. Opt. Soc. Am. B, JOSAB, 8(5):946–958, May 1991.

[108] Wolfgang Ketterle, Kendall B. Davis, Michael A. Joffe, Alex Martin, and David E. Pritchard. High densities of cold atoms in a dark spontaneous-force optical trap. Phys. Rev. Lett., 70:2253–2256, Apr 1993.

[109] Simon Stellmer, Benjamin Pasquiou, Rudolf Grimm, and Florian Schreck. Laser cooling to quantum degeneracy. Phys. Rev. Lett., 110:263003, June 2013.

[110] Takashi Mukaiyama, Hidetoshi Katori, Tetsuya Ido, Ying Li, and Makoto Kuwata-Gonokami. Recoil-limited laser cooling of $^{87}Sr$ atoms near the fermi temperature. Phys. Rev. Lett., 90(11):113002, March 2003.

[111] T. Sleator, T. Pfau, V. Balykin, O. Carnal, and J. Mlynek. Experimental demonstration of the optical Stern-Gerlach effect. Phys. Rev. Lett., 68(13):1996–1999, March 1992.

[112] Shintaro Taie, Yosuke Takasu, Seiji Sugawa, Rekishu Yamazaki, Takuya Tsujimoto, Ryo Murakami, and Yoshiro Takahashi. Realization of a SU(2) × SU(6) system of fermions in a cold atomic gas. Phys. Rev. Lett., 105(19):190401, November 2010.

[113] Simon Stellmer, Rudolf Grimm, and Florian Schreck. Detection and manipulation of nuclear spin states in fermionic strontium. Phys. Rev. A, 84(4):043611, October 2011.

[114] Martin M. Boyd, Tanya Zelevinsky, Andrew D. Ludlow, Sebastian Blatt, Thomas Zanon-Willette, Seth M. Foreman, and Jun Ye. Nuclear spin effects in optical lattice clocks. Phys. Rev. A, 76:022510, Aug 2007.

[115] J. C. Hill, W. Huie, P. Lunia, J. D. Whalen, S. K. Kanungo, Y. Lu, and T. C. Killian. Photoassociative spectroscopy of $^{87}$Sr. Phys. Rev. A, 103:023111, Feb 2021.

[116] T. Zelevinsky, M. M. Boyd, A. D. Ludlow, T. Ido, J. Ye, R. Ciuryło, P. Naidon, and P. S. Julienne. Narrow line photoassociation in an optical lattice. Phys. Rev. Lett., 96:203201, May 2006.

[117] Jeong Ho Han, Jin Hyoun Kang, Moosong Lee, and Y. Shin. Photoassociation spectroscopy of ultracold $^{173}$Yb atoms near the intercombination line. Phys. Rev. A, 97:013401, Jan 2018.

[118] V. Dribinski. Reconstruction of abel-transformable images: The gaussian basis-set expansion abel transform method. Rev. Scientific Instruments, 73:2634, 2002.

[119] E.M. Marti. Scalar and Spinor Excitations in a Ferromagnetic Bose-Einstein Condensate. PhD thesis, University of California Berkeley, 2014.

[120] P.G. Mickelson. Trapping and Evaporation of 87Sr and 88Sr Mixtures. PhD thesis, Rice University, 2010.

[121] W. Ketterle, D.S. Durfee, and D.M. Stamper-Kurn. Making, probing and understanding bose-einstein condensates. arXiv preprint arXiv:cond-mat/9904034v2, 1999.

[122] M.T. DePue, S.L. Winoto, D.J. Han, and D.S. Weiss. Transient compression of a mot and high intensity fluorescent imaging of optically thick clouds of atoms. Optics Communications, 180(1):73–79, 2000.

[123] P. L. Kapitza and P. A. M. Dirac. The reflection of electrons from standing light waves. Mathematical Proceedings of the Cambridge Philosophical Society, 29(2):297–300, 1933.

[124] Chen-Lung Hung, Xibo Zhang, Li-Chung Ha, Shih-Kuang Tung, Nathan Gemelke, and Cheng Chin. Extracting density–density correlations fromin situimages of atomic quantum gases. New Journal of Physics, 13(7):075019, jul 2011.

[125] Jean-Claude Diels and Wolfgang Rudolph. Ultrashort laser pulse phenomena. Elsevier, 2006.

[126] T. Udem, R. Holzwarth, and T. Hänsch. Optical frequency metrology. Nature, 416:233–237, 2002.

[127] Jun Ye and Steven T Cundiff. Femtosecond Optical Frequency Comb Technology: Principle, Operation, and Applications. Kluwer Academic Publishers / Springer, 2005.

[128] T. Fortier and E. Baumann. 20 years of developments in optical frequency comb technology and applications. Commun. Phys., 2, 2019.

[129] H.R. Telle, G. Steinmeyer, A.E. Dunlop, J. Stenger, D.H. Sutter, and U. Keller. Carrier-envelope offset phase control: A novel concept for absolute optical frequency measurement and ultrashort pulse generation. Appl Phys B, 69:327–332, 1999.

[130] J.M. Dudley and J.R. Taylor. Ten years of nonlinear optics in photonic crystal fibre. Nat. Photonics, 3:85–90, 2009.

[131] David J. Jones, Scott A. Diddams, Jinendra K. Ranka, Andrew Stentz, Robert S. Windeler, John L. Hall, and Steven T. Cundiff. Carrier-envelope phase control of femtosecond mode-locked lasers and direct optical frequency synthesis. Science, 288(5466):635–639, 2000.

[132] R. Holzwarth, Th. Udem, T. W. Hänsch, J. C. Knight, W. J. Wadsworth, and P. St. J. Russell. Optical frequency synthesizer for precision spectroscopy. Phys. Rev. Lett., 85:2264–2267, Sep 2000.

[133] W. Hänsel, H. Hoogland, M. Giunta, S. Schmid, T. Steinmetz, R. Doubek, P. Mayer, S. Dobner, C. Cleff, M. Fischer, and R. Holzwarth. All polarization-maintaining fiber laser architecture for robust femtosecond pulse generation. Appl. Phys. B, 123, 2017.

[134] W. Hänsel, M. Giunta, M. Fischer, M. Lezius, and R. Holzwarth. Rapid electro-optic control of the carrier-envelope-offset frequency for ultra-low noise frequency combs. In 2017 Joint Conference of the European Frequency and Time Forum and IEEE International Frequency Control Symposium (EFTF/IFCS), pages 128–129, 2017.

[135] M. Giunta, W. Hänsel, M. Lezius, M. Fischer, and R. Holzwarth. Sub-mhz spectral purity transfer for next generation strontium optical atomic clocks. In Conference on Lasers and Electro-Optics, page SM1L.5. Optical Society of America, 2018.

[136] Long-Sheng Ma, Peter Jungner, Jun Ye, and John L. Hall. Delivering the same optical frequency at two places: accurate cancellation of phase noise introduced by an optical fiber or other time-varying path. Opt. Lett., 19(21):1777–1779, Nov 1994.

[137] S. Falke, M. Misera, U. Sterr, and C. Lisdat. Delivering pulsed and phase stable light to atoms of an optical clock. Appl. Phys. B, 107:301–311, 2012.

[138] T.L. Nicholson, S.L. Campbell, R.B. Hutson, G.E. Marti, B.J. Bloom, R.L. McNally, W. Zhang, M.D. Barrett, M.S. Safronova, G.F. Strouse, W.L. Tew, and J. Ye. Systematic evaluation of an atomic clock at $2 \times 10^{-18}$ total uncertainty. Nat. Comm., 6, 2015.

[139] M.A. Cazalilla and A. M. Rey. Ultracold fermi gases with emergent SU(N) symmetry. Rep. Prog. Phys., 77:124401, Nov 2014.

[140] A. V. Gorshkov, A. M. Rey, A. J. Daley, M. M. Boyd, J. Ye, P. Zoller, and M. D. Lukin. Alkaline-earth-metal atoms as few-qubit quantum registers. Phys. Rev. Lett., 102(11):110503, March 2009.

[141] A. V. Gorshkov, M. Hermele, V. Gurarie, C. Xu, P. S. Julienne, J. Ye, P. Zoller, E. Demler, M. D. Lukin, and A. M. Rey. Two-orbital SU(N) magnetism with ultracold alkaline-earth atoms. Nature Physics, 6(4):289–295, April 2010.

[142] S. Taie, R. Yamazaki, S. Sugawa, and Y. Takahashi. An SU(6) mott insulator of an atomic fermi gas realized by large-spin pmeranchuk cooling. Nature Phys., 8:825–830, November 2012.

[143] F. Scazza, C. Hofrichter, M. Höfer, P. C. De Groot, I. Bloch, and S. Fölling. Observation of two-orbital spin-exchange interactions with ultracold SU(N)-symmetric fermions. Nature Physics, 10(10):779–784, 2014.

[144] Christian Hofrichter, Luis Riegger, Francesco Scazza, Moritz Höfer, Diogo Rio Fernandes, Immanuel Bloch, and Simon Fölling. Direct probing of the mott crossover in the SU(N) fermi-hubbard model. Phys. Rev. X, 6(2):021030, June 2016.

[145] Hideki Ozawa, Shintaro Taie, and Y. Takahashi. Antiferromagnetic spin correlation of SU(N) fermi gas in an optical lattice. Phys. Rev. Lett., 121(22):225303, 2018.

[146] Guido Pagano, Marco Mancini, Giacomo Cappellini, Pietro Lombardi, Florian Schäfer, Hui Hu, Xia-Ji Liu, Jacopo Catani, Carlo Sias, Massimo Inguscio, and Leonardo Fallani. A one-dimensional liquid of fermions with tunable spin. Nature Phys., 10(3):198–201, March 2014.

[147] Bo Song, Yangqian Yan, Chengdong He, Zejian Ren, Qi Zhou, and Gyu-Boong Jo. Evidence for bosonization in a three-dimensional gas of SU($n$) fermions. Phys. Rev. X, 10:041053, Dec 2020.

[148] C. He, Z. Ren, B. Song, E. Zhao, J. Lee, Y. Zhang, S. Zhang, and G. Jo. Collective excitations in two-dimensional SU(N) fermi gases with tunable spin. Phys. Rev. Res., 2:012028, Jan 2020.

[149] Simon Stellmer, Florian Schreck, and Thomas C. Killian. DEGENERATE QUANTUM GASES OF STRONTIUM, chapter CHAPTER 1, pages 1–80. 2104.

[150] M. H. Anderson, J. R. Ensher, M. R. Matthews, C. E. Wieman, and E. A. Cornell. Observation of bose-einstein condensation in a dilute atomic vapor. Science, 269(5221):198–201, 1995.

[151] K. B. Davis, M. O. Mewes, M. R. Andrews, N. J. van Druten, D. S. Durfee, D. M. Kurn, and W. Ketterle. Bose-einstein condensation in a gas of sodium atoms. Phys. Rev. Lett., 75:3969–3973, Nov 1995.

[152] Z. Hadzibabic, C. A. Stan, K. Dieckmann, S. Gupta, M. W. Zwierlein, A. Görlitz, and W. Ketterle. Two-species mixture of quantum degenerate bose and fermi gases. Phys. Rev. Lett., 88:160401, Apr 2002.

[153] F. Schreck, L. Khaykovich, K. L. Corwin, G. Ferrari, T. Bourdel, J. Cubizolles, and C. Salomon. Quasipure bose-einstein condensate immersed in a fermi sea. Phys. Rev. Lett., 87:080403, Aug 2001.

[154] G. Roati, F. Riboli, G. Modugno, and M. Inguscio. Fermi-bose quantum degenerate $^{40}$K$-^{87}$Rb mixture with attractive interaction. Phys. Rev. Lett., 89:150403, Sep 2002.

[155] S. R. Granade, M. E. Gehm, K. M. O'Hara, and J. E. Thomas. All-Optical Production of a Degenerate Fermi Gas. Phys. Rev. Lett., 88(12):120405, March 2002.

[156] Takeshi Fukuhara, Yosuke Takasu, Mitsutaka Kumakura, and Yoshiro Takahashi. Degenerate Fermi Gases of Ytterbium. Phys. Rev. Lett., 98(3):030401, January 2007.

[157] Simon Stellmer, Rudolf Grimm, and Florian Schreck. Production of quantum-degenerate strontium gases. Phys. Rev. A, 87(1):013611, January 2013.

[158] B. J. DeSalvo, M. Yan, P. G. Mickelson, Y. N. Martinez de Escobar, and T. C. Killian. Degenerate fermi gas of $^{87}$sr. Phys. Rev. Lett., 105(3):030402, July 2010.

[159] K. Aikawa, A. Frisch, M. Mark, S. Baier, R. Grimm, and F. Ferlaino. Reaching fermi degeneracy via universal dipolar scattering. Phys. Rev. Lett., 112:010404, Jan 2014.

[160] J. M. McNamara, T. Jeltes, A. S. Tychkov, W. Hogervorst, and W. Vassen. Degenerate Bose-Fermi Mixture of Metastable Atoms. Phys. Rev. Lett., 97(8):080404, August 2006.

[161] G. Valtolina, K. Matsuda, W.G. Tobias, J.-R. Li, L. De Marco, and J. Ye. Dipolar evaporation of reactive molecules to below the fermi temperature. Nature, 588:239–243, 2020.

[162] S. Blatt, T. L. Nicholson, B. J. Bloom, J. R. Williams, J. W. Thomsen, P. S. Julienne, and J. Ye. Measurement of optical feshbach resonances in an ideal gas. Phys. Rev. Lett., 107:073202, Aug 2011.

[163] M. Horikoshi, S. Nakajima, M. Ueda, and T. Mukaiyama. Measurement of universal thermodynamic functions for a unitary fermi gas. Science, 327:442–445, Jan 2010.

[164] S. Nascimbène, N. Navon, K.J. Jiang, F. Chevy, and C. Salomon. Exploring the thermodynamics of a universal fermi gas. Nature, 463:1057–1060, Feb 2010.

[165] Kaden R. A. Hazzard, Victor Gurarie, Michael Hermele, and Ana Maria Rey. High-temperature properties of fermionic alkaline-earth-metal atoms in optical lattices. Phys. Rev. A, 85:041604, Apr 2012.

[166] Lars Bonnes, Kaden R. A. Hazzard, Salvatore R. Manmana, Ana Maria Rey, and Stefan Wessel. Adiabatic loading of one-dimensional SU(N) alkaline-earth-atom fermions in optical lattices. Phys. Rev. Lett., 109:205305, Nov 2012.

[167] Laura Messio and Frédéric Mila. Entropy dependence of correlations in one-dimensional SU(N) antiferromagnets. Phys. Rev. Lett., 109:205306, Nov 2012.

[168] E. A. Burt, R. W. Ghrist, C. J. Myatt, M. J. Holland, E. A. Cornell, and C. E. Wieman. Coherence, correlations, and collisions: What one learns about bose-einstein condensates from their decay. Phys. Rev. Lett., 79:337–340, Jul 1997.

[169] Joschka Wolf, Markus Deiß, Artjom Krükow, Eberhard Tiemann, Brandon P. Ruzic, Yujun Wang, José P. D'Incao, Paul S. Julienne, and Johannes Hecker Denschlag. State-to-state chemistry for three-body recombination in an ultracold rubidium gas. Science, 358(6365):921–924, 2017.

[170] S.-K. Yip, J. Huang, and J. Kao. Theory of SU(N) fermi liquids. Phys. Rev. A, 89:043610, April 2014.

[171] Ye-Ryoung Lee, Myoung-Sun Heo, Jae-Hoon Choi, Tout T. Wang, Caleb A. Christensen, Timur M. Rvachov, and Wolfgang Ketterle. Compressibility of an ultracold fermi gas with repulsive interactions. Phys. Rev. A, 85:063615, Jun 2012.

[172] T. D. Lee and C. N. Yang. Many-body problem in quantum statistical mechanics. i. general formulation. Phys. Rev., 113:1165–1177, Mar 1959.

[173] T. D. Lee and C. N. Yang. Many-body problem in quantum statistical mechanics. ii. virial expansion for hard-sphere gas. Phys. Rev., 116:25–31, Oct 1959.

[174] T. D. Lee and C. N. Yang. Many-body problem in quantum statistical mechanics. iii. zero-temperature limit for dilute hard spheres. Phys. Rev., 117:12–21, Jan 1960.

[175] R. K. Pathria and M. P. Kawatra. Quantum statistical mechanics of a many-body system with square-well interaction. Progress of Theoretical Physics, 27(4):638–652, 04 1962.

[176] P Danielewicz. Quantum theory of nonequilibrium processes, i. Annals of Physics, 152(2):239 – 304, 1984.

[177] Leo P. Kadanoff, Gordon Baym, and David Pines. Quantum Statistical Mechanics. CRC Press, 1 edition, 7 2019.

[178] Stefano Giorgini, Lev P. Pitaevskii, and Sandro Stringari. Theory of ultracold atomic fermi gases. Rev. Mod. Phys., 80:1215–1274, Oct 2008.

[179] C. Menotti, P. Perdi, and S. Stringari. Expansion of an interacting fermi gas. Phys. Rev. Lett., 89:250402, December 2002.

[180] D. Guéry-Odelin. Mean-field effects in a trapped gas. Phys. Rev. A, 66:033613, Sep 2002.

[181] Francesco Scazza. Probing SU(N)-symmetric orbital interactions with ytterbium Fermi gaes in optical lattices. PhD thesis, Ludwig-Maximilians-Universität München, 2015.

[182] B Jackson, P Pedri, and S Stringari. Collisions and expansion of an ultracold dilute fermi gas. Europhysics Letters (EPL), 67(4):524–530, aug 2004.

[183] Stefano Giorgini, Lev P. Pitaevskii, and Sandro Stringari. Theory of ultracold atomic fermi gases. Rev. Mod. Phys., 80:1215–1274, Oct 2008.

[184] Y. Castin and R. Dum. Bose-einstein condensates in time dependent traps. Phys. Rev. Lett., 77:5315–5319, Dec 1996.

[185] C. Sanner, L. Sonderhouse, R.B. Hutson, L. Yan, W.R. Milner, and J. Ye. Pauli suppression of atom-light scattering. arXiv preprint arXiv:2103.02216, 2021.

[186] R. Loudon. The Quantum Theory of Light. Oxford University Press, Third Edit., 2000.

[187] E.M. Purcell. Spontaneous emission probabilities at radio frequencies. Phys. Rev., 69:681, 1946.

[188] D. Kleppner. Inhibited spontaneous emission. Phys. Rev. Lett., 47:233–236, 1981.

[189] R.G. Hulet, E.S. Hilfer, and D. Kleppner. Inhibited spontaneous emission by a rydberg atom. Phys. Rev. Lett., 55:2137–2140, 1985.

[190] L. Novotny and B. Hecht. Principles of Nano-Optics. Cambridge University Press, 2006.

[191] K. Helmerson, M. Xiao, and D.E. Pritchard. Radiative decay of densely confined atoms. In International Quantum Electronics Conference 1990, Book of Abstracts. IEEE, 1990.

[192] A. Imamoglu and L. You. Many-body quantum monte carlo wave-function approach to the dissipative atom-field interaction. Phys. Rev. A., 50:2642–2645, 1994.

[193] J. Javanainen and J. Ruostekoski. Off-resonance light scattering from low-temperature bose and fermi gases. Phys. Rev. A., 52:3033–3046, 1995.

[194] T. Busch, J.R. Anglin, J.I. Cirac, and P. Zoller. Inhibition of spontaneous emission in fermi gases. Europhys. Lett., 44:1–6, 1998.

[195] B. DeMarco and D.S. Jin. Exploring a quantum degenerate gas of fermionic atoms. Phys. Rev. A., 58:R4267–R4270, 1998.

[196] J. Ruostekoski and J. Javanainen. Optical linewidth of a low density fermi-dirac gas. Phys. Rev. Lett., 82:4741–4744, 1999.

[197] A. Görlitz, A.P. Chikkatur, and W. Ketterle. Enhancement and suppression of spontaneous emission and light scattering by quantum degeneracy. Phys. Rev. A., 63:41601, 2001.

[198] R.M. Sandner, M. Müller, A.J. Daley, and P. Zoller. Spatial pauli blocking of spontaneous emission in optical lattices. Phys. Rev. A., 84:43825, 2011.

[199] Roberto Onofrio. All-optical cooling of fermi gases via pauli inhibition of spontaneous emission. Phys. Rev. A, 93:033414, Mar 2016.

[200] Torben Müller, Bruno Zimmermann, Jakob Meineke, Jean-Philippe Brantut, Tilman Esslinger, and Henning Moritz. Local observation of antibunching in a trapped fermi gas. Phys. Rev. Lett., 105:040401, Jul 2010.

[201] Luigi De Marco, Giacomo Valtolina, Kyle Matsuda, William G. Tobias, Jacob P. Covey, and Jun Ye. A degenerate fermi gas of polar molecules. Science, 363(6429):853–856, 2019.

[202] A. P. Vinogradov, V. Yu. Shishkov, I. V. Doronin, E. S. Andrianov, A. A. Pukhov, and A. A. Lisyansky. Quantum theory of rayleigh scattering. Opt. Express, 29(2):2501–2520, Jan 2021.

[203] R. H. Dicke. Coherence in spontaneous radiation processes. Phys. Rev., 93:99–110, Jan 1954.

[204] M. Gross and S. Haroche. Superradiance: An essay on the theory of collective spontaneous emission. Physics Reports, 93(5):301–396, 1982.

[205] Patrizia Weiss, Michelle O Araújo, Robin Kaiser, and William Guerin. Subradiance and radiation trapping in cold atoms. New J. Phys., 20(6):063024, jun 2018.

[206] M. C. W. van Rossum and Th. M. Nieuwenhuizen. Multiple scattering of classical waves: microscopy, mesoscopy, and diffusion. Rev. Mod. Phys., 71:313–371, Jan 1999.

[207] W. Guerin, M.T. Rouabah, and R. Kaiser. Light interacting with atomic ensembles: collective, cooperative and mesoscopic effects. J. Mod. Opt., 64(9):895–907, 2017.

[208] A. Heinz, A. J. Park, N. Šantić, J. Trautmann, S. G. Porsev, M. S. Safronova, I. Bloch, and S. Blatt. State-dependent optical lattices for the strontium optical qubit. Phys. Rev. Lett., 124:203201, May 2020.

[209] Yair Margalit, Yu-Kun Lu, Furkan Cagri Top, and Wolfgang Ketterle. Pauli blocking of light scattering in degenerate fermions. arXiv preprint arXiv:2103.06921, 2021.

[210] Amita B. Deb and Niels Kjærgaard. Observation of pauli blocking in light scattering from quantum degenerate fermions. arXiv preprint arXiv:2103.02319, 2021.

[211] J. Rui, D. Wei, A. Rubio-Abadal, S. Hollerith, J. Zeiher, D.M. Stamper-Kurn, C. Gross, and I. Bloch. A subradiant optical mirror formed by a single structured atomic layer. Nature, 583:369–374, 2020.

[212] A. Piñeiro Orioli and A. M. Rey. Dark states of multilevel fermionic atoms in doubly filled optical lattices. Phys. Rev. Lett., 123:223601, Nov 2019.

[213] Matthew A. Norcia, Matthew N. Winchester, Julia R. K. Cline, and James K. Thompson. Superradiance on the millihertz linewidth strontium clock transition. Science Advances, 2(10), 2016.

[214] M. Schulte, C Lisdat, P.O. Schmidt, U. Sterr, and K. Hammerer. Prospects and challenges for squeezing-enhanced optical atomic clocks. Nature Comm., 11, 2020.

[215] D. E. Chang, Jun Ye, and M. D. Lukin. Controlling dipole-dipole frequency shifts in a lattice-based optical atomic clock. Phys. Rev. A, 69:023810, Feb 2004.

[216] A. Cidrim, A. Piñeiro Orioli, C. Sanner, R. B. Hutson, J. Ye, R. Bachelard, and A. M. Rey. Dipole-dipole frequency shifts in multilevel atoms. arXiv preprint arXiv:2102.05786, 2021.